THE UNIVERSITY *of* EDINBURGH

THE UNIVERSITY
of EDINBURGH

The properties and tunable nature of electrochemically-grown peptide-based hydrogels at single microelectrodes

Written and submitted by

Ian J. Bennett-Wright

in fulfilment of the requirements for

the degree of Doctor of Philosophy

College of Science and Engineering

The University of Edinburgh

Submitted and presented in 2023

Declaration

The contents of this thesis have been written by myself, and unless stated otherwise the work described herein is my own. The contents of this thesis have not been submitted for any other degree or professional qualification.

Ian J. Bennett-Wright

July 2023

Acknowledgements

Firstly, I would like to thank my supervisors: Professor Andrew Mount of the University of Edinburgh, and Professor Dave Adams of the University of Glasgow. I am certain you have received a variation of the following dedicated sentiments several dozen times now, but I will candidly state them again: I will forever be grateful for the opportunity you gave me to undertake this work, and for all of the advice, guidance, support and inspiration you have provided to me over these four long years.

To the Centre for Doctoral Training in Intelligent Sensing and Measurement, headed by Professor Andy Harvey and Professor Ian Underwood, and to all of the admin who kept the boat afloat: thank you for funding and supporting this work, but also for bringing this cohort together. The CDT-ISM has allowed us to form strong bonds with a group of truly incredible people, and I am confident these bonds will last well beyond our graduation dates.

To the glue that holds the Mount group together, Justin Elliot and Ilka Schmüser, I owe a most sincere and heartfelt thank you. The wealth of support and knowledge you have imparted on me has been invaluable. The patience you have given me when I have made myself another point on your list of problems to address has been most appreciated, especially in the twilight months of my writing.

To Kayleigh, Fiona, Shan, Gokhan and Richard: thank you for all the lab and office chats, the group meetings, and the advice and feedback you have given me when it comes to my work and how I present it. You made the Mount group a welcoming space, and as corny as this sounds I think I chose the best time to start my PhD, sitting amongst such brilliant minds.

From the Adams group I would like to give particular thanks to Bart Dietrich and Dave Adams for synthesising the powdered gelators that I required to do every single experiment discussed in this thesis. Without them, the work I would have undertaken would have turned out to be a very different beast. I would also like to give thanks to Ana María Fuentes Caparrós and Max Hill for entertaining my requests to capture images of my electrochemically-grown gels on the fluorescence confocal microscope, even though that project and those images didn't make the cut to the thesis (sorry, guys).

To my parents, Karen Dundas and Terry Bennett-Wright, who have sacrificed so much for me to be where I stand today: I owe thanks for being supportive when I have needed the support, for allowing me to be distant when I have needed the space, and for giving me a place to come home to when I needed an escape. I really could not have asked for more of you both.

To my brother, Hunter, thank you for being just that! I always cherish the little time we are able to share when I occasionally visit home. The feedback you gave me for the first draft of my lay summary in this thesis is just one example of your brightness and honesty. You've played a substantial part in helping me improve my communication over the years.

To my aunt, Sue, your graceful benefaction has saved me at least twice from destitution over the course of my career, so to you I owe many thanks.

To my late grandparents, also graceful benefactors throughout my life, I wish you could see me now. Thank you.

To all my friends, old bonds and new, to those from which I regret to have drifted apart, and to those for which I am glad to have reformed: thank you for giving me the best social network I could ever have asked for. You have all saved me countless times from wallowing in PhDespair, and have replaced many of those bad feelings with fond memories and comradery.

To the transient but bright-burning CISMA team and all of its members, it was a blast while it lasted! Special thanks to those members who joined the Seminar team who put up with my annoying weekly requests, and to Salva (O Captain my Captain) a very heartfelt “Oh Mama!” to you.

Not quite lastly and certainly not leastly, I would like to thank Emma Flockhart: a most loving and understanding partner, a shoulder to cry on when times were tough (this was often), a maker of homes to return to, and a true friend to rely on. I struggled for the longest time to explain to you what exactly this thesis is about, and by no means did I expect you to read any of it past this bit. The fact that you were there to just listen to me ramble about it for a few years, and always steer me back to the world outside of my work and away from the gnawing anxiety of it in my head, is a gift that I cannot put into words how much I appreciate being blessed with. Thank you for letting me be so stubborn, and for reminding me to forgive myself.

Finally, to Emma’s fluffy package deal bonus and constant tripping hazard: Jess, you are the most effective alarm clock this world has ever produced. For that, you deserve commendation, and maybe another snack.

Abstract

Microelectrodes possess enhanced mass transport properties which make them desirable over macroelectrodes in point-of-care electrochemical biosensing platforms. Due to their scale, microelectrode biosensors also face a heightened receptiveness to biofouling, often characterised by the nonspecific binding of large molecules and cells to the sensing layer or electrode surface. This ultimately prevents the biosensor from providing an accurate measure of a chemical target. Anti-fouling, semi-permeable membranes are employed to prevent biofouling at point-of-care biosensors. Recently, peptide-based supramolecular hydrogels have been considered as anti-fouling membranes which can encapsulate and immobilise sensing layers. A pH shift generated by the electrochemical oxidation of hydroquinone triggers the self-assembly of dissolved gelator molecules local to the electrode surface, and the peptide-based gelator molecules aggregate into fibre-like structures that entangle to form the gel in these localised acidic regions.

This thesis first explores the extent to which Carb-Ala hydrogels can be tuned at single 25 µm diameter Pt disc microelectrodes under potentiostatic control. Altering the time and potential applied has allowed for the production of gels with different sizes and densities using the same stock gelator solution, identified by pairing optical microscopy (both *in situ* and *ex situ*) and electrochemical impedance spectroscopy techniques. In doing so, a dynamic process between gel assembly and disassembly has been demonstrated: the gels first undergo a loss in density before a collapse in structure, characterised by a gradual increase in transparency and a gradual increase in the diffusion coefficients of a ferro/ferricyanide redox probe.

This process was first observed during continuous gel growth, likely caused by a shift in the dominance of gelator deprotonation and network disassembly (driven by bulk pH 8 gelator solution flux) over self-assembly (driven by proton generation via hydroquinone oxidation). The gels underwent a similar loss in density followed by structure collapse in buffered pH 4.3 and unbuffered pH 0 solutions, though the rate of gel loss was decreased in the lower pH conditions. The phenomenon was also shown not be exclusive to Carb-Ala, as electrochemical gels of a second peptide-gelator BrAV also underwent these changes on a similar timescale. These observations suggested that gel instability might be driven by a concentration gradient of weakly-bound gelator at the electrode surface and the bulk gelator-less solutions.

Lastly, a simple use-case for these gels as enzyme immobilising layers in a 1st generation enzymatic biosensor is presented. To avoid enzyme leaching with the breakdown of gels, electropolymerisation of Carb-Ala post-gelation was utilised as a way of stabilising the pre-formed, tuned microscale gels. The resulting GOx/Carb-Ala polymer-functionalised glucose biosensors were capable of producing progressively greater signals in the presence of increasing concentrations of glucose (due to the electrochemical oxidation of the H_2O_2 produced by the enzymes), and the calibration curves of each electrode displayed characteristic Michaelis-Menten kinetics. The sensors possessed a biologically relevant linear calibration range of 0-4 mM, a maximum sensitivity of 189 ± 9 µM mM^{-1} cm^2, a LOD of 0.33 mM, and a $t_{1/2}$ of up to 44 days at 37 °C.

Lay Summary

Monitoring the health of patients suffering from types 1 and 2 diabetes is a highly important field of research. Glucometers are a type of biosensor used to measure the concentration of glucose, typically in blood. They possess electrodes with chemical receptors to convert a measurable chemical signal of the glucose into an electrical one that can be read by the user. Modern wearable and implantable devices which continuously monitor glucose are constantly being developed to improve the wellbeing of patients by reducing discomfort and providing improved and regular reports of patient health straight to the user.

A part of this development involves making these sensors smaller and less cumbersome. Scaling down the size of the electrodes (from the macro-scale to the micro-scale) also dramatically increases the sensitivity and speed at which these sensors respond to changes in glucose content, which is important for tracking the health of the patient. However, as these electrodes get smaller, they also become more sensitive to biofouling, a process where cells and large biological molecules from the human body attach to the sensor surface and block it from detecting glucose, leading to sensor failure. Preventing fouling is an important part of the development of biosensors, and to do so, anti-fouling layers are deposited on these sensors as part of the manufacturing process. These anti-fouling layers are often membranes, designed to work like sieves that let the smaller glucose molecules pass through them and towards the sensing layer, whilst excluding the larger biofouling materials from doing the same.

Recently, a class of hydrogel has seen potential to act as a new type of anti-fouling layer. Hydrogels are semi-solid materials, made up mostly of water (“hydro”), held within a densely-packed solid network that can make up less than 1% of the material by weight (“gel”). This particular class of hydrogel is made up of networks of entangled fibres, which themselves are made up of biologically-friendly “gelator” molecules. These gels can be grown directly at the surface of a biosensor electrode, within a solution containing gelator molecules, using an electrically-driven chemical process. The gel-coated biosensors can then be used to detect glucose whilst being protected from biofouling.

This thesis first describes how to tune the final size and density of micro-scale hydrogels grown on micro-scale platinum electrodes. A section of this thesis is then dedicated to explaining when these hydrogels may be unstable, and describes how to keep them stable before using them as anti-fouling membranes. At the end of the thesis, a proof-of-concept glucose biosensor is produced, where the gel is used to protect and hold a glucose-sensing layer on a micro-scale platinum electrode surface.

Table of contents

List of abbreviations

AC	Alternating current
BrAV	Bromonapthalene-alanine-valine (gelator)
BQ	Benzoquinone
BSA	Bovine serum albumin
Carb-Ala	Carbazole-alanine (gelator)
CE	Counter electrode
CV	Cyclic voltammogram
DC	Direct current
DI	Deionised (water)
DPV	Differential pulse voltammetry
EIS	Electrochemical impedance spectroscopy
FAD	Flavin adenine dinucleotide
FFC	Ferro/ferricyanide redox couple
GOx	Glucose oxidase
H_2O_2	Hydrogen peroxide
LOD	Limit of detection
MET	Mediated electron transfer
O	Oxidised reactant
R	Reduced reactant
RE	Reference electrode
QH_2	Hydroquinone
QH^-	Singly deprotonated hydroquinone
Q^{2-}	Doubly deprotonated hydroquinone
SNR	Signal-to-noise ratio
W	Warburg element
WE	Working electrode

List of symbols

A	Electrode surface area	m^2
α_{red}	Transfer coefficient for reduction	Unitless
c	Concentration	mol L^{-1}
$c(x,t)$	Concentration, distance x and time t dependant	mol L^{-1}
C	Capacitance	F
c_{bulk}	Bulk concentration	mol L^{-1}
c_{bulk}'	Apparent bulk concentration	mol L^{-1}
C_{DL}	Double layer capacitance	F
$c_{H+}(x,t)$	Concentration of H^+, distance x and time t dependant	mol L^{-1}
c_{Ox}	Concentration of oxidised species	mol L^{-1}
c_{Ox}^b	Bulk concentration of oxidised species	mol L^{-1}
c_{Red}	Concentration of reduced species	mol L^{-1}
c_{Red}^b	Bulk Concentration of reduced species	mol L^{-1}
c_S	Concentration of substrate	mol L^{-1}
D	Diffusion coefficient	m^2 s^{-1}
D_{H+}	Diffusion coefficient of protons via Grotthuss mechanism	m^2 s^{-1}
D_L	Diffusion coefficient from Y_0	m^2 s^{-1}
D_{NL}	Diffusion coefficient from R_{NL}	m^2 s^{-1}
D_{Ox}	Diffusion coefficient of oxidised species	m^2 s^{-1}
D_{Red}	Diffusion coefficient of reduced species	m^2 s^{-1}
E	Potential	V
$E(t)$	Potential, time t dependant	V
E'	Formal potential	V
E_{AC}	Maximum AC potential	V
E_e	Equilibrium potential	V
E_0	Starting potential (CV scan)	V
E_1	Maximum potential (CV scan)	V
E_2	Minimum potential (CV scan)	V

f	Frequency	Hz (s^{-1})
F	Faraday's constant	A s mol^{-1}
η	Solution viscosity	kg m^{-1} s^{-1}
θ	Phase difference	Unitless
i	Current	A
i	Imaginary number $\sqrt{-1}$	Unitless
$i(t)$	Current, time t dependant	A
i_a	Anodic current	A
i_b	Background/blank current	A
i_c	Cathodic current	A
i_L	Limiting current	A
i_{AC}	Current in relation to E_{AC}	A
i_{max}	Maximum current at enzyme saturation	A
j	Flux	mol m^{-2} s^{-1}
k	Boltzmann constant	m^2 kg s^{-2} K^{-1}
k_{Ox}	Rate of electron transfer via electrochemical oxidation	L m^{-2} s^{-1}
k_{Red}	Rate of electron transfer via electrochemical reduction	L m^{-2} s^{-1}
k^{θ}	Standard rate constant of oxidation/reduction	L m^{-2} s^{-1}
K_M	Michaelis-Menten constant	mol L^{-1}
K_M^{app}	Apparent Michaelis-Menten constant	mol L^{-1}
m	Slope	Variable
n	Number of electrons	Unitless
pK_a	Acid dissociation constant	Unitless
pK_a^{app}	Apparent acid dissociation constant	Unitless
r	Electrode radius	m
R	Gas constant	kg m^2 s^{-2} mol^{-1} K^{-1}
r_{HD}	Hydrodynamic radius	m
σ	Standard error of intercept	Variable
t	Time	s

$t_{1/2}$	Enzymatic biosensor half-life	Unitless
T	Temperature	K
R_{CT}	Charge transfer resistance	Ω
R_{NL}	Resistance due to non-linear diffusion	Ω
R_S	Solution resistance	Ω
v	Scan rate	V s^{-1}
v_{max}	Maximum reaction rate at enzyme saturation	mol L^{-1} s^{-1}
v_R	Volumetric reaction rate	mol L^{-1} s^{-1}
x	distance from electrode surface	m
X^2	Goodness of fit	Unitless
Y_0	Admittance from Warburg element	S
$Z(f)$	Impedance, frequency f dependant	Ω
$\|Z\|$	Impedance in relation to E_{AC}	Ω
Z'	Real component of impedance	Ω
$-Z''$	Imaginary component of impedance	Ω

Chapter 1 – Introduction

1.1 Electrochemical biosensing

Biosensors are highly important devices with many applications in modern civilisation, and are a particularly necessary tool in monitoring the health of patients with chronic diseases. There is great demand for the development of new continuous-monitoring biosensor devices that are smaller, faster responding, and wearable; these traits are highly desirable in the healthcare industry as they significantly reduce workload on healthcare professionals by allowing patients to monitor their own health efficiently. On top of the challenge of achieving the list of traits above, these devices are also expected to have long operational lifetimes, high signal-to-noise ratios (SNR) and be resistant to interferants.[1,2]

Biosensors possess two fundamental components upon which they are classified. First is a sensing layer in which bioreceptors are present. The term "bioreceptor" is an umbrella term for biomolecules (such as aptamers, nucleic acids and enzymes[1,3]) that selectively bind with and subsequently react with or catalyse the reaction of a chemical target typically found in biological systems. The bioreceptors constituting sensing layers are typically fixed in place with immobilising agents. The second component of a biosensor is a transducer that converts a change in chemistry due to the reaction between the bioreceptor and chemical target into a signal. Signals produced by the transducer can then be processed electronically and converted into practical readout, which informs on the quantity or quality of the target analyte (Figure 1.1).[1–6] High specificity of the sensing layer to a chemical target is necessary to avoid interference from the many other chemicals that can be found in analyte solutions, and different bioreceptors are employed depending on the specific application or chemical target.

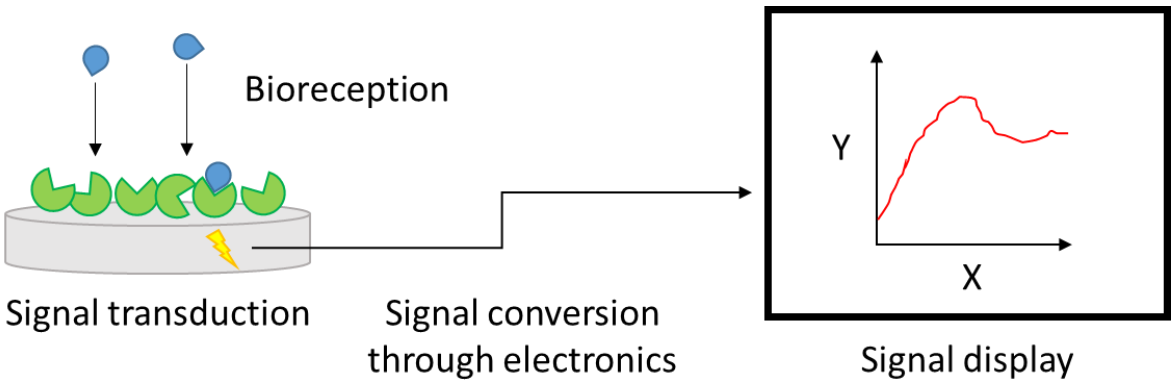

Figure 1.1 The fundamental components of a biosensor. A bioreceptor (green shapes) at the sensing layer selectively reacts with or catalyses the reaction of a chemical target (blue shapes). A chemical change occurs as a result of this process, which is transduced by the transducer. The transduced signal is then converted into data that can be displayed as a digital readout or graphic and be interpreted by an operator.

As their name suggests, electrochemical biosensors transduce the chemical change occurring at sensing layers on or near an electrode into an electrical signal. Signal transduction at electrochemical biosensors can be performed in several ways: current (amperometric),[7–9]

potential (potentiometric),[10] conductivity (conductometric),[11] and electrical impedance (impedimetric)[12] can be measured to infer the presence of a chemical target. Amperometric biosensors, arguably the most common kind of electrochemical biosensor, rely on the application of a fixed applied potential to electrochemically oxidise or reduce an electroactive species. This electroactive species tends to be a chemical product of either the reaction between the bioreceptor with the target biological analyte, or the reaction catalysed by the bioreceptor. The magnitude of current generated as a result of this electrochemical reaction is measured, and is proportional to the concentration of biological target within the bulk solution.[1–6]

This section of the introduction will provide a brief overview of the literature surrounding the development and importance of electrochemical biosensors, the mechanics of enzymatic glucose biosensing, the importance of enzyme immobilisation, and the purpose of semi-permeable membranes.

1.1.1 Microelectrodes in biosensing

There is a drive within the field of electrochemical biosensing to produce new electrode architectures with ever decreasing surface dimensions, not only for the purpose of miniaturising biosensors to improve portability but also in order to enhance the sensor properties.[13–17] Microelectrodes (sometimes referred to as ultramicroelectrodes to highlight the importance of electrode dimensions on the lower end of the micron scale when referring to enhanced properties[18–21]) are electrodes with at least one (and preferably all) surface dimensions on the micron scale, meaning that they can be defined as possessing surface dimensions which are smaller than the thickness of the depletion layers they generate.[21,22] Electrodes at these dimensions hold several advantages with regards to electroanalytical applications over macroelectrodes, due to enhanced mass transport properties at this scale. These advantages include the rapid establishment of steady state currents, lesser IR drops, greater Faradaic current densities (which when applied to sensing provide microelectrodes with enhanced signal-to-noise ratios), a relative insensitivity to convective currents, and the ability to function efficiently in lesser volumes and more resistive sample media.[20–24]

According to Fick's first law, upon the application of a potential at which there is a mass transport limiting current for reaction of a given redox-active species, the depletion of these redox-active species generates a concentration gradient of reactants at the electrode, into which more redox-active species diffuse from the bulk solution.[22] Theoretically, without significant perturbation from movements of the bulk solution (convection), the longer such a potential is applied, the more this depletion layer will expand. At macroelectrodes, the diffusion of electroactive species is predominantly planar to the electrode surface, with a slight radial contribution to diffusion from the edges of the surface (Figure 1.2).[21,25] Solution convection limits the expansion of linear depletion layers generated by macroelectrodes to distances lower than the dimensions of the electrodes themselves.

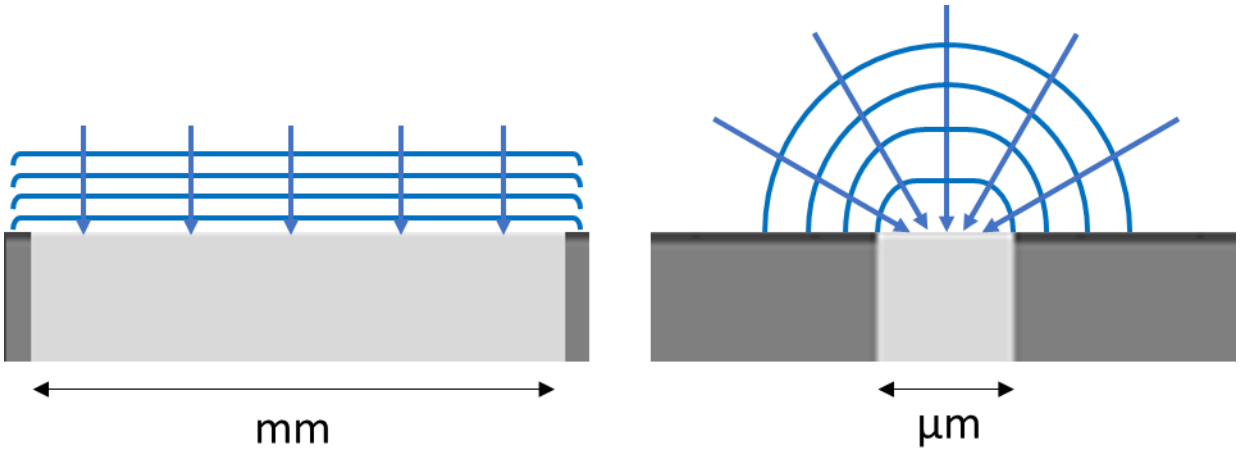

Figure 1.2 Two-dimensional, cross-sectional graphical representations of the linear diffusion profile of a disc macroelectrodes (left) and hemispherical profile of a disc microelectrode (right) respectively. In each case, the depletion layers increase with time, as shown by the successive blue lines. As shown by the arrows, macroelectrodes possess a dominant linear component to their diffusion profile, whereas microelectrodes achieve hemispherical diffusion profiles rapidly, once the size of the depletion layer begins to exceed the dimensions of the electrode surface.

The hemispherical diffusion profile characteristic of microelectrodes is the root of their enhanced properties, and results from increased contributions to flux from the edge of the electrode (Figure 1.2). At short electrolysis times (< 1s),[20–24] the diffusion profile can be approximated to a linear diffusion model, as the depletion layer does not extend to the same distance into solution as the radius of the electrode. Beyond this very short timeframe, as the depletion layer stretches beyond this range, a hemispherical profile develops as fluxes at the edge of the electrode dominate the developing diffusion profile.[20–24] The hemispherical depletion zones at microelectrodes expand in all directions to proportionally counterbalance the consumption of redox active species. This maintains the total rate of mass transfer to microelectrodes, giving them the ability to achieve steady-state currents rapidly. In addition, the inhomogeneous flux results in non-uniform current densities across the electrode surface, with the edge currents and hemispherical diffusion resulting in greater current per electrode unit area in comparison to what is produced at macroelectrodes.[20–24]

1.1.2 Enzymatic biosensors

Enzymatic biosensors possess biocatalytic sensing layers, often immobilised onto electrode surfaces of gold, platinum or conducting carbon electrodes such as graphite or electrode surfaces modified with nanotubes. They function as sensors by catalysing the conversion or breakdown of a particular biologically relevant chemical substrate to other compounds. The enzymes are then regenerated through redox cycling at the active site, ready to facilitate more catalytic reactions.[6,26] Enzyme catalytic activity is strongly influenced by environmental conditions, with most enzymes typically having a narrow operating range of temperatures and pH. Above a certain temperature, enzymes often denature irreversibly into conformations which shut off activity completely. Fortunately, these temperatures are

usually much higher than temperatures relevant to most medical biosensing applications, though even within these operational boundaries reaction and turnover rates vary.[26]

Enzymatic biosensors come in several classifications, referred to commonly as "generations". First generation biosensors, denoted as such due to their being based on the first developmental generation of electrochemical biosensors,[7,27,28] measure the concentration of the target substrate via the electrochemical oxidation or reduction of a product of the enzymatic reaction. For example, oxidase enzymes consume oxygen and produce hydrogen peroxide as a by-product of their catalytic regeneration. The hydrogen peroxide produced at a sensing layer is readily and quantitatively oxidised electrochemically (Equation 1.1), providing a measure of the substrate concentration by proxy:

$$H_2O_2 \rightarrow O_2 + 2e^- + 2H^+ \qquad \textit{Equation 1.1}$$

In amperometric studies, the overall reaction above is typically done by applying a potential of +0.6 V to a platinum working electrode against an Ag/AgCl/Cl^- (often shortened to Ag/AgCl) reference electrode.[6,9,29,30] As enzyme/substrate reactions are generally first-order dependent, currents generated as a result of the sensing process provide a proportional measure of the target substrate, and possess linear relationships with within a certain range of substrate concentration.[5,31]

Arguably the most researched sector of biomedical sensing is in monitoring the health of patients suffering from diabetes mellitus, a health condition in which the patient's body struggles to break down and metabolise glucose.[2,6,32–35] As this condition is one which requires regular or constant monitoring from blood, sweat, interstitial fluids, or other fluid samples, many glucose sensors are designed to be rapidly-produced, point-of-care devices that are capable of being operated without the need for a trained specialist.[1,26,34–38] The miniaturisation of electrode surfaces in electrochemical glucose sensors has also been explored to improve the quality and accuracy of output of data.[9,35,39,40]

Glucose oxidase (GOx), an enzyme of approximately 150-160 kDa,[41,42] is one of the most commonly utilised enzymes in all electrochemical biosensors (Figure 1.3). Though other glucose enzymes exist, GOx is readily available and generally relatively robust, being resilient to environments (temperature ranges, pH, immobilising materials) that other enzymes would find harsh to operate in, making it an ideal enzyme for initial testing of new sensor materials and components. The conception of the first electrochemical glucose sensor involved the use of glucose oxidase immobilised with a cross-linked polymer at an electrode surface,[27] and various first-generation amperometric electrochemical glucose biosensors were designed before the turn of the millennium and the advent of second generation biosensors. The first of these designs used the electrochemical reduction of oxygen as the measure of glucose catalysis,[27,28] though sensors which were designed to oxidise the hydrogen peroxide by-product of glucose catalysis shortly followed,[7] lowering the required potential necessary for the detection and measure of glucose significantly.

Figure 1.3 Crystal structure of glucose oxidase from Aspergillus niger. obtained from the Research Collaboratory for Structural Bioinformatics (RCSB) data centre Protein Data Bank (PDB) archive, structure code 3QVP referring to crystallographic data published in Kommoju et al.[43]

GOx catalyses the oxidation reaction of β-D-glucose (henceforth referred to as glucose) to D-glucono-δ-lactone (henceforth referred to as glucono-δ-lactone, (Equation 1.2).

$$\mathrm{GOx(FAD)} + \mathrm{Glucose} \rightarrow \mathrm{GOx(FADH_2)} + \mathrm{Glucono\text{-}\delta\text{-}lactone} \qquad \textit{Equation 1.2}$$

The flavin adenine dinucleotide (FAD) co-factor bound within the GOx enzyme is reduced by the acceptance of two protons and two electrons (to $FADH_2$), facilitating the electron transfer process during the conversion of glucose. The FAD is then regenerated through re-oxidation by oxygen in solution, producing hydrogen peroxide as a by-product (Equation 1.3), which can then be detected electrochemically to provide a proportionate measure of glucose in the sample volume.[2,33,35,44,45]

$$\mathrm{GOx(FADH_2)} + \mathrm{O_2} \rightarrow \mathrm{GOx(FAD)} + \mathrm{H_2O_2} \qquad \textit{Equation 1.3}$$

1.1.3 Developmental differences between 1st, 2nd and 3rd generation enzymatic biosensors

Though enzymes are highly selective to specific target molecules, this selectivity does not directly translate to the biosensor upon immobilisation at an electrode surface. Oxidases can also lose catalytic function through inhibition. For example, the bisulfite anion is known to turn off the catalytic function of oxidases by stopping the FAD co-factor from functioning.[46,47] First generation amperometric oxidase sensors detect target substrates through the electrochemical oxidation of hydrogen peroxide. However, the +0.6 V potential applied (at Pt against an Ag/AgCl/Cl^- reference) to do so is also sufficient to oxidise other small chemical compounds. For instance, when measuring the concentration of glucose in biological media such as human blood, one must consider that these samples can include interferants such as uric acid and ascorbic acid which are redox active at the same potentials as hydrogen peroxide. The presence of these interferants can produce additional currents that do not represent the substrate reaction, and thus provide incorrect amperometric measurements of glucose.[26,29,45,48]

The issues of interference, lack of co-substrates (e.g. insufficient oxygen in solution for oxidases) and the need for external co-factors (e.g. dehydrogenases lack the internal FAD co-factor necessary for catalytic action, so FAD must be included as an external co-factor in the sensing layer)[2,26] are resolved when moving to second and third generation biosensors. Second generation enzyme biosensors function through mediated electron transfer (MET), engaging in redox chemistry with a mediator (such as solubilised ferrocene and solid osmium polymers) that carries electrons from enzyme co-factor to the electrode surface.[29] Mediators reduce the redox potential required to detect enzymatic reactions to the redox potential of the mediator, avoiding interferant electrochemistry. Mediators also remove the dependence on the O_2 co-substrate that oxidase enzymatic sensors have, allowing them to function more effectively within biological media.[26,29] Solid mediators such as osmium polymers can also reduce biosensor response times, due to the transmission of electrical signals being mass transport independent.[29] Third generation biosensors go a step further by attempting to directly wire the redox centres of immobilised enzymes directly to electrode surfaces, removing the dependency on co-substrates, co-factors, and mediators.[26,31]

Unfortunately, second and third generation biosensors also suffer from issues. The mediators in second generation biosensors are often made from toxic, non-biocompatible materials, meaning additional bio-friendly layers need to be added to separate and protect biological material from these mediators, complicating sensors design and even restricting mass transport of substrate. In addition, electron transfer from enzyme to surface requires specific enzyme orientations, which if not controlled when immobilising during sensing layer production can lead to weak connections, and thus weak responses to substrate recognition and reaction.[2,26,35] Third generation biosensors are still a nascent technology,[26] and on top of the issues mentioned above, works interpreted as evidence of direct electron transfer from GOx enzymes to electrode surfaces have recently been refuted.[41]

All this to say: first generation biosensors, despite having issues that are resolved by the later generations, are the most established and arguably easiest to implement platform for proof-

of-principle testing. Though scarcely seen in modern studies, first generation glucose biosensors benefit from the robustness of the GOx enzyme, which allows studies to focus on the characterisation and functionality of new materials for enzyme immobilisation and anti-fouling properties of membranes.[8,49–51]

1.1.4 Biofouling and interference

Electrochemical biosensors can experience failure in several areas. Enzymatic sensing layers can lose activity due to changes in environmental conditions such as temperature changing beyond enzyme operational range, the presence of inhibiting species turning off the catalytic function of enzymes, and by enzymes leaching out of the biosensor over time. In addition to these failure points, biofouling (also known as biological passivation) must be addressed. Biofouling is defined as the nonspecific adsorption of macromolecules and cells to an electrode surface, sensing layer and/or membrane. The effect of this adsorption is the passivation of whichever part of the sensor has experienced the fouling, which can manifest as uncontrollable changes to the magnitude or variability of an electrode sensor response to stimuli.[26,52,53] Electrode passivation involves adsorption directly onto electrode surfaces, though the surfaces of electrochemical biosensors are usually thoroughly functionalised due to the sensing layers anchored to them, hindering further passivation in this form.[52,54] This often makes sensing layer/membrane passivation the more common of the two faults for enzymatic biosensors, where large macromolecules block substrates from accessing a significant area of the sensor, significantly reducing the ability of that layer to function (Figure 1.4).[52]

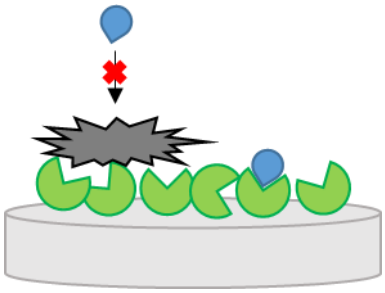

Figure 1.4 Biofouling via sensing layer/membrane passivation. The target substrates (blue) are prevented from reaching the enzyme sensing layer (green) due to the nonspecific adsorption of a large macromolecule (black) atop the sensing layer.

It is vital that biofouling is accounted for when designing sensors for *in vivo* sensing of non-pre-treated biological media, which are full of materials that can foul a biosensor. This is especially important for electrochemical sensors with electrode surfaces on the micro and nanoscale, which due to their scale are more significantly impacted by sensor passivation through adsorption of macromolecules and cells. The pre-emptive removal of biofouling species from a medium of interest is the most definitive answer to the prevention of biological passivation. However, this answer quickly becomes impractical for point-of-care biosensors. The time, effort and resources required to pre-treat media to remove biofouling material is not only an inefficient process, but can also alter the sample (e.g. potentially by changing substrate concentrations), and additionally defeats the purpose of a rapid response, easy to

use, continuous monitoring point-of-care biosensor. Therefore, the use of protective anti-fouling layers built into the biosensor becomes the most practical solution.

Anti-fouling prevention is typically achieved with permselective or semi-permeable membranes. These layers act as sensor-localised molecular filters that discriminate molecules and particles through properties such as electrostatic charge and size, allowing target analytes and substrates to diffuse through and towards the sensing layer whilst preventing biofouling materials from doing the same. Additionally, whilst the influence of interferants can be removed through the use of second and third generation sensing layers, anti-interference layers can also be incorporated into first generation biosensors to prevent the effect.[26,52]

Anti-fouling polymeric membranes can be drop-coated,[17] spin-coated[11] or vapour-deposited[55] across biosensors to form gels that prevent biofouling. Polymeric hydrogels like those of polyethylene glycol diacrylate (PEGDA) have been used to trap enzymes and prevent macromolecules and cells in whole blood samples from biofouling components necessary for sensing.[56] Permselective layers such as overoxidised polyprrole (PPy_{OX}) can reject and prevent the transport of interferants such as ascorbic acid and uric acid[8,49] Zwitterionic polymers and self-assembled monolayers have been shown to prevent biofouling and also exhibit bactericidal properties.[57–60] Polymer gel coatings such as those made whole or in part with polymers such as Nafion and PDMS can prevent biofouling via size-exclusion and prevent the transport of anionic interferants.[5,26,52,61,62] Materials like Nafion have also been grown as thin films directly at surfaces by electropolymerisation, though this method has been used for enzyme immobilisation rather than as anti-fouling layer production.[26]

1.1.5 Enzyme immobilisation techniques

Enzyme immobilisation is fundamental to the operation of enzymatic biosensors. Without an immobilising agent to anchor, bond, trap or encapsulate the enzyme near the electrode surface, enzymes that make up the sensing layer will leak into liquids in which the sensor is immersed. By preventing sensing layer leakage, immobilisation increases the functional lifetime of the biosensor, improving sensor operational stability and improving storage period lifetime.[2,63] As with variable factors like the temperature and pH of the surrounding solution, the choice of immobilisation method can affect the catalytic activity of enzymes. Though immobilising layers can increase sensor lifetime by holding enzymes in place, restricting the motion of enzymes through space and the movement of specific enzyme components required to undergo catalysis can have an adverse effect on the productivity of a given enzyme. Therefore, immobilisation methods should be carefully considered so as to mitigate loss of enzyme activity.[1,9,31,63]

Methods of enzyme immobilisation can be broadly broken down into four main categories (Figure 1.5):[1,26,64] covalent bonding to a surface, cross-linking between enzymes, surface adsorption, and encapsulation/entrapment. Covalent bonding and cross-linking of enzymes both involve chemically bonding enzymes, either onto surfaces or to other enzymes, and sometimes require those enzymes to be modified first to allow for chemical bonding. These immobilisation methods make for sensors with high operational stability, though do not entirely eliminate the problem of enzyme leaching.[64] In addition, common cross-linkers like glutaraldehyde, which make sensing layers that are chemically stable,[12,33] also restrict enzyme

mobility and confine conformational shapes so that the catalytic activity of the bound enzymes are significantly reduced.[64]

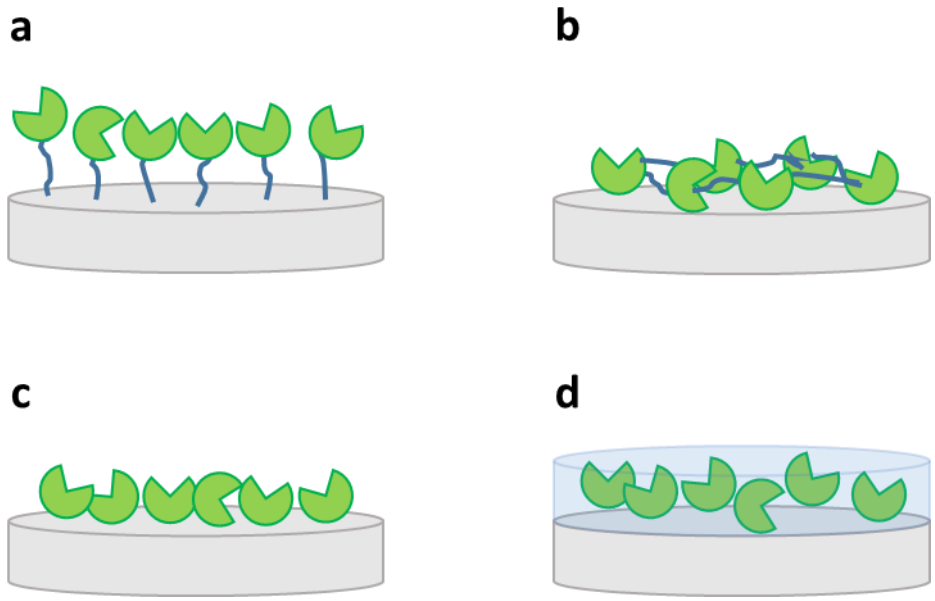

Figure 1.5 The four fundamental methods of immobilising enzymes, summarised by Imam et al.[64]: (a) covalent bonding of enzymes to surfaces; (b) cross-linking between enzymes; (c) adsorption of enzymes at surfaces; (d) enzyme encapsulation/entrapment.

Surface adsorption and encapsulation/entrapment processes often bind enzymes through physical rather than chemical bonding. Enzyme adsorption is accomplished by using surfaces modified with complementing functionalities and materials like metal oxide nanoparticles,[10,11,38] which bind through intermolecular interactions to enzymes. This method often requires a high load of enzymes to make efficient adsorption possible, wasting much of the enzyme in the process. Additionally, due to often weak binding with the modified electrode surfaces, enzyme adsorption requires additional layers to prevent enzyme leaching.[64]

Encapsulation or entrapment methods physically confine enzymes within the gaps of matrices.[1,9,64–66] Gels are commonly used for this immobilisation method, and are typically grown around the enzyme in a sol-gel transition that traps the enzyme in the growing matrix.[64,66] As previously discussed, the environment to which an enzyme is exposed affects its activity and effectiveness as a biological catalyst. Matrices such as those found in gels therefore look to replicate the biological membrane environment to which enzymes are most suited.[1] Although enzyme leaching is still an issue that can occur over time (e.g. as a membrane breaks down), this method of immobilisation often offers reduced leaching and increased operational stability compared to adsorption methods.[1,64] These factors make encapsulation within materials such as gels a particularly effective and enzyme-friendly method of enzyme immobilisation. The work in this thesis attempts to develop encapsulation and entrapment of enzymes using electrochemically grown supramolecular hydrogels.

1.2 Supramolecular hydrogels

Gels are soft solid-like materials composed of a solvent contained within a three-dimensional solid-phase network. Hydrogels, as their name suggests, have an aqueous liquid phase immobilised within the cross-linked matrix. These networks make can make up less than 2 wt% of the entire material,[67,68] yet are still capable of significantly slowing the flow of the liquid phase. This is understood to be due to the surface tension and capillary forces generated through the multitude of gaps and pores within the entangled structure of these networks.[67] The type of bonding between the monomer units that compose the cross-linked networks, the cross-linkages, and the medium these networks contain within them, are factors used to classify the gel.

The solid-phase gel networks are generally broken down into the categories of polymeric and supramolecular. The networks in polymeric gels are composed of polymers that are cross-linked through covalent bonds.[69,70] In comparison, supramolecular gels, also known as molecular gels,[71] are built from a network of self-assembled low molecular weight gelator molecules (LMWGs), aggregated together through interactions such as hydrogen bonding, π-π stacking and other non-covalent interactions.[72] Whilst polymeric gels are more structurally robust due to the chemically bonded cross-linked fibres constituting their networks, supramolecular hydrogels benefit from thermodynamic reversibility, which means they are capable of being disassembled with ease under certain conditions.[73–76] In this case, gelator molecules which initially formed the networked supramolecular structure can be dissolved back into aqueous solvent, whilst retaining the ability to self-assemble again by applying another trigger to grow a new fibrous network.[72]

The next section of the introduction will provide a brief overview of the mechanics and methods of triggering self-assembly, how surfaces have been used to influence gelation, and will discuss the control over gelation offered by electrochemical techniques.

1.2.1 Self-assembly

All supramolecular gels are formed by first dissolving monomer units into a solution. The process of self-assembly is hierarchically complex, with molecular and aggregate interactions occurring on different length scales.[67,68,77] In water, molecular interactions between gelator molecules and the solvent environment dictate how these monomers bind together into colloidal aggregates. The dimensions and morphologies of these aggregates are dependent on the molecular structure of the gelator molecules themselves as well as the environmental conditions such as solvent hydrophobicity, temperature, pH, and salt concentration.[78–82] For example, when initially solvated in water, gelator molecules tend to aggregate in order to increase favourable gelator/gelator interactions such as H-bonding and π-π stacking, and to minimise unfavourable hydrophobic interactions with water. The structure and size of these gelator aggregates can vary, with common structures being micelles, sheets, and fibres, and can be identified and studied using analytical techniques such as small angle neutron and x-ray scattering.[80,83–87]

When conditions within these solutions are changed in such a way that make these aggregates more insoluble within their medium, these aggregates undergo further structural

changes, often growing in size in order to minimise the unfavourable intermolecular interactions with the solvent. If conditions within a gelator solution are such that a critical gelation concentration is achieved within a given volume, these changes can trigger aggregates to self-assemble further. For example, in aqueous solutions it is common for peptide-based gelators to form worm-like micelles that grow in size, forming 1D fibres which begin to entangle and then cross-link with other aggregates to form three-dimensional hydrogel networks (Figure 1.6).[71,80,88–91]

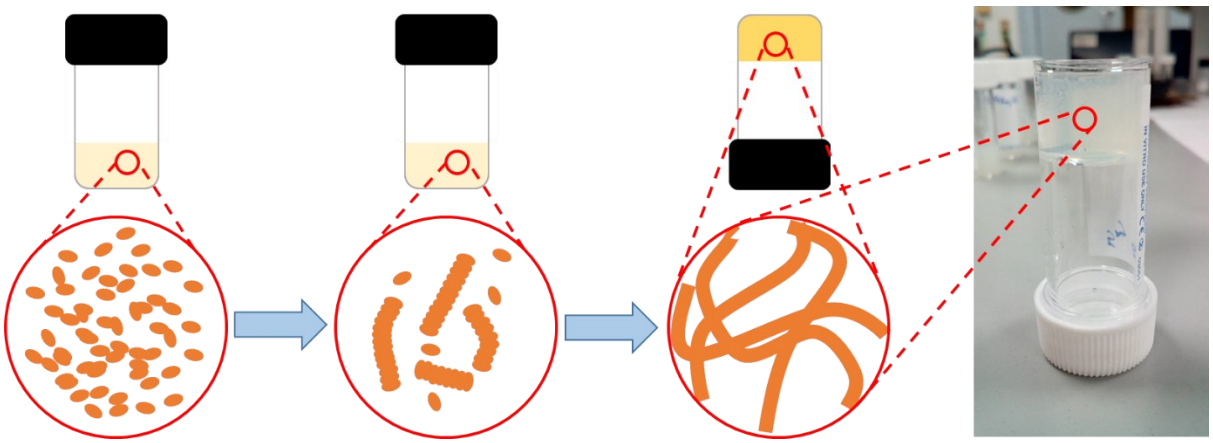

Figure 1.6 Depictions of the three hierarchical levels of supramolecular gel self-assembly. When dissolved, the gelator molecules (depicted as orange discotic shapes in this figure) interact with the solvent and other gelator molecules, aggregating through intermolecular bonds to form aggregates such as 1D fibres. Those aggregates undergo further changes when conditions within the solution decrease solubility, which can lead to further changes in aggregate structure (to minimise unfavourable interactions with the solution environment), such as fibre growth, and subsequent entanglement and cross-linkage into 3D networks. These 3D networks constitute the final gel. An example on the right shows a supramolecular hydrogel grown within the confines of a 5 mL vial, which has the structural integrity to be inverted without collapsing.

1.2.2 Methods of triggering self-assembly

Gelation in water through self-assembly is a delicate non-linear process, following different pathways through the influence of various factors. When carefully considered, one can control the self-assembly processes and yield gels with predictable properties.[79,89,90,92,93] Factors that play an important role in how self-assembly proceeds include temperature, ionic strength, pH, and surface properties such as roughness and topography. Along with the factors above, methods of triggering gelation vary, with different methods also having fundamental effects on how the hierarchical growth proceeds and yielding gels with differing properties.[82,94] Such methods include solution heat-cool cycles,[79,95–97] additions of aqueous solutions to organic gelator solutions (solvent-switches),[94,98,99] additions of salt to high pH gelator solutions,[100] using enzymes to synthesise gelator molecules or chemical fuels in solution,[73,74,101,102] and via pH-switches.

pH-switching techniques involve inducing a pH drop within a gelator solution to protonate dissolved and deprotonated gelator molecules, which usually feature carboxylate functional groups. By lowering the pH sufficiently below the apparent acid dissociation constant of the

gelator aggregate pK_a^{app}, the carboxylate functionalities are protonated to carboxylic acids. This process reduces gelator electrostatic repulsion and increases molecule/aggregate hydrophobicity, allowing aggregates to entangle and cross-link, triggering self-assembly (Figure 1.7).[80,90–92] The simplest acid-trigger involves the addition of a dilute acid to a gelator solution,[103,104] though this method was refined to the point of allowing homogenous gelation to occur throughout the bulk of gelator solutions through the addition of glucono-δ-lactone as an acid precursor.[105,106] Other methods developed to control bulk pH shifts include the enzymatic control of pH,[107] the hydrolysis reaction of boronic acid and glucose,[108] shining UV light on a photoacid generator,[109,110] and the autoxidation of dopamine.[84]

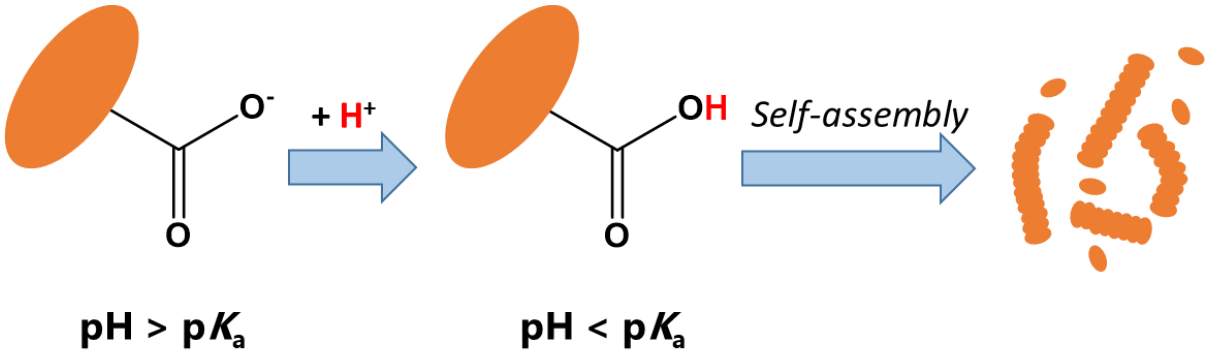

Figure 1.7 Simplified process of pH-triggered self-assembly of gelator molecules (displayed here as orange discotic shapes) with carboxylate functionalities. When pH of an aqueous gelator solution is lowered from where pH measures greater than the gelator molecule/aggregate pK_a^{app} to where pH measures lower than the gelator molecule/aggregate pK_a^{app}, the carboxylate functionality is protonated. This decreases the solubility of the gelator, triggering self-assembly.

Spatial control of supramolecular self-assembly has also been studied using modified surfaces which localise gelation within specific volumes. Gelation can be assisted and nucleated through various surface modifications, such as those that attract and form intermolecular bonds with dissolved gelator molecules,[111–115] those modified with catalysts/enzymes that synthesise gelators and trigger their assembly locally,[116–121] and through modified surfaces that release protons to protonate gelators with carboxylate functionalities.[122,123]

1.2.3 Electrochemical pH-triggered gelation

Electrochemical techniques offer both spatial and temporal control over gelation. This is generally achieved by reducing or oxidising a chemical species within a gelator solution, in order to generate a concentration gradient (typically a pH gradient) in which a gelation trigger is localised.[124] The application of potentials to drive redox currents is required to induce this process, and can be adjusted or turned on and off without removing the electrodes from the gelator solution. This combined spatiotemporal control therefore allows for the growth of hydrogels with shapes, sizes and densities that can be tuned through fine control of the electrochemistry.[124] The electrodeposition of chitosan and alginate gels has been triggered via the generation of high pH zone,[125–131] whilst dissipative cysteine-based gels have been fuelled electrochemically.[132] Johnson *et al.* were first to use the electrochemical oxidation of hydroquinone to generate a low pH zone at a macroelectrode surface, facilitating the self-

assembly of a dipeptide gelator.[75] The inclusion of hydroquinone lowers the required potential for proton production necessary for gelation, which would otherwise be achieved through the oxidation of water. This method was developed primarily to prevent the production of O_2 gas, as the bubbles of gas trapped within the growing gel networks would reduce the structural strength of the gels by increasing network heterogeneity.[75] The two-electron electrochemical oxidation of hydroquinone to benzoquinone[133] produces a local pH drop at the working electrode, triggering self-assembly within the low pH region (Figure 1.8).[124,134] Other studies have used this electrochemical pH-trigger to grow hydrogels with agrose,[135] cysteine[136], and other dipeptide-based gelators[75,76,137–142].

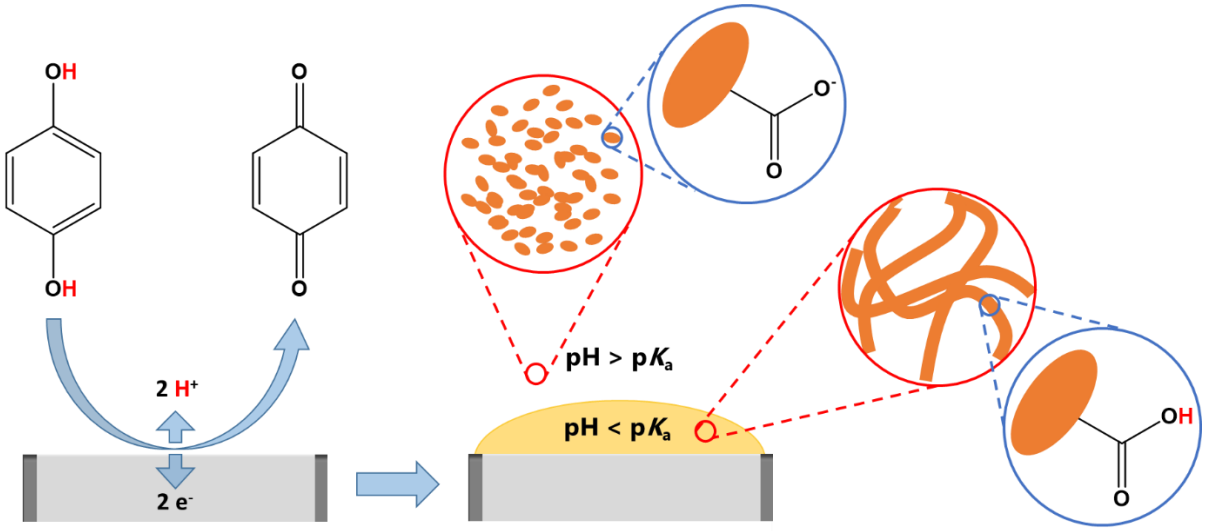

Figure 1.8 Generation of pH shift at electrode surface, produced via the electrochemical oxidation of hydroquinone to benzoquinone by application of a redox potential. In the bulk solution where pH is greater than the gelator pK_a^{app} (outside the acidic zone, pH > pK_a^{app}) carboxylate functionalities of dipeptide gelator molecules (depicted here as orange discotic shapes) remain deprotonated. Gelator molecules within the acidic zone (hemisphere-like shape at electrode surface, pH < pK_a^{app}) are protonated, initiating pH-triggered self-assembly into 1D aggregates that entangle to form a 3D gel network.

1.2.4 Supramolecular hydrogels as materials in biosensing applications

Synthetic hydrogels are capable of size-exclusion, and with fine-tuning of gelation the networks of these materials are capable of mimicking the structure and properties of biological tissues.[69] This makes hydrogels excellent soft materials for various medical applications,[71,72] and suitable scaffolds for the encapsulation of enzymes within and under their networks, acting as both semi-permeable membranes for anti-fouling purposes and for enzyme immobilisation.[5] Polymeric hydrogels and electropolymerised films are commonly employed as anti-fouling coatings[36,51,52,58,61] and enzyme immobilising layers.[8,9,49,56,65,143] Supramolecular hydrogels have also been selected for prospective biomedical applications, with self-assembled peptide-based hydrogels being applied in cell-growth,[95,96,144] drug delivery,[97,145] tissue engineering,[146] and recently as immobilisation layers[147] and anti-fouling layers[99,140] in electrochemical biosensors.

In a novel example of utilising peptide-based hydrogels in biosensing, Wang *et al.*[99] produced dopamine biosensors by incorporating the antibiotic ciprofloxacin and catalytic gold nanoparticles into supramolecular hydrogel matrices at glassy carbon macroelectrodes. These gels were formed by drop-coating the gelator solution (in which the antibiotic and nanoparticles could be dispersed) at the macroelectrodes, triggering gelation via a DMSO-to-water solvent-switch, and trapping the new components in the resulting fibrous gel network. The gold nanoparticles allowed for the catalysis of dopamine into dopamine quinone, detected via the electrochemical catalytic regeneration of the nanoparticles. In addition, the antibacterial property of the ciprofloxacin-doped hydrogels prevented membrane biofouling from *E. coli*, and allowed the sensor to detect and measure dopamine concentration in the testing medium with only a slight reduction in current responses in comparison to the tests without the bacteria being present.[99]

Most relevant to the work presented in this thesis, Piper *et al.*[140] investigated the anti-fouling properties of a supramolecular hydrogel membrane grown upon a peptide nucleic acid self-assembled sensing monolayer at an array of Pt nanoelectrode surfaces. They utilised the electrochemical oxidation of hydroquinone to galvanostatically control the pH-triggered self-assembly of a carbazole-capped alanine gelator, Carb-Ala, the electrodeposition of which had been established in a previous work.[139] Other similarly structured peptide gelators capped with carbazole functionalities were found to possess low cytotoxicity towards HeLa cells, in gelator solution concentrations of up to 0.1 wt%.[148] This factor highlighted the potential suitability of hydrogels made from Carb-Ala and other gelators of this family when applied as novel anti-fouling layers for electrochemical biosensors. When compared against an unprotected sensor, Piper *et al.* found that the Carb-Ala gel prevented bovine serum albumin (BSA) adsorption onto the sensing monolayer.[140] By following BSA adsorption through changes in charge transfer at the sensing electrode, they found the sensor without the hydrogel membrane had experienced biofouling immediately upon exposure to the buffered solution, whilst the hydrogel-coated sensor experienced no change over 3 hours of testing, thereby proving its ability to prevent biofouling from BSA.[140]

1.3 Thesis objectives

The self-assembly of supramolecular hydrogels constructed with peptide-based gelator units at microelectrode surfaces has been explored in only a few studies.[132,136,140] How aggregate entanglement proceeds from surface to bulk solution is not fully understood when gelation is initiated through electrochemically induced pH-triggers at microelectrode surfaces. Knowledge of these mechanisms is valuable, as the localised growth of these physically bonded networks provides a great platform for the production of soft, biologically friendly, membranous materials that mimic biological matter for biosensing applications. With fine tuning of properties seemingly achievable through delicate control over electrochemical parameters and techniques, and materials such as the Carb-Ala gelator having shown to exhibit anti-fouling properties through size exclusion,[140] it stands to reason that the density of these hydrogel networks could be tuned to create membranes that can exclude or trap smaller macromolecules. For such a study, the firm platform of first generation biosensing can be applied to test these tuned hydrogels as semi-permeable membranes and immobilising layers for enzymes.

The objectives in this thesis are as follows:

1. To explore the extent to which electrochemically triggered hydrogel growth can be tuned at microelectrode surfaces to yield gels with differing properties, such as size and density, though the introduction of slight changes to electrochemical settings rather than changes in the gelator solution.
2. To characterise final microscale hydrogel properties by coupling low-cost electrochemical analytical techniques with optical analytical techniques to understand how the self-assembly of gelator molecules and aggregates proceeds at these scales *in situ*.
3. To apply these electrochemically grown hydrogels to enzymatic biosensing, as semi-permeable membranes and immobilising layers for first generation glucose biosensing.

1.4 References

1 D. Grieshaber, R. MacKenzie, J. Vörös and E. Reimhult, *Sensors*, 2008, **8**, 1400–1458.

2 S. A. Pullano, M. Greco, M. G. Bianco, D. Foti, A. Brunetti and A. S. Fiorillo, *Theranostics*, 2022, **12**, 493–511.

3 J. E. Frew, H. Allen and O. Hill, *Anal. Chem.*, 1987, **59**, 933–944.

4 D. J. Caruana and S. Howorka, *Mol. Biosyst.*, 2010, **6**, 1548–1556.

5 D. R. Thévenot, K. Toth, R. A. Durst and G. S. Wilson, *Biosens. Bioelectron.*, 2001, **16**, 121–131.

6 P. D'Orazio, *Clin. Chim. Acta*, 2003, **334**, 41–69.

7 G. G. Guilbault and G. J. Lubrano, *Anal. Chim. Acta*, 1973, **64**, 439–455.

8 F. Palmisano, R. Rizzi, D. Centonze and P. G. Zambonin, *Biosens. Bioelectron.*, 2000, **15**, 531–539.

9 P. N. Bartlett and D. J. Caruana, *Analyst*, 1992, **117**, 1287–1292.

10 K. Khun, Z. H. Ibupoto, J. Lu, M. S. Alsalhi, M. Atif, A. A. Ansari and M. Willander, *Sensors Actuators, B Chem.*, 2012, **173**, 698–703.

11 S. K. Mahadeva and J. Kim, *Sensors Actuators, B Chem.*, 2011, **157**, 177–182.

12 P. Naderi Asrami, S. A. Mozaffari, M. Saber Tehrani and P. Aberoomand Azar, *Int. J. Biol. Macromol.*, 2018, **118**, 649–660.

13 H. L. Woodvine, J. G. Terry, A. J. Walton and A. R. Mount, *Analyst*, 2010, **135**, 1058–1065.

14 I. Schmueser, A. J. Walton, J. G. Terry, H. L. Woodvine, N. J. Freeman and A. R. Mount, *Faraday Discuss.*, 2013, **164**, 295–314.

15 N. J. Freeman, R. Sultana, N. Reza, H. Woodvine, J. G. Terry, A. J. Walton, C. L. Brady, I. Schmueser and A. R. Mount, *Phys. Chem. Chem. Phys.*, 2013, **15**, 8112–8118.

16 R. Sultana, N. Reza, N. J. Kay, I. Schmueser, A. J. Walton, J. G. Terry, A. R. Mount and N. J. Freeman, *Electrochim. Acta*, 2014, **126**, 98–103.

17 M. Falk, R. Sultana, M. J. Swann, A. R. Mount and N. J. Freeman, *Bioelectrochemistry*, 2016, **112**, 100–105.

18 J. Heinze, *Angew. Chem. - Int. Ed.*, 1993, **32**, 1268–1288.

19 C. Amatore, C. Pebay, L. Thouin, A. Wang and J. Warkocz, *Anal. Chem.*, 2010, **82**, 6933–6939.

20 R. J. Forster, *Chem. Soc. Rev.*, 1994, **23**, 289–297.

21 A. J. Bard and L. R. Faulkner, *Electrochemical Methods: Fundamentals and Applications*, John Wiley & Sons, New York, 2nd ed., 2001, vol. 677.

22 K. Stulik, C. Amatore, K. Houb, V. Marecek and W. Kutner, *Pure Appl. Chem.*, 2000, **72**,

1483–1492.

23 C. M. A. Brett and A. M. O. Brett, *Electroanalysis*, Oxford University Press Inc., New York, 1st edn., 1998.

24 A. C. Fisher, *Electrode Dynamics*, Oxford University Press Inc., New York, 1st edn., 1996.

25 K. Ngamchuea, S. Eloul, K. Tschulik and R. G. Compton, *J. Solid State Electrochem.*, 2014, **18**, 3251–3257.

26 G. Rocchitta, A. Spanu, S. Babudieri, G. Latte, G. Madeddu, G. Galleri, S. Nuvoli, P. Bagella, M. I. Demartis, V. Fiore, R. Manetti and P. A. Serra, *Sensors*, 2016, **16**, 1–21.

27 L. C. Clark and C. Lyons, *Ann. N. Y. Acad. Sci.*, 1962, **102**, 29–45.

28 S. J. Updike and G. P. Hicks, *Nature*, 1967, **214**, 986–988.

29 P. Kavanagh and D. Leech, *Phys. Chem. Chem. Phys.*, 2013, **15**, 4859–4869.

30 S. B. Hall, E. A. Khudaish and A. L. Hart, *Electrochim. Acta*, 1998, **43**, 579–588.

31 M. Mehrvar and M. Abdi, *Anal. Sci.*, 2004, **20**, 1113–1126.

32 N. S. Oliver, C. Toumazou, A. E. G. Cass and D. G. Johnston, *Diabet. Med.*, 2009, **26**, 197–210.

33 S. B. Bankar, M. V. Bule, R. S. Singhal and L. Ananthanarayan, *Biotechnol. Adv.*, 2009, **27**, 489–501.

34 A. Rebel, M. A. Rice and B. G. Fahy, *J. Diabetes Sceience Technol.*, 2012, **6**, 396–411.

35 B. Purohit, A. Kumar, K. Mahato and P. Chandra, in *Miniaturized Biosensing Devices*, eds. P. Chandra and K. Mahato, Springer Singapore, Singapore, 1st edn., 2022, pp. 149–175.

36 N. A. Peppas and D. S. Van Blarcom, *J. Control. Release*, 2016, **240**, 142–150.

37 S. M. Khor, J. Choi, P. Won and S. H. Ko, *Nanomaterials*, 2022, **12**, 1–23.

38 A. Jędrzak, M. Kuznowicz, T. Rębiś and T. Jesionowski, *Bioelectrochemistry*, 2022, **145**, 108071–108080.

39 N. Matsumoto, X. Chen and G. S. Wilson, *Anal. Chem.*, 2002, **74**, 362–367.

40 M. D. Prakash, S. L. Nihal, S. Ahmadsaidulu, R. Swain and A. K. Panigrahy, *Silicon*, 2022, 1–7.

41 P. N. Bartlett and F. A. Al-Lolage, *J. Electroanal. Chem.*, 2018, **819**, 26–37.

42 H. J. Hecht, D. Schomburg, H. Kalisz and R. D. Schmid, *Biosens. Bioelectron.*, 1993, **8**, 197–203.

43 P.-R. Kommoju, Z. Chen, R. C. Bruckner, F. S. Mathews and M. S. Jorns, *Biochemistry*, 2011, **50**, 5521–5534.

44 C. Chen, Q. Xie, D. Yang, H. Xiao, Y. Fu, Y. Tan and S. Yao, *RSC Adv.*, 2013, **3**, 4473–4491.

45 W. Jia, K. Wang and X. Xia, *Trends Anal. Chem.*, 2010, **29**, 306–318.

46 B. E. Swoboda and V. Massey, *J. Biol. Chem.*, 1966, **241**, 3409–3416.

47 M. Fish and H. Sands, *J. Biol. Chem.*, 1990, **265**, 19665–19671.

48 J. Wang, *Chem. Rev.*, 2008, **108**, 814–825.

49 A. Guerrieri, G. E. De Benedetto, F. Palmisano and P. G. Zambonin, *Biosens. Bioelectron.*, 1998, **13**, 103–112.

50 K. Sakdaphetsiri, S. Teanphonkrang and A. Schulte, *ACS Omega*, 2022, **7**, 19347–19354.

51 K. Ino, A. Tamura, K. Hiramoto, M. T. Fukuda, Y. Nashimoto and H. Shiku, *Chem. Lett.*, 2020, 1–5.

52 N. Wisniewski and M. Reichert, *Colloids Surfaces B Biointerfaces*, 2000, **18**, 197–219.

53 S. P. Nichols, A. Koh, W. L. Storm, J. H. Shin and M. H. Schoenfisch, *Chem. Rev.*, 2013, **113**, 2528–2549.

54 D. P. Manica, Y. Mitsumori and A. G. Ewing, *Anal. Chem.*, 2003, **75**, 4572–4577.

55 S. H. Baxamusa, L. Montero, J. M. Dubach, H. A. Clark, S. Borros and K. K. Gleason, *Biomacromolecules*, 2008, **9**, 2857–2862.

56 J. Dai, H. Zhang, C. Huang, Z. Chen and A. Han, *Anal. Chem.*, 2020, **92**, 16122–16129.

57 Y. Huang, T. Masuda and M. Takai, *ACS Appl. Polym. Mater.*, 2021, **3**, 631–639.

58 L. R. Carr, H. Xue and S. Jiang, *Biomaterials*, 2011, **32**, 961–968.

59 I. Banerjee, R. C. Pangule and R. S. Kane, *Adv. Mater.*, 2011, **23**, 690–718.

60 E. Ostuni, R. G. Chapman, M. N. Liang, G. Meluleni, G. Pier, D. E. Ingber and G. M. Whitesides, *Langmuir*, 2001, **17**, 6336–6343.

61 H. Zhang and M. Chiao, *J. Med. Biol. Eng.*, 2015, **35**, 143–155.

62 R. Trouillon, Z. Combs, B. A. Patel and D. O'Hare, *Electrochem. Commun.*, 2009, **11**, 1409–1413.

63 L. Cao, in *Comprehensive Biotechnology*, Elsevier B.V., Second Edi., 2011, vol. 2, pp. 461–476.

64 H. T. Imam, P. C. Marr and A. C. Marr, *Green Chem.*, 2021, **23**, 4980–5005.

65 X. Chen, N. Matsumoto, Y. Hu and G. S. Wilson, *Anal. Chem.*, 2002, **74**, 368–372.

66 W. Jin and J. D. Brennan, *Anal. Chim. Acta*, 2002, **461**, 1–36.

67 L. A. Estroff and A. D. Hamilton, *Chem. Rev.*, 2004, **104**, 1201–1217.

68 P. Terech and R. G. Weiss, *Chem. Rev.*, 1997, **97**, 3133–3159.

69 A. Yamauchi, in *Gels Handbook Vol. 1*, eds. Y. Osada, K. Kajiwara, T. Fushimi, O. Irasa, Y. Hirokawa, T. Matsunaga, T. Shimomura, L. Wang and H. Ishida, Elsevier, 1st edn., 2001, pp. 4–12.

70 Y. Osada, in *Gels Handbook Vol. 1*, eds. Y. Osada, K. Kajiwara, T. Fushimi, O. Irasa, Y.

Hirokawa, T. Matsunaga, T. Shimomura, L. Wang and H. Ishida, Elsevier, 1st edn., 2001, pp. 13–25.

71 D. K. Smith, in *Molecular Gels: Structure and Dynamics*, ed. R. G. Weiss, The Royal Society of Chemistry, London, 1st edn., 2018, pp. 300–371.

72 M. Anthamatten, M. Chau, P. Y. W. Dankers, B. W. Greenland, W. Hayes, E. Kumacheva, P. Li, R. Liu, O. Okay, A. C. H. Pape, T. Rossow, S. Seiffert, S. E. Sriskandha and H. Therien-Aubin, *Supramolecular Polymer Networks and Gels*, Springer International, 1st edn., 2015.

73 S. Toledano, R. J. Williams, V. Jayawarna and R. V Ulijn, *J. Am. Chem. Soc*, 2006, **128**, 1070–1071.

74 S. Panja, C. Patterson and D. J. Adams, *Macromol. Rapid Commun.*, 2019, **1900251**, 1–6.

75 E. K. Johnson, D. J. Adams and P. J. Cameron, *J. Am. Chem. Soc*, 2010, **132**, 5130–5136.

76 Y. Liu, E. Kim, R. V Ulijn, W. E. Bentley and G. F. Payne, *Adv. Funct. Mater.*, 2011, **21**, 1575–1580.

77 K. Kajiwara, in *Gels Handbook Vol. 1*, eds. Y. Osada, K. Kajiwara, T. Fushimi, O. Irasa, Y. Hirokawa, T. Matsunaga, T. Shimomura, L. Wang and H. Ishida, Elsevier, 1st edn., 2001, pp. 122–171.

78 D. J. Adams, L. M. Mullen, M. Berta, L. Chen and W. J. Frith, *Soft Matter*, 2010, **6**, 1971–1980.

79 E. R. Draper, H. Su, C. Brasnett, R. J. Poole, S. Rogers, H. Cui, A. Seddon and D. J. Adams, *Angew. Chem. - Int. Ed.*, 2017, **56**, 10467–10470.

80 A. Z. Cardoso, A. E. Alvarez Alvarez, B. N. Cattoz, P. C. Griffiths, S. M. King, W. J. Frith and D. J. Adams, *Faraday Discuss.*, 2013, **166**, 101–116.

81 L. Chen, T. O. McDonald and D. J. Adams, *RSC Adv.*, 2013, **3**, 8714–8720.

82 C. Colquhoun, E. R. Draper, R. Schweins, M. Marcello, D. Vadukul, L. C. Serpell and D. J. Adams, *Soft Matter*, 2017, **13**, 1914–1919.

83 E. R. Draper, B. Dietrich, K. McAulay, C. Brasnett, H. Abdizadeh, I. Patmanidis, S. J. Marrink, H. Su, H. Cui, R. Schweins, A. Seddon and D. J. Adams, *Matter*, 2020, **2**, 764–778.

84 E. R. Cross, S. M. Coulter, A. M. Fuentes-Caparrós, K. McAulay, R. Schweins, G. Laverty and D. J. Adams, *Chem. Commun.*, 2020, **56**, 8135–8138.

85 K. McAulay, H. Wang, A. M. Fuentes-Caparrós, L. Thomson, N. Khunti, N. Cowieson, H. Cui, A. Seddon and D. J. Adams, *Langmuir*, 2020, **36**, 8626–8631.

86 A. M. Fuentes-Caparrós, F. De Paula Gómez-Franco, B. Dietrich, C. Wilson, C. Brasnett, A. Seddon and D. J. Adams, *Nanoscale*, 2019, **11**, 3281–3291.

87 K. McAulay, L. Thomson, L. Porcar, R. Schweins, N. Mahmoudi, D. J. Adams and E. R. Draper, *Org. Mater.*, 2020, **2**, 108–115.

88 E. R. Draper and D. J. Adams, *Chem. Soc. Rev.*, 2018, **47**, 3395–3405.

89 J. Raeburn, A. Z. Cardoso and D. J. Adams, *Chem. Soc. Rev.*, 2013, **42**, 5143–5156.

90 E. R. Draper and D. J. Adams, *Chem*, 2017, **3**, 390–410.

91 M. Wallace, J. A. Iggo and D. J. Adams, *Soft Matter*, 2015, **11**, 7739–7747.

92 E. R. Draper and D. J. Adams, *Langmuir*, 2019, **35**, 6506–6521.

93 B. Yang, D. J. Adams, M. Marlow and M. Zelzer, *Langmuir*, 2018, **34**, 15109–15125.

94 J. Raeburn, C. Mendoza-Cuenca, B. N. Cattoz, M. A. Little, A. E. Terry, A. Zamith Cardoso, P. C. Griffiths and D. J. Adams, *Soft Matter*, 2015, **11**, 927–935.

95 S. Mandal, T. Dube, A. K. Mohapatra, S. Choudhury, F. Khanam, P. Yadav, V. S. Chauhan, J. Mishra and J. J. Panda, *Int. J. Pept. Res. Ther.*, 2021, **27**, 2795–2808.

96 J. J. Panda, R. Dua, A. Mishra, B. Mittra and V. S. Chauhan, *ACS Appl. Mater. Interfaces*, 2010, **2**, 2839–2848.

97 J. J. Panda, A. Mishra, A. Basu and V. S. Chauhan, *Biomacromolecules*, 2008, **9**, 2244–2250.

98 L. Chen, J. Raeburn, S. Sutton, D. G. Spiller, J. Williams, J. S. Sharp, P. C. Griffiths, R. K. Heenan, S. M. King, A. Paul, S. Furzeland, D. Atkins and D. J. Adams, *Soft Matter*, 2011, **7**, 9721–9727.

99 W. Wang, R. Han, K. Tang, S. Zhao, C. Ding and X. Luo, *Anal. Chim. Acta*, 2021, **1154**, 338295–338301.

100 L. Chen, G. Pont, K. Morris, G. Lotze, A. Squires, L. C. Serpell and D. J. Adams, *Chem. Commun.*, 2011, **47**, 12071–12073.

101 M. Hughes, P. W. J. M. Frederix, J. Raeburn, L. S. Birchall, J. Sadownik, F. C. Coomer, I. H. Lin, E. J. Cussen, N. T. Hunt, T. Tuttle, S. J. Webb, D. J. Adams and R. V. Ulijn, *Soft Matter*, 2012, **8**, 5595–5602.

102 J. Boekhoven, J. M. Poolman, C. Maity, F. Li, L. Van Der Mee, C. B. Minkenberg, E. Mendes, J. H. Van Esch and R. Eelkema, *Nat. Chem.*, 2013, **5**, 433–437.

103 C. Tang, A. M. Smith, R. F. Collins, R. V Ulijn and A. Saiani, *Langmuir*, 2009, **25**, 9447–9453.

104 I. Ziemecka, G. J. M. Koper, A. G. L. Olive and J. H. Van Esch, *Soft Matter*, 2013, **9**, 1556–1561.

105 D. J. Adams, M. F. Butler, W. J. Frith, M. Kirkland, L. Mullen and P. Sanderson, *Soft Matter*, 2009, **5**, 1856–1862.

106 L. Chen, K. Morris, A. Laybourn, D. Elias, M. R. Hicks, A. Rodger, L. Serpell and D. J. Adams, *Langmuir*, 2010, **26**, 5232–5242.

107 S. Panja and D. J. Adams, *Chem. Commun.*, 2019, **55**, 47–50.

108 S. Grigoriou, E. K. Johnson, L. Chen, D. J. Adams, T. D. James and P. J. Cameron, *Soft*

Matter, 2012, **8**, 6788–6791.

109 J. Raeburn, T. O. McDonald and D. J. Adams, *Chem. Commun.*, 2012, **48**, 9355–9357.

110 L. Thomson, R. Schweins, E. R. Draper and D. J. Adams, *Macromol. Rapid Commun.*, 2020, **41**, 2000093–2000098.

111 B. Xing, C. Yu, K. Chow, P. Ho, D. Fu and B. Xu, *J. Am. Chem. Soc*, 2002, **124**, 14846–14847.

112 A. M. Bieser and J. C. Tiller, *Chem. Commun.*, 2005, **0**, 3942–3944.

113 Y. Liu, X. D. Xu, J. X. Chen, H. Cheng, X. Z. Zhang and R. X. Zhuo, *Colloids Surfaces B Biointerfaces*, 2011, **87**, 192–197.

114 M. G. F. Angelerou, A. Sabri, R. Creasey, P. Angelerou, M. Marlow and M. Zelzer, *Chem. Commun.*, 2016, **52**, 4298–4300.

115 M. G. F. Angelerou, P. W. J. M. Frederix, M. Wallace, B. Yang, A. Rodger, D. J. Adams, M. Marlow and M. Zelzer, *Langmuir*, 2018, **34**, 6912–6921.

116 R. J. Williams, A. M. Smith, R. Collins, N. Hodson, A. K. Das and R. V Ulijn, *Nat. Nanotechnol.*, 2008, **4**, 19–24.

117 M. P. Conte, K. H. A. Lau and R. V Ulijn, *ACS Appl. Mater. Interfaces*, 2017, **9**, 3266–3271.

118 C. Vigier-Carrière, T. Garnier, D. Wagner, P. Lavalle, M. Rabineau, J. Hemmerlé, B. Senger, P. Schaaf, F. Boulmedais and L. Jierry, *Angew. Chem. - Int. Ed.*, 2015, **54**, 10198–10201.

119 C. Vigier-Carrière, D. Wagner, A. Chaumont, B. Durr, P. Lupatelli, C. Lambour, M. Schmutz, J. Hemmerlé, B. Senger, P. Schaaf, F. Boulmedais and L. Jierry, *Langmuir*, 2017, **33**, 8267–8276.

120 A. G. L. Olive, N. H. Abdullah, I. Ziemecka, E. Mendes, R. Eelkema and J. H. Van Esch, *Angew. Chem. - Int. Ed.*, 2014, **53**, 4132–4136.

121 M. Criado-Gonzalez, J. Y. Runser, A. Carvalho, F. Boulmedais, P. Weiss, P. Schaaf and L. Jierry, *Polymer*, 2022, **261**, 125398–125404.

122 D. Spitzer, V. Marichez, G. J. M. Formon, P. Besenius and T. M. Hermans, *Angew. Chem. - Int. Ed.*, 2018, **57**, 11349–11353.

123 Y. Wang, F. Versluis, S. Oldenhof, V. Lakshminarayanan, K. Zhang, Y. Wang, J. Wang, R. Eelkema, X. Guo and J. H. van Esch, *Adv. Mater.*, 2018, **30**, 1707408–1707414.

124 E. R. Cross, *SN Appl. Sci.*, 2020, **2**, 1–11.

125 X. L. Luo, J. J. Xu, J. L. Wang and H. Y. Chen, *Chem. Commun.*, 2005, 2169–2171.

126 J. Gong, L. Wang, K. Zhao and D. Song, *Electrochem. Commun.*, 2008, **10**, 123–126.

127 J. Gong, T. Liu, D. Song, X. Zhang and L. Zhang, *Electrochem. Commun.*, 2009, **11**, 1873–1876.

128 K. Yan, Y. Liu, J. Zhang, S. O. Correa, W. Shang, C. C. Tsai, W. E. Bentley, J. Shen, G. Scarcelli, C. B. Raub, X. W. Shi and G. F. Payne, *Biomacromolecules*, 2018, **19**, 364–373.

129 S. Wu, K. Yan, Y. Zhao, C. C. Tsai, J. Shen, W. E. Bentley, Y. Chen, H. Deng, Y. Du, G. F. Payne and X. Shi, *Adv. Funct. Mater.*, 2018, **28**, 1–12.

130 C. A. Da Silva, J. Wang and I. R. Minev, *Nat. Commun.*, 2022, **13**, 1–10.

131 Y. Yin, H. Zeng, S. Zhang, N. Gao, R. Liu, S. Cheng and M. Zhang, *Anal. Chem.*, 2023, **95**, 3390–3397.

132 S. Selmani, E. Schwartz, J. T. Mulvey, H. Wei, A. Grosvirt-Dramen, W. Gibson, A. I. Hochbaum, J. P. Patterson, R. Ragan and Z. Guan, *J. Am. Chem. Soc.*, 2022, **144**, 7844–7851.

133 M. Quan, D. Sanchez, M. F. Wasylkiw and D. K. Smith, *J. Am. Chem. Soc.*, 2007, **129**, 12847–12856.

134 E. R. Cross, K. McAulay and D. J. Adams, in *Polypeptide Materials*, ed. M. G. Ryadnov, Humana, New York, 2021, pp. 179–188.

135 Y. Liu, Y. Cheng, H. Wu, E. Kim, R. V Ulijn, G. W. Rubloff, W. E. Bentley and G. F. Payne, *Langmuir*, 2011, **27**, 7380–7384.

136 V. Lakshminarayanan, L. Poltorak, E. J. R. Sudhölter, E. Mendes and J. van Esch, *Electrochim. Acta*, 2020, **350**, 136352–136362.

137 E. K. Johnson, L. Chen, P. S. Kubiak, S. F. Mcdonald, D. J. Adams and P. J. Cameron, *Chem. Commun.*, 2013, **49**, 8698–8700.

138 J. Raeburn, B. Alston, J. Kroeger, T. O. McDonald, J. R. Howse, P. J. Cameron and D. J. Adams, *Mater. Horizons*, 2014, **1**, 241–246.

139 P. S. Kubiak, S. Awhida, C. Hotchen, W. Deng, B. Alston, T. O. McDonald, J. Adams and P. J. Cameron, *Chem. Commun.*, 2015, **51**, 10427–10430.

140 A. Piper, B. M. Alston, D. J. Adams and A. R. Mount, *Faraday Discuss.*, 2018, **210**, 1–17.

141 E. R. Cross and D. J. Adams, *Soft Matter*, 2019, **15**, 1522–1528.

142 C. Patterson, B. Dietrich, C. Wilson, A. R. Mount and D. Adams, *Soft Matter*, 2022, **18**, 1064–1070.

143 K. Labus, K. Wolanin and Ł. Radosiński, *Catalysts*, 2020, **10**, 489–511.

144 T. Liebmann, S. Rydholm, V. Akpe and H. Brismar, *BMC Biotechnol.*, 2007, **7**, 88–98.

145 P. Tiwari, R. Verma, A. Basu, R. M. Christman, A. K. Tiwari, D. Waikar and A. Dutt Konar, *ChemistrySelect*, 2017, **2**, 6623–6631.

146 Y. Wang, Z. Zhang, L. Xu, X. Li and H. Chen, *Colloids Surfaces B Biointerfaces*, 2013, **104**, 163–168.

147 G. Fusco, L. Chronopoulou, L. Galantini, A. Zerillo, Z. M. Rasik, R. Antiochia, G. Favero, A. D'Annibale, C. Palocci and F. Mazzei, *Microchem. J.*, 2018, **137**, 105–110.

148 A. D. Martin, A. B. Robinson and P. Thordarson, *J. Mater. Chem. B*, 2015, **3**, 2277–2280.

Chapter 2 – Fundamental theory and general experimental

2.1 Electrochemistry theory

2.1.1 The thermodynamics of charge transfer at Pt electrodes

The tightly packed lattice of platinum atoms arranged within platinum electrodes allows the atomic orbitals of those atoms to overlap, creating a near continuum (or band) of electron energy levels. This band is then partially filled to a maximum energy given by the Fermi level E_F. These electrons are delocalised throughout the metal, making the electrode electrically conductive.[1] Charge transfer at an electrode surface is governed by the difference in energy between the electrode E_F, and the lowest unoccupied molecular orbital (LUMO) or highest occupied molecular orbital (HOMO) energies of a given electroactive reactant. The "direction" in which electrons will spontaneously transfer depends on which of these are lower or higher in energy. If the reactant possesses a HOMO with higher energy than the E_F of the electrode, the electron should transfer from this donor orbital to a vacant orbital in the electrode, oxidising the reactant. Likewise, if the reactant possesses a LUMO or partially filled HOMO which can accept an electron, and the electrode E_F is at a higher energy than this reactant orbital, an electron should spontaneously transfer from the electrode to the reactant, reducing the reactant (Figure 2.1). The applied electrode potential, E, determines this Fermi level energy.[1,2]

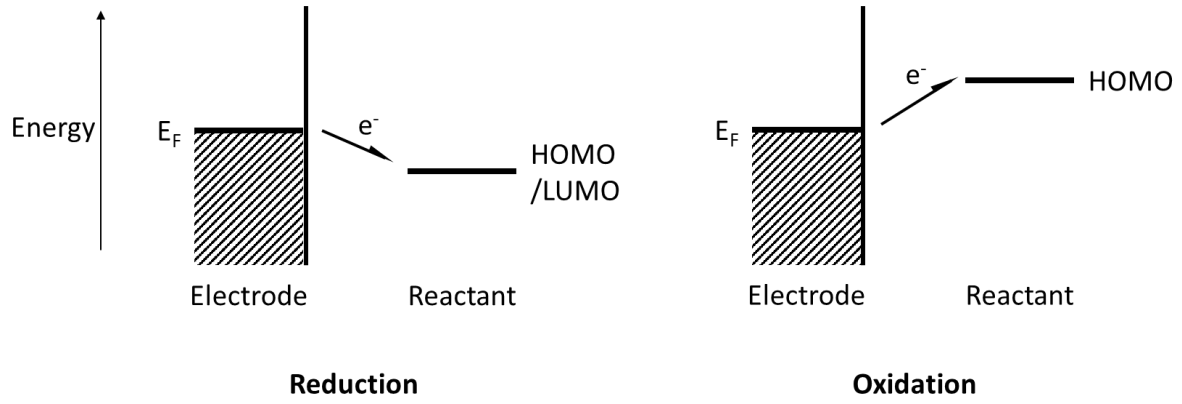

Figure 2.1 Heterogeneous electron transfer between energy levels of an electrode and reactant during reduction (left) and oxidation (right). The energies of the Fermi level (E_F) and reactant HOMO or LUMO determine which way electrons are transferred.

For an electrochemically reversible reaction with fast kinetics, a dynamic equilibrium is rapidly established with the following overall charge transfer reaction at an electrode:

$$\mathrm{O} + n\mathrm{e}^- \rightleftharpoons \mathrm{R} \qquad \textit{Equation 2.1}$$

where O is the oxidised reactant, R is the reduced reactant, and n electrons are transferred. When an electrode is inserted into a solution containing O and R and no E is applied, an equilibrium potential E_e is established at the electrode. When a potential E is applied to the electrode through a potentiostat, the local activities of O and R will change through oxidation or reduction. This relationship is given by the Nernst equation:

$$E = E' + \frac{RT}{nF}\ln\left(\frac{c_{\mathrm{Ox}}}{c_{\mathrm{Red}}}\right) \qquad \textit{Equation 2.2}$$

where E' is the formal potential of the redox reaction, R is the gas constant, T is the temperature, F is Faraday's constant, and c_{Ox} and c_{Red} are the concentrations of the oxidised and reduced species respectively. Redox reactions between the electrode and electroactive species in the solution become thermodynamically viable by applying a potential E, leading to electrolysis (the oxidation/reduction of reactants).[1,2] The potential applied to an electrode, its distribution, the movement of electroactive reactants in the solution through mass transfer, and the rates (flux) and nature of the electrochemical reactions at the electrode surface all contribute to the rate at which electrons are transferred across the electrode/solution interface (the current).[1]

2.1.2 Mass transport

The rate of reaction at an electrode surface is governed by the slowest of either reaction kinetics or of mass transport, the physical movement of reactants through the electrolytic solution to enable their reaction at the electrode. Mass transport encompasses three different processes: convection, migration, and diffusion. Convection occurs when mechanical forces such as solution stirring, or heat gradients, or chemical compositional gradients within the solution act to transport reactants within the solution. Migration occurs when the electric fields generated at or near the electrode/solution interface cause charged redox species and ions to move within them.[1] The conversion of reactants to products during electrolysis leads to a depletion of reactants at and around the electrode. Since reactants will initially be naturally spread throughout the solution homogenously before any electrochemistry occurs, this uneven distribution of reactants (created through electrolysis at the electrode) then generates a net flux of reactant towards the electrode surface to restore this homogeneity. This constant replenishment of reactant due to redox electrochemistry is known as diffusion. Fick's first and second laws describe the flux and change in concentration with time and distance due to diffusion:[1–3]

$$j = -D\frac{\partial c}{\partial x} \qquad \textit{Equation 2.3}$$

$$\frac{\partial c}{\partial t} = D\frac{\partial^2 c}{\partial x^2} \qquad \textit{Equation 2.4}$$

where j is the flux, D is the diffusion coefficient, c is the concentration, x is the (one-dimensional) distance from and perpendicular to the electrode surface, and t is the time.[1–3] Assuming first order kinetics, flux becomes:

$$j = k_{\mathrm{Red}}c_{\mathrm{Ox}} \qquad \textit{Equation 2.5}$$

and:

$$j = k_{\mathrm{Ox}}c_{\mathrm{Red}} \qquad \textit{Equation 2.6}$$

where k_{Ox} and k_{Red} are rates of electron transfer through electrochemical oxidation and reduction respectively.[1]

2.1.3 Depletion layers at electrodes

Over time, with continued passage of current, the volume from which reactant is drawn must expand as reactants continue to undergo redox chemistry at the electrode surface. This volume is called the diffusion or depletion layer.[1,3] The current passed at an electrode surface as a function of time is dependent not only on the concentration of reactant, but also on the area of that electrode. The Cottrell equation describes the diffusion controlled current response $i(t)$ at a macroelectrode with time t, when a step in potential is applied:

$$i(t) = nFAc_{\text{bulk}}\sqrt{\frac{D}{\pi t}} \qquad \textit{Equation 2.7}$$

where n is the number of electrons transferred, F is Faraday constant, A is the surface area of the electrode, c_{bulk} is the bulk concentration of electroactive material, and D is the diffusion coefficient of the redox active species. This direct proportionality between current and surface area means that a disc macroelectrode with a radius on the scale of mm will be capable of passing currents roughly in the µA-mA range (when considering that D typically lies roughly in the range of 10^{-9}-10^{-10} m^2 s^{-1}).[2,4] As time passes, providing this fixed potential is continually applied, the size of the depletion layer increases. As mentioned in Chapter 1 Section 1.1.1, electroactive reactants predominantly diffuse perpendicularly towards a macroelectrode during electrolysis, whilst the edges of a macroelectrode make minor contributions to the current. However, the size of the depletion layers generated at a macroelectrode are limited by natural solution convection.[5,6]

The Cottrell equation can also be used to describe the current passed at a microelectrode at very short electrolysis times t, when the depletion layer's thickness is far smaller than the microelectrode dimensions.[4,6,7] However, When the thickness of the depletion layer at a microelectrode becomes comparable to or greater than the radius of the microelectrode r, the microelectrode diffusion profile changes from a linear profile (with perpendicular diffusion) to a hemispherical profile (with radial diffusion).[4,6–8] Fick's second law, when hemispherical diffusion is established, then becomes:

$$\frac{\partial c}{\partial t} = D\left(\frac{\partial^2 c}{\partial r^2} + \frac{1}{r}\frac{\partial c}{\partial r} + \frac{\partial^2 c}{\partial x^2}\right) \qquad \textit{Equation 2.8}$$

The flux of diffusing redox active chemicals gradually reaches a constant at microelectrodes, resulting in a constant current limited by diffusion.[2,3] This limiting current i_L is described by the Saito equation:[9]

$$i_{\text{L}} = 4nFDc_{\text{bulk}}r \qquad \textit{Equation 2.9}$$

2.2 Electrochemical techniques

2.2.1 The three-electrode system

A circuit is completed when two electrodes (connected via a potentiostat through external wiring) are immersed in an electrolytic solution. Upon application of a redox potential, in order to generate a flow of charge through the solution to complete the circuit, one reactant is oxidised at one electrode, whilst another is reduced at the other. The electrode at which the reaction of interest takes place is known as the working electrode (WE). The other electrode (where the other reaction is occurring) is known as the counter electrode (CE).[2] The CE is designed to possess a far greater surface area than the WE, allowing it to pass greater currents. This ensures that the current, measured in the external circuit, is determined by the rate of electron transfer reactions occurring at the WE.[2] The distribution and absolute values of potential at the WE and CE, which determine the rates of these redox reactions, is unknown. Therefore, a third electrode known as a reference electrode (RE) is often included in an electrochemical cell. This RE passes no current in the cell, and is designed with its own contained system of an electrochemically reversible redox couple which is separated from the solution via an ion permeable frit. A common example of a reference electrode is the silver/silver chloride electrode (Ag/AgCl/Cl^-), which has the following overall redox reaction:

$$AgCl_{(s)} + e^- \rightleftharpoons Ag_{(s)} + Cl^-_{(aq)} \qquad \textit{Equation 2.10}$$

Due to the high, fixed activities/concentrations of $Ag_{(s)}$, $AgCl_{(s)}$ and $Cl^-_{(aq)}$ the RE contains, it possesses a potential which is stable and fixed. Current is passed between the WE and CE, and potential differences are measured and controlled between the WE and RE. The WE and RE are kept far enough away from each other so as not to affect mass transport and to maintain a stable potential.[10] Thus, the potential at the WE, *E*, can be accurately and reliably controlled with respect to the fixed potential of the RE. These three electrodes complete the three-electrode system used in all experimentation presented in this thesis (Figure 2.2).[2]

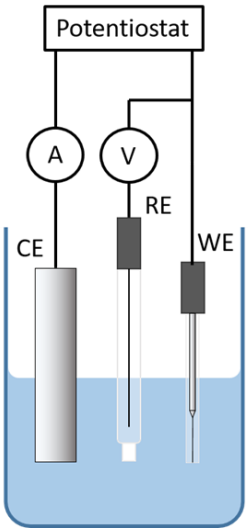

Figure 2.2 A three-electrode system featuring a working electrode (WE), reference electrode (RE) and counter electrode (CE), all connected to a potentiostat. Current is passed between the WE and CE in the electrolytic solution, whilst the potential at the WE is measured with respect to the RE.

2.2.2 Cyclic voltammetry

Cyclic voltammetry is a method of investigating reactions at a WE surface, achieved by scanning linearly between two potentials, and examining the changes in the current response. It is usually the first electroanalytical method employed to identify potential ranges for reactions of interest. When a potential E is applied that differs from the formal potential E', a current will begin to pass which affects the rates of oxidation/reduction of reactions k_{Ox} and k_{Red} at the electrode surface:

$$k_{\mathrm{Ox}} = k^{\theta}\, exp\left[\frac{nF(1-\alpha_{\mathrm{Red}})(E-E')}{RT}\right] \qquad \textit{Equation 2.11}$$

$$k_{\mathrm{Red}} = k^{\theta}\, exp\left[\frac{-nF\alpha_{\mathrm{Red}}(E-E')}{RT}\right] \qquad \textit{Equation 2.12}$$

where k^{θ} is the standard rate constant of oxidation/reduction, and α_{Red} is the transfer coefficient for reduction. As k_{Ox} and k_{Red} change through varying E, current at the electrode becomes:

$$i = nAFj \qquad \textit{Equation 2.13}$$

and by substituting in Equation 2.5 and Equation 2.6:

$$i = nAF(k_{\mathrm{Ox}}c_{\mathrm{Red}} - k_{\mathrm{Red}}c_{\mathrm{Ox}}) \qquad \textit{Equation 2.14}$$

which can be separated into:

$$i_{\mathrm{a}} = nAFk_{\mathrm{Ox}}c_{\mathrm{Red}} \qquad \textit{Equation 2.15}$$

and

$$i_{\mathrm{c}} = -nAFk_{\mathrm{Red}}c_{\mathrm{Ox}} \qquad \textit{Equation 2.16}$$

where i_{a} and i_{c} are the anodic and cathodic currents respectively (the sum of which is the measured current), and c_{Red} and c_{Ox} are the concentrations of reducing and oxidising redox species at the electrode surface. If the potential is swept from equilibrium potential E_{e} to increasingly positive potentials, more redox active reactant diffuses towards the electrode to be oxidised. This produces a depletion zone with reduced reactant concentration, slowing the rate of oxidation k_{Ox} as the concentration depletes faster. As reactants cannot be drawn from the bulk fast enough to continue oxidation, the reaction becomes limited by the rate of diffusion, and the current decreases.[1]

When studying oxidation, after selecting a potential to begin the scan (E_0), the potential is swept in the oxidative direction at a given scan rate (measured in V s^{-1}) to a maximum (E_1), then swept in the reverse reductive direction to a minimum (E_2), before returning to the starting potential (Figure 2.3a). As a digital method, the potential and a current response is measured in small 'steps' of the scan. The result of this data collection is a cyclic voltammogram (CV), which presents the current response plotted at each measured potential in both forwards and backwards scan directions (Figure 2.3b).[1] It is important to note here

that microelectrodes and macroelectrodes produce their own characteristic shapes in a CV. A macroelectrode will yield a voltammogram with more pronounced, broader oxidation and reduction peaks in the forward and backward sweeps.[11] The enhanced hemispherical diffusion associated with microelectrodes allows for a greater flux of reactant at the electrode surface as the depletion zone grows, generating sharper waves in the CV (Figure 2.3b).[1,2,4]

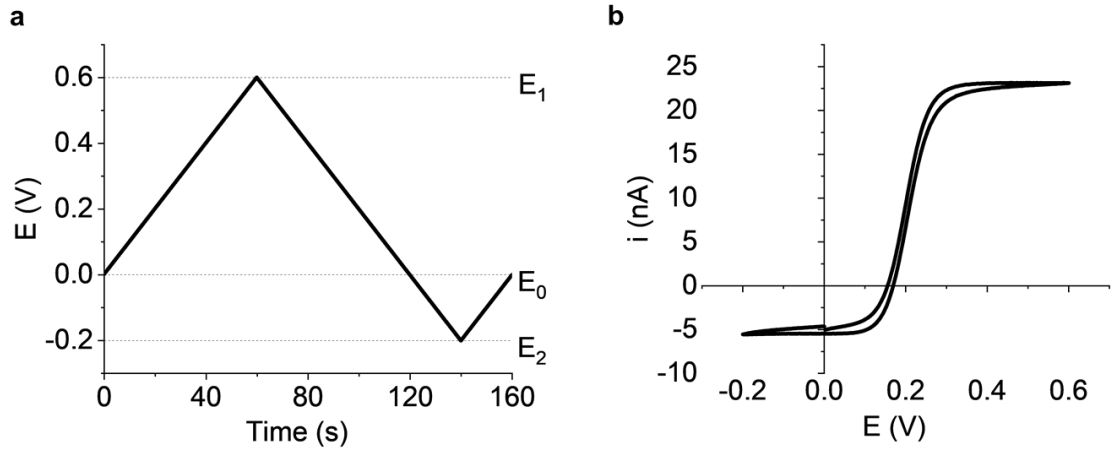

Figure 2.3 An example of cyclic voltammetry a ferrocyanide solution (see Section 2.4.2), at a Pt disc microelectrode (25 µm diameter), scanned at a rate of v = 10 mV s^{-1} at T = 25 °C, starting at E_0 = 0 V. (a) The potential cycle of a CV over a 160 second time scale. Initial scan direction positive, reaching maximum potential (E_1 = 0.6 V), before scanning in negative direction to minimum potential (E_2 = -0.2 V), and then returning to E_0 by scanning in positive direction once again. (b) The resulting CV, with potential recorded at the WE plotted against the recorded current.

In the CV above (Figure 2.3b) ferrocyanide ions are oxidised at the Pt microelectrode at applied potentials above 0.1 V (against an Ag/AgCl reference). Here, the limiting current i_L is given by:

$$i_{\mathrm{L}} = nAFk_{\mathrm{Ox}}(c_{\mathrm{Red}} + c_{\mathrm{Ox}}) \qquad \textit{Equation 2.17}$$

Dividing this by the anodic current (Equation 2.5) gives the following equation:

$$\frac{i_{\mathrm{L}}}{i} = 1 + \frac{c_{\mathrm{Ox}}}{c_{\mathrm{Red}}} \qquad \textit{Equation 2.18}$$

which when rearranged and substituted into the Nernst equation (Equation 2.2) gives the following relationship:

$$E = E' + \frac{RT}{nF}\ln\left(\frac{i_{\mathrm{L}} - i}{i}\right) \qquad \textit{Equation 2.19}$$

Plotting *E* against the natural log in a modified Tafel plot (Figure 2.4) produces a straight line with a slope *RT*/*nF* and an intercept of *E'*, where ln([i_L-*i*]/*i*) = 0 (i.e. $i = i_L/2$), $E = E' = E_{1/2}$, the half-wave potential of the oxidation wave in the forward scan.[6]

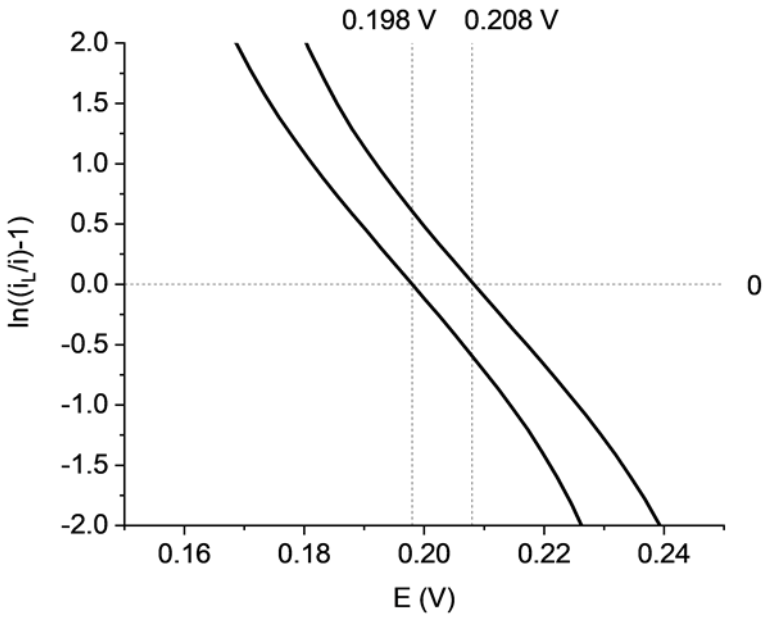

Figure 2.4 A modified Tafel plot to the CV featured in Figure 2.3b, windowed in the range of 0.15 V to 0.25 V, where ferrocyanide/ferricyanide redox chemistry occurs. Dashed lines on the y-axis at 0 x-axis at 0.196 V to show E-intercept corresponding to $E_{1/2}$ in the forward (0.198 V) and reverse (0.208 V) scans. The difference in $E_{1/2}$ in these scans is due to differences in double-layer charge at the electrode surface.

Each electroactive species in an electrochemical cell will react when applied potentials match or exceed the redox potential of that reactant, so a CV can feature multiple waves if multiple redox active species are dissolved in solution. The 'solvent limits' of a given electrolyte are potential limits beyond which the solvent will begin to oxidise or reduce. In the case of aqueous solutions this typically produces oxygen gas at positive (oxidative) potentials, and hydrogen gas at negative (reductive) potentials. For example, the solvent limits for 0.1 M $H_2SO_{4(aq)}$ at a Pt microelectrode are marked by a sharp decrease in reductive currents and increase in oxidative currents passed at approximately -0.3 V and 1.6 V respectively (Figure 2.5).

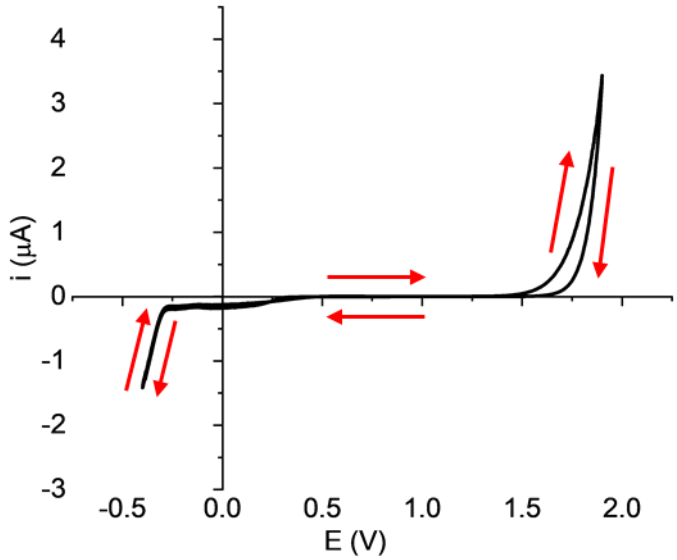

Figure 2.5 An example of a CV recorded in a solution containing 0.1 M $H_2SO_{4(aq)}$, at a Pt disc microelectrode (25 μm diameter). Scanned at a rate of v = 0.1 V s^{-1} between -0.4 V and 1.8 V, at T = 25 °C, starting at E = 0 V. Solvent limits can be seen at -0.3 V and 1.6 V.

2.2.3 Chronopotentiometry

Chronopotentiometry is a technique used to measure variations in potential at the WE as a function of time whilst a typically fixed current is passed. The steady consumption of reactants corresponds to plateau regions in the potential-time plot (Figure 2.6). Over long periods of time, the depletion zone grows, and the diffusion of a given electroactive species to the electrode can decrease to rates that fail to satisfy the fixed current. This leads to other electroactive species being required to satisfy the current demand through other electron transfer reactions. This transition to new reactants appears as sharp increases in potential over short periods of time in the transient. Setting higher fixed currents leads to the system requiring new electron transfer reactions (once the mass transfer limiting rate of the first reaction has been exceeded), meaning plateaus of stable electron transfer last for shorter periods of time. For reasons explained further in Chapter 3, this technique is not featured in this work, but is described here to provide context and for comparison against chronoamperometry (see Section 2.2.4).

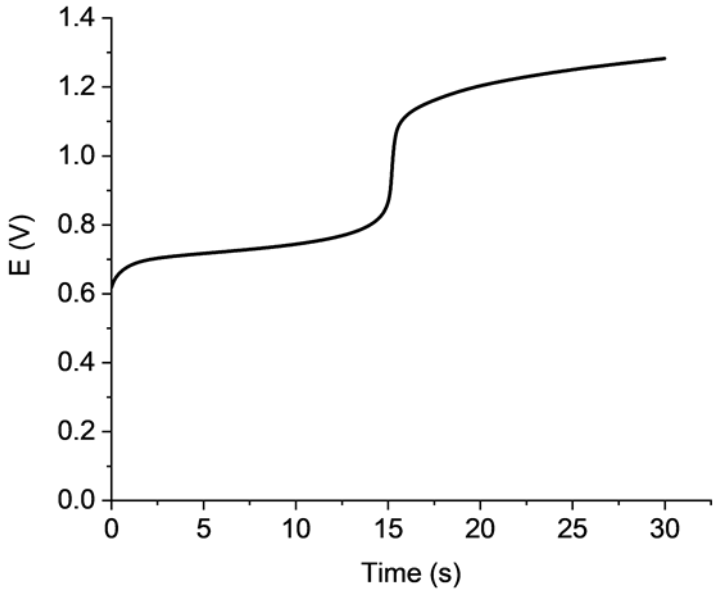

Figure 2.6 An example of a potential-time transient in 10 mL 10 mg/mL Carb-Ala gelator solution (pH 8, see Section 2.4.2) containing hydroquinone (67.5 mM) and NaCl (1 mM) at a Pt disc macroelectrode (2 mm diameter), i = 300 mA, T = 25 °C. The two known electroactive species added to this aqueous solution are hydroquinone and the Carb-Ala gelator (see Section 2.3.1). Hydroquinone, having the lower oxidative potential, is oxidised until its diffusion to the electrode surface cannot meet the demands of the electrode kinetics. After approximately 13 seconds, to maintain the fixed current, the system raises potential to oxidise the Carb-Ala gelator, creating a second plateau in the potential-time transient.

2.2.4 Chronoamperometry

In chronoamperometry the potential at the WE is stepped out of the open circuit potential, and current at the WE is measured as a function of time. The stepping of potential to different fixed values allows chemical species in a solution to become electroactive, granted that the stepped potential matches or exceeds the redox potentials of those species.[6] Knowledge of those oxidative potentials is acquired typically through a CV (see Section 2.2.1), which can detail at what potential the electrochemical redox of a given species becomes diffusion-limited.[6] Diffusion-limited currents acquired at those potentials (at macroelectrodes) are described by the Cottrel equation (Equation 2.7). The fixed potential in chronoamperometry only allows for a defined set of chemical species to react at the electrode surface and provide a current. Thus, under this potentiostatic control, the concentration gradient and therefore the current decrease with time, until diffusion (and natural convection) reach a steady state (Figure 2.7).[1,6] This steady state is reached quickly at microelectrodes, whereas macroelectrodes do not reach this condition due to competition with solution convection affecting overall mass-transport.[4,6]

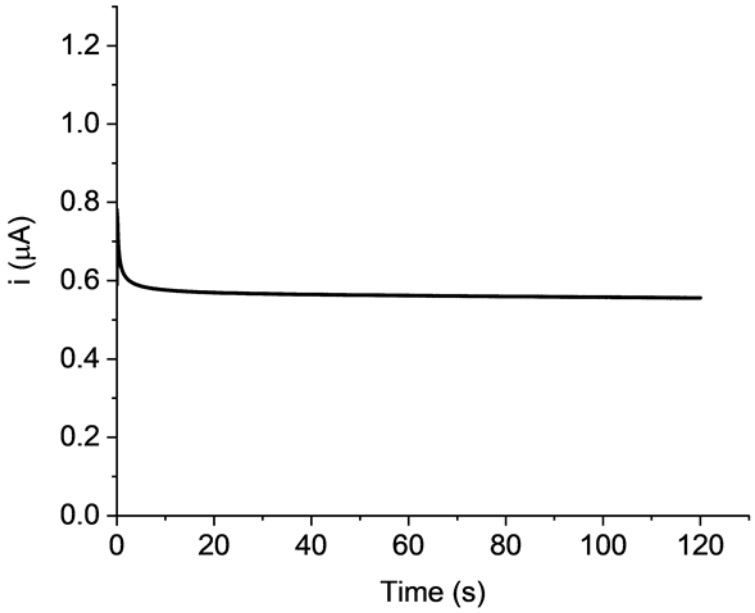

Figure 2.7 An example of a *current-time transient in 1 mL solution (pH 8) containing hydroquinone (67.5 mM) and NaCl (1 mM) at a Pt disc microelectrode (25 µm diameter), E = 0.7 V, T = 25 °C. Hydroquinone is drawn to the microelectrode surface to be oxidised, eventually settling to a steady state of diffusion, marked by the steady current of 0.6 µA reached after approximately 3 seconds.*

In this thesis, chronoamperometry serves two functions. In Chapter 3, it is used as a method of selectively oxidising hydroquinone within gelator solutions without allowing other chemicals in the gelator solutions (such as the gelator molecules) to be electrochemically active. The current-time response is then analysed to inform on cumulative charge passed and to identify changes in oxidation rate. In Chapter 5, chronoamperometry is used in the context of amperometric glucose biosensing, as the magnitude of a current provides a real-time measurement of hydrogen peroxide concentration.

2.2.5 Differential pulse voltammetry

Differential pulse voltammetry (DPV) is used to measure current responses at the WE to pulses of potential. These potential pulses (typically on the order of 100 mV) are typically held for less than a second, and the difference in current before and at the end of a pulse, Δ*i*, is recorded. The potential is then stepped up by values lower than the pulses (on the order of 1-10 mV for 100 mV pulses), and the process is repeated for the new potential window. These Δ*i* for each pulse are plotted against the end of a potential pulse at the WE, producing a redox waveform featuring peaks (Figure 2.8).[6] These peaks correspond approximately with the half-wave potentials $E_{1/2}$ seen in redox waves of cyclic voltammograms and their Tafel plots (Figure 2.3b, Figure 2.4), and represent the formal potential, where both the oxidised and reduced species are present in equal concentrations.[2,6] DPV has been used in this work to rapidly identify $E_{1/2}$, thus the formal potential, to apply during electrochemical impedance spectroscopy experiments, detailed next.

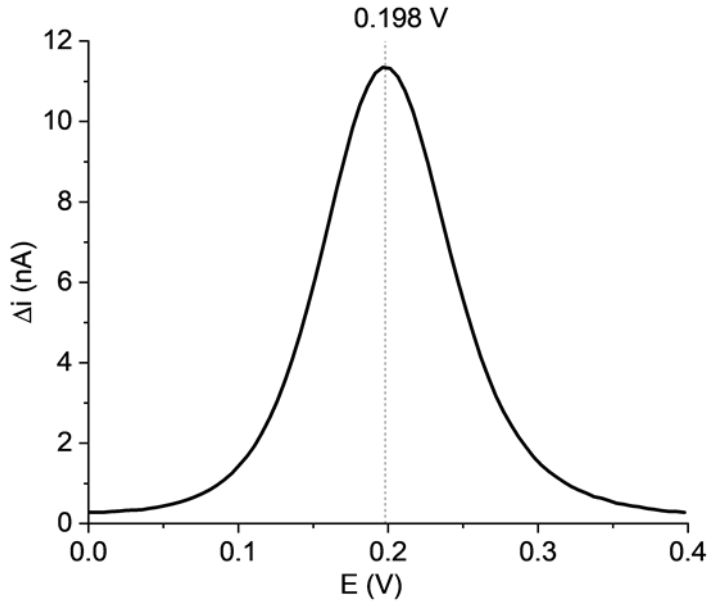

Figure 2.8 An example of a redox waveform. DPV was conducted between 0 V and 0.4 V at a 25 µm diameter Pt working microelectrode in a three-electrode system, within a ferrocyanide solution (see Section 2.4.2). The peak of the waveform depicted here at 0.196 V represents the half-wave potential $E_{1/2}$ for the oxidation of ferrocyanide to ferricyanide (see Section 2.3.4). The potential at the peak of this waveform is applied during electrochemical impedance spectroscopy experiments.

2.2.6 Electrochemical impedance spectroscopy

Impedance spectroscopy encompasses several techniques used to understand fundamental processes occurring within electrochemical cells. In electrochemical impedance spectroscopy (EIS, also referred to as A.C. impedance spectroscopy), the response of a WE to an oscillating sinusoidal potential $E(t)$ (an A.C. potential perturbation superimposed on a fixed D.C. potential), is measured in terms of the current $i(t)$, which gives the impedance $Z(f)$ (as in Ohm's law, where dividing a voltage by a current gives a resistance):[12]

$$Z(f) = \frac{E(t)}{i(t)} \qquad \textit{Equation 2.20}$$

The frequency of the A.C. potential is swept from a high frequency (f, on the order of kHz) to a low frequency (on the order of Hz), usually by applying successive logarithmically spaced frequencies.[1,12] $E(t)$ applied at the WE during EIS is superimposed on a D.C. potential (set to $E_{1/2}$, obtained using DPV as described in Section 2.2.5), possesses a frequency of oscillation f, and a maximum potential E_{AC}:

$$E(t) = E_{AC}\sin(2\pi f t) \qquad \textit{Equation 2.21}$$

Application of $E(t)$ across an electrochemical cell causes an oscillating current $i(t)$ to flow. The reaction lags behind the changes in applied potential, due to the limitation imposed by the kinetics of chemical reactions and diffusion of reactants for redox chemistry. Thus, a phase

difference θ is created between the applied potential and the resulting current with amplitude i_{AC}:[12]

$$i(t) = i_{\mathrm{AC}} \sin(2\pi f t + \theta) \qquad \textit{Equation 2.22}$$

Inserting Equation 2.21 and Equation 2.22 into Equation 2.20 gives:

$$Z(f) = |Z| \frac{\sin(2\pi f t)}{\sin(2\pi f t + \theta)} \qquad \textit{Equation 2.23}$$

where $|Z|$ = E_{AC}/i_{AC}. Using Euler's relation (note that the non-italicised "i" represents the imaginary number $\sqrt{-1}$):

$$\exp(\mathrm{i}x) = \cos(x) + \mathrm{i}\sin(x) \qquad \textit{Equation 2.24}$$

Equation 2.23 can be expressed in complex notation:[12]

$$Z(f) = |Z| \exp(\mathrm{i}\theta) = |Z|(\cos(\theta) + \mathrm{i}\sin(\theta)) \qquad \textit{Equation 2.25}$$

and simplified to:

$$Z(f) = Z' + \mathrm{i}Z'' \qquad \textit{Equation 2.26}$$

where *Z'* is the 'real' component (equal to $|Z|\cos(\theta)$, analogous to resistance, in-phase) and *Z''* is the 'imaginary' component (equal to $|Z|\sin(\theta)$, out-of-phase). This Cartesian representation allows for plotting *Z''* against *Z'*, in what is known as a Nyquist plot, in which each frequency applied to the WE over the EIS experiment is represented by a coordinate (*Z'*, *-Z''*).[12] Properties of the electrochemical cell, electron transfer kinetics, and information on mass transport, can all be extracted from a Nyquist plot. Knowledge and understanding of these phenomena can be used to build an 'equivalent circuit', a model that uses analogous electrical circuit components to represent how those real processes and features affect the currents, their amplitudes and phase angles, passed at the WE.[6,12] The established Randles circuit models the redox electrochemistry occurring at the surface of single, planar macroelectrodes (Figure 2.9).[12]

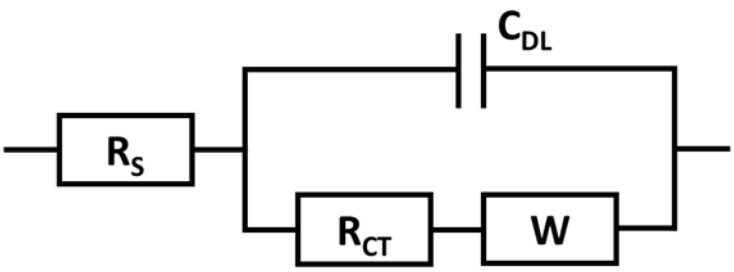

Figure 2.9 The Randles circuit, an equivalent circuit used to model macroelectrode responses to an A.C. potential frequency sweep within an electrolytic solution.

As the A.C. potential frequency is swept from high (kHz) to low (Hz) during EIS, the Nyquist plot takes on a distinct shape based on the processes occurring during the sweep and the type of electrode being examined. The equivalent circuit explains this with a 'path of least resistance' at any given frequency. The first component of the Randles circuit models the

solution resistance (R_S), which is always present within the electrochemical cell and is thus placed in series with the other components. The circuit is then split into parallel components to represent the double-layer charging and the summation of contributions to the faradaic process at the WE. Sweeping from high to low kHz signal frequencies during EIS, the ion double-layer formed as a result of electrostatic attraction to charges distributed across the electrode surface gains charge, and is represented by a capacitor (C_{DL}). Faradaic charge transfer across this electrode-solution interface also possesses an associated resistance (R_{CT}), and in parallel with this resistor is a Warburg element (W) which models linear diffusion towards the electrode surface.[6,12]

The Nyquist plot for a macroelectrode possesses several characteristic features. C_{DL} is characterised by a variation in the imaginary component:

$$-Z'' = \frac{1}{2\pi f C} \qquad \textit{Equation 2.27}$$

so as the A.C. potential is swept from high to low frequencies during EIS, the imaginary $-Z''$ increases in magnitude. This forms a semicircle in the Nyquist plot, starting at coordinate $Z' = R_S$ at high kHz frequencies, that arcs down towards $Z' = R_{CT}$ at lower kHz frequencies (Figure 2.10).[1] The Warburg element adds a 45° linear slope in the low frequency region of the Nyquist plot, modelling the planar mass transfer towards the macroelectrode during electrolysis.

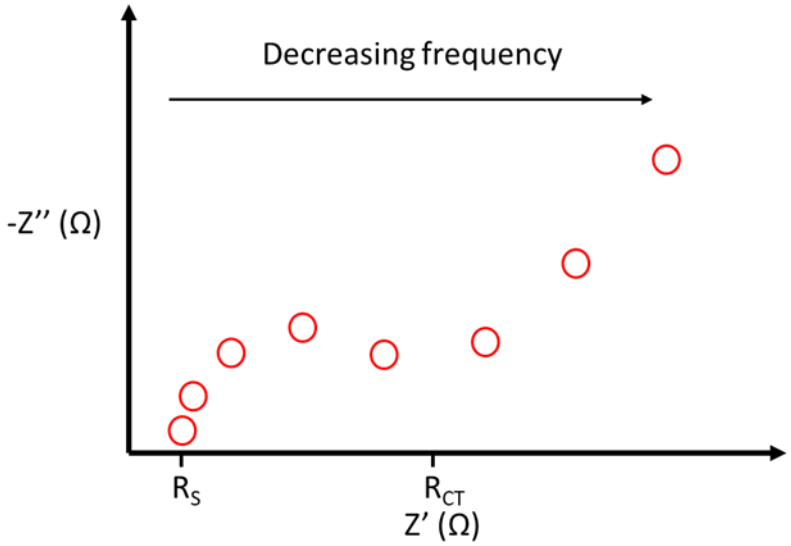

Figure 2.10 The characteristic Nyquist plot of a macroelectrode response to an A.C. frequency sweep in an electrolytic solution.

At microelectrodes, hemispherical diffusion evolves as the frequency of the A.C. voltage decreases from the hundreds to single-digit Hz range. The Warburg element alone therefore becomes insufficient to represent the enhanced mass transport at microelectrodes. To model this, a component representing non-linear diffusion is added to the equivalent circuit: the established modified Randles circuit features a resistor (R_{NL}) in parallel with the Warburg diffusional element (Figure 2.11). Nyquist plots of microelectrodes therefore feature a second characteristic semicircle in the low frequency range (Figure 2.12).[13,14]

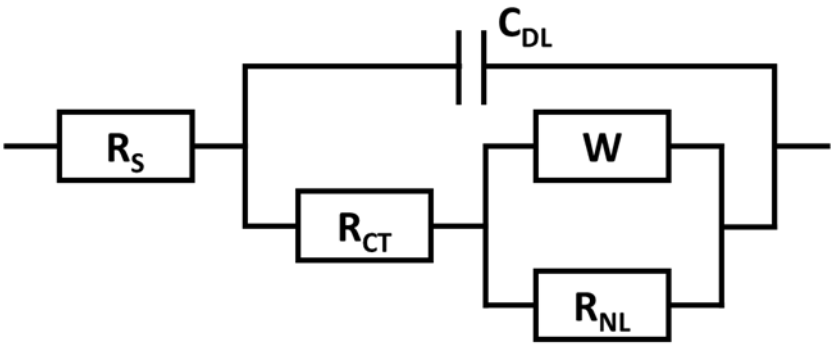

Figure 2.11 The modified Randles circuit, an equivalent circuit used to model microelectrode responses to an A.C. potential frequency sweep within an electrolytic solution.

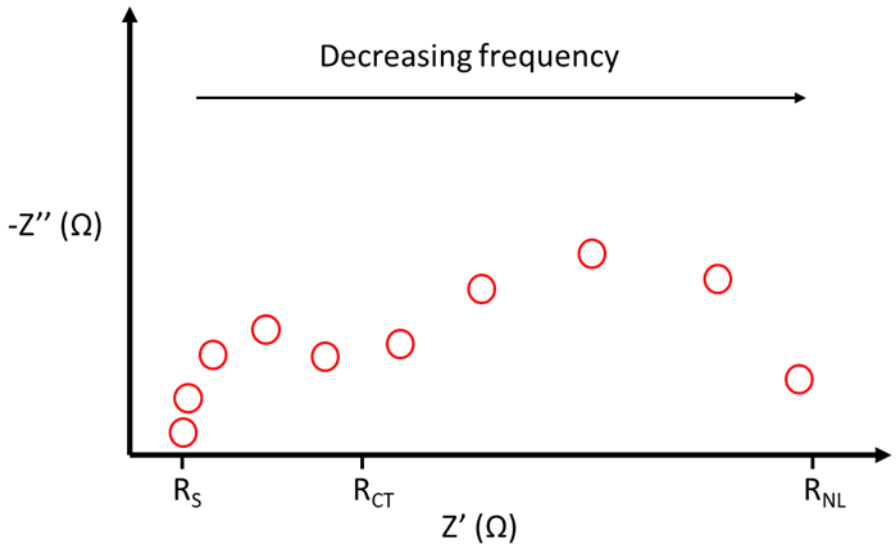

Figure 2.12 The characteristic Nyquist plot of a microelectrode response to an A.C. frequency sweep in an electrolytic solution.

2.2.7 Extracting diffusion coefficients from EIS data

The Warburg element *W* and resistance due to non-linear diffusion R_{NL} model the diffusion processes at disc microelectrodes. Starting with the equation for the Warburg coefficient σ (Equation 2.28),[6] a diffusion coefficient can be obtained from Y_0, the value of admittance obtained from fitting the Warburg element of the modified Randles circuit (Figure 2.11):

$$\sigma = \frac{1}{(\sqrt{2}Y_0)} = \frac{RT}{n^2F^2A\sqrt{2}}\left(\frac{1}{D_{\mathrm{Ox}}{}^{\frac{1}{2}}c_{\mathrm{Ox}}{}^{\mathrm{b}}} + \frac{1}{D_{\mathrm{Red}}{}^{\frac{1}{2}}c_{\mathrm{Red}}{}^{\mathrm{b}}}\right) \qquad \textit{Equation 2.28}$$

where *R* is the ideal gas constant, *T* is the temperature, *A* is the surface area of the electrode, D_{Ox} and D_{Red} are the diffusion coefficients of the oxidised and reduced species respectively, and $c_{Ox}{}^{b}$ and $c_{Red}{}^{b}$ are the bulk concentrations of the oxidised and reduced species respectively. When the formal potential *E'* – determined via modified Tafel plot (Figure 2.4) or DPV (Figure 2.8) – is applied to a solution containing the ferrocyanide anion, an equal

concentration of ferricyanide and ferrocyanide is produced within the diffusion field at the electrode surface. At E', $c_{Ox} = c_{Red} = c_0/2$, where c_0 is the total concentration of electroactive material within the diffusion field. If an approximation can be made where $D_{Ox}^{1/2} = D_{Red}^{1/2} = D^{1/2}$ for the ferro/ferricyanide (FFC) redox pair,[15] then the Warburg coefficient can be rearranged to obtain an equation for D_L, the diffusion coefficient calculated from estimations of linear diffusion (Equation 2.29):

$$D_{\mathrm{L}} = \left(\frac{4RTY_0}{n^2F^2Ac_{\mathrm{bulk}}}\right)^2 \qquad \textit{Equation 2.29}$$

By combining the Saito equation (Equation 2.9) with the equation that relates limiting current i_L to R_{NL} (Equation 2.30),[9,16] a second diffusion coefficient D_{NL} can be extracted from R_{NL}, obtained at the formal potential (Equation 2.31):

$$i_{\mathrm{L}} = \frac{4RT}{nFR_{\mathrm{NL}}} \qquad \textit{Equation 2.30}$$

$$D_{\mathrm{NL}} = \frac{RT}{R_{\mathrm{NL}}n^2F^2c_{bulk}r} \qquad \textit{Equation 2.31}$$

Equation 2.29 and *Equation 2.31* are used throughout this work to extract diffusion coefficients from values obtained from the Warburg element W and resistance due to non-linear diffusion R_{NL}.

2.3 Electroactive species in this work

2.3.1 Carb-Ala gelator

The most important chemical in this thesis is the gelator carbazole-alanine, shortened to Carb-Ala (Figure 2.13), nicknamed such due to the capping carbazole functionality on the N-terminus of the alanine. Carb-Ala has been used in a few works as the peptide-based gelator of choice for electrochemical pH-triggered gelation,[17,18] and has been cited for a unique property in being capable of electrochemical polymerisation (when potentials above the oxidation potential of the gelator, approximately +0.8 V, are applied). This has been shown to enable the production of thin, porous polymer layers at electrode surfaces.[17] These polymers are similar but not identical to polycarbazole, as the polymer chains retain the alanine group of the Carb-Ala monomer.[17] This additional property offers prospect for the gelator, as Carb-Ala self-assembly and polymerisation can be selectively controlled through electrochemical methods to yield completely different types of supramolecular and polymeric materials. The pK_a^{app} of Carb-Ala is approximately 6 according to pH titration (Figure 2.14), meaning that in aqueous solutions of pH < 6 the gelator protonates and undergoes self-assembly, forming fibres which entangle to form a hydrogel.[17]

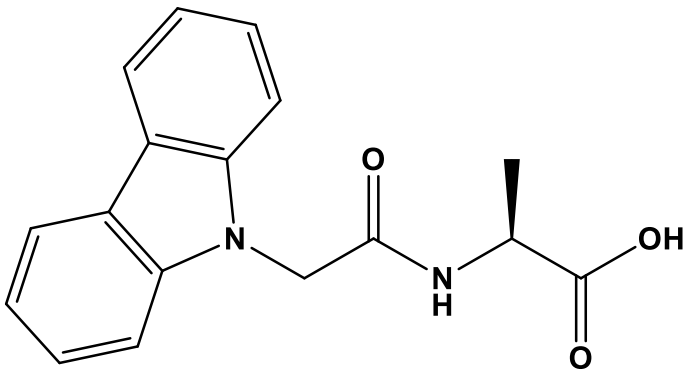

Figure 2.13 Molecular structure of the Carb-Ala gelator.

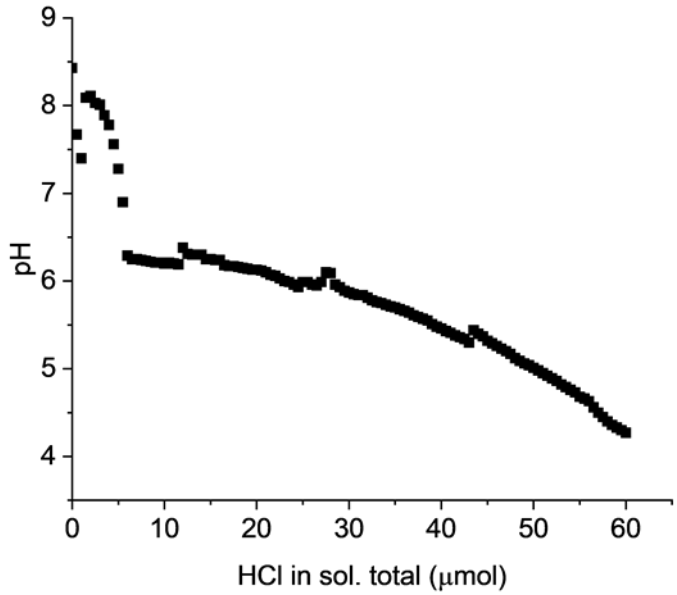

Figure 2.14 pH titration of a 2 mL aqueous solution (initial pH 8.5) containing 10 mg/mL Carb-Ala gelator (20 mg, 67.5 μmol, 33.8 mM). 0.1 M $HCl_{(aq)}$ added in 5 μL aliquots and pH measured after stirring solution post aliquot addition. Plateau starting at approximately pH 6 indicates buffering of pH due to protonation and self-assembly of Carb-Ala.

2.3.2 BrAV gelator

A second gelator, BrAV (also referred to as 6Br2NapAV in the literature[19,20]), is featured in Chapter 4 of this work in a comparative study against Carb-Ala. BrAV is an alanine-valine dipeptide gelator, with the alanine being capped at the N-terminus on the second carbon of a 6-bromonaphthalene group (Figure 2.15). pK_a^{app} of BrAV is approximately 5.8,[21,22] and it too is known to form networks of entangled fibres when pH is lowered below this value.[23]

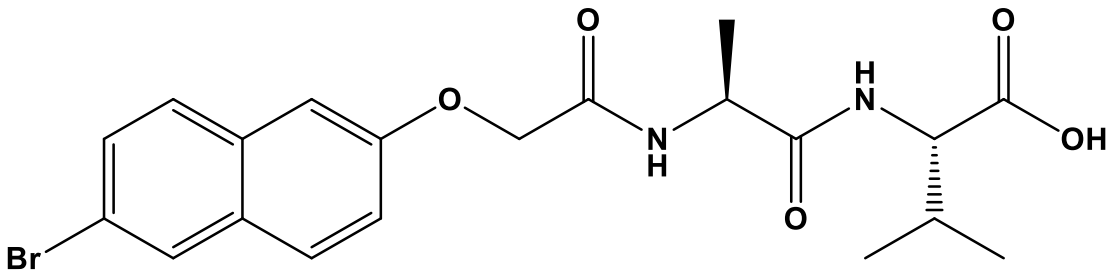

Figure 2.15 Molecular structure of the BrAV gelator.

2.3.3 Hydroquinone

The most important reaction in this thesis is the electrochemical oxidation of hydroquinone, responsible for generating the localised pH shift necessary for the spatiotemporally controlled, acid-triggered self-assembly of supramolecular gels at electrode surfaces.[17,18,20,21,24–27] In buffered solutions, or unbuffered solutions where the concentration of protons is greater than the concentration of hydroquinone, hydroquinone

electrochemistry can be simplified to a two electron, two proton, reversible reaction (Figure 2.16, Equation 2.32) between hydroquinone (QH_2) and benzoquinone (Q):[28]

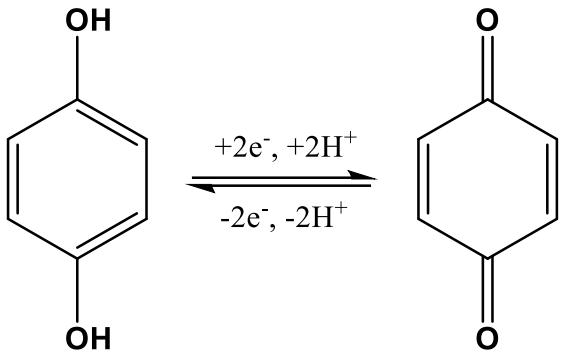

Figure 2.16 Simplified redox chemistry between hydroquinone (left) and benzoquinone (right) in buffered and unbuffered low pH solutions.

$$QH_{2(aq)} \rightleftharpoons Q_{(aq)} + 2H^{+}_{(aq)} + 2e^{-} \qquad \textit{Equation 2.32}$$

The energetics of this reaction are greatly dependent on the activity/concentration (i.e. the pH) of protons, with a single unit pH change (at 298 K) equating to a change in electrode potential of +59 mV.[29] This electrochemistry changes in highly basic, unbuffered solutions, specifically where the concentration of protons is less than the concentration of hydroquinone.[28] Hydroquinone has pK_a = 9.85,[28] thus deprotonation occurs above pH 10:

$$QH_{2(aq)} + OH^{-}_{(aq)} \rightleftharpoons QH^{-}_{(aq)} + H_2O_{(l)} \qquad \textit{Equation 2.33}$$

Singly deprotonated hydroquinone has pK_a = 11.84:[28]

$$QH^{-}_{(aq)} + OH^{-}_{(aq)} \rightleftharpoons Q^{2-}_{(aq)} + H_2O_{(l)} \qquad \textit{Equation 2.34}$$

It is important that hydroquinone deprotonation and oxidation at high pH is prevented before electrochemistry is utilised for two reasons. First, more electrochemical oxidation is required to generate enough protons to overcome and shift the alkaline pH below the pK_a^{app} of a given gelator to trigger gelation. Second, electrochemically oxidising $QH^{-}_{(aq)}$ and $Q^{2-}_{(aq)}$ generates less protons (necessary for a pH trigger) per mole of hydroquinone $QH_{2(aq)}$. To avoid these issues, solutions containing hydroquinone were kept below pH 9 throughout this thesis.

2.3.4 Ferrocyanide

The reversible redox reaction of ferrocyanide to ferricyanide is used in this thesis to study diffusion of the redox species towards WEs through hydrogels grown at those surfaces. The redox equation is as follows:

$$[Fe(CN)_6]^{4-}_{(aq)} \rightleftharpoons [Fe(CN)_6]^{3-}_{(aq)} + e^{-} \qquad \textit{Equation 2.35}$$

Though FFC in equal molarity is a common choice of reversible redox couple in electrochemical experimentation,[13] in this thesis only the ferrocyanide ion has been dissolved into solution, and instead a localised equimolar concentration of ferrocyanide and ferricyanide ions is generated in microscale volumes at WEs, as described in Section 2.2.5.

2.3.5 Hydrogen peroxide

The electrochemistry of hydrogen peroxide (H_2O_2) becomes relevant in Chapter 5 of this work as an electroactive species which oxidises at Pt electrodes with applied potentials of +0.6 V against Ag/AgCl/Cl^- (3M).[30] It is generated in this work through the GOx enzyme catalysed oxidation of glucose by oxygen, and the concentration of H_2O_2 is used as a measure of the concentration of glucose.[31–35] However, the electrochemical oxidation of H_2O_2 at Pt is a more complicated process than the overall chemical equation presented in Chapter 1 Section 1.1.2. The following multi-step mechanism is established in great detail by Hall *et al.*,[30,36,37] and is briefly described here. H_2O_2 first reversibly binds to an oxidised Pt(II) binding site $Pt(OH)_2$, which is essentially equivalent to hydrated platinum oxide, PtO:

$$H_2O_{2(aq)} + Pt(OH)_{2(s)} \rightleftharpoons Pt(OH)_2 \cdot H_2O_{2(s)} \qquad \textit{Equation 2.36}$$

The peroxide then undergoes a reversible oxidation at the Pt site:

$$Pt(OH)_2 \cdot H_2O_{2(s)} \rightleftharpoons Pt_{(s)} + 2H_2O_{(l)} + O_{2(g)} \qquad \textit{Equation 2.37}$$

Finally, the surface oxide $Pt(OH)_2$ binding site is regenerated through the electrochemical oxidation of water to complete the catalytic cycle:

$$Pt_{(s)} + 2H_2O_{(l)} \rightarrow Pt(OH)_{2(s)} + 2e^- + 2H^+_{(aq)} \qquad \textit{Equation 2.38}$$

The $Pt(OH)_2$ surface can be returned to due to the reversibility of the former reactions, regardless of whether potentials where Equation 2.38 occurs are being applied. However, it is important to note that the surface hydrated oxide regeneration reaction presented in Equation 2.38 is the source of Faradaic currents generated at the Pt WE that are used as a measure of H_2O_2 concentration.[30,36,37]

2.4 Materials and reagents

2.4.1 General aqueous solutions

All aqueous solutions and mixtures used in this work have been prepared with 18.2 MΩ UV purified deionised (DI) water. All pH measurements in this work were recorded using a Fisherbrand Hydrus 400 pH meter with a Mettler Toledo InLab Routine Pro pH probe at room temperature (typically 20-25 °C, measured with a K-type thermocouple). The pH meter was calibrated daily with Fluka Analytical buffer solutions between ranges 4-7 or 7-10, depending on the pH of experimental solutions to be measured.

0.1 M $NaCl_{(aq)}$ solutions were prepared by dissolving sodium chloride crystals (58 mg, 1 mmol, >99.5% purity, Fisher Scientific) in 10 mL DI water. 0.1 M $NaOH_{(aq)}$ solutions were prepared by dissolving NaOH pellets (40 mg, 1 mmol, ≥98% purity, Fluka Analytical) in 10 mL DI water. 0.1 M $HCl_{(aq)}$ solutions were prepared by mixing concentrated $HCl_{(aq)}$ (65 µL 37-38% concentrated solution, 1 mmol, Sigma Aldrich) in 10 mL DI water. 0.1 M $H_2SO_{4(aq)}$ solutions were prepared in 1 L batches by mixing concentrated $H_2SO_{4(aq)}$ (5.6 mL 95-97% concentrated solution, 100 mmol Sigma Aldrich) in 994.7 mL DI water. 1 M glucose solutions were prepared in 100 mL batches by dissolving D-(+)-glucose (18 g, 100 mmol, ≥95% purity, Sigma Aldrich) in 100 mL DI water, and refrigerating 4 °C. The glucose in these solutions was allowed to naturally mutarotate (from predominantly α-D-glucose to an equilibration between α-D-glucose and β-D-glucose, the latter of which GOx is selective to[32]) over at least 24 hours before use.

2.4.2 Gelator solution preparation

'Gelator solutions' in this work refer to aqueous solutions in which 10 mg/mL of either the Carb-Ala or BrAV gelator is dissolved. These solutions are prepared by first dissolving Carb-Ala (400 mg, 1.35 mmol, 33.8 mM) or BrAV (400 mg, 0.886 mmol, 22.2 mM) in 40 mL DI water containing an equimolar amount of NaOH (54.0 mg, 1.35 mmol, 33.8 mM or 35 mg, 0.886 mmol, 22.2 mM). From these batches, volumes of 1 mL are extracted for electrochemical gel growth experiments. To these 1 mL volumes, 10 µL 0.1 M $NaCl_{(aq)}$ is added as an electrolyte (making up approximately 1 mM when added), and a 2:1 molar ratio of hydroquinone to gelator is added (7.43 mg, 67.5 µmol, 67.5 mM or 4.89 mg, 44.4 µmol 44.4 mM, >99% purity, Sigma Aldrich) is added to the solution. The pH values of these solutions are then adjusted to at least pH 8.00 (no greater than pH 8.10) using 1-2 µL aliquots of 0.1 M $NaOH_{(aq)}$.

The Carb-Ala and BrAV gelators are synthesised as powders in-house by Bart Dietrich and Dave Adams of the Adams Group, at the University of Glasgow. Synthetic methods, chemical analyses, and purity analyses for the Carb-Ala and BrAV gelators can be found in the supplementary information provided for the works of Kubiak *et al.*[17] and Patterson *et al.*[20] respectively.

2.4.3 Buffer solution preparation

0.1 M citric acid/trisodium citrate buffer solution was prepared in 1 L batches by dissolving citric acid (10 g, 52.0 mmol, ≥95% purity, Sigma Aldrich) and trisodium citrate dihydrate (14 g, 47.6 mmol >99% purity, Fisher Scientific) in 1 L DI water. The pH of this buffer solution typically measures between 4.25 and 4.35. This buffered pH range (corresponding to the concentrations of citric acid to trisodium citrate) was selected as it lies well below the pK_a^{app}

of Carb-Ala (see Figure 2.14, Section 2.3.1), theoretically maintaining gelator molecule protonation and therefore hydrogel stability when transferred to this solution.

Phosphate-buffered saline (PBS) solution was made up in 1 L batches by dissolving 1 × PBS tablets (140 mM NaCl, 10 mM phosphate buffer, 3 mM KCl, pH 7.4 at 25 °C, Millipore) per 1 L DI water. pH of this buffer measured 7.4 at 25 °C

2.4.4 Ferrocyanide solution preparation

'Ferrocyanide solutions' in this work consist of 10 mM potassium hexacyanoferrate(II) trihydrate (42.3 mg, 0.100 mmol, 99% purity, Scientific Laboratory Supplies) and 0.1 KCl (74.5 mg, 1.00 mmol, >99% purity, Sigma Aldrich) in 10 mL citric acid/trisodium citrate buffer solution (see Section 2.4.3).

2.4.5 Glucose oxidase solution preparation

10 mg/mL glucose oxidase solutions were prepared in one of two ways. The first method, done by Richard Bennett of the Mount group in the University of Edinburgh, begins by dissolving 10 mg of lyophilised glucose oxidase powder from *Aspergillus niger* (enzyme specific activity = 248 U/mg, Sigma Aldrich) into 1 mL DI water to make up a 10 mg/mL solution. This batch would then be separated into 25 uL aliquots, each stored in 0.5 mL Eppendorf® tubes at approximately -20 °C. These frozen solutions were allowed to warm to room temperature when required for experimental work, and were used for electrode drop-coating. The second method involves dissolving 10 mg glucose oxidase from *Aspergillus niger* into 1 mL Carb-Ala gelator solution at pH 8. Once dissolved, the pH was adjusted to between pH 8.00 and pH 8.10 using 1-2 µL aliquots of 0.1 M $NaOH_{(aq)}$. This solution was then used immediately for experimentation.

The specific activity of a given batch of GOx enzyme can be found in the diagrams of experiments in Chapter 5 of this thesis, and is quoted in U/mg (units per milligram).

2.5 Experimental setup

2.5.1 Electrode cleaning process

The working electrodes used in this thesis were cleaned before starting each experiment to remove any residual adsorbed passivating material. An electrode would first be mechanically polished by performing 60 figure-of-eight motions on each of three microfiber cloth pads soaked with water-alumina slurries of sequentially lower particle sizes (1 µm, 0.3 µm, and 0.05 µm diameter particle sizes), prepared with MicroPolish^{TM} Alumina (Buehler) in DI water, by-volume ratio of 1:1. After completing a polish on a pad, the electrode was rinsed with DI water. Fifteen cyclic voltammetry scans in 10 mL 0.1 M $H_2SO_{4(aq)}$, at a rate of 0.1 V/s between -0.4 V and 1.90 V, were performed to electrochemically clean the electrode post-polish (shown previously in Figure 2.3b), using H_2/base and O_2/acid production at the solvent limits to both mechanically and chemically clean the electrode surface.

2.5.2 Electrochemical cell

The three types of commercial WE (all produced by IJ Cambria Scientific Ltd) used in this thesis are a Pt disc macroelectrode (2 mm diameter), a Pt disc microelectrode (25 µm diameter), and a carbon fibre disc microelectrode (33 µm diameter). The RE is a silver/silver chloride electrode (Ag/AgCl/Cl^- (1M), CH Instruments Inc.). The CE was produced in house by electron beam evaporation of a thin film (50 nm) Pt onto a Si wafer surface oxidised to SiO_2, on which a Ti adhesion layer (10 nm) had been predeposited. When submerged, approximately 1 cm^2 of this Pt chip's surface area was exposed to solution. Vessels in which electrolytic solutions are contained and electrodes are submerged vary throughout this thesis. Electrochemistry was generally housed within Pyrex glass or polypropylene containers, the volumes of which were adjusted to sizes suitable for the space available and volumes of solution necessary during a given experiment. For example, when hydrogels were grown at micro or macroelectrode surfaces, to conserve valuable gelator, solutions of 1 mL were used, and in these cases a cone-ended 15 mL polypropylene Falcon® tube cut to size was used as a container for these solutions and electrodes (Figure 2.17). All electrochemical procedures and measurements were recorded using a Metrohm Ltd. AutoLab PGSTAT128N potentiostat with Nova 1.11 software.

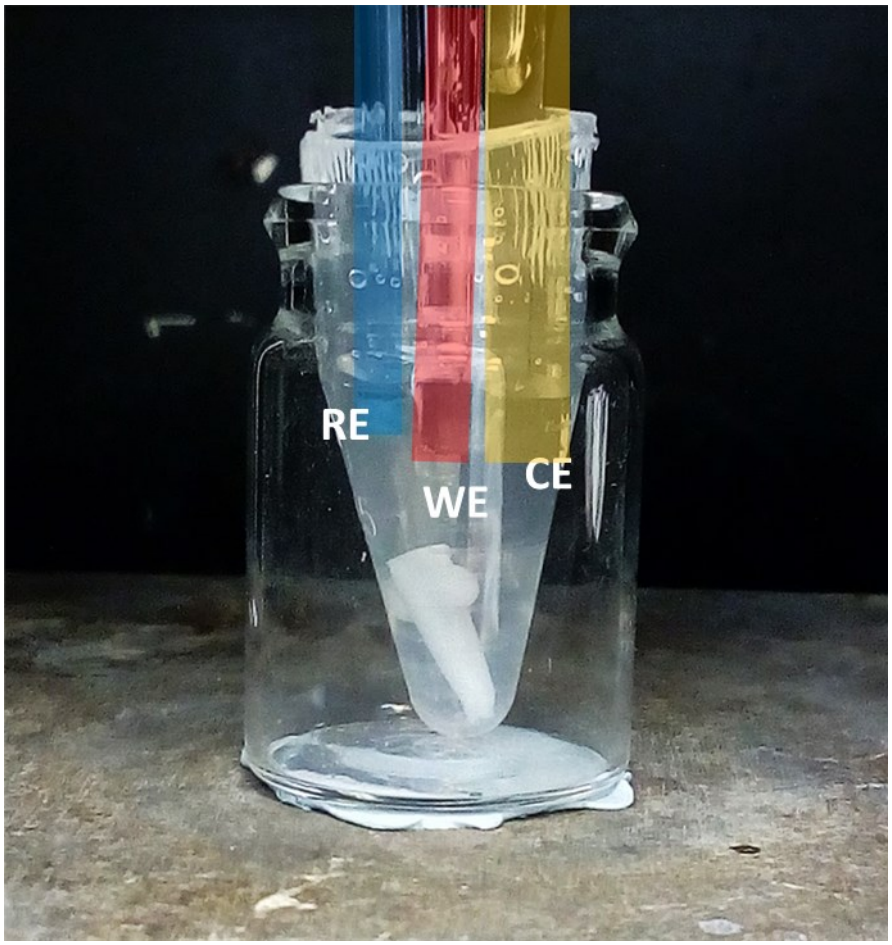

Figure 2.17 A three-electrode system set up within the end of 15 mL polypropylene Falcon® tube, cut to a volume of approximately 2 mL. WE (highlighted in red), CE (yellow) and RE (blue) are all submerged in a 1 mL volume of liquid, along with a magnetic stirrer.

2.5.3 Faraday cage and temperature control

Unless otherwise stated, all electrochemical experimentation in this work was carried out within a grounded Faraday cage, housing an in-house-built extended water bath unit. The in-house extended water bath unit circulates water from a Lauda Eco Silver / Eco E4 commercial water bath, situated outside of the Faraday cage (Figure 2.18, Figure 2.19), allowing the temperature of experiments within the cage to be modulated and controlled. Temperature of the in-house extended water bath was measured with a K type thermocouple, and was kept at a fixed temperature of either 25 °C or 37 °C (the temperature set is stated in the individual experiments within this work) by adjusting the temperature of the commercial water bath. The extended water bath was designed to firmly suspend an electrochemical cell within it, removing the requirement to store the larger water bath within the cage. Replacement of the commercial water bath in the cage also reduces the intrusion of AC hum in electrochemical measurements, which would occur whenever power was supplied to the commercial water bath, as power cabling would need to be threaded into the cage. In addition to these components, a hotplate with magnetic stirrer was also stored within the cage for the purpose of stirring solutions during biosensor experimentation (used in Chapter 5).

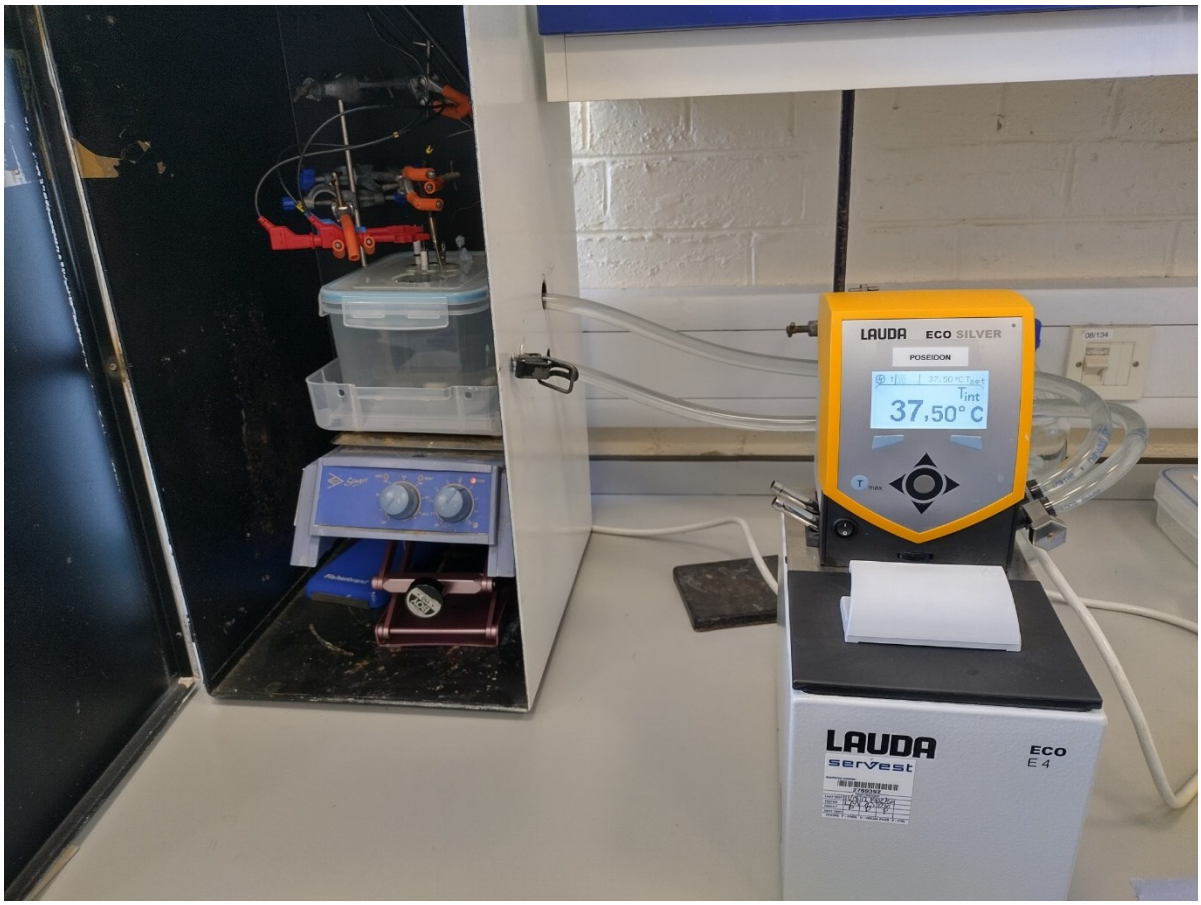

Figure 2.18 External view of general experimental setup for electrochemistry in this work. Temperature control within the in-house extended water bath (left) is provided by a coupled commercial water bath outside the Faraday cage (right).

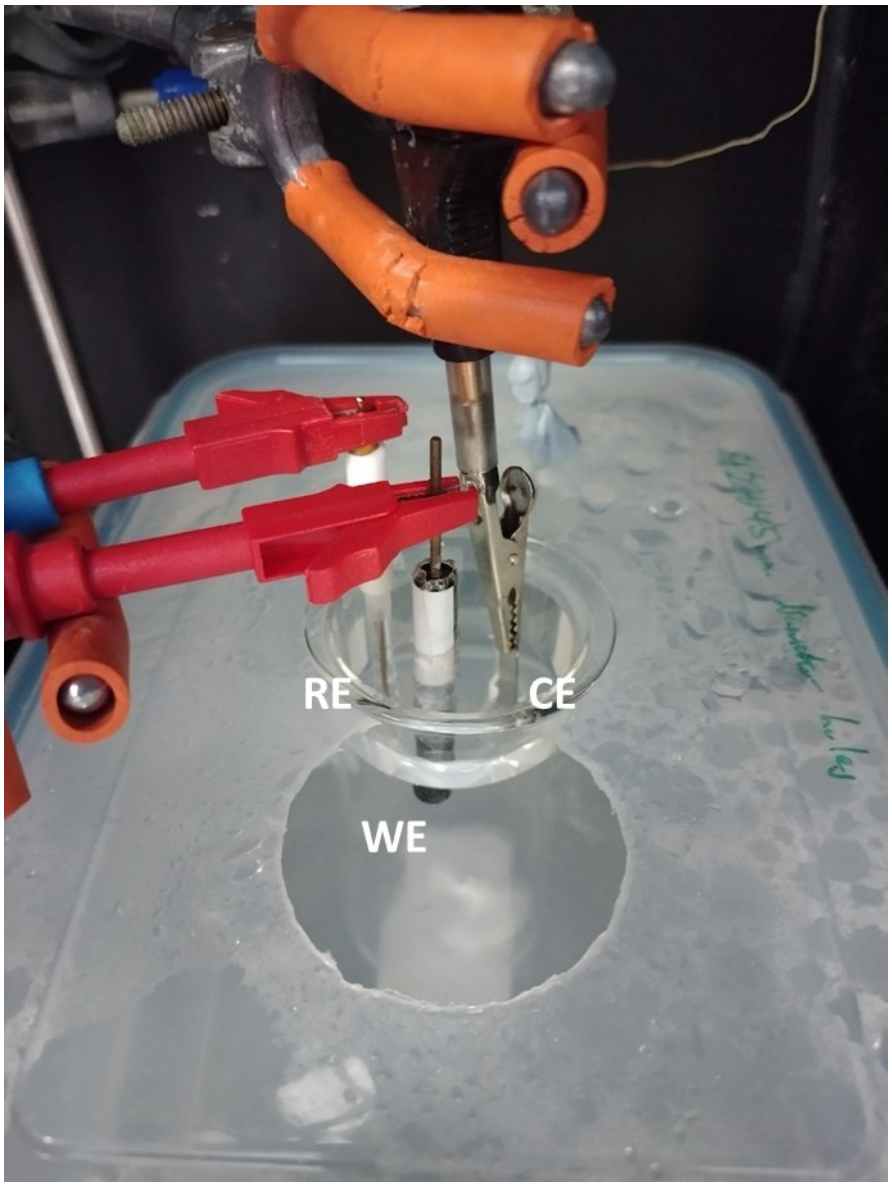

Figure 2.19 Internal view of general experimental setup for electrochemistry in this work. Three-electrode system (labelled WE, CE and RE) is submerged in an aqueous solution, contained within a beaker resting suspended at the top of the extended water bath in the Faraday cage.

2.5.4 Imaging hydrogels

A Yenway ISH500 microscope (PL10X/22 eyepiece, LMPlan, 10x/0.3, ∞/0, WD/2.2) with CMOS camera and YenCam software was used to inspect and capture images of Carb-Ala gels grown at Pt microelectrodes in this work. The YenCam software was calibrated to measure dimensions on the image plane (Figure 2.20).

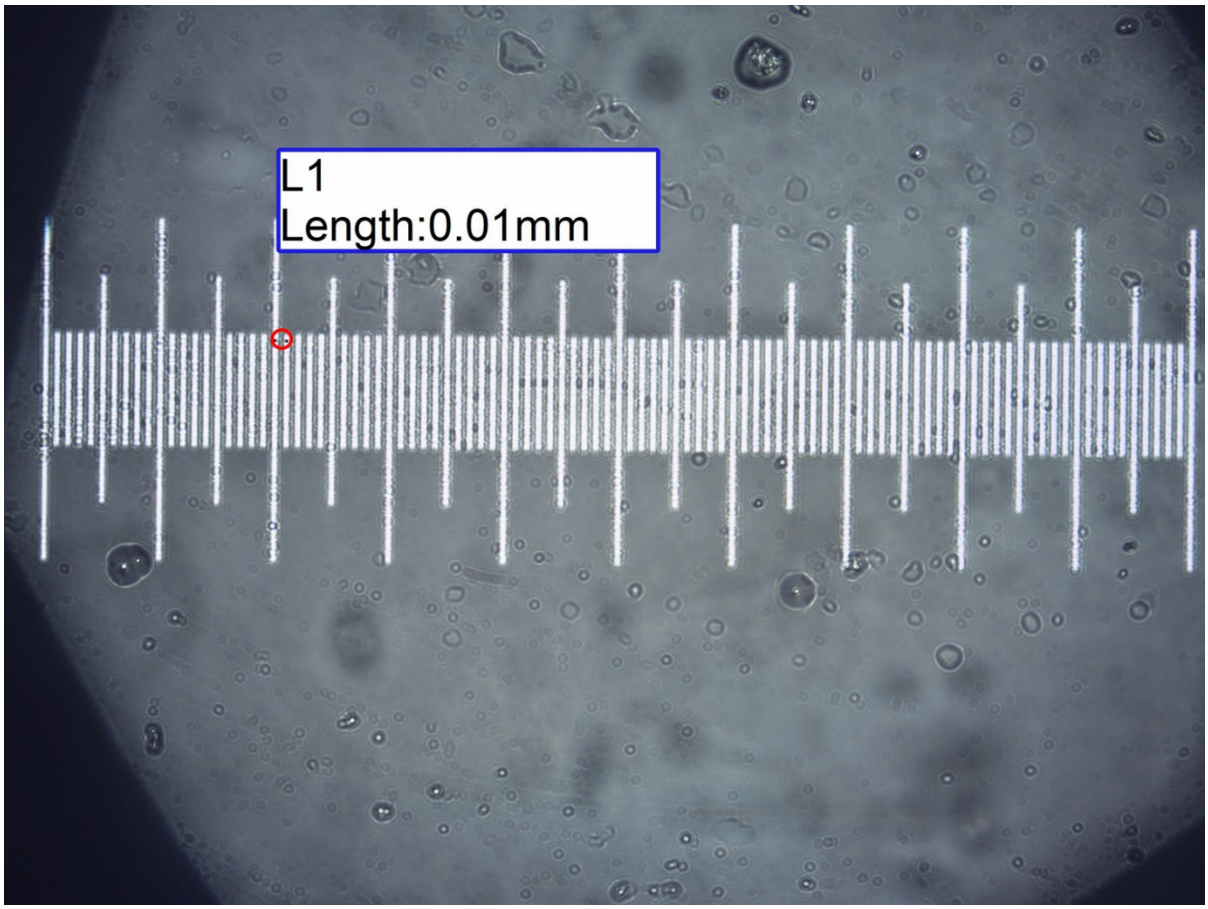

Figure 2.20 Image of calibration rule slide at 1000x magnification (10x at eyepiece, 100x at object). 10 µm separation between smallest divisions. YenCam software measures width of smallest division (line between two points, circled in red) as 10 µm, confirming calibration.

Imaging of hydrogels was set to a total of 100 times magnification (10x at eyepiece, 10x at object). The surface of the commercial microelectrodes were viewed side-on, so that the length of the electrodes appeared parallel to the image plane. It is important to note that the curvature of the glass casing housing the commercial microelectrodes also applied an additional magnification factor of 1.6 to the Pt wires encased within them. This factor was determined by comparing the actual width of the Pt wires (stated by the manufacturer) to the width of the wires measured under the microscope, which was calibrated as shown above (Figure 2.20). This made those wires appear to have diameters of 40 µm as opposed to the actual diameters of 25 µm (Figure 2.21). The dimensions of the hydrogels grown at these microelectrodes were measured using Fiji[38] software. The software allows for the measurement of the heights, widths and cross-sectional areas of the hydrogels.[39,40]

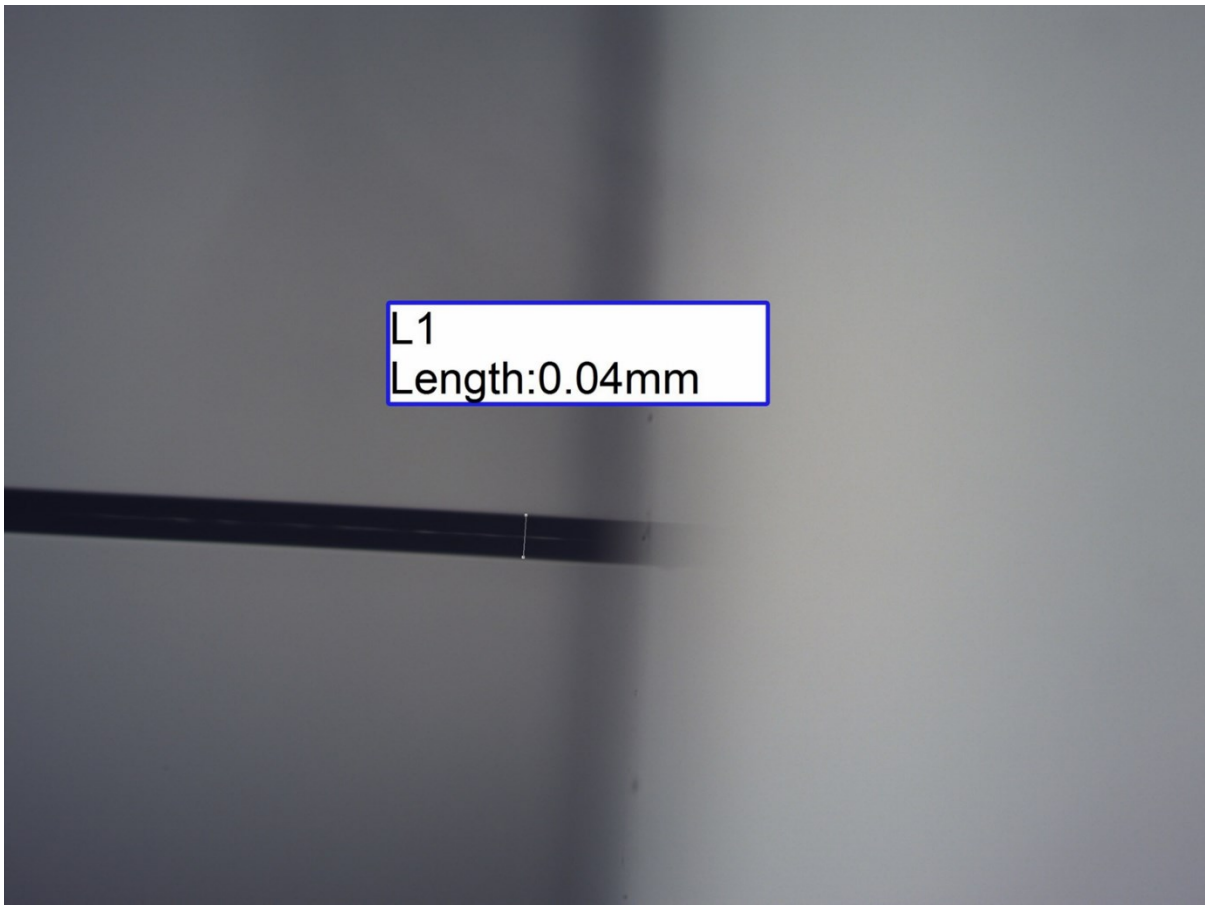

Figure 2.21 Image depicting side-on view of end of commercial Pt microelectrode at 100x magnification (10x at eyepiece, 10x at object). Near-horizontal Black line in centre of image is of backlit 25 µm Pt wire encased in glass, is tapered at glass/air interface. Width of encased Pt wire measures 40 µm in YenCam software, however, this is due to the additional magnification of the wire due to curvature of the glass it is encased within.

In Chapter 3 Section 3.5.6 and 3.5.11, Carb-Ala hydrogel growth was monitored under the microscope *in situ*. These experiments, which each span a 3 hour period, were carried out within a vessel that was open to air, constructed from a petri dish and epoxy resin sealed piece of polypropylene tube (maximum volume approx. 5 mL). These experiments were carried out outside of a Faraday cage due to space requirements (Figure 2.22). Solution evaporation would occur over long periods of time due to the openness of the vessel, reducing the volume of the solution minutely. This would affect the experiment by drifting focal point at the electrode, which would need to be adjusted on the order of single µm in hourly periods. This drift was accounted for by adjusting the focal point of the microscope at several points of time during a given experiment. In addition, the aqueous solution also caused a slight change in magnification of the whole images by a factor of 1.18. This factor was obtained by comparing the dimensions of the Pt wires and hydrated gels outside and within aqueous solutions, and was accounted for in gel dimension measurements.

Figure 2.22 Experimental setup for 3 hour potentiostatic Carb-Ala gel growth experiments. Features petri dish with open-topped ~5 mL vessel, sealed with epoxy resin to base of dish. The three-electrode system features a Pt disc microelectrode (25 µm) and Ag/AgCl/Cl$^-$ reference electrode (both fixed in slots at the side of the vessel and sealed with silicone rubber), with a Pt sputter-coated silicon chip counter electrode (rested in the vessel). The vessel is filled with 5 mL 10 mg/mL Carb-Ala gelator solution.

2.6 References

1 A. C. Fisher, *Electrode Dynamics*, Oxford University Press Inc., New York, 1st edn., 1996.

2 C. M. A. Brett and A. M. O. Brett, *Electroanalysis*, Oxford University Press Inc., New York, 1st edn., 1998.

3 J. Heinze, Ultramicroelectrodes in Electrochemistry, *Angew. Chem. - Int. Ed.*, 1993, **32**, 1268–1288.

4 R. J. Forster, Microelectrodes : New Dimensions in Electrochemistry, *Chem. Soc. Rev.*, 1994, **23**, 289–297.

5 K. Ngamchuea, S. Eloul, K. Tschulik and R. G. Compton, Planar diffusion to macro disc electrodes — what electrode size is required for the Cottrell and Randles-Sevcik equations to apply quantitatively ?, *J. Solid State Electrochem.*, 2014, **18**, 3251–3257.

6 A. J. Bard and L. R. Faulkner, *Electrochemical Methods: Fundamentals and Applications*, John Wiley & Sons, New York, 2nd ed., 2001, vol. 677.

7 K. Stulik, C. Amatore, K. Houb, V. Marecek and W. Kutner, MICROELECTRODES . DEFINITIONS, CHARACTERIZATION , AND APPLICATIONS (Technical Report), *Pure Appl. Chem.*, 2000, **72**, 1483–1492.

8 C. Amatore, C. Pebay, L. Thouin, A. Wang and J. Warkocz, Difference between Ultramicroelectrodes and Microelectrodes : Influence of Natural Convection, *Anal. Chem.*, 2010, **82**, 6933–6939.

9 Y. Saito, A Theoretical Study on the Diffusion Current at the Stationary Electrodes of Circular and Narrow Band Types, *Rev. Polarogr.*, 1968, **15**, 177–187.

10 D. Grieshaber, R. MacKenzie, J. Vörös and E. Reimhult, Electrochemical biosensors - Sensor principles and architectures, *Sensors*, 2008, **8**, 1400–1458.

11 N. Elgrishi, K. J. Rountree, B. D. Mccarthy, E. S. Rountree, T. T. Eisenhart and J. L. Dempsey, A Practical Beginner ' s Guide to Cyclic Voltammetry, *J. Chem. Educ.*, 2018, **95**, 197–206.

12 J. R. Macdonald, W. B. Johnson, I. D. Raistrick, D. R. Franceschetti, M. C. H. McKubre, D. D. Macdonald, B. Sayers, N. Bonanos, B. C. H. Steele, E. P. Butler, W. L. Worrell, A. Goossens, E. Barsoukov, B. E. Conway and N. Wagner, *Impedance Spectroscopy Theory, Experiment, and Application*, John Wiley & Sons, Hoboken, New Jersey, 2nd edn., 2005.

13 H. L. Woodvine, J. G. Terry, A. J. Walton and A. R. Mount, The development and characterisation of square microfabricated electrode systems, *Analyst*, 2010, **135**, 1058–1065.

14 P. Los, G. Zabinska, A. Kisza, L. Christie, A. Mount and P. G. Bruce, Electrochemical studies of heterogeneous reduction of tetracyanoquinodimethane in poly (ethylene oxide) electrolytes using ac impedance and cyclic voltammetry at an ultramicroelectrode, *Phys. Chem. Chem. Phys.*, 2000, **2**, 5449–5454.

15 S. J. Konopka and B. Mcduffie, Diffusion Coefficients of Ferri- and Ferrocyanide Ions in Aqueous Media , Using Twin-Electrode Thin-Layer Electrochemistry IqT, *Anal. Chem.*,

1970, **42**, 1741–1746.

16 I. Schmueser, A. J. Walton, J. G. Terry, H. L. Woodvine, N. J. Freeman and A. R. Mount, A systematic study of the influence of nanoelectrode dimensions on electrode performance and the implications for electroanalysis and sensing, *Faraday Discuss.*, 2013, **164**, 295–314.

17 P. S. Kubiak, S. Awhida, C. Hotchen, W. Deng, B. Alston, T. O. McDonald, J. Adams and P. J. Cameron, Polymerization of low molecular weight hydrogelators to form electrochromic polymers, *Chem. Commun.*, 2015, **51**, 10427–10430.

18 A. Piper, B. M. Alston, D. J. Adams and A. R. Mount, Functionalised microscale nanoband edge electrode (MNEE) arrays: the systematic quantitative study of hydrogels grown on nanoelectrode biosensor arrays for enhanced sensing in biological media, *Faraday Discuss.*, 2018, **210**, 1–17.

19 G. Pont, L. Chen, D. G. Spiller and D. J. Adams, The effect of polymer additives on the rheological properties of dipeptide hydrogelators, *Soft Matter*, 2012, **8**, 7797–7802.

20 C. Patterson, B. Dietrich, C. Wilson, A. R. Mount and D. Adams, Electrofabrication of large volume di- and tripeptide hydrogels via hydroquinone oxidation, *Soft Matter*, 2022, **18**, 1064–1070.

21 J. Raeburn, B. Alston, J. Kroeger, T. O. McDonald, J. R. Howse, P. J. Cameron and D. J. Adams, Electrochemically-triggered spatially and temporally resolved multi-component gels, *Mater. Horizons*, 2014, **1**, 241–246.

22 M. Wallace, J. A. Iggo and D. J. Adams, Using solution state NMR spectroscopy to probe NMR invisible gelators, *Soft Matter*, 2015, **11**, 7739–7747.

23 L. Chen, K. Morris, A. Laybourn, D. Elias, M. R. Hicks, A. Rodger, L. Serpell and D. J. Adams, Self-Assembly Mechanism for a Naphthalene - Dipeptide Leading to Hydrogelation, *Langmuir*, 2010, **26**, 5232–5242.

24 E. K. Johnson, D. J. Adams and P. J. Cameron, Directed Self-Assembly of Dipeptides to Form Ultrathin Hydrogel Membranes, *J. Am. Chem. Soc*, 2010, **132**, 5130–5136.

25 Y. Liu, E. Kim, R. V Ulijn, W. E. Bentley and G. F. Payne, Reversible Electroaddressing of Self-assembling Amino-Acid Conjugates, *Adv. Funct. Mater.*, 2011, **21**, 1575–1580.

26 E. K. Johnson, L. Chen, P. S. Kubiak, S. F. Mcdonald, D. J. Adams and P. J. Cameron, Surface nucleated growth of dipeptide fibres, *Chem. Commun.*, 2013, **49**, 8698–8700.

27 E. R. Cross and D. J. Adams, Probing the self-assembled structures and pKa of hydrogels using electrochemical methods, *Soft Matter*, 2019, **15**, 1522–1528.

28 M. Quan, D. Sanchez, M. F. Wasylkiw and D. K. Smith, Voltammetry of quinones in unbuffered aqueous solution: Reassessing the roles of proton transfer and hydrogen bonding in the aqueous electrochemistry of quinones, *J. Am. Chem. Soc.*, 2007, **129**, 12847–12856.

29 J. D. Roberts and M. C. Caserio, in *Basic Principles of Organic Chemistry*, Addison-Wesley, Menlo Park, California, 2nd edn., 1977, pp. 1287–1341.

30 S. B. Hall, E. A. Khudaish and A. L. Hart, Electrochemical oxidation of hydrogen peroxide at platinum electrodes. Part III: Effect of temperature, *Electrochim. Acta*, 1999, **44**, 2455–2462.

31 S. B. Bankar, M. V. Bule, R. S. Singhal and L. Ananthanarayan, Glucose oxidase - An overview, *Biotechnol. Adv.*, 2009, **27**, 489–501.

32 S. A. Pullano, M. Greco, M. G. Bianco, D. Foti, A. Brunetti and A. S. Fiorillo, Glucose biosensors in clinical practice: Principles, limits and perspectives of currently used devices, *Theranostics*, 2022, **12**, 493–511.

33 C. Chen, Q. Xie, D. Yang, H. Xiao, Y. Fu, Y. Tan and S. Yao, Recent advances in electrochemical glucose biosensors: A review, *RSC Adv.*, 2013, **3**, 4473–4491.

34 W. Jia, K. Wang and X. Xia, Elimination of electrochemical interferences in glucose biosensors, *Trends Anal. Chem.*, 2010, **29**, 306–318.

35 B. Purohit, A. Kumar, K. Mahato and P. Chandra, in *Miniaturized Biosensing Devices*, eds. P. Chandra and K. Mahato, Springer Singapore, Singapore, 1st edn., 2022, pp. 149–175.

36 S. B. Hall, E. A. Khudaish and A. L. Hart, Electrochemical oxidation of hydrogen peroxide at platinum electrodes. Part I: An adsorption-controlled mechanism, *Electrochim. Acta*, 1998, **43**, 579–588.

37 S. B. Hall, E. A. Khudaish and A. L. Hart, Electrochemical oxidation of hydrogen peroxide at platinum electrodes. Part II: effect of potential, *Electrochim. Acta*, 1998, **43**, 2015–2024.

38 J. Schindelin, I. Arganda-Carreras, E. Frise, V. Kaynig, M. Longair, T. Pietzsch, S. Preibisch, C. Rueden, S. Saalfeld, B. Schmid, J. Y. Tinevez, D. J. White, V. Hartenstein, K. Eliceiri, P. Tomancak and A. Cardona, Fiji: An open-source platform for biological-image analysis, *Nat. Methods*, 2012, **9**, 676–682.

39 E. R. Cross, The electrochemical fabrication of hydrogels: a short review, *SN Appl. Sci.*, 2020, **2**, 1–11.

40 E. R. Cross, K. McAulay and D. J. Adams, in *Polypeptide Materials*, ed. M. G. Ryadnov, Humana, New York, 2021, pp. 179–188.

Chapter 3 – Tuning electrochemical gelation of dipeptide-based hydrogels at single microelectrodes

3.1 Introduction

Peptide-based gelator molecules are capable of self-assembling and forming hydrogels in regions of aqueous solution where pH is sufficiently below the pK_a^{app} of the gelator. Self-assembly of these molecules proceeds through the formation of hydrogen bonds and π-π stacking interactions with other peptide gelators in order to shield the hydrophobic components of the monomer units from the surrounding aqueous solution.[1] The two-electron electrochemical oxidation of hydroquinone facilitates the production of a localised pH shift to trigger the self-assembly of dipeptide-based gelators.[2,3] Unlike global shifts in pH via the addition of an acid or acid-precursor to bulk gelator solution,[4,5] the electrochemical pH trigger offers spatiotemporal control of gel formation, confining the growth of hydrogels within the low pH volume (Figure 3.1).[2,3] By lowering the required potential for proton production necessary for gelation, this in turn lowers the evolution of O_2 gas due to water oxidation, increasing the homogeneity of entanglement within the gel.[1,6]

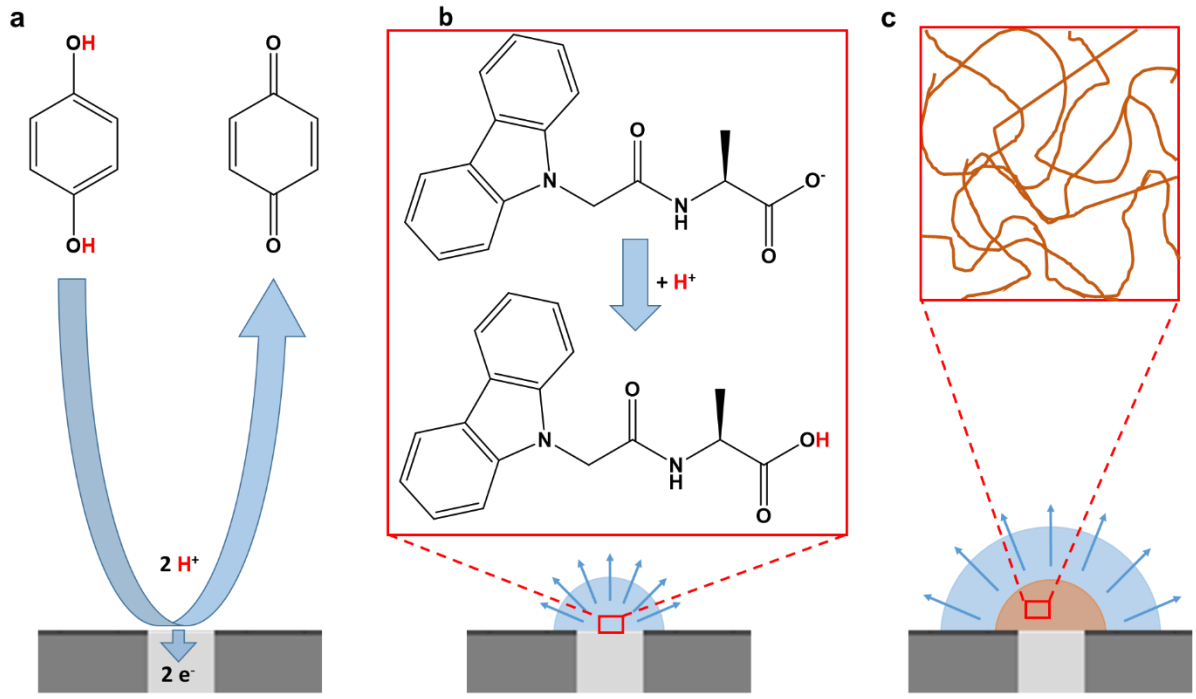

Figure 3.1 General process of electrochemical gelation at a single microelectrode surface. (a) The oxidation of hydroquinone to benzoquinone by application of a suitable potential produces protons. (b) The acidic volume expands, and Carb-Ala gelator molecules are protonated, initiating pH-triggered self-assembly where pH is lower than the gelator pK_a^{app} within the low pH zone. (c) Entanglement of the self-assembled aggregates produces a hydrogel within the low pH zone.

It is only in the last decade that techniques of electrochemically growing supramolecular gels have been developed at macroelectrode surfaces,[1,2,14,6–13] and even more recently some initial work has been conducted on nanoelectrode surfaces.[15] However, there is currently little to no information on the properties and spatiotemporal growth of hydrogels at microelectrode surfaces. Due to their size, microelectrodes reach steady-state currents far faster than macroelectrodes are capable of, possess greater Faradaic current densities (resulting in enhanced SNR) and have lower iR drops (the reduction in applied potential at WE due to the solution resistance between RE and WE). They are therefore relatively unaffected by convection, and can function efficiently in more resistive media.[16–19] These properties make microelectrodes ideal for the quantitative detection of low concentrations of chemical species, an application that is particularly relevant to biosensing.[20,21] There is therefore potential interest in growing hydrogels at microelectrode surfaces for the intent of integrating them as anti-fouling membranes into biosensing systems.

This application for electrochemically grown hydrogels has previously been explored by Piper *et al.* at nanoscale Pt electrode arrays,[15] though that work also demonstrated some unwanted reactions that affect the final properties of electrochemical gels, facilitated by galvanostatic gel growth conditions. When hydroquinone local to the electrode surface has been depleted, the electrochemical system can require other electroactive species to be oxidised in order to continue passing the fixed current. Water splitting with resulting oxygen gas production then occurs, which leads to bubble formation in growing hydrogels.[1,6,15,22] Such inhomogeneity within self-assembled networks is a trait that should be avoided to prevent poor gel structural integrity.[6,23] In addition, allowing the system to reach water splitting potentials means that any other electroactive species (that has an oxidation potential above hydroquinone and below that of water) will also be oxidised. This leads to the second unwanted factor resulting from galvanostatic gel growth: Carb-Ala (Figure 3.1), a peptide-based gelator, has been shown to undergo polymerisation when electrochemically oxidised at a WE surface.[11]

Most studies have utilised galvanostatic control to induce electrochemically-triggered gelation of dipeptide-based supramolecular gels.[11,22] As far as the author is aware, the first study that utilised potentiostatic control to induce gelation of a low molecular weight gelator was that of Kubiak *et al.*,[11] where the growth of a Carb-Ala hydrogel was followed by intentional polymerisation of the network by the application of cyclic voltammetry. How the presence or lack of the resulting polymer affects gel self-assembly and functionalised electrode properties has not yet been explored. Rather than using chronopotentiometry, this chapter explores the use of chronoamperometry to promote the self-assembly of Carb-Ala at microelectrode surfaces. This potentiostatic method allows only electroactive species with redox potentials at or below the selected potential to be involved in redox chemistry. The motivation behind using this method fundamentally lies in avoiding gelator and water oxidation: it ensures the selective oxidation of hydroquinone alone promotes electrochemical acid-triggered self-assembly, and excludes the polymerisation of Carb-Ala.

Various spectroscopic, microscopic and rheological techniques have allowed the properties and growth of electrochemical gels to be studied, however the scale of microelectrode gels and the complications that come with their restricted size limits the number of techniques

that can be used to study them. This chapter will investigate whether the final properties of the electrochemical gels can be better tuned by fixing the potential rather than the current, and whether this results in controllable and reproducible characteristics, as analysed/probed using electrochemical and optical techniques. In particular, the application of EIS, which had previously been employed by Piper *et al.* as a primary method of studying the diffusional properties of nanoelectrode arrays functionalised with supramolecular hydrogels,[15] will be explored here to investigate its suitability as a method of characterising electrochemically grown hydrogels.

In this chapter, hydroquinone electrochemistry at single Pt disc microelectrodes will first be characterised, before demonstrating the use of chronoamperometry as a viable method of promoting the growth of Carb-Ala hydrogels through the selective oxidation of hydroquinone. Next, microelectrodes functionalised with potentiostatically-grown Carb-Ala gels, grown on the order of minutes for varying periods and at different potentials, will be characterised with thorough analysis via EIS and optical microscopy. Lastly, the effects of allowing potentiostatic hydrogel growth to proceed on longer timescales on the order of hours will be studied using microscopic techniques and through analysis of current-time transients.

3.2 Characterising hydroquinone electrochemistry

3.2.1 Aqueous solutions with and without Carb-Ala gelator

Before beginning any experimental work studying electrochemically grown hydrogels, an understanding of how hydroquinone electrochemistry would change in aqueous solutions with the dissolved Carb-Ala gelator was required. Typical CVs for Pt disc microelectrodes in pH 8 aqueous solutions containing hydroquinone with and without the Carb-Ala gelator can be found in Figure 3.2.

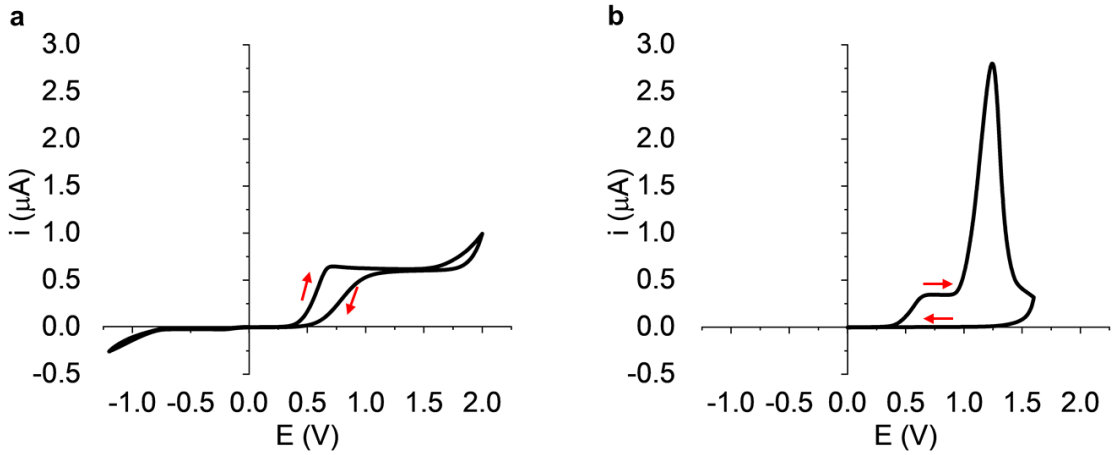

Figure 3.2 CVs in 10 mL aqueous solutions (pH 8) containing hydroquinone (67.5 mM) and NaCl (1 mM), at a Pt disc microelectrode (25 µm diameter), with starting potential E = 0 V, initial scan direction positive, scan rate v = 0.1 V s^{-1}, T = 25 °C. (a) E scanned between -1.2 V and 2.0 V. (b) With added 10 mg/mL Carb-Ala, E scanned between 0 V and 1.6 V.

In the solution without gelator (Figure 3.2a), a broad potential range was swept to clearly establish the hydroquinone redox chemistry within the solution redox limits. The hydroquinone oxidation wave lay between +0.3 V and +1.0 V. A difference in half-wave potentials between the forward and reverse scans of 250 mV was observed, attributed to the result of a local pH change at the microelectrode surface. At neutral pH, given the electrochemical oxidation of hydroquinone is approximately $2e^-$ $2H^+$,[3] at 25 °C the reduction potential should shift by +59 mV for every 1 unit decrease in pH.[24] This potential shift of 250 mV would therefore equate to a decrease in pH of 4-5 units, meaning in the forward scan the pH local to the electrode surface is likely to have dropped from the initial measured pH 8 to approximately below pH 4. This would be sufficiently low enough to trigger the self-assembly of the Carb-Ala gelator (see titration curve, Figure 2.14, Chapter 2 Section 2.3.1)

The maximum anodic currents corresponding to hydroquinone oxidation for the forward and reverse scans measured 0.65 µA and 0.60 µA respectively. It was initially assumed that the slight difference in current in the forward and reverse scans could be indicative of a change in the diffusion coefficient of hydroquinone (as *n* and *r* were not expected to change). As shown in the Saito equation[25] (Equation 2.9, Chapter 2 Section 2.1.3), the limiting current i_L at a microelectrode is proportional to the diffusion coefficient of the electroactive redox species (in this case, hydroquinone). The forward scan elapsed 20 seconds, and in this time 9.7 µC of charge was passed: this would equate to approximately 0.05 nmol of oxidised

hydroquinone, which is a negligible amount compared to the initial 6.75 mol of hydroquinone in the 10 mL solution (Figure 3.2a). Since the bulk concentration of hydroquinone did not deviate significantly in this time, it is more likely that the slight peak in the forward scan was due to the setting up of steady-state conditions at the electrode surface rather than a change in *D* for hydroquinone with pH. Therefore, the steady-state current due to hydroquinone oxidation in the forward scan should be taken from the range of 1.2 V to 1.5 V, as 0.62 µA.

The CV potential range was then narrowed for the solution containing the Carb-Ala gelator (Figure 3.2b). An anodic wave with a limiting current of 0.34 µA was measured in this solution. This wave started at 300 mV and was again identified as the oxidation of hydroquinone. Given that the concentration of hydroquinone was the same in this solution as in the previous solution (without the gelator), the decrease in current strongly indicated a change in mass transport of hydroquinone due to the addition of the gelator to the solution. Considering the Saito equation[25] (Equation 2.9, Chapter 2 Section 2.1.3), the variables that could feasibly undergo a change corresponding to the drop in current for the hydroquinone oxidation electrochemistry are the concentration of hydroquinone c_{bulk}, the radius of the electrode *r* and the diffusion coefficient *D* of hydroquinone. As stated prior, the amount of hydroquinone consumed from the total in the bulk is negligible in this case, so c_{bulk} can be treated as unchanged.

Though the radius of the electrode will remain unchanged, a change in available surface area is likely, due to a combination of minor fouling in the gelator solution and the unknown process of adsorption/anchoring of the supramolecular structures to the electrode surface. It can also be assumed that the hydrogel slows the flow of the aqueous phase.[26] These reductions in rate due to adsorption and reduced flow through the gel are thus the more likely causes for the reduced currents in the gelator solution, and can be encompassed by a reduction in *D.*

D for the gelator-less solution (Figure 3.2a) equates to approximately 9.5×10^{-10} m^2 s^{-1}, whereas *D* for the solution containing the Carb-Ala gelator in the forward scan (Figure 3.2b) dropped to 5.2×10^{-10} m^2 s^{-1}. The decreased *D* for hydroquinone in the Carb-Ala gelator solution (Figure 3.2b) suggests a change in solution viscosity η, according to the Stokes-Einstein equation (Equation 3.1):

$$D = \frac{kT}{6\pi\eta r_{HD}} \qquad \textit{Equation 3.1}$$

where *k* is the Boltzmann constant, *T* is the temperature and r_{HD} is the hydrodynamic radius of hydroquinone. A change in r_{HD} in the presence of Carb-Ala was thought to be unlikely. It is more likely that the solution had become more viscous due to the addition of the gelator. However, a doubling in solution viscosity also could be a misinterpretation of the reason for such a change in *D*. It must also be considered that the flow of solution through the Carb-Ala hydrogel network (which presumably will have grown at the Pt microelectrode surface) will be slowed, which could also simulate a significant local increase in viscosity.

In addition to this change in limiting current, the voltammogram recorded in this gelator solution did not feature this oxidation wave in the reverse scan (Figure 3.2b), indicating that hydroquinone D was reduced to 0 $m^2 s^{-1}$ in the reverse scan. An irreversible peak also was observed in the forward scan of this voltammogram, the base of which began at +0.9 V, and reached a peak current at +1.2 V of 2.80 µA. This peak decreased towards the end of the forward scan of the CV, continuing to drop on the reverse scan, and reaching a near zero current. This irreversible peak in the anodic sweep is consistent with observations from previous studies, where the onset of Carb-Ala gel oxidation (polymerisation) is observed above +0.75 V.[11] The lack of hydroquinone oxidation in the reverse sweep implies that once the Carb-Ala local to the electrode surface was oxidised, the polymerised material passivated the electrode, preventing further electrochemistry from occuring.

3.2.2 Assessing chronoamperometry as a technique for electrochemical gelation

The main benefit of fixing the applied potential lies in the ability to select which electroactive species are involved in the redox chemistry. In the case of the Carb-Ala gelator solutions, it is possible for hydroquinone to be oxidised without gelator oxidation (which would also lead to polymerisation in the case of Carb-Ala[11]) or water oxidation competing with this process. This can be done by applying potentials between 0.6 V and 0.9 (as indicated by the flat portion in the voltammogram of the Carb-Ala gelator solution, Figure 3.2b). Thus, it was decided that +0.7 V would be a suitable fixed potential to apply for the purpose of generating an acidic volume necessary for the electrochemical acid-trigger, without these additional effects taking place. This method of inducing selective hydroquinone oxidation and electrochemical gel growth was first tested using a 2 mm diameter Pt disc macroelectrode, by applying +0.7 V for 120 seconds in a solution with 100 mM of additional NaCl electrolyte. After this chronoamperometry experiment was completed, the macroelectrode was removed from the gelator solution, and excess solution around the electrode was wicked away with tissue paper. Doing so revealed a near-hemispherical Carb-Ala gel (Figure 3.3), which had grown as a result of this potentiostatic method. This gel had grown to a diameter of approximately 3 mm, and to an apparent height of 0.5 mm (measured using Fiji[27] software). This experiment was repeated two additional times, with each run being conducted in the same gelator solution using the same design of Pt macroelectrode. The current-time transients recorded in these identical experiments were plotted together, along with a set of three other transients recorded using a solution containing an equal concentration of hydroquinone but without the gelator (Figure 3.4).

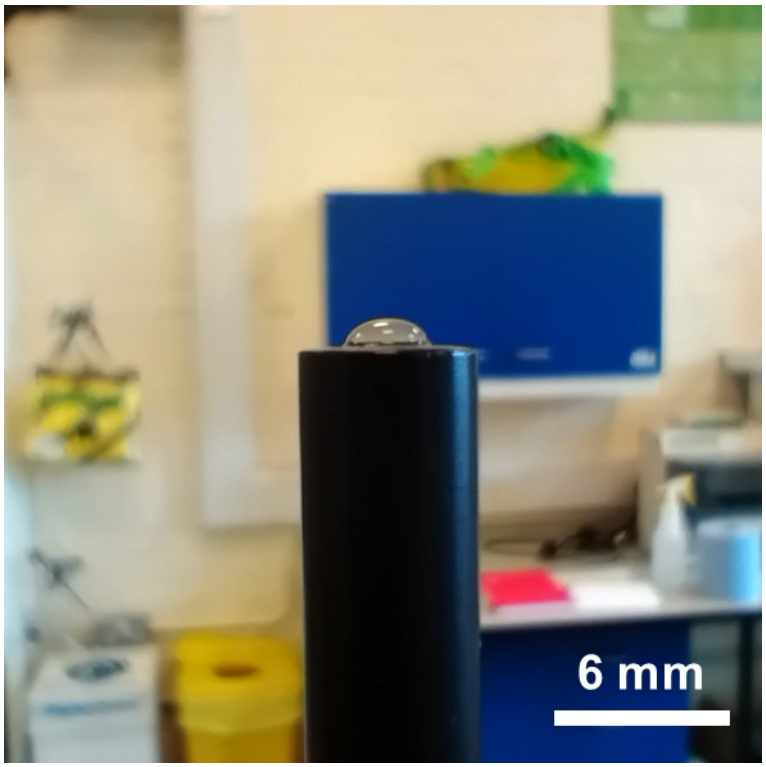

Figure 3.3 Image of a 2 mm diameter Pt disc macroelectrode with a potentiostatically grown Carb-Ala gel, 120 seconds at 0.7 V, T = 25 °C. 10 mL 10 mg/mL Carb-Ala gelator solution (34 mM, pH 8) contained hydroquinone (67.5 mM) and NaCl (100 mM). Electrode removed from gelator solution and inverted before being photographed as shown.

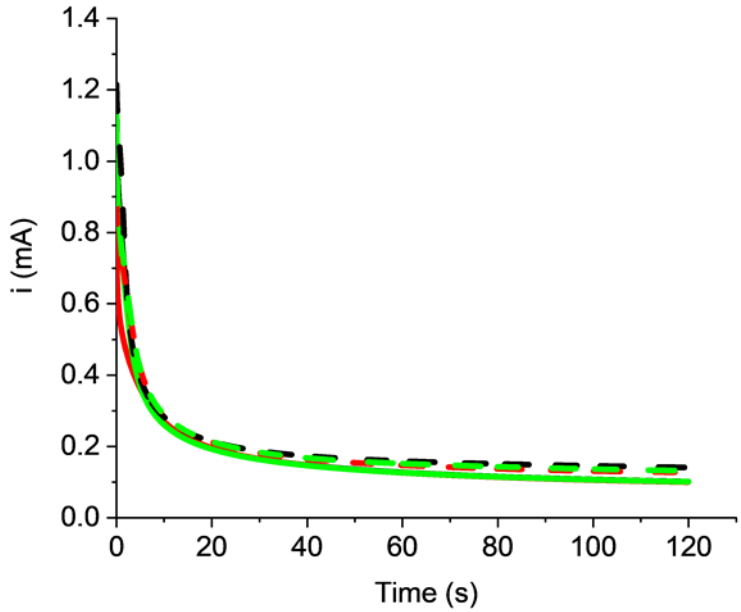

Figure 3.4 Current-time transients in 10 mL aqueous solutions (pH 8) at Pt macroelectrodes (2 mm diameter), 120 seconds at 0.7 V (time measured after stepping from open circuit potential), T = 25 °C. Solid lines = 10 mg/mL Carb-Ala gelator (34 mM), hydroquinone (67.5 mM) and NaCl (10 mM); dashed lines = hydroquinone (67.5 mM) and NaCl (10 mM).

The two sets of transients were similar, though currents recorded in the gelator solution (solid lines, Figure 3.4) were lower at all times compared to the solutions without gelator (dashed lines, Figure 3.4). For example, in the first 3 seconds where linear diffusion had developed, the average currents across the three electrodes were recorded as 472 ± 40 µA for the gelator solution and 544 ± 29 µA for the solution without gelator. Using the Cottrel equation (Equation 2.7, Chapter 2 Section 2.1.3), this corresponds to diffusion coefficient values of 1.25 and 1.67 × 10^{-9} m^2 s^{-1} respectively, which agrees with the hypothesis made Section 3.2.1 regarding reductions to diffusion coefficients with the presence of gelator in the solution. With the question of feasibility answered for this method of gel growth, the next step was to see if the method could also be applied to single microelectrodes. To do this, 25 µm Pt disc microelectrodes replaced the Pt disc macroelectrodes, and +0.7 V was again applied for 120 seconds in solutions with and without the Carb-Ala gelator (Figure 3.5).

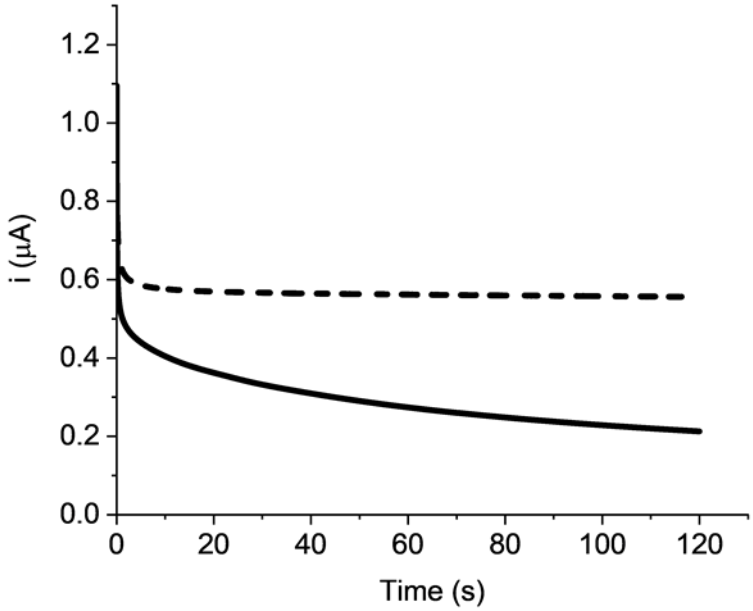

Figure 3.5 Current-time transients in 1 mL aqueous solutions (pH 8) at Pt microelectrodes (25 µm diameter), 120 seconds at 0.7 V (time measured after stepping from open circuit potential), T = 25 °C. Solid line = 10 mg/mL Carb-Ala gelator (34 mM), hydroquinone (67.5 mM) and NaCl (1 mM); dashed line = hydroquinone (67.5 mM) and NaCl (1 mM).

Microelectrodes establish a hemispherical diffusion profile (thus giving steady-state currents) readily, a condition that macroelectrodes are incapable of reaching due to solution convection.[18,28] This effect was displayed with the microelectrode that was placed in the solution without the gelator (dashed black line, Figure 3.5), which reached a steady current of 0.63 µA in the first second of the experiment. Unexpectedly, the current slightly dropped beyond this time, finalising at 0.56 µA after 120 seconds of +0.7 V applied potential. This is likely a result of some electrode fouling over time, i.e. a reduction in available microelectrode surface area. Using the Saito equation (Equation 2.9, Chapter 2 Section 2.1.3),[25] assuming a

steady state is reached after 1 second of applied potential, *D* of hydroquinone equates to 9.7×10^{-10} m^2 s^{-1}, agreeing with the value calculated in Section 3.2.1.

More importantly, the microelectrode placed in the 10 mg/mL Carb-Ala gelator solution passed significantly lower currents (decreasing to 0.46 µA in the first 3 seconds) and experienced a greater decrease in current over the 120 second time period, finalising at 0.21 µA after 120 seconds at +0.7 V (solid line, Figure 3.5). Using the Saito equation again,[25] this translates as a drop in hydroquinone *D* to 7.8×10^{-10} m^2 s^{-1} in the first second of the experiment, and to 3.3×10^{-10} m^2 s^{-1} after 120 seconds. This effect was likely caused by the continued growth of hydrogel decreasing the diffusion coefficient of hydroquinone over time, as well as a fixed contribution from solution viscosity with the addition of Carb-Ala gelator (according to Stokes-Einstein equation, Equation 3.1). To investigate the differences in diffusional properties of the bare and gel-coated microelectrodes further, EIS was employed. Both three-electrode systems were submersed in pH 4.3 buffered solution (0.1 M citric acid/trisodium citrate) containing a ferrocyanide ion redox probe, and Nyquist plots were separately recorded for the bare and gel-functionalised microelectrodes (Figure 3.6).

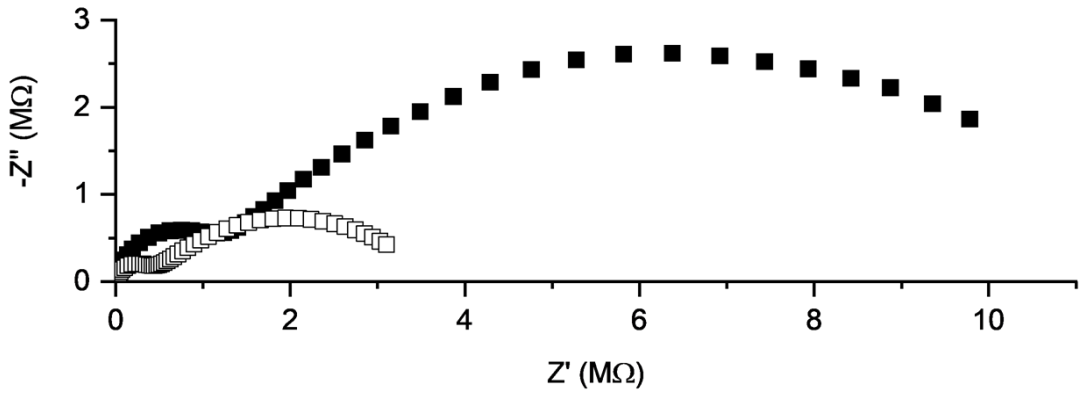

Figure 3.6 Nyquist plots of bare and Carb-Ala gel-coated Pt microelectrodes (25 µm diameter) in ferrocyanide solution (67.5 mM potassium ferrocyanide, 0.1 M citric acid/trisodium citrate buffer, pH 4.3) during EIS, 100 kHz to 0.1 Hz sweep, T = 25 °C. Filled squares = microelectrode functionalised with potentiostatically grown Carb-Ala gel (0.7 V, 120s); hollow squares = bare microelectrode.

There was a stark difference between the Nyquist plots of the bare and gel-functionalised microelectrodes, especially in the lower frequency range of the data. At first glance, the increase in impedance for the gel-functionalised electrode from the bare electrode implied a decrease in diffusion coefficient for the FFC redox couple (discussed in further detail in Sections 3.3 and 3.4). To add to this electrochemical information, the gel-coated electrode was removed from solution, and an image of the microscale gel (in air, surrounding liquid wicked away) was captured using optical microscopy (Figure 3.7). This preliminary data from EIS and microscopy motivated the use of both of these techniques for further study of the properties of electrochemical supramolecular hydrogels. First, EIS data for the bare Pt disc microelectrodes would be checked for consistency and would be used to provide a baseline data set from which to compare future EIS data of gel-functionalised electrodes.

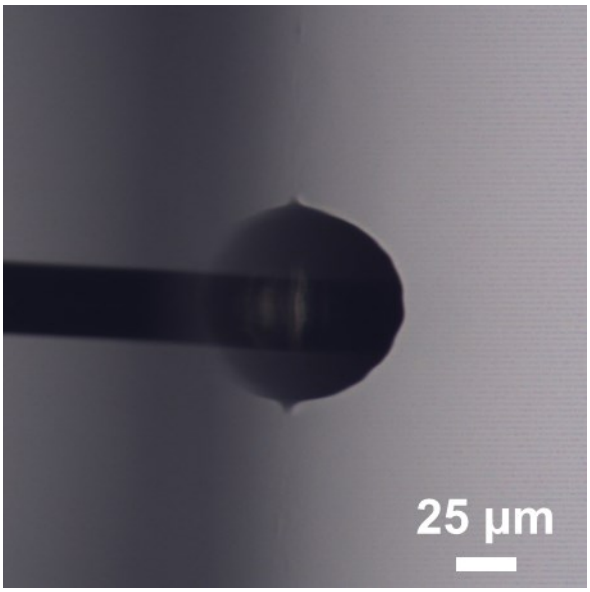

Figure 3.7 Example capture of Carb-Ala gel at commercial Pt microelectrode surface (25 µm diameter), grown at 0.7 V for 120 seconds, 25 °C. Side-on view, 100x magnification, protruding from electrode surface (right of image). Note Pt wire within the electrode's glass casing and the reflection of the hemispherical gel within the glass (left of image).

The work in this section provides strong evidence to the notion that the calculated reductions to mass transport of hydroquinone and the FFC redox pair at the Pt disc microelectrodes are a result of the Carb-Ala hydrogel grown at the microelectrode surface. Rounding this set of experiments off, to confirm that submersion in the gelator solution prior to gel growth did not factor in to these changes to diffusion at the microelectrode, two more Nyquist plots were recorded for the same polished/electrochemically cleaned Pt disc microelectode in the pH 4.3 buffered ferrocyanide solution (Figure 3.8).

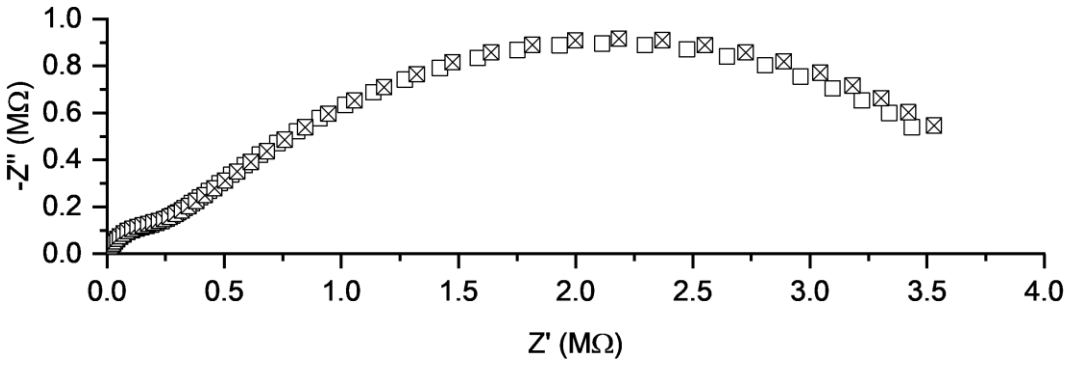

Figure 3.8 Nyquist plots of bare Pt microelectrode (25 µm diameter) in ferrocyanide solution (67.5 mM potassium ferrocyanide, 0.1 M citric acid/trisodium citrate buffer, pH 4.3) during EIS, 100 kHz to 0.1 Hz sweep, T = 25 °C. Hollow squares = bare microelectrode; hollow squares with crossed interior = bare microelectrode after submersion in 10 mg/mL Carb-Ala gelator solution for 120 seconds.

The first of these Nyquist plots was recorded for the bare electrode (hollow squares, Figure 3.8), and the second was recorded with the same bare electrode post-submersion in a 10 mg/mL Carb-Ala gelator solution for a period of 120 seconds to simulate the gel growth time in prior experiments (hollow squares with crossed interior, Figure 3.8). A marginal increase in impedance can be seen for the electrode briefly submerged in the gelator solution prior to EIS, most notably in the lower frequency domain, indicating a slight decrease in mass transport to the electrode surface. However, these two Nyquist plots mostly overlap, and in the higher frequency domain where charge transfer is concerned this overlap indicates a negligible amount of adsorption to the electrode surface. Compared to the Nyquist plot for the gel-coated electrode (black squares, Figure 3.6) the differences in Nyquist plots within Figure 3.8 are insignificant. This confirms that changes to charge transfer and mass transport properties are caused by the growth of the hydrogel.

3.2.3 The pH at Pt electrodes during and after electrochemical gel growth

With a minor adjustment to an equation which describes semi-infinite spherical diffusion at a spherical electrode,[28] the development of the concentration profile of an electrochemically active species reacting at a planar disc electrode of radius r can be estimated with the following equation:

$$c(x,t) = c_{\text{bulk}}\left(1 - \frac{r}{x+r}\operatorname{erfc}\left(\frac{x}{2\sqrt{Dt}}\right)\right) \qquad \textit{Equation 3.2}$$

where $c(x,t)$ is the concentration of an electrochemically active species at distance x from the electrode at time t, the bulk concentration of the electroactive species c_{bulk} is equivalent to $c(\infty,0)$, and the complementary error function produces a unitless value. It is assumed here that the potential applied to the electrode is such that the electroactive species is reacting rapidly, and thus the concentration of that species at the electrode surface $c(0,t)$ is zero. Assuming the 25 µm Pt disc microelectrode reaches limiting currents i_L within the first second of applied constant potential +0.7 V, D was calculated using the Saito equation for the 10 mg/mL Carb-Ala gelator solution and gelator-less solutions at times of 0.1, 1, 10, and 100 seconds (from current-time transients in Figure 3.5). Using Equation 3.2, a concentration profile was then constructed that demonstrates the consumption of hydroquinone at the Pt microelectrode at different times in both solutions, represented as a fraction c/c_{bulk} against x (Figure 3.9). In both solutions, the ratio c/c_{bulk} approaches zero closer to the electrode surface, and the concentration profile for hydroquinone looks identical within the first 0.1 seconds for both the gelator and gelator-less solutions. This approach begins at greater distance x with increasing time t (i.e. as the depletion zone grows). However, the depletion zone in the solution without the gelator (dotted lines, Figure 3.9) expands at a faster rate than in the 10 mg/mL Carb-Ala sol (solid lines, Figure 3.9). This is because (though a limiting current is initially reached in both cases), beyond this time the mass transport of hydroquinone in the 10 mg/mL Carb-Ala gelator solution is reduced by the presence of the growing hydrogel slowing the flow of hydroquinone.

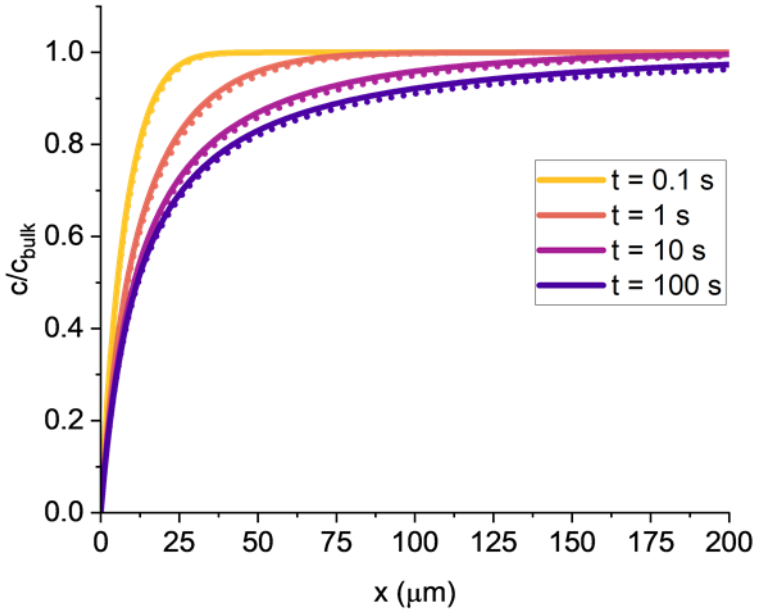

Figure 3.9 Concentration profiles for hydroquinone (67.5 mM) at a Pt disc microelectrode (25 µm diameter), calculated using the Saito equation[25] (Equation 2.9, Chapter 2 Section 2.1.3) and Equation 3.2 with data from recorded transients in Figure 3.5, T = 25 °C. Solid lines = 10 mg/mL Carb-Ala gelator (34 mM), hydroquinone (67.5 mM) and NaCl (1 mM); dashed lines = hydroquinone (67.5 mM) and NaCl (1 mM). Colour gradient of lighter to darker plots corresponds to logarithmically increasing times (0.1 seconds to 100 seconds) in 0.7 V, 120 second current-time transient.

Equation 3.2 can be further adapted to construct an equation that models the production of protons at the disc microelectrode. First, the brackets that contain the error function can be switched in polarity (instead of being subtracted from 1) to simulate a source from which protons diffuse out.

Next, the bulk concentration of hydroquinone c_{bulk} should be replaced with a value that represents the concentration of H^+ produced at the surface. For this, it has been assumed that the concentration of protons at the electrode surface at any time should be equal to two times the bulk concentration of hydroquinone, to simulate the $2e^-$ $2H^+$ reaction.[3] This apparent bulk concentration of hydroquinone c_{bulk}' can be calculated by solving the Saito equation (Equation 2.9, Chapter 2 Section 2.1.3)[25], inputting known i_L from current-time transients (Figure 3.5) and the previously calculated diffusion coefficient for hydroquinone at the microelectrode 9.5×10^{-10} m^2 s^{-1} (Section 3.2.1). c_{bulk}' for a given time in the transient can then be multiplied by two to approximate the concentration of H^+ at the electrode surface. Finally, this formula can then be summed with the known bulk concentration of protons $c_{H+}(\infty,0)$, derived from pH 8 of the gelator solution. Overall, the equation described for the concentration of protons, $c_{H+}(x,t)$, takes the form:

$$c_{H^+}(x,t) = c_{H^+}(\infty,0) + 2c_{bulk}'\left(\frac{r}{x+r}\operatorname{erfc}\left(\frac{x}{2\sqrt{D_{H+}t}}\right)\right) \qquad \textit{Equation 3.3}$$

where D_{H+} = 7 × 10^{-9} m^2 s^{-1}, assuming that H^+ undergo mass transport under the Grotthuss mechanism for proton diffusion,[29] and that transport of protons does not change with gel growth/presence (unlike hydroquinone). The proton concentration profile of protons at the electrode for times of 0.1, 1, 10 and 100 seconds can then plotted against *x* by converting $c_{H+}(x,t)$ to a pH (Figure 3.10).

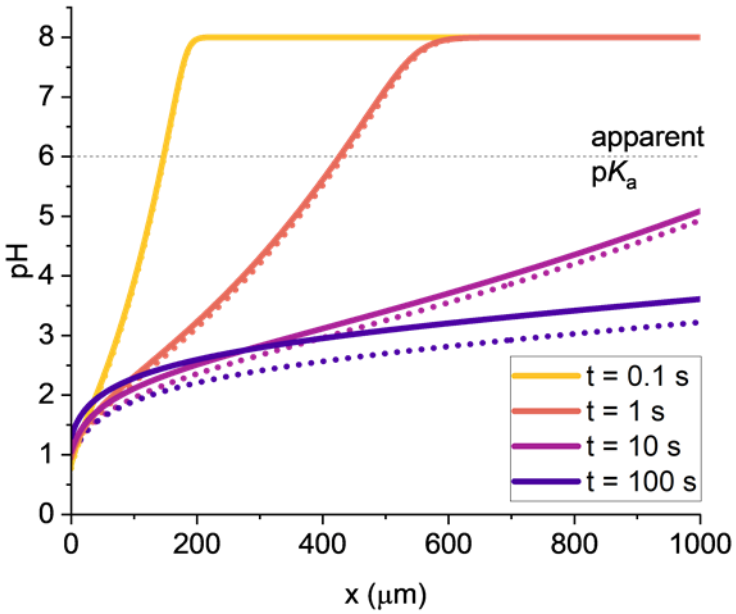

Figure 3.10 pH profiles at a Pt disc microelectrode (25 μm diameter), calculated using the Saito equation[25] (Equation 2.9, Chapter 2 Section 2.1.3) and Equation 3.3 with data from recorded transients in Figure 3.5, T = 25 °C. Solid lines = 10 mg/mL Carb-Ala gelator (34 mM), hydroquinone (67.5 mM) and NaCl (1 mM); dashed lines = hydroquinone (67.5 mM) and NaCl (1 mM). Colour gradient of lighter to darker plots corresponds to logarithmically increasing times (0.1 seconds to 100 seconds) in 0.7 V, 120 second current-time transient. A dashed line at pH = 6 has been added to place pK_a^{app} of the Carb-Ala gelator into context.

The pK_a^{app} of 10 mg/mL Carb-Ala, found by titrating with acid from pH 8 gelator solution, is approximately 6 (Chapter 2 Section 2.3.1). This means that gelator protonation and therefore gelation should occur when the pH of the solution drops to (and below) pH 6. For example, the model presented in Figure 3.10 suggests that pH < 6 after 0.1 seconds of potentiostatic hydroquinone oxidation at distances up to 150 μm from the Pt microelectrode: this implies that a growing gel could have extended to this distance within this very short timeframe, and even grow to sizes well into the range of mm after 10 seconds of applied potential. It is then interesting to see that proton diffusion is modelled to extend far further into the bulk solution than the Carb-Ala gel dimensions observed visually under microscopy would suggest. In comparison, Figure 3.7 shows that this microscale gel had only grown tens of μm into the gelator solution.

In order to understand the reasons behind this discrepancy, it is important to consider that Equation 3.3 does not account for bulk solution convection and buffering. The transport of

protons is likely to be significantly inhibited by buffering from the gelator aggregates consuming protons to produce the growing supramolecular structure. Buffering from the gelator with pH drop has previously been demonstrated in a pH titration curve in this thesis (Figure 2.14, Chapter 2 Section 2.3.1), and it is likely that this buffering also occurs at the electrode surface during potentiostatic gel growth. In this way, the growing hydrogel could reduce the rate at which protons diffuse out into the bulk solution, where bulk solution convection can further affect proton transport. Another concession made by this model is that the concentration of protons is calculated as double an apparent bulk concentration of hydroquinone at the surface, where in reality the concentration of hydroquinone at the surface is 0 (Figure 3.9).

As in the concentration profile for hydroquinone (Figure 3.9), there appears to be an increasing difference in pH with time between the gelator and gelator-less solutions. At t = 0.1 seconds, these pH profiles are overlapped (yellow lines, Figure 3.10), though at 1 second the low pH zone generated at the electrode within the gelator-less solution begins to deviate to lower pH (higher H^+ concentrations) than in the gelator solution (Figure 3.10). After 100 seconds, this difference is as estimated as 0.6 units between the gelator-less solution (dark blue dotted lines, Figure 3.10) and the gelator solution (dark blue solid lines, Figure 3.10). Once again, the equation used to produce this model (Equation 3.3) does not account for buffering and the effect of the gel on the transport of protons. Whilst it is interesting to consider how a pH gradient evolves at an electrode with and without the presence of a peptide-based gelator, the information presented in Figure 3.10 should not be taken as accurate to reality.

3.3 Baseline EIS response of bare Pt disc microelectrodes

3.3.1 Establishing data fitting methodology

First, a baseline set of EIS measurements was collected for bare commercial Pt microelectrodes from which to compare gel-coated microelectrodes. EIS was conducted in the ferrocyanide solution with four cleaned commercial 25 µm diameter disc microelectrodes. Each experiment was conducted at the same temperature (set at 25 °C in a water bath, measured with K-type thermocouple), and the resulting Nyquist plots of these bare microelectrodes (including the Nyquist plot for the bare electrode in Figure 3.6) are plotted together (Figure 3.11).

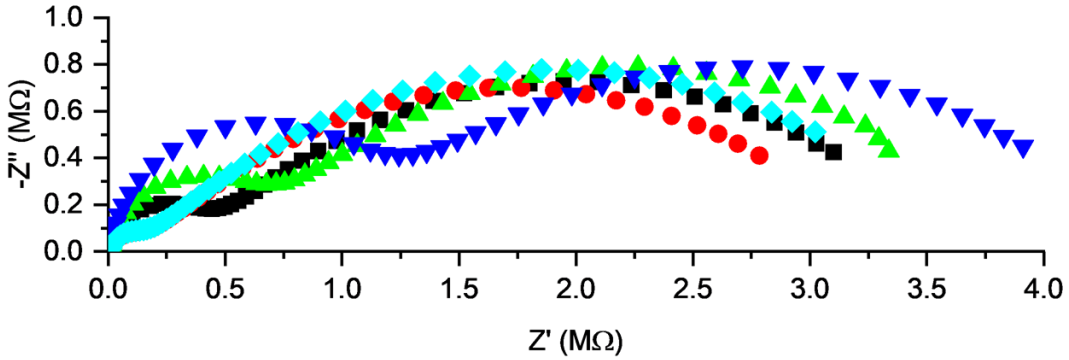

Figure 3.11 Nyquist plots of five bare Pt microelectrodes (25 µm diameter) in ferrocyanide solution during EIS, 100 kHz to 0.1 Hz sweep, T = 25 °C. Black squares = electrode 1, red circles = electrode 2, green triangles (up) = electrode 3, blue triangles (down) = electrode 4, teal diamonds = electrode 5.

To interpret these Nyquist plots, the established modified Randles circuit (Figure 2.11, Chapter 2 Section 2.2.6) was used as the model for the redox electrochemistry occurring at the surface of these single microelectrodes.[30] It features an additional non-linear resistor in parallel with the Warburg diffusional element (in comparison to the standard Randles circuit applicable to a macroelectrode, Figure 2.9, Chapter 2 Section 2.2.6).[31] In the Nova software used in this work, experimental EIS data were first fitted to this equivalent circuit with the weighting factor applied. Doing so weights fitting of the equivalent circuit components that model the high frequency end of the EIS data, these components being R_S, C_{DL} and R_{CT} from the modified Randles circuit (Figure 2.11, Chapter 2 Section 2.2.6). With the weight factor turned off, the data as a whole are fitted, minimising the least squared fitting errors without weighting bias. How the application of the weight factor would affect the estimated equivalent circuit components and their associated errors was assessed. First, the EIS data for each of the five microelectrodes were fitted to the modified Randles circuit with the weight factor applied (Figure 3.12, Table 3.1).

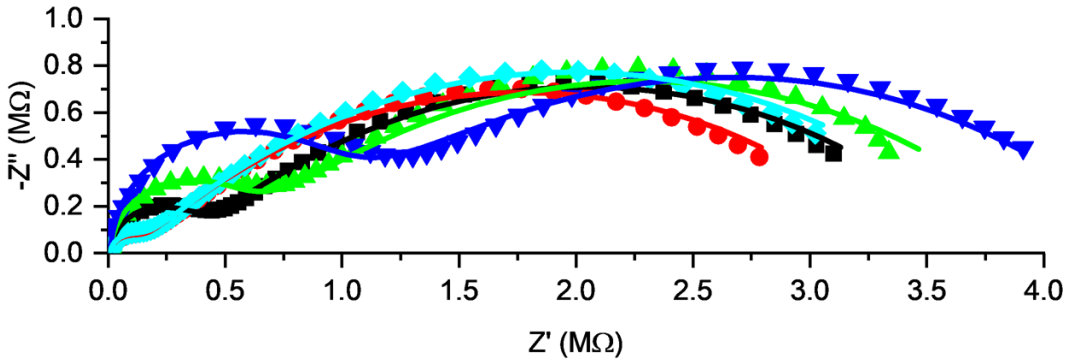

Figure 3.12 Nyquist plots of bare Pt microelectrodes (25 µm diameter) in ferrocyanide solution during EIS, T = 25 °C. Scatter points represent recorded impedance, solid lines represent weighted fitted data using the modified Randles circuit: black squares = electrode 1, red circles = electrode 2, green triangles (up) = electrode 3, blue triangles (down) = electrode 4, teal diamonds = electrode 5.

Visually, there was a clear variance between the first semicircles (high frequency region) in each Nyquist plot (Figure 3.12). This suggests there were differences between the surfaces of these electrodes. Each fitted data set was given a goodness of fit by the Nova software, indicated by the χ^2 distribution: the lower this value was, the closer the fitted data (and thus the fitted plots in Figure 3.12) were to the real EIS data. In addition, the error in each equivalent circuit parameter (also produced by the Nova software) informed on how accurately the program had estimated those individual parameters from the fitted EIS data (Table 3.1).

Table 3.1 Nyquist plot data and estimated errors for bare 25 µm diameter Pt disc electrodes. Features fitted EIS data of bare microelectrodes with weight factor applied (as shown in Figure 3.12) to the modified Randles circuit (Figure 2.11, Chapter 2 Section 2.2.6).

	25 µm diameter Pt disc microelectrodes, weight factor on				
Component	**1**	**2**	**3**	**4**	**5**
R_S (kΩ)	9.9 ± 0.5	9.6 ± 0.5	11.1 ± 0.5	11.2 ± 0.6	10.0 ± 0.5
C_{DL} (pF)	111 ± 1	116 ± 2	128 ± 2	157 ± 2	140 ± 12
R_{CT} (kΩ)	339 ± 6	116 ± 2	540 ± 10	913 ± 18	124 ± 2
Y_0 (nS)	101 ± 2	110 ± 2	91.0 ± 2.0	83.6 ± 1.9	110 ± 2
R_{NL} (MΩ)	3.41 ± 0.07	3.30 ± 0.07	3.52 ± 0.08	3.57 ± 0.08	3.72 ± 0.08
χ^2	0.0738	0.0480	0.169	0.189	0.0254

Fitting errors were low compared to the equivalent circuit parameters (Table 3.1), which justified the use of the modified Randles circuit as a suitable model to interpret the EIS data. Each electrode possessed slightly varying R_S, though the errors for this resistance placed them within experimental error of a common value (approximately 10 kΩ), meaning these were essentially identical. Each electrode had a distinct R_{CT} value beyond the others' estimated errors (Table 3.1). It is proposed that these differences correspond to slight variations in surface cleanliness, with the electrodes with lower R_{CT} having the cleanest surfaces. As for where these variations in cleanliness came from, the microelectrodes were exposed to the atmosphere when allowed to dry after the CV cleaning process: one possibility is that this could have allowed them to collect particulate matter from the air as they dried.

Y_0 and R_{NL} values were similar across the five microelectrodes, though the estimated errors imply that these electrodes were not identical. It was hypothesised that these values were actually the same within experimental error, and that the weight factor had skewed these values in order to fit the higher frequency components more closely to the real data. This hypothesis was investigated by refitting the five Nyquist plots to the modified Randles circuit with the weight factor off, to see whether there would be any significant differences in the components' values (Figure 3.13, Table 3.2).

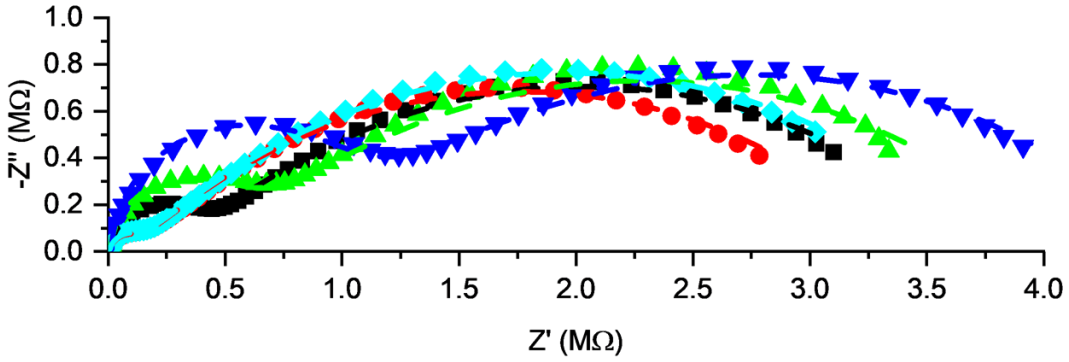

Figure 3.13 Nyquist plots of bare Pt microelectrodes (25 µm diameter) in ferrocyanide solution during EIS, T = 25 °C. Scatter points represent recorded impedance, dashed lines represent unweighted fitted data using the modified Randles circuit: black squares = electrode 1, red circles = electrode 2, green triangles (up) = electrode 3, blue triangles (down) = electrode 4, teal diamonds = electrode 5.

Table 3.2 Nyquist plot data and estimated errors for bare 25 µm diameter Pt disc electrodes. Features fitted EIS data of bare microelectrodes without weight factor applied (as shown in Figure 3.13) to the modified Randles circuit (Figure 2.11, Chapter 2 Section 2.2.6).

25 µm diameter Pt disc microelectrodes, weight factor off					
Component	**1**	**2**	**3**	**4**	**5**
R_S **(kΩ)**	10.3 ± 5.6	8.24 ± 6.07	10.6 ± 12.4	15.1 ± 9.0	7.54 ± 5.11
C_{DL} **(pF)**	117 ± 6	115 ± 15	144 ± 9	165 ± 4	131 ± 15
R_{CT} **(kΩ)**	337 ± 7	112 ± 6	540 ± 15	962 ± 11	115 ± 5
Y_0 **(nS)**	101 ± 1	109 ± 1	91.6 ± 1.7	91.2 ± 1.2	107 ± 1
R_{NL} **(MΩ)**	3.40 ± 0.01	3.29 ± 0.01	3.50 ± 0.03	3.60 ± 0.02	3.68 ± 0.01
χ^2	0.0133	0.0138	0.0443	0.0149	0.00936

Though the differences in fitting quality between these Nyquist plots (Figure 3.13) and the previous (Figure 3.12) cannot be discerned by eye, the goodness of fit χ^2 improved across all five electrodes with the weight factor turned off (Table 3.2). In addition, the higher frequency components were estimated with greater errors. R_S was affected most by this change in method, being estimated with errors that were physically unrealistic, 50-100% greater than with the weight factor applied (Table 3.2). With this said, given the large errors seen in the non-weighted fit, the values are consistent with the R_S remaining unchanged between weighted and non-weighted fitting. The C_{DL} and R_{CT} components faced little significant change between weighted and unweighted fitting, with errors remaining roughly the same, indicating that these components are fitted comparably between weighted and non-weighted fits (Table 3.1, Table 3.2).

As expected, the increased goodness of the non-weighted fit can largely be attributed to the more accurate fitting of the low frequency parameters in the EIS data – Y_0 and R_{NL}. These components were therefore obtained with lower error with the weight factor off, though the values obtained from weighted and non-weighted fits were consistent within error. To reiterate, the R_S values obtained from the weighted fits were physically realistic and had the lowest estimated error. This raised the question of whether all other parameters could also be determined with similarly low error without weighting by fixing R_S to the mean value obtained from the weighted fit (Table 3.1, Figure 3.14, Table 3.3).

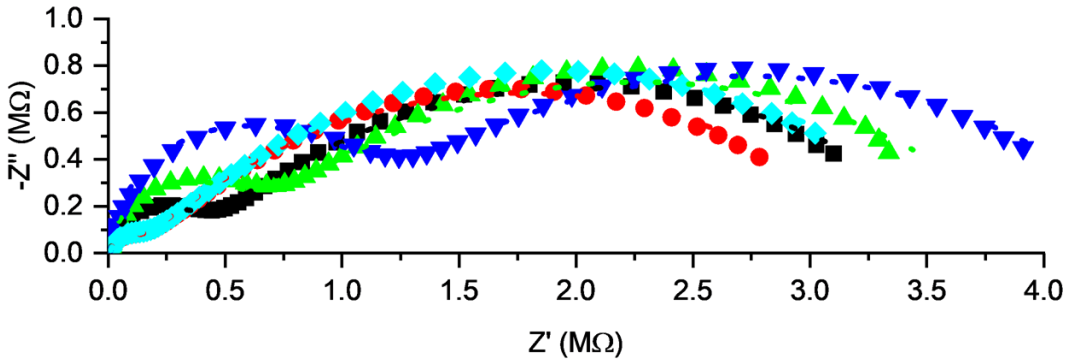

Figure 3.14 Nyquist plots of bare Pt microelectrodes (25 µm diameter) in ferrocyanide solution during EIS, T = 25 °C. Scatter points represent recorded impedance, dotted lines represent unweighted fitted data using the modified Randles circuit with R_S values fixed to the weighted R_S values: black squares = electrode 1, red circles = electrode 2, green triangles (up) = electrode 3, blue triangles (down) = electrode 4, teal diamonds = electrode 5.

Table 3.3 Nyquist plot data and estimated errors for bare 25 µm diameter Pt disc electrodes. Features fitted EIS data of bare microelectrodes with R_S value fixed (italicised, obtained from Table 3.1) without weight factor applied (as shown in Figure 3.6) to the modified Randles circuit (Figure 2.11, Chapter 2 Section 2.2.6).

25 µm diameter Pt disc microelectrodes, weight factor off, Fixed R_S					
Component	**1**	**2**	**3**	**4**	**5**
R_S (kΩ)	*9.92*	*9.63*	*11.1*	*11.2*	*9.98*
C_{DL} (pF)	116 ± 4	117 ± 11	143 ± 7	176 ± 3	136 ± 11
R_{CT} (kΩ)	337 ± 6	110 ± 5	527 ± 13	969 ± 9	114 ± 4
Y_0 (nS)	101 ± 1	109 ± 1	91.1 ± 1.6	91.5 ± 1.0	107 ± 1
R_{NL} (MΩ)	3.40 ± 0.02	3.29 ± 0.01	3.50 ± 0.02	3.60 ± 0.02	3.68 ± 0.01
χ^2	0.0133	0.0139	0.0422	0.0105	0.00941

Fixing R_S to the mean from the weighted fit, whilst keeping the weight factor off, resulted in the other components, their errors, and χ^2 factors being close to identical to those values obtained when not fixing R_S (Table 3.2). Since fixing R_S to the value obtained from the weighted fit made no practical difference to the other components when not including the weight factor, the larger errors possessed by R_S values from fitting without the weight factor could be ignored.

Overall, fitting these EIS data sets with the weight factor off, after fixing R_S at the mean value obtained from the weighted fit, seemed to be the most effective method of accurately estimating the values for the remaining parameters. χ^2 and the estimated errors of these components were suitably low, and there were no significant differences in the values for Y_0 and R_{NL} between these equivalent circuit fitting methods. Thus, this method was chosen for the fitting of Nyquist plot data from these single microelectrodes for this work.

3.3.2 Extracting diffusion coefficients from EIS data

Using Equation 2.29 and Equation 2.31 from Chapter 2 Section 2.2.7, diffusion coefficients D_L and D_{NL} for the FFC redox pair were calculated from estimated Y_0 and R_{NL} values obtained with the weight factor off and R_S fixed (Table 3.4).

Table 3.4 Diffusion coefficients D_L and D_{NL} calculated from Y_0 and R_{NL} values (and associated estimated errors) respectively, using Equation 2.29 and Equation 2.31 respectively. Obtained from fitted EIS data of bare Pt microelectrodes with weight factor applied (Table 3.1).

25 µm diameter Pt disc microelectrodes, weight factor on, Fixed R_S					
Component	**1**	**2**	**3**	**4**	**5**
D_L **(× 10^{-10} m^2 s^{-1})**	4.76 ± 0.08	5.54 ± 0.08	3.90 ± 0.14	3.93 ± 0.09	5.42 ± 0.07
D_{NL} **(× 10^{-10} m^2 s^{-1})**	6.27 ± 0.02	6.47 ± 0.02	6.08 ± 0.04	5.92 ± 0.02	5.78 ± 0.02

Average D_L and D_{NL} were 4.71 ± 0.78 and 6.10 ± 0.27 × 10^{-10} m^2 s^{-1} respectively. The mean diffusion coefficient for the FFC redox pair in aqueous media is expected to be approximately 7 × 10^{-10} m^2 s^{-1}.[32,33] Though neither lies within experimental error of the literature value, the D_{NL} values being closer compared to the D_L values indicates that R_{NL} may be the more accurate source for estimating the diffusion coefficient of the FFC redox pair at the single microelectrodes.

3.4 Measuring Carb-Ala hydrogel growth under potentiostatic conditions as a function of time

3.4.1 Applied potential 0.7 V, gel growth time 120 seconds

In addition to the first Carb-Ala gel grown at a Pt disc microelectrode in Section 3.2.2, the experiment was repeated for a total of five times, The current-time transients obtained by applying 0.7 V for 120 seconds within 1 mL 10 mg/mL Carb-Ala gelator solutions were plotted together (Figure 3.15).

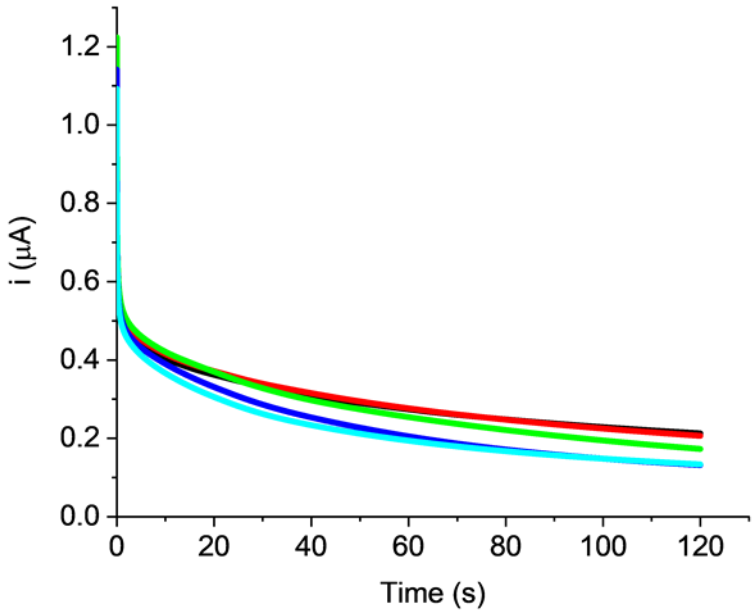

Figure 3.15 Current-time transients in 1 mL 10 mg/mL Carb-Ala gelator solutions (pH 8) containing hydroquinone (67.5 mM) and NaCl (1 mM), at Pt microelectrodes (25 µm diameter), 120 seconds at 0.7 V (stepped from open circuit potential), T = 25 °C. Black = electrode 1, red = electrode 2, green = electrode 3, blue = electrode 4, teal = electrode 5.

The current-time transients all display a gradual decrease in current response due to a drop in hydroquinone diffusion coefficient with time (previously seen and discussed in Section 3.2.2). In addition, some of the electrodes passed currents that were lower than the others for all times. This indicates that each electrode was oxidising different amounts of hydroquinone over the 120 second period of potentiostatic gel growth. To exemplify this, the changes in current were translated to cumulative charge passed over each experiment (Figure 3.16). These experiments were conducted in sequence from electrode 1 to electrode 5 in the same gelator solution. The total magnitude of charge passed between each successive experiment (indicated by the final cumulative charge at 120 seconds for each electrode) was observed to decrease from electrode 2 onwards, going from 35.6 µC for electrode 2 to 26.7 µC for electrode 5 (Figure 3.16).

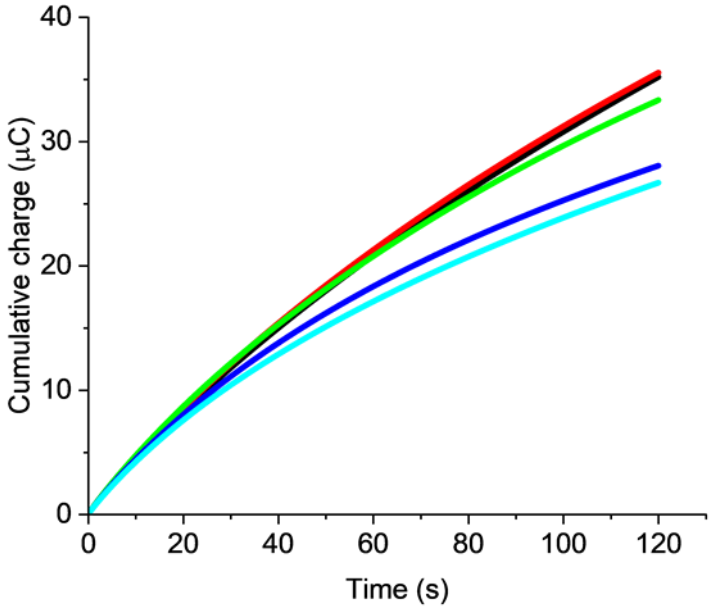

Figure 3.16 Cumulative charge passed during potentiostatic gel-growth of Carb-Ala gels in 1 mL 10 mg/mL Carb-Ala gelator solutions (pH 8) containing hydroquinone (67.5 mM) and NaCl (1 mM), at Pt microelectrodes (25 µm diameter), 120 seconds at 0.7 V (stepped from open circuit potential), T = 25 °C. Black = electrode 1, red = electrode 2, green = electrode 3, blue = electrode 4, teal = electrode 5.

Information regarding variance in gel density between the microelectrodes can be inferred from the cumulative charge passed during gel growth. Since all five electrodes passed similar currents at the beginning of the gel growth step (1.10-1.22 µA, Figure 3.15), this means that there were no significant differences in Pt surface area that could account for the differences in cumulative charge. However, it can be inferred that microelectrodes 4 and 5 grew gels that lowered the rate of diffusion of hydroquinone more effectively than microelectrodes 1-3, meaning microelectrodes 4 and 5 likely grew denser gels. Though it was expected that the final size and density of these gels would be dependent on the rate of diffusion of hydroquinone to the electrode surface (which would change over time with the growth of hydrogel),[14] it was surprising to see this variance in cumulative charge between electrodes (Figure 3.16). The time for which hydroquinone was electrochemically oxidised during chronoamperometry was fixed at 120 seconds, and the self-assembly mechanisms were not expected to change significantly from one microelectrode to another. This process was therefore expected to generate near-identically shaped and structured gels at each electrode. Instead, the differences in cumulative charge due to hydroquinone oxidation suggested otherwise.

EIS was then employed to characterise the properties of these five Carb-Ala hydrogel-coated microelectrodes and confirm the assertions above. The functionalised microelectrodes were each studied as the WE in a three-electrode system within the buffered ferrocyanide solution. EIS data were recorded, and as described in Section 3.3 the Nyquist plots were again fitted to the established Randles circuit for a microelectrode (Figure 2.11, Chapter 2 Section 2.2.6) with

the weight factor first applied to extract an accurate R_S value. The data were then fitted to the same circuit without the weight factor, with the R_S parameter fixed to the value obtained in the weighted fit, to obtain the most accurate values for the other components (fits shown in Figure 3.17, parameters in Table 3.5).

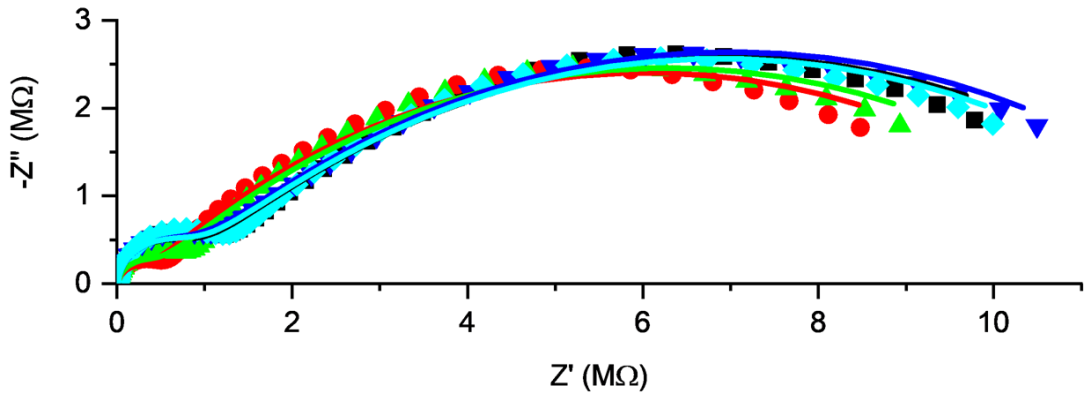

Figure 3.17 Nyquist plots of potentiostatic Carb-Ala gel coated (0.7 V, 120 seconds) Pt microelectrodes (25 µm diameter) in ferrocyanide solution during EIS, T = 25 °C. Scatter points represent recorded impedance, solid lines represent unweighted fitted data with R_S values fixed to the weighted R_S values using the modified Randles circuit: black squares = electrode 1, red circles = electrode 2, green triangles (up) = electrode 3, blue triangles (down) = electrode 4, teal diamonds = electrode 5.

Each of the R_S values of these 120 second, 0.7 V Carb-Ala gel-coated Pt microelectrodes (estimated with the weight factor applied) were within experimental error of each other, sharing a common value of approximately 18 kΩ (Table 3.5). This was almost double the R_S obtained for the bare microelectrodes, at around 10 kΩ (Table 3.3). It is possible that this increase in R_S was due to a reduction in the diffusion rate of inert ions through the gels. It was expected that accompanying this change in R_S could be a change in C_{DL} values from the bare to the gel-functionalised electrodes, as the presence of gel could have an effect on the area and the evolution of the ion double layer at the WE. However, there was not enough evidence warrant a claim that there was a significant change in C_{DL} due to hydrogel presence. The magnitude of variation in C_{DL} values for the bare electrodes (Table 3.3) places the C_{DL} values of the five gel-coated microelectrodes within experimental error (Table 3.5). Likewise, R_{CT} values for the gel functionalised microelectrode were, when averaged, the same within experimental error as the bare microelectrodes. The lack of significant differences in R_{CT} and C_{DL} with gel presence demonstrates that the Carb-Ala hydrogels have little effect on the charge transfer process and redox reactions occurring at the microelectrode surfaces.

Table 3.5 Data and estimated errors for 120 second, 0.7 V Carb-Ala gels grown at 25 µm diameter Pt disc electrodes. Features total charge passed during gel-growth step (as shown in Figure 3.16), EIS data of gel functionalised microelectrodes fitted to the modified Randles circuit (Figure 2.11, Chapter 2 Section 2.2.6) with weight factor not applied (as shown in Figure 3.17), R_S values fixed (italicised). D_L and D_{NL} are calculated using Equation 2.29 and Equation 2.31 respectively.

0.7 V 120s gels, 25 µm dia. Pt disc micro., weight factor off, fixed R_S					
Component	**1**	**2**	**3**	**4**	**5**
Cumulative Charge (µC)	35.2	35.6	33.3	28.6	26.7
R_S (kΩ)	*19.0*	*17.1*	*18.1*	*18.4*	*18.3*
C_{DL} (pF)	116 ± 12	101 ± 29	101 ± 22	108 ± 9	109 ± 11
R_{CT} (kΩ)	770 ± 41	270 ± 40	380 ± 43	733 ± 37	763 ± 43
Y_0 (nS)	45.5 ± 0.8	51.1 ± 0.9	48.2 ± 0.9	37.1 ± 0.5	41.3 ± 0.7
R_{NL} (MΩ)	12.4 ± 0.1	11.6 ± 0.1	11.8 ± 0.1	12.6 ± 0.1	12.3 ± 0.1
χ^2	0.0704	0.102	0.104	0.0409	0.0670
D_L ($\times 10^{-10}$ m^2 s^{-1})	0.972 ± 0.033	1.23 ± 0.04	1.09 ± 0.04	0.648 ± 0.018	0.801 ± 0.028
D_{NL} ($\times 10^{-10}$ m^2 s^{-1})	1.72 ± 0.02	1.84 ± 0.02	1.80 ± 0.02	1.69 ± 0.01	1.73 ± 0.02

In contrast, Y_0 values for the gel-coated electrodes decreased significantly to 37-51 nS, compared to values for the bare electrodes of 91-109 nS (Table 3.3, Table 3.5). R_{NL} values were also much greater in magnitude (11.6-12.6 MΩ) than those obtained for the bare electrodes (3.3-3.7 MΩ). Translating these Y_0 and R_{NL} values to diffusion coefficients (using Equation 2.29 and Equation 2.31 respectively) yielded D_L and D_{NL} values for these gel-functionalised electrodes that were on average 80% and 70% lower than those calculated for the bare electrodes (Table 3.4, Table 3.5). The significant changes to these values with gel presence is clear evidence that the Carb-Ala hydrogels slow the transport of the FFC redox pair.

As stated when regarding relative differences in cumulative charge passed during gel growth, microelectrodes 4 and 5 were expected to have produced the densest gels. The magnitude of D_L and D_{NL} values for these gel-functionalised microelectrodes correlate to some degree with this expectation, as microelectrodes 4 and 5 possess the lowest D_L values in the group. However, D_{NL} of microelectrodes 1, 4 and 5 are the same within experimental error. Likewise, microelectrodes 2 and 3 possessed R_{NL} and respective D_{NL} that are the same within experimental error, and outside the error range of microelectrodes 1, 4 and 5. Despite these

differences, the hydrogels grown at each of the five Pt microelectrodes appear to affect the transport of the FFC redox pair to approximately the same degree. This indicates that each of the five gels possess similar global densities (averaged across the entire volume of the gels).

D_{NL} for this group of gel-functionalised microelectrodes range from 1.69-1.84 × 10^{-10} m^2 s^{-1} (Table 3.5). As seen before with the five bare microelectrodes (Table 3.4), the D_L values for these gel-coated microelectrodes are slightly less consistent and lower in magnitude than each respective D_{NL} value, ranging from 0.6-1.2 × 10^{-10} m^2 s^{-1} (Table 3.5). The magnitude of average D_L for the bare electrodes equates to approximately 77% that of average D_{NL} for those electrodes (Table 3.4), whereas for the gel-coated electrodes average D_L equates to 54% that of average D_{NL} (Table 3.5). This greater relative difference between D_L and D_{NL} for the gel-coated electrodes indicates that the gels could have heterogeneous structures, with the hydrogels being the most dense at the Pt surface, and gradually less so towards the bulk solution.

The frequency applied during EIS affects the distance from the microelectrode that electroactive species are drawn from and involved in redox reactions. After ion double-layer formation and charge transfer processes occur at shorter timescales, linear diffusion begins to develop close to the electrode surface, and as the frequency is decreased further, a hemispherical diffusion profile develops at a longer range from the microelectrode.[31] Theoretically, the properties of an electrochemically-grown hydrogel could be probed at different frequencies in EIS, and it was thought possible to assess the separation between D_L and D_{NL} at different distances from the Pt surface. To determine the validity of this hypothesis, the EIS data for the 0.7 V 120 second Carb-Ala gels was refitted to the modified Randles circuit in a windowed frequency range: a range of 100 kHz to 10 Hz was selected (Figure 3.18, Table 3.6).

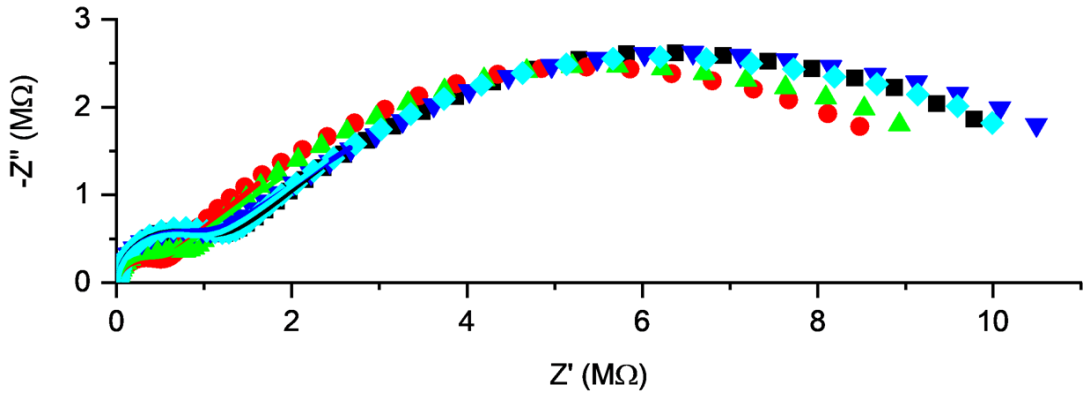

Figure 3.18. Nyquist plots of potentiostatic Carb-Ala gel coated (0.7 V, 120 seconds) Pt microelectrodes (25 µm diameter) in ferrocyanide solution during EIS, T = 25 °C. Scatter points represent recorded impedance, solid lines represent unweighted fitted data with R_S values fixed to the weighted R_S values, within the frequency range of 100 kHz - 10 Hz, using the modified Randles circuit: black squares = electrode 1, red circles = electrode 2, green triangles (up) = electrode 3, blue triangles (down) = electrode 4, teal diamonds = electrode 5.

Table 3.6. Data and estimated errors for 120 second, 0.7 V Carb-Ala gels grown at 25 µm diameter Pt disc electrodes. Features EIS data of gel functionalised microelectrodes fitted to the modified Randles circuit (Figure 2.11, Chapter 2 Section 2.2.6) within the frequency range of 100 kHz - 10 Hz, with weight factor not applied (as shown in Figure 3.18), R_S values fixed (italicised). D_L and D_{NL} are calculated using Equation 2.29 and Equation 2.31 respectively.

0.7 V 120s gels, 25 µm dia. Pt disc micro., 100 kHz-10Hz					
Component	**1**	**2**	**3**	**4**	**5**
R_S (kΩ)	*19.0*	*17.1*	*18.1*	*18.4*	*18.3*
C_{DL} (pF)	132 ± 1	110 ± 8	106 ± 12	120 ± 1	123 ± 5
R_{CT} (kΩ)	971 ± 7	384 ± 19	440 ± 35	884 ± 9	880 ± 29
Y_0 (nS)	57.6 ± 0.5	64.8 ± 1.8	55.2 ± 2.7	43.3 ± 0.4	51.7 ± 1.8
R_{NL} (MΩ)	27.8 ± 3.2	22 ± 7.3	12.9 ± 0.1	16.2 ± 0.8	21.2 ± 5.2
χ^2	0.00505	0.153	0.300	0.00623	0.131
D_L ($\times 10^{-10}$ m^2 s^{-1})	1.56 ± 0.03	1.98 ± 0.04	1.43 ± 0.14	0.882 ± 0.016	1.26 ± 0.08
D_{NL} ($\times 10^{-10}$ m^2 s^{-1})	0.766 ± 0.078	0.968 ± 0.322	1.66 ± 0.48	1.31 ± 0.07	1.00 ± 0.25

Across the five electrodes, the magnitude of Y_0 values were on average 22% greater when compared to estimations from the full 100 kHz to 0.1 Hz range, which translates to an increase in D_L of 50% (Table 3.5, Table 3.6). This change in D_L is insignificant however, as average D_L in the 100 kHz to 10 Hz window ($1.42 \pm 0.40 \times 10^{-10}$ m^2 s^{-1}) and average D_L in the full 100 kHz to 0.1 Hz range ($0.95 \pm 0.23 \times 10^{-10}$ m^2 s^{-1}) each lie within experimental error of the other. The R_{NL} values in the 100 kHz to 10 Hz window were more poorly estimated, ranging from 12.9-27.8 MΩ with errors of 5-33% (Table 3.6). This variance and greater error in R_{NL} values is to be expected, given that the windowed frequency range excludes the low frequency window of the EIS data where hemispherical diffusion develops. Since an accurate estimation of R_{NL} cannot be made, the variance and error in these estimated values for R_{NL} (and thus D_{NL}) in the 100 kHz to 10 Hz frequency window should be ignored, and conclusions on differences in hydrogel density at different heights from the Pt surface cannot be made from these estimated values.

The size of these gels were then measured optically to determine whether gel morphology was consistent between the five microelectrodes. The dimensions of each of the five hydrogels were measured (using Fiji[27] software). For each gel, a cross-sectional area was recorded, as well as the width and height that the hemisphere-like gel grew from the centre of the Pt microdisc (Table 3.7).

Table 3.7 Dimensions of potentiostatically grown, 0.7 V 120 second Carb-Ala gels at 25 µm diameter Pt disc microelectrodes (an example of which is featured in Figure 3.7).

0.7 V 120s gels, 25 µm dia. Pt disc micro., weight factor off, fixed R_S					
Component	**1**	**2**	**3**	**4**	**5**
Gel Width (µm)	109	107	110	96.6	98.3
Gel Height (µm)	59.1	50.0	60.0	53.3	52.9
Gel Cross-Sectional Area (μm^2)	4840	4070	5290	3820	3910

Interestingly, none of the five gels were perfectly hemispherical in shape: the half gel width (the radius of the gel at the plane parallel to the electrode surface) was measured to be smaller than the gel height (the radius of the gel at the plane perpendicular to the electrode surface) for microelectrodes 1, 3, 4 and 5. This observation is explored later in Section 3.4.5. In addition, the gel grown at microelectrode 2 was the only one of the five that had a half-width greater than the height, which was thought to be due to the gel being dehydrated and contracting before being measured under the microscope.

In summary, potentiostatically grown Carb-Ala hydrogels grown at five separate single Pt disc microelectrodes (25 µm diameter, 0.7 V applied for 120 seconds) possess consistencies in density and shape. The potentiostatic oxidation of hydroquinone leads to self-assembly of Carb-Ala that has a measurable effect in reducing both the gel growth current and the diffusion coefficient *D* of the FFC redox probe. These gel-functionalised electrodes feature a greater separation between diffusion coefficients D_L and D_{NL} than that seen for the bare microelectrodes. This effect may be a result of the hydrogels having greater densities at shorter distances from the electrode surface, though unfortunately this cannot be proven with EIS. The dimensions of these hydrogels also show that they are not perfect hemispheres in shape. Importantly, EIS provides a method to explore how changing experimental parameters can affect the diffusional and dimensional properties of the electrochemical hydrogels.

3.4.2 Hydroquinone oxidation and gelator solution "age"

In Section 3.4.1, five Carb-Ala hydrogels were grown sequentially at separate 25 µm diameter Pt disc microelectrodes. Each gel was grown using the same 1 mL 10 mg/mL Carb-Ala gelator solution. There appeared to be a trend of decreasing cumulative charge due to hydroquinone oxidation with each sequential use of the same gelator solution: this started with microelectrode 2 at 35.6 µC, and ended with microelectrode 5 at 26.7 µC (Figure 3.16, Table 3.5). It is understood that the cumulative charge passed in these current-time transients is directly correlated with the amount of hydroquinone oxidised. This would imply that the concentration of protons produced during the potentiostatic gel growth process was decreasing with each successive electrode.

Another observation was made regarding a colour change of the gelator solution. Upon addition of hydroquinone to the gelator solution, a faint yellow colour was visible, identified as the oxidation of hydroquinone (Figure 3.19).[1] Occasionally, the initial addition of dilute $NaOH_{(aq)}$ during this adjustment would produce a dark-green colour where the $NaOH_{(aq)}$ was introduced, which quickly dissipated when stirred in solution. This was possibly due to the formation of quinhydrone, an insoluble charge-transfer complex formed of hydroquinone and quinone.[24] Importantly, the faint yellow colour of the solution slowly increased in intensity towards an orange/brown colour over time, even without the application of any electrochemical work. Known factors that exacerbate and accelerate the oxidation of hydroquinone in solution (other than electrochemically-induced oxidation) include exposure to oxygen and natural light.[1,14] During the times these solutions were used for the experiments described in this work, they were exposed to air and placed out of direct sunlight.

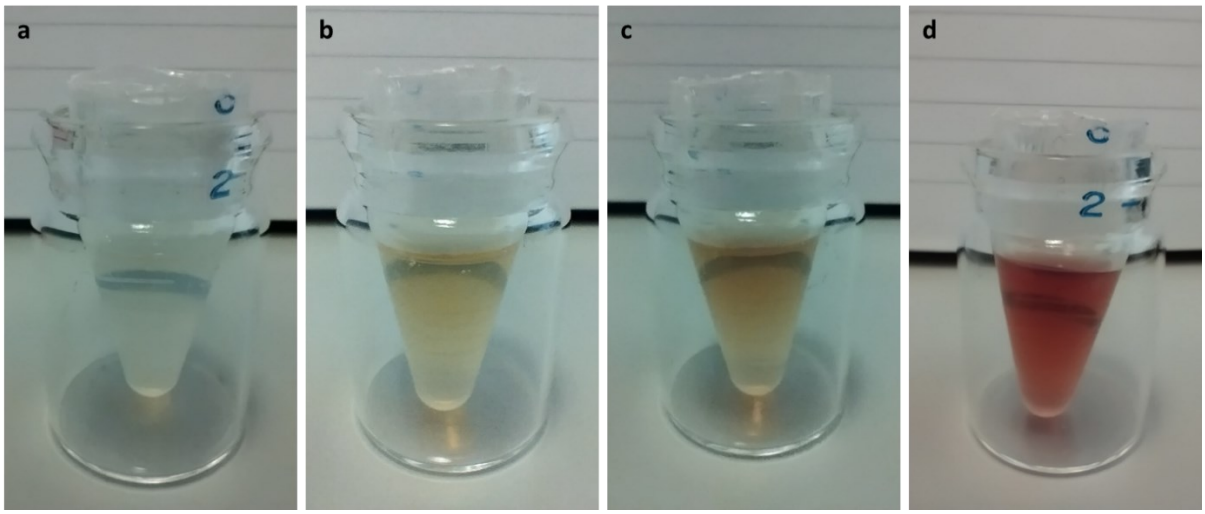

Figure 3.19 Gradual change in colour of 10 mg/mL Carb-Ala gelator solution after addition of hydroquinone (67.5 mM), without the application of any electrochemical work. (a) No pH adjustment (~pH 6-7 after addition of hydroquinone), solution colour largely unchanged. (b) Post-pH adjustment to pH 8 (with µL aliquots of 0.1 M $NaOH_{(aq)}$), faint yellow colour visible. (c) Post-experimentation use (for growth of electrochemical hydrogels at single microelectrodes), solution has darkened in colour. (d) One day after experimentation, solution has turned deep orange/brown.

This gradual colour change observed in both the gelator solution used in electrochemical work and the solution not used for any electrochemistry (Figure 3.19) was initially speculated to indicate a significant decrease in hydroquinone concentration over time. By extension, it was thought that this could explain the decrease in cumulative charge passed after each successive gel-growth step in the same gelator solution (Figure 3.16, Table 3.5).

However, the initial currents recorded during electrochemical gel growth did not decrease with each electrode: in sequence, initial currents of 1.10 µA, 1.15 µA, 1.22 µA, 1.14 µA and 1.09 µA were recorded for the five microelectrodes at time 0 seconds (Figure 3.15). In the first 5 seconds, currents had dropped to 0.44 µA, 0.45 µA, 0.46 µA, 0.43 µA and 0.41 µA respectively. The lack of a discernible and significant trend in initial currents from microelectrode 2 onwards indicates that the concentration of hydroquinone had not

decreased over the time that this solution had been used for experimentation. In addition, the approximate total concentration of hydroquinone electrochemically oxidised based on the total cumulative charge passed at each of the five microelectrodes was 0.8 µM (Table 3.5). Compared to the initial concentration of hydroquinone in the gelator solution at 67.5 mM, this was insignificant. Overall, it is highly unlikely that the gradual decrease in cumulative charge with each successive microelectrode was due to a decrease in hydroquinone concentration.

It was then thought more likely that an impurity, one which was acting to interfere with the electrochemical oxidation of hydroquinone, was the cause for this drop in cumulative charge. To answer this question, the effect that time could be having on the electrochemistry of hydroquinone or self-assembly of Carb-Ala in the basic aqueous solutions was studied. A 10 mg/mL Carb-Ala gelator solution, which had previously been prepared with hydroquinone and adjusted to pH 8 with microlitre additions of 0.1 M $NaOH_{(aq)}$, was allowed to "age" over 16 hours. After this period had passed, the solution had turned dark brown, and was henceforth referred to as the "aged" gelator solution. The solution pH was re-adjusted to pH 8, the three electrode system including a 25 µm Pt disc microelectrode was introduced to solution, and gel growth was promoted at the microelectrode by applying 0.7 V for 120 seconds (Figure 3.20, Table 3.8)

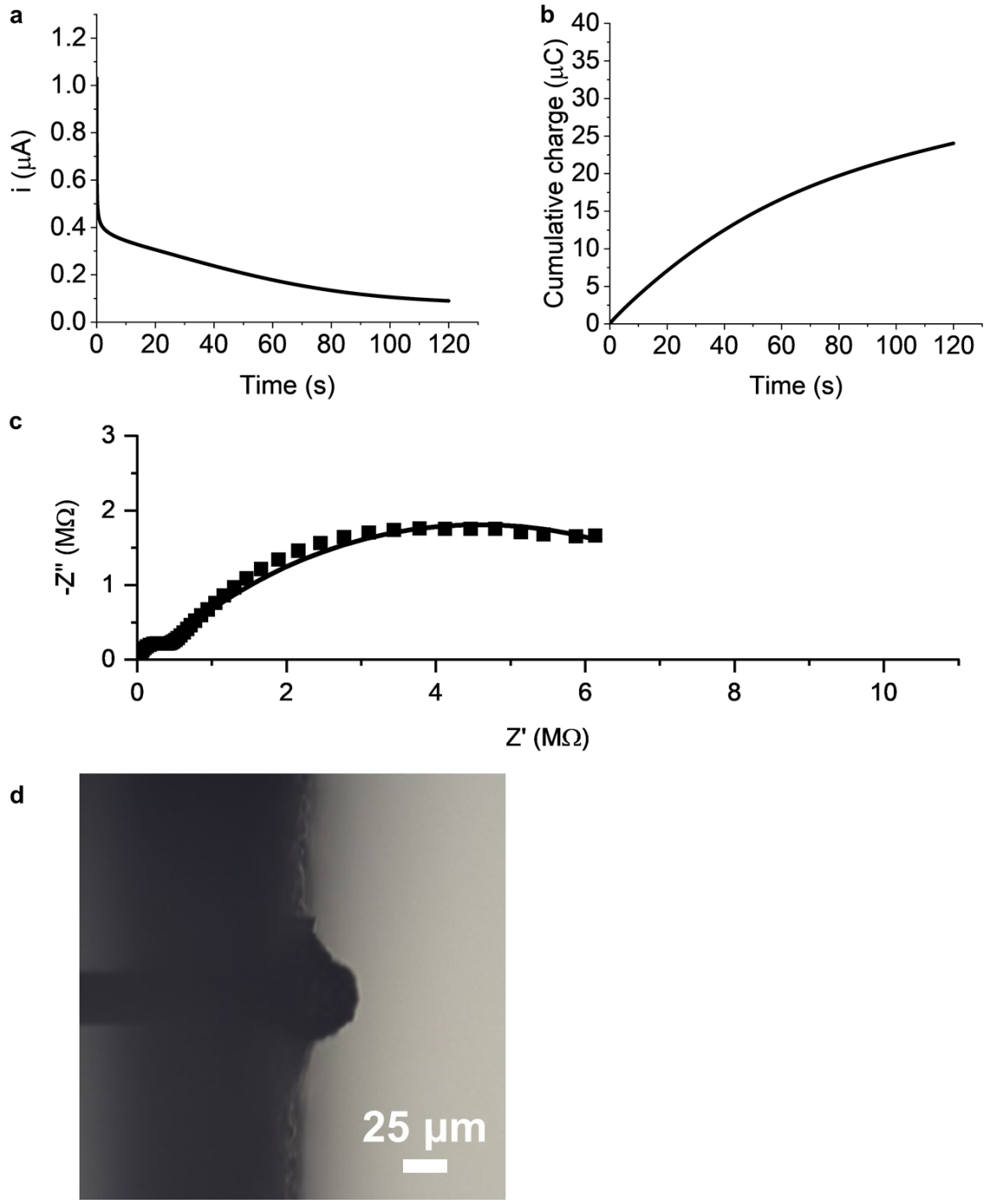

Figure 3.20. Potentiostatic growth of a Carb-Ala gel on a Pt microelectrode (25 μm diameter) at 0.7 V for 120 seconds using a gelator solution which was allowed to sit over 16 hours after addition of hydroquinone, 25 °C. (a) Current-time transient of hydroquinone oxidation in gelator solution. (b) Cumulative charge passed during gel-growth step, calculated by integrating area under current-time transient in (a). (c) Recorded (scatter points) and fitted (solid line) Nyquist plots of gel-functionalised electrodes in ferrocyanide solution, obtained with weight factor off and R_S fixed to R_S obtained from weighted fit. (d) Capture of Carb-Ala gel at commercial microelectrode surface, side-on view, 100x magnification.

Table 3.8. Data and estimated errors for 120 second, 0.7 V Carb-Ala gel grown at 25 µm diameter Pt disc electrode using Carb-Ala gelator solution "aged" for 16 hours. Features total charge passed during gel-growth step (Figure 3.20b), fitted EIS data of gel functionalised microelectrodes (Figure 3.20c) to the modified Randles circuit (Figure 2.11, Chapter 2 Section 2.2.6) with weight factor off and R_S fixed to weighted value. Diffusion coefficients D_L and D_{NL} were calculated using Equation 2.29 and Equation 2.31 respectively. Gel dimensions also featured (Figure 3.20d).

0.7 V 120s gel, 25 µm dia. Pt disc micro., 16 hours after hydroquinone addition	
Component	
Cumulative Charge (µC)	24.0
R_S (kΩ)	*17.2*
C_{DL} (pF)	113 ± 26
R_{CT} (kΩ)	216 ± 22
Y_0 (nS)	76.0 ± 1.1
R_{NL} (MΩ)	8.72 ± 0.09
χ^2	0.0786
D_L ($\times 10^{-10}$ m^2 s^{-1})	2.71 ± 0.08
D_{NL} ($\times 10^{-10}$ m^2 s^{-1})	2.44 ± 0.02
Gel Width (µm)	80.8
Gel Height (µm)	43.8
Gel Cross-Sectional Area (µm^2)	2500

The total charge passed for the gel growth step in this "aged" solution was lower in comparison to those Carb-Ala gels grown immediately after hydroquinone addition and pH adjustment to the gelator solution (Figure 3.20b, Table 3.8). This confirmed that the suspected decrease in cumulative charge was occurring with time after hydroquinone addition and gelator solution pH adjustment. It was initially hypothesised that the decrease in currents and cumulative charges was due to a decrease in Pt surface area. This was thought to be a result of the formation of a chemical species that had formed in the "aged" solution over time, which had adsorbed to the surface of the Pt microelectrode and caused

passivation. This was refuted by the estimated R_S and C_{DL} values, which were comparable to those of the previous 120 second 0.7 V Carb-Ala gels: the R_{CT} value for this gel-coated microelectrode was relatively low in comparison to the electrodes in the prior gel-growth experiments (Table 3.5, Table 3.8), which suggests that the Pt surface area had not decreased. Y_0 and R_{NL} values (and corresponding diffusion coefficients) for this gel-functionalised microelectrode lay between that of the bare electrodes (Table 3.3) and the previous 120 second 0.7 V gel-functionalised electrodes (Table 3.5). Coupled with this, the dimensions of the gel grown in the "aged" solution (Table 3.8) were also less than all those of the previous experiments (Table 3.7).

Studying this phenomenon further, two 10 mL 10 mg/mL Carb-Ala gelator solutions were prepared to compare their differences in hydroquinone electrochemistry. The first was prepared with the addition of hydroquinone 9 days in advance, pH adjusted to pH 8, and was pH adjusted to pH 8 once more on the day of experimentation: this solution was referred to as the "old" solution. The second had hydroquinone added to it on the day of the experiment and was used immediately after pH adjustment, referred to as the "fresh" solution. Cyclic voltammetry was carried out with each solution, five cycles each, and the resulting voltammograms were plotted together (Figure 3.21).

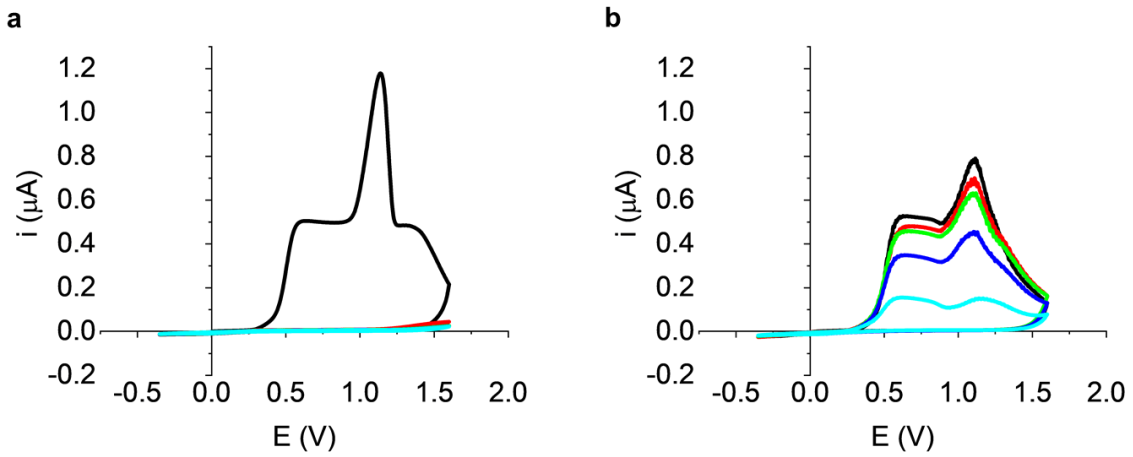

Figure 3.21 CVs in 10 mL 10 mg/mL Carb-Ala gelator solutions (pH 8) at Pt microelectrode (25 μ diameter). Starting potential E = 0 V, initial scan direction positive, 5 cycles in sequence (differentiated by colour: black = cycle 1, red = cycle 2, green = cycle 3, blue = cycle 4, teal = cycle 5) between -0.4 V and 1.6 V, scan rate v = 0.1 V s^{-1}, T = 25 °C. (a) "Fresh" solution, hydroquinone (67.5 mM) added on day of experiment. (b) "Old" solution, hydroquinone (67.5 mM) added 9 days prior to experiment.

The first CV sweeps for each microelectrode in the "fresh" and "old" 10 mg/mL Carb-Ala gelator solutions were studied first (Figure 3.21). These cycles had similar features to the CV recorded prior (Figure 3.2), and also possessed the same anodic peak current for the oxidation of hydroquinone, approximately 500 nA. This was to be expected, as the same amount of hydroquinone was be oxidised in each case, and hydroquinone concentration had already been shown not to decrease significantly with time or due to electrochemical oxidation.

In each of the cycles that featured hydroquinone oxidation in the forward scan, there was a slight drop in current within the region where hydroquinone oxidation should be rate-limited,

from approximately 0.6 V to 0.9 V (Figure 3.21). Significantly, this drop was more pronounced in the “old” solution (Figure 3.21b). These waves not being flat during this portion of the voltammogram suggested that something in the solution was affecting the ability of the system to readily oxidise hydroquinone, and that the “old” solution contained more of this unknown material.

At more positive potentials a sharp peak was observed, as seen in Section 3.2.1, due to the polymerisation of the gel.[11] It is interesting that the initial CV in the “fresh” solution produced the highest peak current and greatest charge, with subsequent CVs resulting in almost no current (Figure 3.21a). This was a sign that the self-assembled Carb-Ala molecules closest to the electrode surface had polymerised and passivated the Pt microelectrode. This had the effect of blocking access by hydroquinone to the Pt surface after the first cycle, which in turn would prevent the hydrogel from growing any further.

In contrast, in the “old” solution, instead of these features disappearing immediately after the first cycle, they instead diminished slowly over the next four cycles (Figure 3.21b). This indicated that the polymerisation process – which had passivated the electrode surface in the “fresh” gelator solution (Figure 3.21a) – was also being hindered in the “old” solution (Figure 3.21b). These observations led to a question of whether an impurity was interfering with the electrochemistry.

It then became of interest to study the effect that this unknown impurity had on the electrochemistry, as a function of time and of relative impurity concentration. First, chronoamperometry was used to examine the total charge passed over a fixed period in the 10 mL 10 mg/mL “fresh” and “old” Carb-Ala solutions. This was followed by recording further current-time transients after additions of the “old” solution into the “fresh” solution (Figure 3.22, Table 3.9). Potential was fixed to +0.7 V to avoid Carb-Ala polymerisation, so as to study the effect that an increasing concentration of unknown impurity had on the electrochemical oxidation of hydroquinone and hydrogel self-assembly.

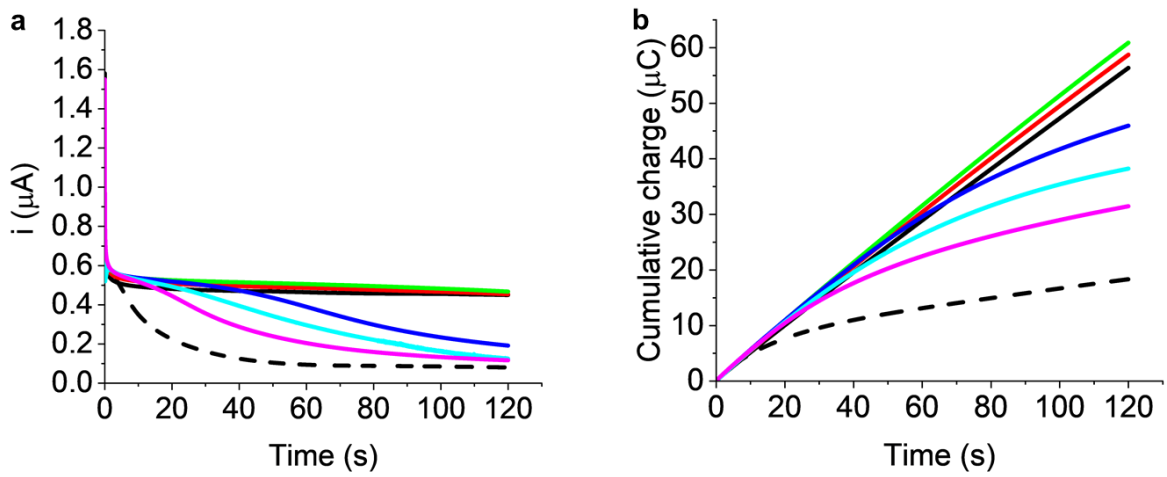

Figure 3.22 Current-time transients (a) and charge-time transients (b) at Pt microelectrode (25 μm diameter), 0.7 V for 120 seconds, 25 °C. Recorded in "old" 10 mg/mL Carb-Ala gelator solution and "fresh" 10 mg/mL Carb-Ala gelator solution with portions of "old" solution added in aliquots. Black dashed line = "old" solution; black solid line = "fresh" solution; red = "fresh" solution + 1 mL "old" solution; green = "fresh" solution + 2 mL "old" solution; blue = "fresh" solution + 5 mL "old" solution; teal = "fresh" solution + 7.5 mL "old" solution; magenta = "fresh" solution + 10 mL "old" solution.

Table 3.9 Cumulative charge passed for each experiment in Figure 3.22.

Volume "fresh" solution (mL)	Volume "old" solution (mL)	Total volume of solution (mL)	Cumulative Charge (μC)
-	10.0	10.0	18.3
10.0	-	10.0	56.4
10.0	1.0	11.0	58.7
10.0	2.0	12.0	60.9
10.0	5.0	15.0	46.0
10.0	7.5	17.5	38.2
10.0	10.0	20.0	31.5

The cell using 10 mL of the "old" solution produced a current-time transient that reached a current of approximately 100 nA, and over the 120 second period passed 18.3 μC. The cell containing 10 mL of the "fresh" solution reached 500 nA, and passed 56.4 μC over the same period. After this, 1 mL aliquots of the "old" solution were added to the "fresh" solution, and chronoamperometry was repeated for each addition. The first 2 mL of "old" 10 mg/mL Carb-Ala gelator introduced to the "fresh" solution made little difference to the current-time transients of the "fresh" solution (Figure 3.22), though cumulative charge over the 120 second period did increase slightly to 60.9 μC (Table 3.9).

Once 5 mL total of the "old" solution was present in the "fresh" solution, cumulative charge dropped to 46.0 μC. The transient in this experiment reached plateau at approximately 500 nA (Figure 3.22), but this was only maintained for a period of 30 seconds. After this point, the

transient approached a new plateau of 100 nA, characteristic of the “old” gelator solution. Adding further volumes of the “old” solution decreased the final cumulative charge further. The 20 mL total volume solution (composed of equal volumes of the “fresh” and “old” gelator solutions) was unable to maintain the 500 nA current, and the transient for this solution featured an inflection at 10 seconds before sloping towards 100 nA.

This new information confirms that the concentration of protonated hydroquinone was not the cause of the lower current. The presence of an impurity has a negative effect on rate of electrochemical hydroquinone oxidation, and thus a negative effect on the rate of hydrogel growth. The identity of this impurity has not been established, and the mechanism by which it affects the ability of the electrochemical system to produce electrochemical gels is currently unknown. There is room for further exploration into understanding this phenomenon, however this problem was instead bypassed in this work: the experiments detailed in this section exemplify the necessity to prepare gelator solutions with hydroquinone only when an experiment is to be conducted shortly after hydroquinone addition. After this short study, gelator solutions prepared in later experiments would be discarded after 3-5 hours of experimental use.

3.4.3 Applied potential 0.7 V, gel growth time 60 seconds

At this point, Carb-Ala hydrogels potentiostatically grown at single Pt microelectrodes were shown to be observable and measurable at microelectrode surfaces using optical microscopy under visible light (Figure 3.7, Table 3.7). Gel-coated microelectrode diffusional properties could also be estimated by converting Y_0 and R_{NL} components obtained from estimated values of the modified Randles circuit (Table 3.5), showing a decrease in the D for the FFC redox pair. It was thought that altering the time allowed for current to pass during the potentiostatic gel growth step would yield hydrogels with differing dimensions and diffusional properties. For example, applying 0.7 V to a 10 mg/mL Carb-Ala solution for a time period shorter than 120 seconds would oxidise a lower total concentration of hydroquinone. This was expected to have the effect of yielding smaller gels, of possibly different density, compared to those seen in Section 3.4.1. To test this hypothesis, gel growth time was adjusted from 120 seconds to 60 seconds (Figure 3.23, Table 3.10).

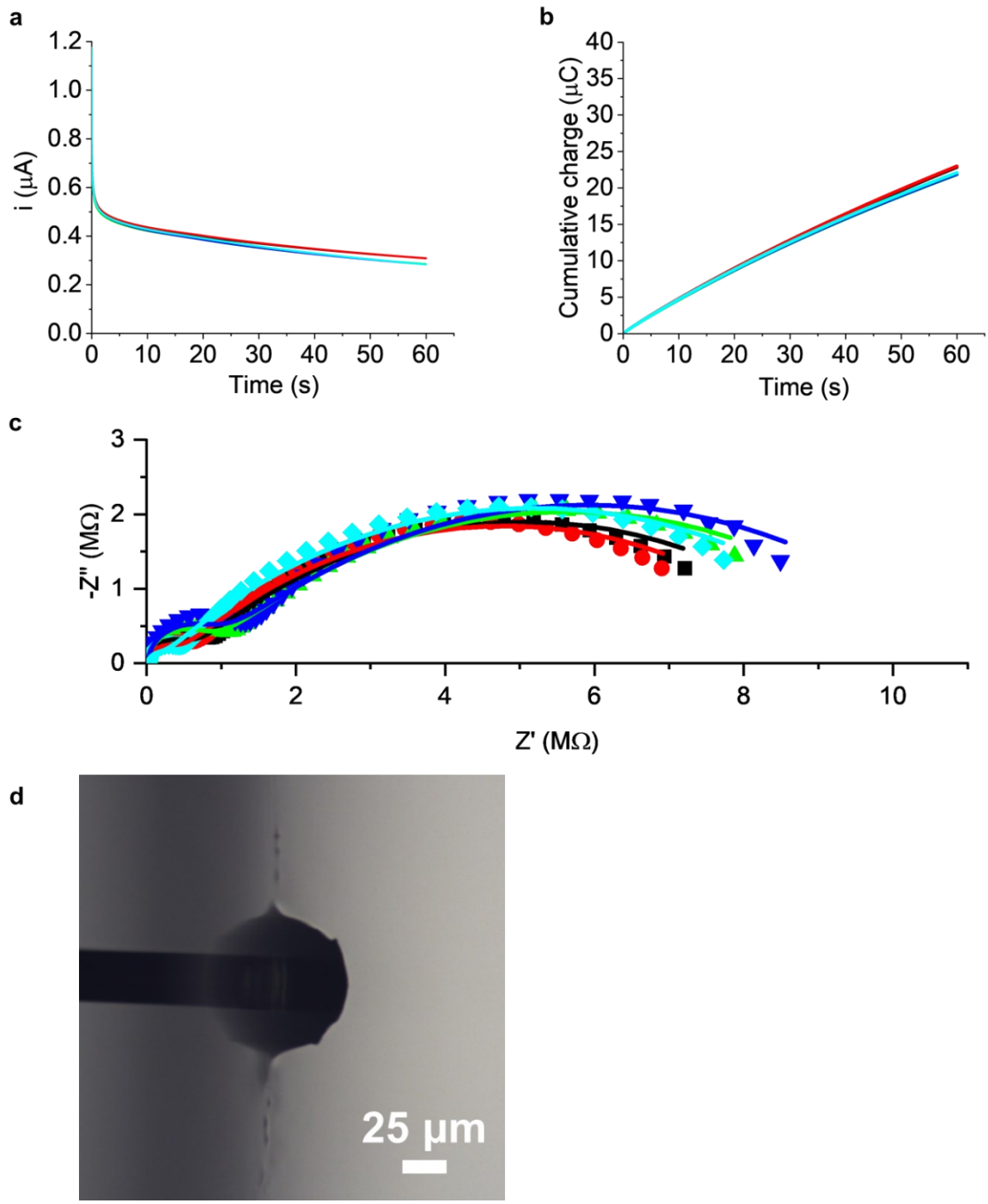

Figure 3.23 Potentiostatic growth of Carb-Ala gels on a Pt microelectrode (25 μm diameter) at 0.7 V for 60 seconds, 25 °C. (a) Current-time transients of hydroquinone oxidation in gelator solution. (b) Cumulative charge passed during gel-growth step, calculated by integrating area under current-time transients in (a). (c) Recorded (scatter points) and fitted (solid lines) Nyquist plots of gel-functionalised electrodes in ferrocyanide solution, obtained with weight factor off and R_S fixed to R_S obtained from weighted fit. Black squares = experiment 1, red circles = experiment 2, green triangles (up) = experiment 3, blue triangles (down) = experiment 4, teal diamonds = experiment 5. (d) Example capture of Carb-Ala gel at commercial microelectrode surface, side-on view, 100x magnification.

Table 3.10 Data and estimated errors for 60 second, 0.7 V Carb-Ala gels grown at 25 µm diameter Pt disc electrodes. Features total charge passed during gel-growth step (as shown in Figure 3.23b), fitted EIS data of gel functionalised microelectrodes (as shown in Figure 3.23c) to the modified Randles circuit with weight factor off and R_S fixed to weighted value (Figure 2.11, Chapter 2 Section 2.2.6). Diffusion coefficients D_L and D_{NL} were calculated using Equation 2.29 and Equation 2.31 respectively, and dimensions of gels (an example of which is featured in Figure 3.23d) are also tabulated.

0.7 V 60s gels, 25 µm dia. Pt disc micro., weight factor off, fixed R_S					
Component	**1**	**2**	**3**	**4**	**5**
Cumulative Charge (µC)	22.8	23.0	21.8	21.9	22.1
R_S (kΩ)	*15.4*	*14.9*	*15.8*	*19.3*	*15.8*
C_{DL} (pF)	98.3 ± 14.2	95.8 ± 14.9	103 ± 8	106 ± 11	83.2 ± 29.5
R_{CT} (kΩ)	515 ± 35	368 ± 27	765 ± 29	834 ± 45	180 ± 36
Y_0 (nS)	58.8 ± 1.2	58.5 ± 1.0	57.2 ± 0.9	46.6 ± 1.0	48.5 ± 0.8
R_{NL} (MΩ)	9.12 ± 0.11	8.86 ± 0.08	9.78 ± 0.09	10.2 ± 0.11	10.0 ± 0.09
χ^2	0.112	0.0749	0.0640	0.0983	0.0843
D_L ($\times 10^{-10}$ m^2 s^{-1})	1.62 ± 0.07	1.61 ± 0.05	1.54 ± 0.05	1.02 ± 0.04	1.11 ± 0.04
D_{NL} ($\times 10^{-10}$ m^2 s^{-1})	2.33 ± 0.03	2.40 ± 0.02	2.18 ± 0.02	2.09 ± 0.02	2.13 ± 0.02
Gel Width (µm)	100	108	105	162	103
Gel Height (µm)	57.4	52.0	56.2	43.3	55.8
Gel Cross-Sectional Area (µm^2)	3940	4130	4400	4120	4340

Reducing the gel growth time to 60 seconds had the expected effect of reducing the total cumulative charge passed. The average cumulative charge for this group was 22.3 µC, reduced from an average of 31.9 µC for the 120 second 0.7 V gels (Table 3.5, Table 3.10). The lower charge indicated a lower amount of hydroquinone oxidised, however the Carb-Ala gels grown for 60 seconds at 0.7 V had surprisingly similar final dimensions (average cross-sectional areas of 4190 ± 190 µm^2, Table 3.10) compared to the 120 second Carb-Ala gels (4390 ± 650 µm^2, Table 3.7).

There was an instance of a Carb-Ala gel in this 60 second 0.7 V group having a distinctly shorter final height and greater width than the average of the group (electrode 4, Table 3.10). The

unusual linear dimensions of this gel appeared not to have a noteworthy effect on the cross-sectional area, the corresponding equivalent circuit components, nor were these unusual dimensions the result of a significantly deviated cumulative charge applied during the growth step. It was speculated that the shape of this gel might have been a result of a collapse in structure due to damage caused during transfer from solution to position under microscope.

The electrodes upon which these gels were grown possessed Y_0 and R_{NL} components with values between those of the bare and 0.7 V 120 second Carb-Ala gel-coated single microelectrodes. R_{NL} values of these 60 second 0.7 V Carb-Ala gel-coated electrodes ranged from 9.1-10.2 MΩ, compared to 11.6-12.6 MΩ for the 120 second gels and 3.3-3.7 MΩ for the bare Pt microelectrodes (Table 3.3, Table 3.5, Table 3.10). As a result, the corresponding diffusion coefficients calculated for these 60 second gel-coated electrodes were slightly greater than those of the 120 second gels, and lower than those of the bare microelectrodes. Average D_L values for the 120 second and 60 second gel-coated electrodes were close (0.95 ± 0.23 and $1.38 \pm 0.29 \times 10^{-10}$ m^2 s^{-1} respectively, Table 3.5, Table 3.10), though D_{NL} values between the two groups were more clearly distinct (2.23 ± 0.14 and $1.76 \pm 0.06 \times 10^{-10}$ m^2 s^{-1} respectively, Table 3.5, Table 3.10). Overall, these experiments show that increasing the time for which the potentiostatic gel-growth method is used appears to increase the final Carb-Ala gel density, whilst hydrogel dimensions appear to remain largely unchanged over the 60-120 second timeframe.

3.4.4 Applied potential 0.7 V, gel growth time 300 seconds

In continuation, given the apparent relation between hydrogel density and increasing potentiostatic gel growth time, Carb-Ala gels were grown at 0.7 V for 300 seconds (Figure 3.24, Table 3.11) with the expectation that further gel growth time could cause the diffusion coefficients of these functionalised electrodes to decrease further.

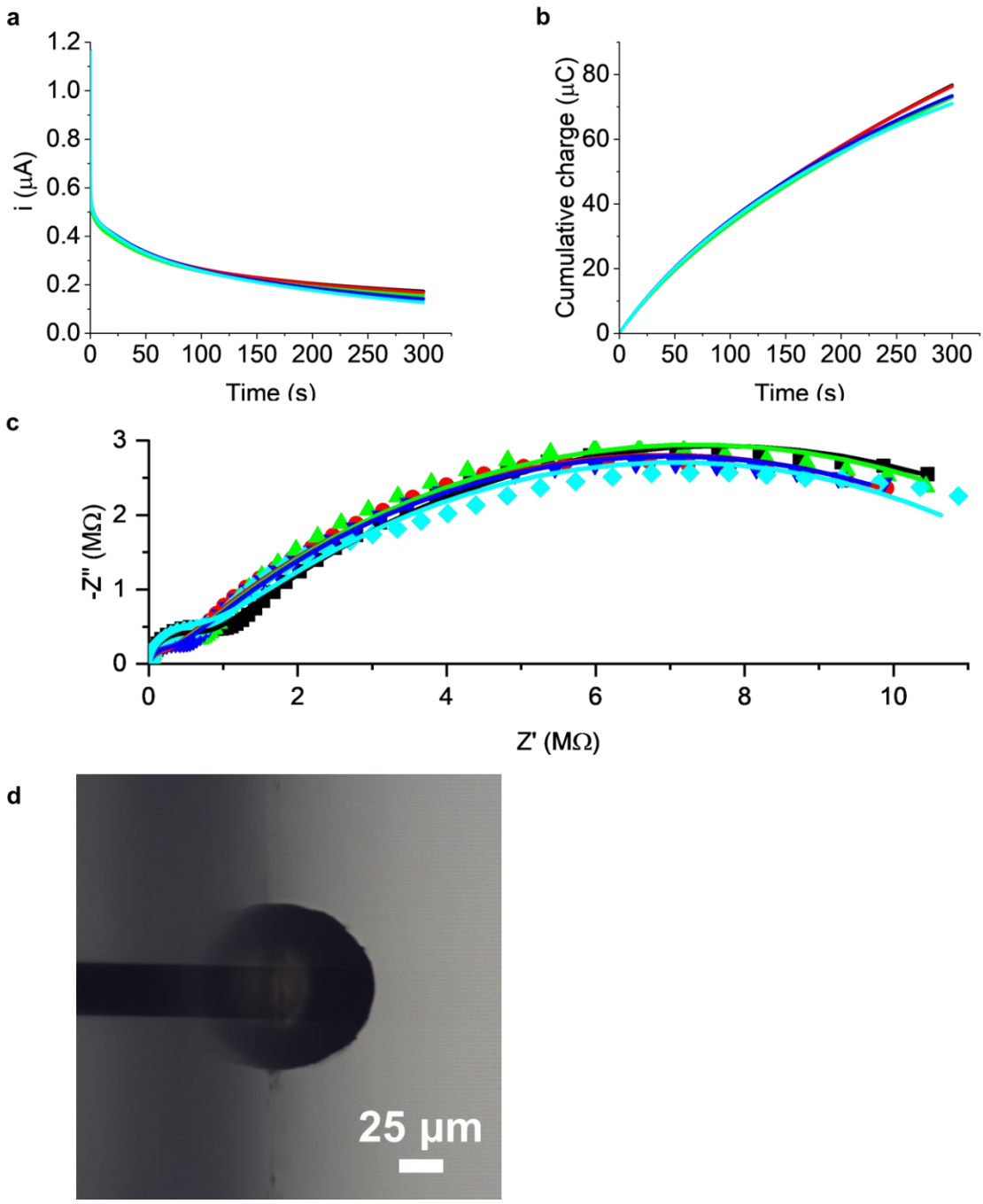

Figure 3.24 Potentiostatic growth of Carb-Ala gels on a Pt microelectrode (25 µm diameter) at 0.7 V for 300 seconds, 25 °C. (a) Current-time transients of hydroquinone oxidation in gelator solution. (b) Cumulative charge passed during gel-growth step, calculated by integrating area under current-time transients in (a). (c) Recorded (scatter points) and fitted (solid lines) Nyquist plots of gel-functionalised electrodes in ferrocyanide solution, obtained with weight factor off and R_S fixed to R_S obtained from weighted fit. Black squares = experiment 1, red circles = experiment 2, green triangles (up) = experiment 3, blue triangles (down) = experiment 4, teal diamonds = experiment 5. (d) Example capture of Carb-Ala gel at commercial microelectrode surface, side-on view, 100x magnification.

Table 3.11 Data and estimated errors for 300 second, 0.7 V Carb-Ala gels grown at 25 µm diameter Pt disc electrodes. Features total charge passed during gel-growth step (as shown in Figure 3.24b), fitted EIS data of gel functionalised microelectrodes (as shown in Figure 3.24c) to the modified Randles circuit with weight factor off and R_S fixed to weighted value (Figure 2.11, Chapter 2 Section 2.2.6). Diffusion coefficients D_L and D_{NL} were calculated using Equation 2.29 and Equation 2.31 respectively, and dimensions of gels (an example of which is featured in Figure 3.24d) are also tabulated.

0.7 V 300s gels, 25 µm dia. Pt disc micro., weight factor off, fixed R_S					
Component	**1**	**2**	**3**	**4**	**5**
Cumulative Charge (µC)	76.7	76.4	72.9	73.4	71.0
R_S (kΩ)	*20.0*	*17.8*	*18.4*	*18.5*	*18.9*
C_{DL} (pF)	98.0 ± 8.7	81.0 ± 20.1	80.7 ± 25.1	93.3 ± 13.5	126 ± 17
R_{CT} (kΩ)	630 ± 27	203 ± 29	270 ± 46	286 ± 22	657 ± 60
Y_0 (nS)	45.3 ± 0.5	43.5 ± 0.5	41.0 ± 0.7	45.8 ± 0.4	34.4 ± 0.7
R_{NL} (MΩ)	14.1 ± 0.1	13.5 ± 0.1	14.2 ± 0.1	13.4 ± 0.1	12.9 ± 0.1
χ^2	0.0336	0.0358	0.0851	0.0233	0.0788
D_L ($\times 10^{-10}$ m^2 s^{-1})	0.966 ± 0.021	0.891 ± 0.019	0.790 ± 0.026	0.988 ± 0.017	0.555 ± 0.023
D_{NL} ($\times 10^{-10}$ m^2 s^{-1})	1.51 ± 0.01	1.58 ± 0.01	1.50 ± 0.01	1.58 ± 0.01	1.65 ± 0.02
Gel Width (µm)	132	129	134	136	134
Gel Height (µm)	74.1	72.4	78.3	74.9	75.4
Gel Cross-Sectional Area (µm^2)	7480	7040	7990	7850	7490

Contrary to the observation regarding hydrogel sizes and gel growth time in Section 3.4.3, this experiment shows instead that hydrogel dimensions do not slow down at the 120 second timeframe. Extrapolating from results in the previous sections, and assuming there would be to linearity to the gel growth under chronoamperometry, it was expected that the cumulative charge passed and final gel cross-sectional area after 300 seconds would equate to averages of approximately 50 µC and 5000 µm respectively. Neither of these expectations were met, as the average cumulative charge passed due to hydroquinone oxidation equates to 74.1 ± 2.4 µC, and the average cross-sectional areas of the 300 second gels measures 7570 ± 370 µm^2 (Table 3.11). The cause for this effect is unknown, as experimental conditions used here were identical to those used to grow Carb-Ala gels for 60 and 120 seconds.

The prediction of growth time affecting the final diffusional properties of the microelectrode held for this experiment. Y_0 and R_{NL} values for these microelectrodes were on average lower and greater (respectfully) than those of the 120 second and 60 second potentiostatic gel experiments. This translated to diffusion coefficients which continued the trend of decreasing with gel growth time. Here, average D_{NL} was calculated to be $1.56 \pm 0.06 \times 10^{-10}$ $m^2 s^{-1}$, compared to 1.76 ± 0.06 and $2.23 \pm 0.14 \times 10^{-10}$ $m^2 s^{-1}$ for the 120 and 60 second gels respectively (Table 3.5, Table 3.10, Table 3.11). The decreasing rate of reduction in D_L and D_{NL} with gel growth time indicates that the hydrogel densities approach a minimum value, and that this value may be reached soon after 300 seconds of continued potentiostatic gel growth.

As seen before in Section 3.4.1, when fitting EIS data to the modified Randles circuit without the weight factor applied, it was common to see the Nova software sacrifice good estimations for the high frequency components in favour of compensating for the lower frequency components. The C_{DL} and R_{CT} components for this set of microelectrodes were all estimated with high errors, which allowed the Y_0 and R_{NL} components to be estimated with lower errors (Table 3.11). The effect of this compensation becomes prominent when comparing the real and fitted Nyquist plots for the microelectrodes functionalised with 300 second potentiostatic Carb-Ala gels (solid lines, Figure 3.24c). The endpoints of the first hemispheres in the fitted Nyquist plots (high-frequency range) tended towards poor estimation, which allowed the endpoint of the second hemispheres (low-frequency range) to be more closely positioned to the endpoint of the real data.

Some of the electrodes in this experiment featured bumps in the second hemisphere of the real EIS data, found at the onset of the linear diffusion profile (data points, Figure 3.24c). These indicate an additional, unaccounted for electrochemical phenomenon occurring in the lower frequency range. The most pronounced example of this effect was seen for electrode 5 in this dataset, which featured a bump starting at the onset of linear diffusion at 1 MΩ in the Z' axis and terminating at around 3 MΩ on the Z' axis (Figure 3.25).

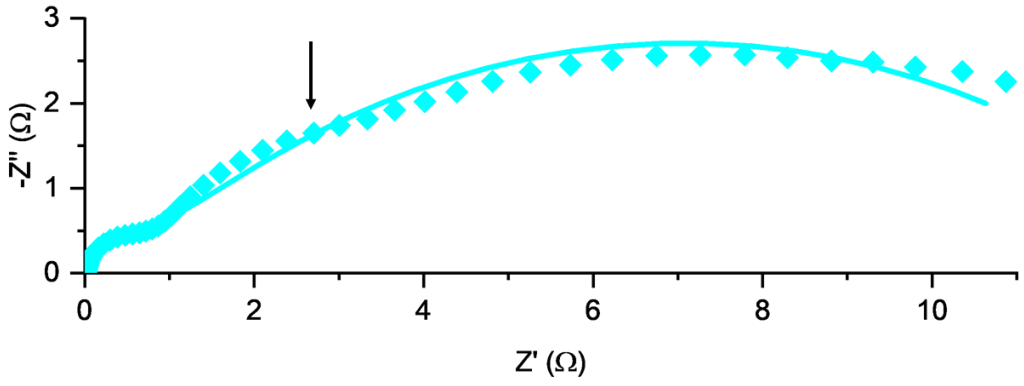

Figure 3.25 Nyquist plot of microelectrode 5 (Figure 3.24) a potentiostatic Carb-Ala gel coated (0.7 V, 300 seconds) Pt microelectrode (25 µm diameter) in ferrocyanide solution during EIS, 25 °C. Scatter points represent recorded impedance, solid line represents unweighted fitted data with R_S values fixed to the weighted R_S values using the modified Randles circuit. An arrow indicates the end of what appears to be a third hemispherical shape in the plot, corresponding to an unknown electrochemical process, terminating at approximately 3 MΩ on the Z' axis.

This accentuated feature, which was present in the other Nyquist plots in this group to a lesser degree, raised a question to the possibility of the same feature being masked or convoluted (and thus unaccounted for) in the Nyquist plots of gel coated electrodes in the prior experiments at 60 and 120 seconds. Given the frequency/timeframe in which this additional feature is found in the real data, it suggests the evolution of a new diffusional effect with the continued growth of hydrogel.

It is possible that a transition towards increased heterogeneity developing throughout the hydrogels at long growth periods could be a cause for this feature, though this has not been confirmed here. The equivalent circuit model applied in this work (Figure 2.11, Chapter 2 Section 2.2.6) fits the data in this set overall, and succeeds in retaining valuable information regarding changes to redox couple transport (Table 3.11), making it a suitable model to represent the gel-functionalised microelectrodes and to characterise the tuned properties of the hydrogels.

3.4.5 Summary of data for applied potential 0.7 V, gel growth time 60-300 seconds

Averages and standard deviations of the gel dimensions and the electrode EIS data obtained from the three groups of 0.7 V potentiostatic gel growth experiments (Sections 3.4.1, 3.4.3, and 3.4.4), as well as the EIS data for the bare Pt microelectrodes (Section 3.3), are compiled below to highlight trends (Table 3.12). The average fixed R_S values (which as a reminder were estimated from weighted fitting of EIS data) increased by approximately 80% from the bare to 300 second gel-coated electrodes. This indicates a slowing in the mobility of the background electrolyte ions near the electrode surface due to increasing hydrogel density. C_{DL} and R_{CT} values appear to be within experimental error and thus consistent between each of the experiments, with the varying errors indicating variation between electrode surfaces in each experiment. This confirms that the kinetics of the electrochemical hydroquinone oxidation is not affected by the growing gel structure at the electrode surface.

Table 3.12 Averages and standard deviations of data for bare and 0.7 V Carb-Ala gel-coated 25 µm diameter Pt disc electrodes (compiled from Table 3.3, Table 3.4, Table 3.5, Table 3.7, Table 3.10 and Table 3.11). Average and standard deviation dimensions for the group of gels grown for 60 seconds (italicised) were obtained after excluding the data for the gel grown on microelectrode 4 in that group (Table 3.10) from the calculation.

0.7 V Carb-Ala Gel Growth Experiments, 25 µm dia. Pt disc micro., weight factor off, fixed R_S				
Gel growth time (s)	0 (Bare)	60	120	300
Cumulative Charge (µC)	-	22.3 ± 0.5	31.9 ± 4.0	74.1 ± 2.4
R_S (kΩ)	10.4 ± 3.0	16.2 ± 1.7	18.2 ± 0.7	18.7 ± 0.8
C_{DL} (pF)	134 ± 21	97.2 ± 8.7	107 ± 6	95.9 ± 18.7
R_{CT} (kΩ)	413 ± 355	532 ± 272	583 ± 239	409 ± 216
Y_0 (nS)	99.9 ± 8.3	53.9 ± 5.9	44.6 ± 5.5	42.0 ± 4.7
R_{NL} (MΩ)	3.49 ± 0.16	9.59 ± 0.58	12.1 ± 0.4	13.6 ± 0.5
D_L ($\times 10^{-10}$ m^2 s^{-1})	4.71 ± 0.78	1.38 ± 0.29	0.947 ± 0.229	0.838 ± 0.176
D_{NL} ($\times 10^{-10}$ m^2 s^{-1})	6.10 ± 0.27	2.23 ± 0.14	1.76 ± 0.06	1.56 ± 0.06
Gel Width (µm)	-	*104 ± 3*	104 ± 6	133 ± 3
Gel Height (µm)	-	*55.4 ± 2.3*	55.1 ± 4.3	75.0 ± 2.2
Gel Cross-Sectional Area (µm^2)	-	*4200 ± 210*	4390 ± 650	7570 ± 370

Stepping up the time passed in each potentiostatic gel growth experiment on the order of minutes had a significant effect on the cumulative charge, i.e., the amount of hydroquinone oxidised, and by extension the amount of dissolved Carb-Ala being protonated and self-assembling. This correlated with a decrease in transport to the electrode surfaces, as shown with increasing R_{NL} and decreasing Y_0 values (Table 3.12). D_L and D_{NL} decreased significantly from the bare to gel-coated electrodes, especially in the first 60 seconds of potentiostatic Carb-Ala gel growth where both D values dropped to a third of the calculated values for the bare electrode (Table 3.12). Beyond this timeframe, changes in D_L and D_{NL} (i.e., changes in Y_0 and R_{NL}) were less pronounced, suggesting that these changes to microelectrode diffusional properties would cease soon after the 300 seconds of gel growth time. The effect of potentiostatic gel growth time on the diffusion coefficients of the 25 µm diameter single disc

Pt microelectrodes, the cumulative charge, and Carb-Ala gel cross-sectional areas measured under microscopy are presented below (Figure 3.26).

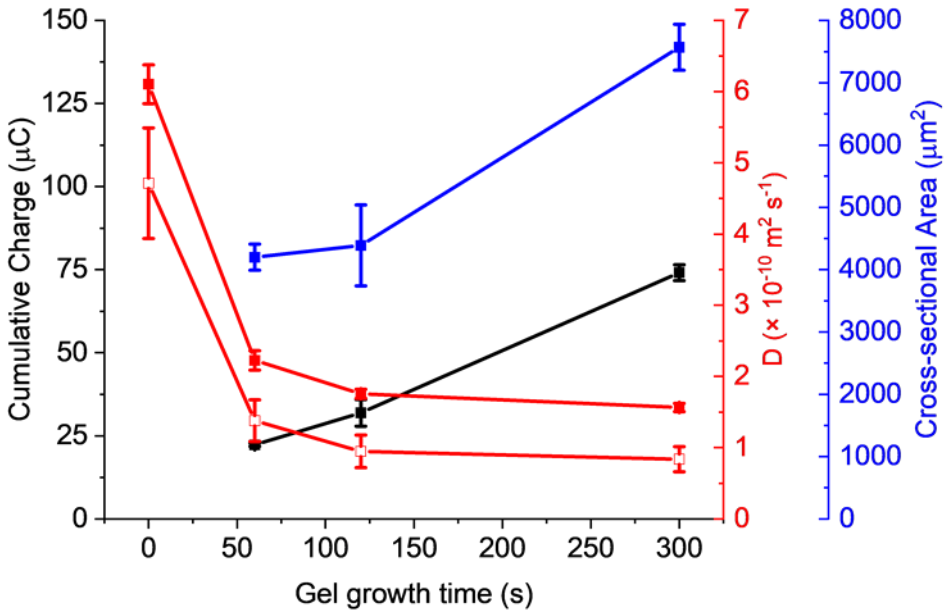

Figure 3.26 Plots summarising trends in gel cross-sectional area, cumulative charge, and diffusion coefficients in relation to varying 0.7 V potentiostatic gel growth times of Carb-Ala gels, grown at 25 µm diameter Pt disc electrodes (data from Table 3.12). Square points represent averages; error bars represent standard deviations. Black squares = Cumulative charge, red squares (filled) = D_{NL}, red squares (hollow) = D_L, blue squares = gel cross-sectional area.

Whilst the average diffusion coefficients of the FFC redox pair appeared to be approaching a minimum with time, Carb-Ala hydrogel dimensions were suggested to be increasing with time, potentially beyond the 300 second experiment. How long these gels could continue to grow for with the potential applied, and when a minimum diffusion coefficient would be reached, was explored in Section 3.4.6. As stated previously in Section 3.4.1, the dimensions of these gels gave an indication that they were not exactly hemispherical in shape. It has recently been shown at macroelectrodes that the growth of electrochemically-grown supramolecular hydrogels is consistent with the control of proton diffusion.[14] To test whether this is the case for these microelectrodes, an equivalent approach was followed. Assuming the gels were hemispherical, the estimated gel cross-sectional area normal to the electrode through the centre of the Pt wire, *A*, was calculated:

$$A = \pi r^2/2 \qquad \textit{Equation 3.4}$$

where r would be either the height of the gel or half the width of the gel. Then, additionally, the three-dimensional random walk model (Equation 3.5)[28] is considered:

$$r^2 = 6Dt \qquad \textit{Equation 3.5}$$

Gel cross-sectional area can be estimated by substituting Equation 3.5 into Equation 3.4, assuming the Grotthuss mechanism for proton diffusion, where D_{H+} = 7 × 10^{-9} m^2 s^{-1},[29] and that gel growth is limited solely by the rate of diffusion of protons produced via hydroquinone oxidation:

$$A = 3\pi D_{H+} t \qquad \textit{Equation 3.6}$$

Using Equation 3.4 and Equation 3.6, average gel cross-sectional areas were calculated and compared to the measured average gel cross-sectional areas (Table 3.13).

Table 3.13 Measured and calculated cross-sectional dimensions of potentiostatically grown 0.7 V Carb-Ala hydrogels at 25 µm diameter Pt disc electrodes. Features average measured cross-sectional areas with standard deviations (from Table 3.12), cross-sectional areas calculated from averages and standard deviations of measured gel half-widths and heights (also from Table 3.12, Equation 3.4), and cross-sectional areas estimated from calculated area of proton diffusion (Equation 3.6). Calculated and measured cross-sectional areas for the group of gels grown for 60 seconds (italicised) were obtained after excluding the data for the gel grown on microelectrode 4 in that group (Table 3.10) from the calculation.

0.7 V Carb-Ala Gel Cross-sectional areas, 25 µm dia. Pt disc micro., weight factor off, fixed R_S			
Gel growth time (s)	60	120	300
Measured Area (µm²)	*4200 ± 210*	4390 ± 650	7570 ± 370
Calculated Area from Gel Width (µm²)	*4250 ± 270*	4260 ± 510	6950 ± 280
Calculated Area from Gel Height (µm²)	*4810 ± 410*	4760 ± 740	8840 ± 510
Estimated Area from D_{H+} (µm²)	3960000	7920000	19800000

The two cross-sectional areas calculated by substituting gel width and gel height into Equation 3.4 serve to highlight that these gels do not possess perfect hemispherical shapes (Table 3.13). Interestingly, the cross-sectional areas of the 60 second, 120 second and 300 second gels calculated using the measured heights are 13%, 12% and 27% greater (respectively) than those calculated using half-widths. Moreover, when estimating gel dimensions using Equation 3.6, the calculated gel cross-sectional areas are three orders of magnitude greater than the average measured areas of the gels (Table 3.13). These calculations highlight two important factors: first, the low pH zone generated due to hydroquinone oxidation, which the hydrogels should theoretically be shaped by, may not be perfectly hemispherical at all distances from the electrode surface; second, the discrepancy between the estimated and measured gel

cross-sectional areas indicates that the growth of these gels is not simply limited by proton diffusion.

Microelectrodes are known for possessing greater radial contributions to their diffusion profiles.[34] As discussed by Amatore *et al*. in a study of the evolution of diffusion layers at Pt disc microelectodes,[19,35] the flux of $FeCH_2OH^+$ product formed under potentiostatic conditions (probed using electrochemical scanning microscopy) was found to be significantly increased in axis perpendicular to the electrode surface. This was deduced to be a result of competing diffusional fluxes of incoming $FeCH_2OH$ and outgoing $FeCH_2OH^+$, as well as a contribution from natural convection. This could explain why hydrogels produced in this study also possess near-hemispherical dimensions. It is reasonable to expect, in the context of potentiostatic Carb-Ala hydrogel growth (conducted at electrode surfaces very similar to those used by Amatore *et al*.[19,35]), that the proton concentration gradient similarly skews more perpendicular from the disk. The incoming radial flow of hydroquinone, combined with the convection of a pH 8 gelator solution that likely buffers the expanding acidic volume, could result in the growth of these nearly-hemispherical Carb-Ala hydrogels.

Addressing the second factor, though there are only three data points to make a judgement from, the rate of gel growth exhibited here is not linear nor at the same scale as the theoretical expansion of the acidic volume. In order for gelation to occur, pH in a given volume must be lower than the pK_a^{app} of the gelator in question.[4] Thus, protonation and gelator self-assembly only occurs within volumes at the electrode surface where pH is lower than gelator pK_a^{app}, and due to the buffering effect provided by the pH 8 bulk gelator solution, gel growth will be limited.

3.4.6 *In situ* study of electrochemical hydrogel growth with time, applied potential 0.7 V

Given the proposed contribution of buffering to the acidic volume generated at the microelectrode surface with hydroquinone oxidation, it is likely that the hydrogel will reach a maximum size when proton and buffer fluxes are in equilibrium at interface between the hydrogel and the bulk solution. EIS conducted post-growth also appears to show diffusional rates for the FFC redox pair decreasing towards a minimum, due to changes in gel density that may also reach a final state. The object of the experiments in this section was to confirm these expectations as a function of time, by recording measurements of the gel *in situ* during growth.

The current method of recording images of these microscale Carb-Ala gels involved placing the ends of the disc microelectrodes under a microscope, so that the Pt surface was in plane with the viewing angle. Images were recorded after the electrodeposition process was ceased, which provided snapshots of the hydrogel at certain points in time on the order of minutes (as seen in Section 3.2.2, Section 3.4.3 and Section 3.4.4). An *in situ* recording of hydrogel growth at the single microelectrodes had not been conducted. An experiment was therefore set up wherein the current-time transient and growth of a Carb-Ala hydrogel at a Pt microelectrode could be recorded in tandem, to capture how potentiostatic electrochemical gelation evolved over the initial 0-10 seconds, tens of minutes, and hours.

Due to the nature of this experiment requiring a microscope and camera, it was set up outside of a Faraday cage. Details for this experimental setup can be found in Chapter 2 Section 2.5.4. A potential of +0.7 V was applied within a 5 mL 10 mg/mL Carb-Ala gelator solution for a total of 3 hours. The growing hydrogel was then recorded under microscopy. Snapshots of the hydrogel at eight different times were collected from the full recording to obtain a general understanding of the progression of gel growth over the 3 hour period (Figure 3.27).

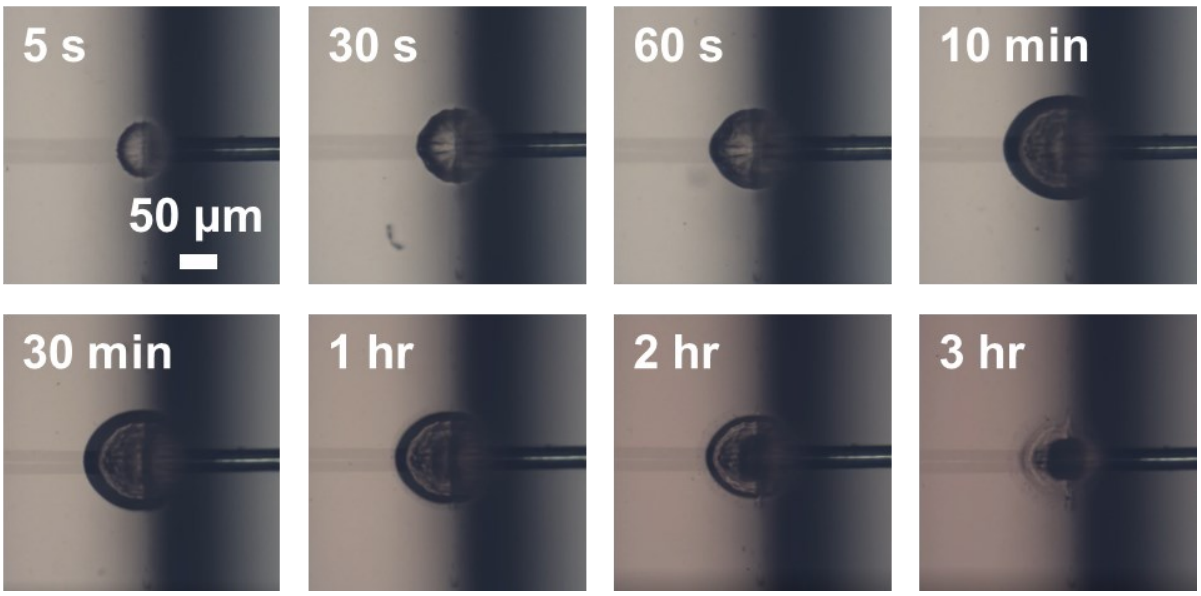

Figure 3.27 Images of Carb-Ala hydrogel at Pt microelectrode (25 µm diameter disc) surface, side-on view, 100x magnification, at various stages of 3 hour (10800 second) 0.7 V potentiostatic gel growth experiment. From top left to bottom right: 5 seconds, 30 seconds, 60 seconds, 10 minutes, 30 minutes, 1 hour, 2 hours, 3 hours. Images showcase a gradual change in transparency, but not overall gel size, from 1 hour into the experiment to the end of the 3 hour period.

The initial visual information at these eight timeframes showed that the Carb-Ala hydrogel had expanded in size for the first 10 minutes (Figure 3.27). Beyond this point, the growth rate of the gel appeared to slow markedly, and eventually halted after approximately 30 minutes, confirming the expectation that the gel would reach a maximum size after a period of sustained applied potential. Once dimensions had seemingly stabilised, the gel began to exhibit a change in opacity. At the 1 hour mark, starting from the outermost edge of the gel, the darker shade of the hydrogel gradually receded towards the Pt surface, with the colour of the changed region resembling that of the bulk solution. Though it did not appear to shrink for the remaining duration of the experiment, the outline of the gel became faintly visible.

Two explanations for this phenomenon were proposed: first, the gel had lost density, from the outside-in, marked by the direction of the change in opacity; second, a re-structuring or re-organisation of the aggregate network leading may have occurred, leading to an alignment of supramolecular fibre structures that affected material transparency. Carb-Ala hydrogel dimensions were measured, post-recording, at 1 second intervals for the first 5 seconds of the recording, at 5 second intervals from 5-60 seconds, and in increasingly spaced time-intervals as the experiment proceeded. The dimensions of the hydrogel, the current, and the

cumulative charge were plotted together against time for the first 15 minutes of gel growth time (Figure 3.28).

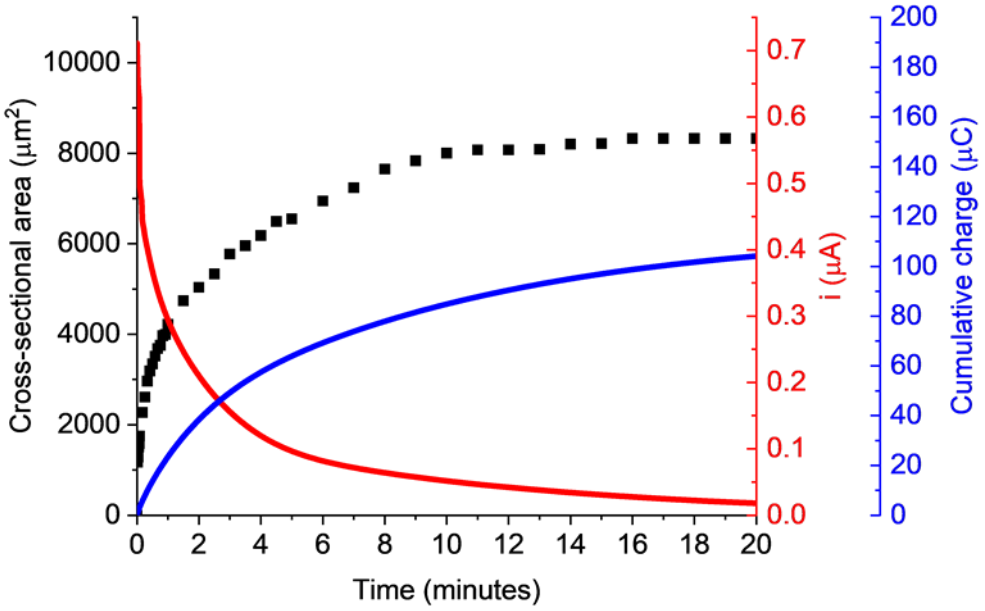

Figure 3.28 Initial 20 minutes of potentiostatic Carb-Ala gel growth at a Pt microelectrode (25 µm diameter) in 5 mL 10 mg/mL Carb-Ala gelator solution (pH 8), 0.7 V, T = 25 °C. Gel cross-sectional area (black squares), current-time transients of hydroquinone oxidation (red line) and cumulative charge (blue line, calculated by integrating area under current-time transient) plotted together.

It is satisfying that the currents, cumulative charge, and gel dimensions measured over the first 5 minutes of this long-period experiment are consistent with the *ex situ* values recorded previously. At 1 minute, the gel had grown to a cross-sectional area of 4220 µm^2 after a total charge of 23.2 µC had been passed from electrochemical hydroquinone oxidation (Figure 3.28). This is within two standard deviations of the averages recorded for the prior 60 second experiments (Table 3.12). Similarly, at 2 minutes, this had progressed to 5040 µm^2 and 38.0 µC, and at 300 seconds to 6550 µm^2 and 63.7 µC, which agreed within error with previous experimental results.

Patterson *et al.* have shown how the cross-sectional area of peptide-based hydrogels – grown with galvanostatic control at macroelectrodes – expands linearly at early times.[14] In this study, gel cross-sectional area was also expected to grow linearly at early times, given that the microelectrode would establish a hemispherical diffusion profile quickly, and the expansion of the low pH zone would follow Equation 3.6 (assuming *D* was constant). Though this was the case from 1-10 seconds, with rate of cross-sectional gel growth measured as 122 µm^2 s^{-1} with a standard error of 7 µm^2 s^{-1} , there was an initial jump of 1200 µm^2 in cross-sectional area from time 0-1 seconds (Figure 3.29). This burst in initial gel growth appears to be caused by the rapid transition from a linear diffusion regime to a hemispherical regime in the sub-1 second timescale, after which gel growth rate is slowed because of the newly established and enhanced mass transport of chemical species.

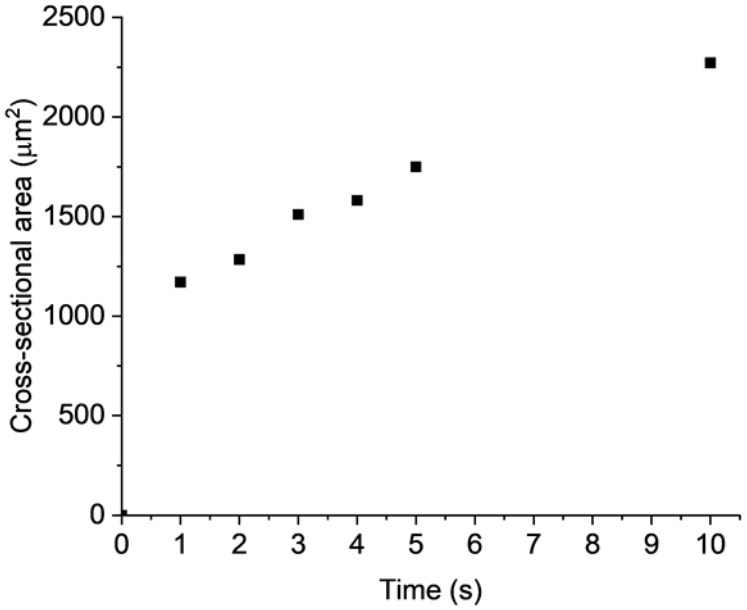

Figure 3.29 Initial 10 seconds of potentiostatic Carb-Ala gel growth at a Pt microelectrode (25 μm diameter) in 5 mL 10 mg/mL Carb-Ala gelator solution (pH 8), 0.7 V, T = 25 °C. Showcases rabid burst of initial gel growth at sub-1 second timescale, indicating the establishment of a hemispherical diffusion regime from a linear diffusion regime. 1-10 second timescale presents linear gel growth afforded by enhanced transport.

After the first 16 minutes, the dimensions of the Carb-Ala gel reached a maximum. Cross-sectional area settled at 8330 μm^2 for 5 minutes, and subsequently dropped to 7960 μm^2 after 35 minutes, and the gel stayed at this size for the remaining duration of the experiment (Figure 3.30). After 160 minutes, the current-time transient reached a steady current of 4.6 nA.

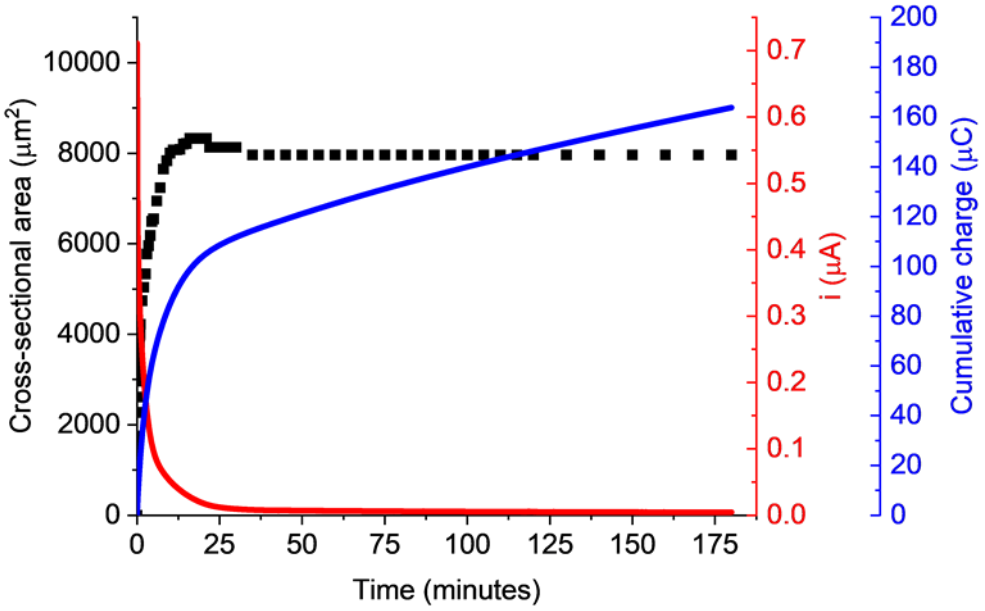

Figure 3.30 3 hours (10800 seconds) potentiostatic Carb-Ala gel growth at a Pt microelectrode (25 µm diameter), in 5 mL 10 mg/mL Carb-Ala gelator solution (pH 8), 0.7 V, T = 25 °C. Gel cross-sectional area (black squares), current-time transients of hydroquinone oxidation (red line) and cumulative charge (blue line, calculated by integrating area under current-time transient) plotted together.

The hydrogel ceased to increase in size after 35 minutes (Figure 3.30), the reason for which was understood to be the bulk solution buffering the acidic volume. This would prevent a significant pH drop necessary for triggering Carb-Ala gelation from expanding past a certain distance from the Pt microelectrode (where convection would become the dominant mass transfer process). Beyond this time, the dimensions of the gel and currents passed were constant (Figure 3.30), however the images show that the gel was not in a static state from this point onward (Figure 3.27). The acidic zone was still being produced during this time, and in combination with incoming buffer flux, gel density appeared to be changing dynamically with time, without the dimensions of the hydrogel changing.

Theoretical gel cross-sectional areas were calculated from the measured widths and heights of the gel at the same times, using Equation 3.4. The measured cross-sectional area was displayed with the progression of the calculated areas (again, assuming the gel was hemispherical) with time (Figure 3.31).

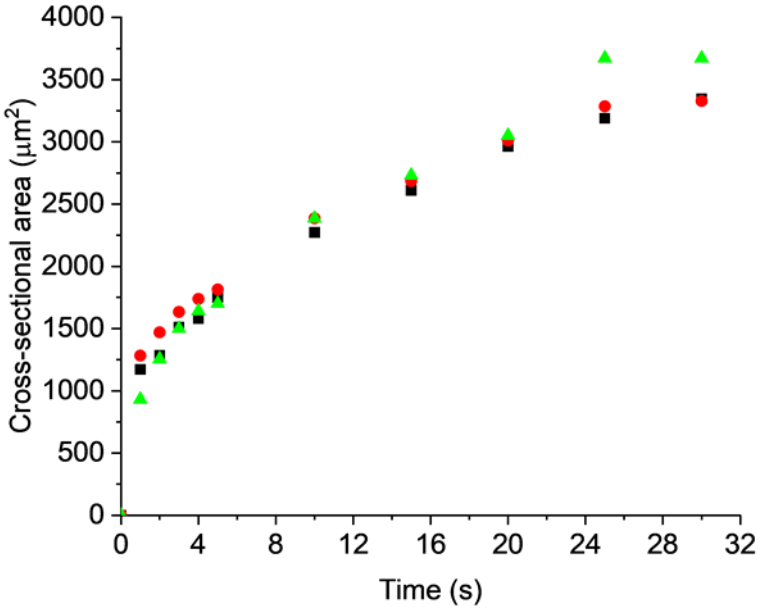

Figure 3.31 Initial 30 seconds of potentiostatic Carb-Ala gel growth at a Pt microelectrode (25 µm diameter) in 5 mL 10 mg/mL Carb-Ala gelator solution (pH 8), 0.7 V, T = 25 °C. Gel cross-sectional area (black squares), and calculated cross-sectional areas (Equation 3.4) using gel width (red circles) and height (green triangles) are plotted together.

It is interesting that, in the first 10 seconds of the experiment, the radius of the cross-section of the gel was slightly greater in the plane parallel to the Pt surface (where width was measured) than in the perpendicular plane (where height was measured). This was reflected in the calculated cross-sectional areas from these two linear measurements (Figure 3.31). However, beyond this timeframe the height of the gel became greater than half the width. This observation persisted for the remaining duration of the experiment (Figure 3.32), as was seen in the analysis of average Carb-Ala gel dimensions in Table 3.13, Section 3.4.5.

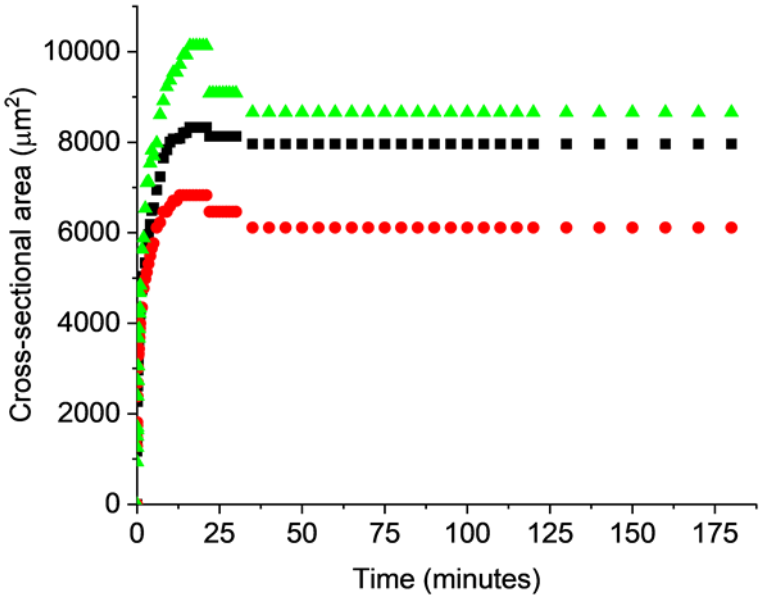

Figure 3.32 3 hours (10800 seconds) potentiostatic Carb-Ala gel growth at a Pt microelectrode (25 µm diameter) in 5 mL 10 mg/mL Carb-Ala gelator solution (pH 8), 0.7 V, T = 25 °C. Gel cross-sectional area (black squares), and calculated cross-sectional areas (Equation 3.4) using gel width (red circles) and height (green triangles) are plotted together.

This change in radial dimensions also suggests a change in diffusion regime. In the initial timescale of 0-1 seconds, the diffusion profile for the flux of H^+ product morphed from a linear to a hemispherical regime. Following this, the height (perpendicular radius) of the gel surpassing the width (parallel radius) marked the development of a skewed hemispherical diffusion profile, consistent with the *ex situ* gel observations in Section 3.4.5.

3.4.7 Applied potential 0.6 V, gel growth time 120 seconds

This chapter has primarily focussed on potentiostatic Carb-Ala gel growth at microelectrodes whilst avoiding electrochemical oxidation of the Carb-Ala gelator. However, it was also of interest to explore the tuneability of hydrogel properties when applying potentials on or near the thresholds of the diffusion-limited hydroquinone oxidation potential range, as seen in the CV for the 10 mg/mL Carb-Ala gelator solution (Figure 3.2b). To compare with the work pertaining to tuning gelation of Carb-Ala at single microelectrodes shown previously in this chapter, it was decided that gel growth time would be set to 120 seconds. First, 0.6 V was selected to observe what effects a potential at the threshold of the diffusion-limited potential range for hydroquinone would have on the potentiostatically grown gels (Figure 3.33, Table 3.14). The magnitude of cumulative charge passed, the fitted EIS data and calculated diffusion coefficients, and the measured hydrogel dimensions, were all indistinguishable from those of the 0.7 V 120 second Carb-Ala gel-coated microelectrodes (Table 3.12, Table 3.14). This is reassuring to see: due to the potential of 0.6 V still being enough to pass a mass transport limited current, it stands to reason that no significant differences to the gel/microelectrode characteristics should be observed.

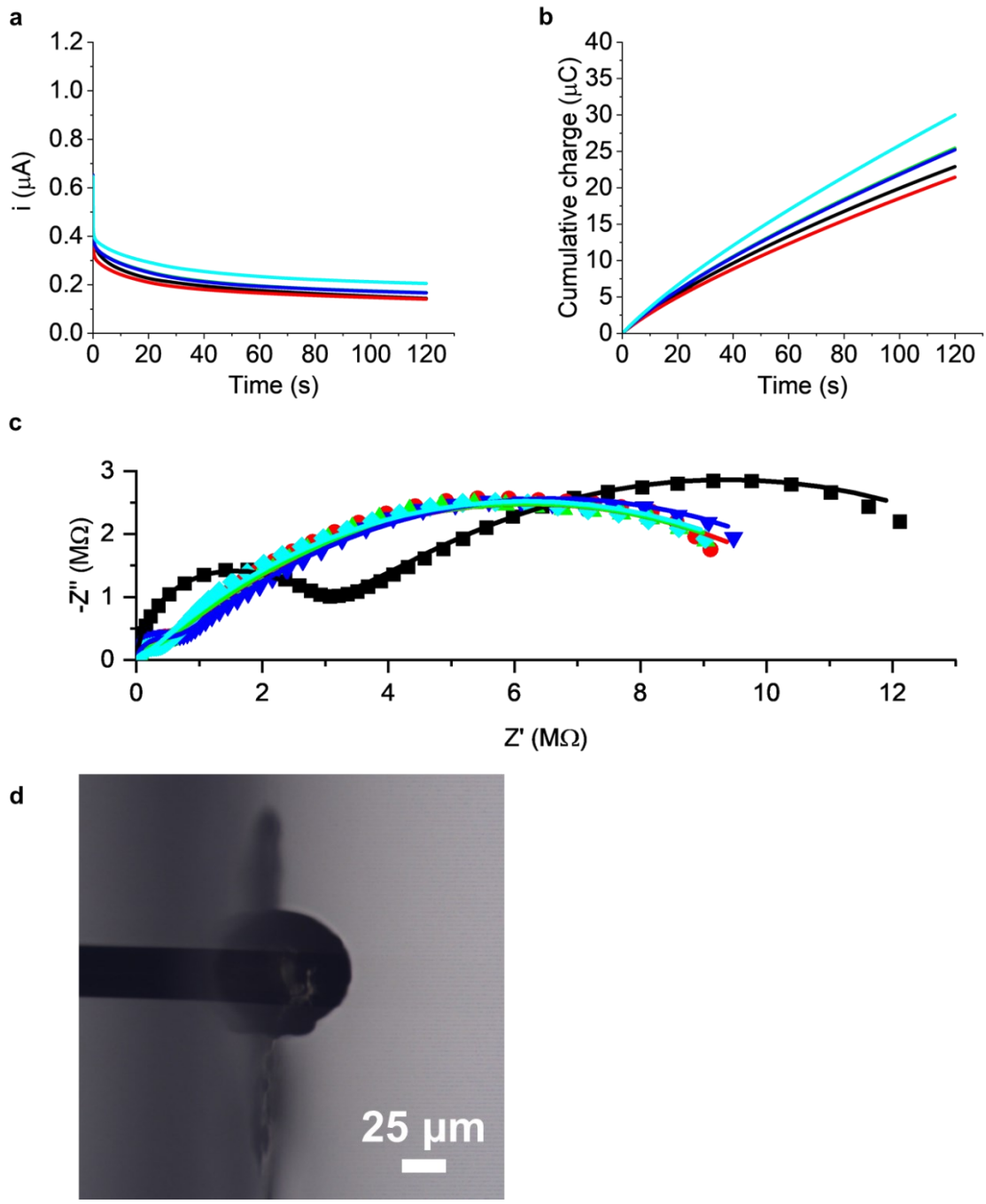

Figure 3.33 Potentiostatic growth of Carb-Ala gels on a Pt microelectrode (25 μm diameter) at 0.6 V for 120 seconds, 25 °C. (a) Current-time transients of hydroquinone oxidation in gelator solution. (b) Cumulative charge passed during gel-growth step, calculated by integrating area under current-time transients in (a). (c) Recorded (scatter points) and fitted (solid lines) Nyquist plots of gel-functionalised electrodes in ferrocyanide solution, obtained with weight factor off and R_S fixed to R_S obtained from weighted fit. Black squares = experiment 1, red circles = experiment 2, green triangles (up) = experiment 3, blue triangles (down) = experiment 4, teal diamonds = experiment 5. (d) Example capture of Carb-Ala gel at commercial microelectrode surface, side-on view, 100x magnification.

Table 3.14 Data and estimated errors for 120 second, 0.6 V Carb-Ala gels grown at 25 µm diameter Pt disc electrodes. Features total charge passed during gel-growth step (as shown in Figure 3.33b), fitted EIS data of gel functionalised microelectrodes (as shown in Figure 3.33c) to the modified Randles circuit with weight factor off and R_S fixed to weighted value (Figure 2.11, Chapter 2 Section 2.2.6). Diffusion D_L and D_{NL} were calculated using Equation 2.29 and Equation 2.31 respectively, and dimensions of gels (an example of which is featured in Figure 3.33d) are also tabulated.

0.6 V 120s gels, 25 µm dia. Pt disc micro., weight factor off, fixed R_S					
Component	**1**	**2**	**3**	**4**	**5**
Cumulative Charge (µC)	22.9	21.4	25.4	25.2	30
R_S (kΩ)	*17.0*	*16.9*	*16.5*	*16.8*	*16.3*
C_{DL} (pF)	107 ± 3	91.0 ± 21.7	99.5 ± 15.3	104 ± 10	72.0 ± 28.0
R_{CT} (kΩ)	2540 ± 36	297 ± 43	264 ± 23	497 ± 24	135 ± 31
Y_0 (nS)	48.2 ± 0.7	39.0 ± 0.7	45.0 ± 0.4	45.4 ± 0.5	45.1 ± 0.6
R_{NL} (MΩ)	13.7 ± 0.1	11.9 ± 0.1	11.9 ± 0.1	12.3 ± 0.1	12.1 ± 0.1
χ^2	0.0332	0.0686	0.0255	0.0276	0.0469
D_L ($\times 10^{-10}$ m^2 s^{-1})	1.09 ± 0.03	0.716 ± 0.024	0.953 ± 0.018	0.967 ± 0.020	0.956 ± 0.023
D_{NL} ($\times 10^{-10}$ m^2 s^{-1})	1.55 ± 0.01	1.79 ± 0.01	1.78 ± 0.01	1.73 ± 0.01	1.75 ± 0.01
Gel Width (µm)	87.8	78.9	92.4	88.7	96.2
Gel Height (µm)	55.0	50.7	55.0	55.0	62.1
Gel Cross-Sectional Area (µm^2)	3670	3000	3880	3750	4150

3.4.8 Applied potential 0.8 V, gel growth time 120 seconds

The Carb-Ala gelator is known to electropolymerise, and has typically been observed doing so under cyclic voltammetry and galvanostatic experiments. The CVs of the 10 mg/mL Carb-Ala solutions in this work have shown that the onset potential for this polymerisation is around 0.9 V (Figure 3.2b, Figure 3.21). It was thought that a competition between electrochemical oxidation of hydroquinone and Carb-Ala could yield gels with properties unique from the prior experiments at lower potentials. Thus, Carb-Ala hydrogels were grown by applying 0.8 V for 120 seconds to study the effects of this competition (Figure 3.34, Table 3.15).

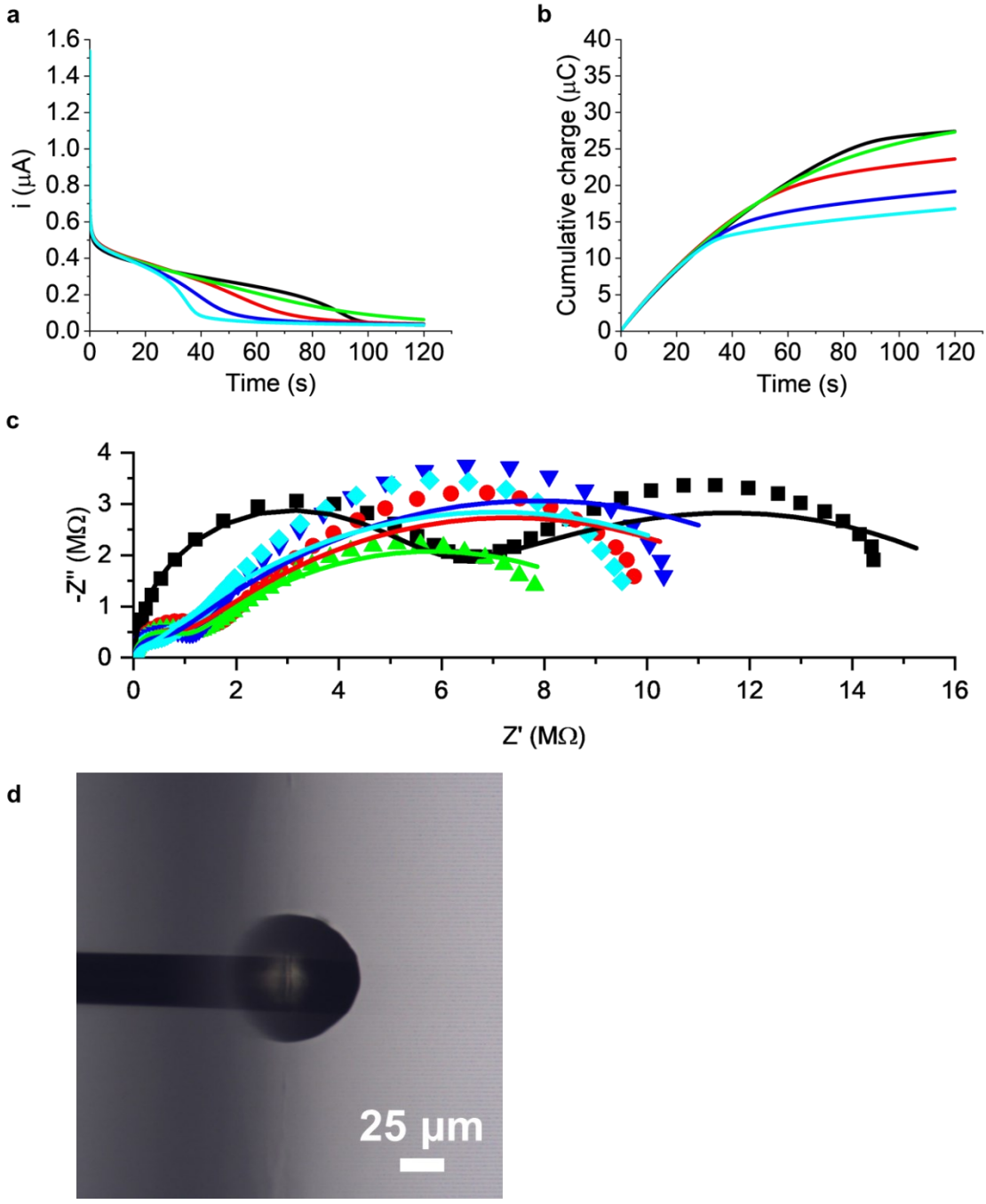

Figure 3.34 Potentiostatic growth of Carb-Ala gels on a Pt microelectrode (25 μm diameter) at 0.8 V for 120 seconds, 25 °C. (a) Current-time transients of hydroquinone oxidation in gelator solution. (b) Cumulative charge passed during gel-growth step, calculated by integrating area under current-time transients in (a). (c) Recorded (scatter points) and fitted (solid lines) Nyquist plots of gel-functionalised electrodes in ferrocyanide solution, obtained with weight factor off and R_S fixed to R_S obtained from weighted fit. Black squares = experiment 1, red circles = experiment 2, green triangles (up) = experiment 3, blue triangles (down) = experiment 4, teal diamonds = experiment 5. (d) Example capture of Carb-Ala gel at commercial microelectrode surface, side-on view, 100x magnification.

Table 3.15 Data and estimated errors for 120 second, 0.8 V Carb-Ala gels grown at 25 µm diameter Pt disc electrodes. Features total charge passed during gel-growth step (as shown in Figure 3.34b), fitted EIS data of gel functionalised microelectrodes (as shown in Figure 3.34c) to the modified Randles circuit with weight factor off and R_S fixed to weighted value (Figure 2.11, Chapter 2 Section 2.2.6). Diffusion coefficients D_L and D_{NL} were calculated using Equation 2.29 and Equation 2.31 respectively, and dimensions of gels (an example of which is featured in Figure 3.34d) are also tabulated.

0.8 V 120s gels, 25 µm dia. Pt disc micro., weight factor off, fixed R_S					
Component	**1**	**2**	**3**	**4**	**5**
Cumulative Charge (µC)	27.4	23.6	27.3	19.2	16.8
R_S (kΩ)	*21.2*	*20.5*	*18.3*	*20.0*	*19.7*
C_{DL} (pF)	112 ± 5	111 ± 29	121 ± 12	107 ± 63	138 ± 131
R_{CT} (kΩ)	5170 ± 130	810 ± 112	857 ± 39	540 ± 176	270 ± 180
Y_0 (nS)	35.8 ± 1.6	42.9 ± 1.9	60.8 ± 1.3	39.8 ± 2.4	42.2 ± 2.5
R_{NL} (MΩ)	13.3 ± 0.3	13.1 ± 0.3	9.97 ± 0.13	14.7 ± 0.5	13.6 ± 0.4
χ^2	0.128	0.463	0.113	0.994	0.877
D_L (× 10^{-10} m^2 s^{-1})	0.604 ± 0.055	0.866 ± 0.076	1.74 ± 0.08	0.743 ± 0.090	0.837 ± 0.099
D_{NL} (× 10^{-10} m^2 s^{-1})	1.60 ± 0.03	1.62 ± 0.04	2.14 ± 0.03	1.45 ± 0.05	1.56 ± 0.05
Gel Width (µm)	96.2	97.8	99.1	94.1	92.8
Gel Height (µm)	52.5	56.6	56.6	53.3	55.0
Gel Cross-Sectional Area ($µm^2$)	3660	4200	4310	3700	3750

As seen in the prior 0.7 V experiments, the cumulative charge for each successive electrode decreased, though the total cumulative charges for the 0.8 V Carb-Ala gels were on average lower than seen in the 0.7 V experiment (Table 3.12, Table 3.15). This was due to a consistent drop in current that occurred midway through each of the current-time transients, decreasing from approximately 400 nA to 40 nA (Figure 3.34a, Figure 3.34b), and is likely the cause of Carb-Ala polymerisation leading to electrode surface passivation. The build-up of polymer directly at the Pt microelectrode surface would restrict access for hydroquinone to engage in electrochemical oxidation. The drops in current signify a sudden reduction in available redox species or redox species diffusion, which a growing microscale polymer at a microelectrode

surface could facilitate. Consequently, these gels were also smaller on average than those grown by applying 0.7 V for the same period of time (Table 3.12, Table 3.15).

Ignoring the R_{CT} value for electrode 1 in this group, which was abnormally large in comparison to the values of the four other electrodes, average R_{CT} was in this set was identical within experimental error to the 0.7 V 120 second gels, at 619 ±271 kΩ compared to 583 ±239 kΩ of the 0.7 V set (Table 3.12, Table 3.15). The R_{NL} and Y_0 components of the 0.8 V Carb-Ala gel-coated electrodes were more inconsistent between the sequential electrodes than those for the electrodes in lower potential experiments. More interestingly, the Nyquist plots recorded in this experiment featured an unusual, narrow shape to the semi-circular section representing microelectrode diffusion properties in the lower frequency range (Figure 3.34c).

This unusual shape to the Nyquist plots did not allow them to be modelled accurately with the modified Randles circuit (Figure 2.11, Chapter 2 Section 2.2.6), and wellness of fit suffered heavily with the estimated fitting well overshooting the low frequency end of the plots (Figure 3.34c, Table 3.15). A similar issue was experienced with the set of Carb-Ala functionalised microelectrodes in Section 3.4.4, where the gels grown for 300 seconds at 0.7 V featured an additional bump convoluted in the low frequency end of the Nyquist plot (Figure 3.24).

Given the poor fitting as seen visually and demonstrated by high χ^2 values (Figure 3.34c, Table 3.15), how close these calculated diffusion coefficients are to reality is questionable. Ultimately, there is a need for an equivalent circuit model that explains this unusual shape in the lower frequency range of these Nyquist plots, though this study has not focussed on that particular goal. Here, a controlled change in diffusion coefficient due to fine-tuning of experimental conditions is of more importance than an exact numerical value for the diffusion coefficient of the FFC redox probe.

3.4.9 Applied potential 1.0 V, gel growth time 120 seconds

In terms of applied potentials, the final point of interest in this study was to investigate how potentiostatic electrochemical gelation would proceed when potential was fixed further into the range where Carb-Ala oxidation competes with hydroquinone oxidation. Carb-Ala gels were grown at each of the five Pt disc microelectrodes by applying 1.0 V for 120 seconds (Figure 3.35, Table 3.16).

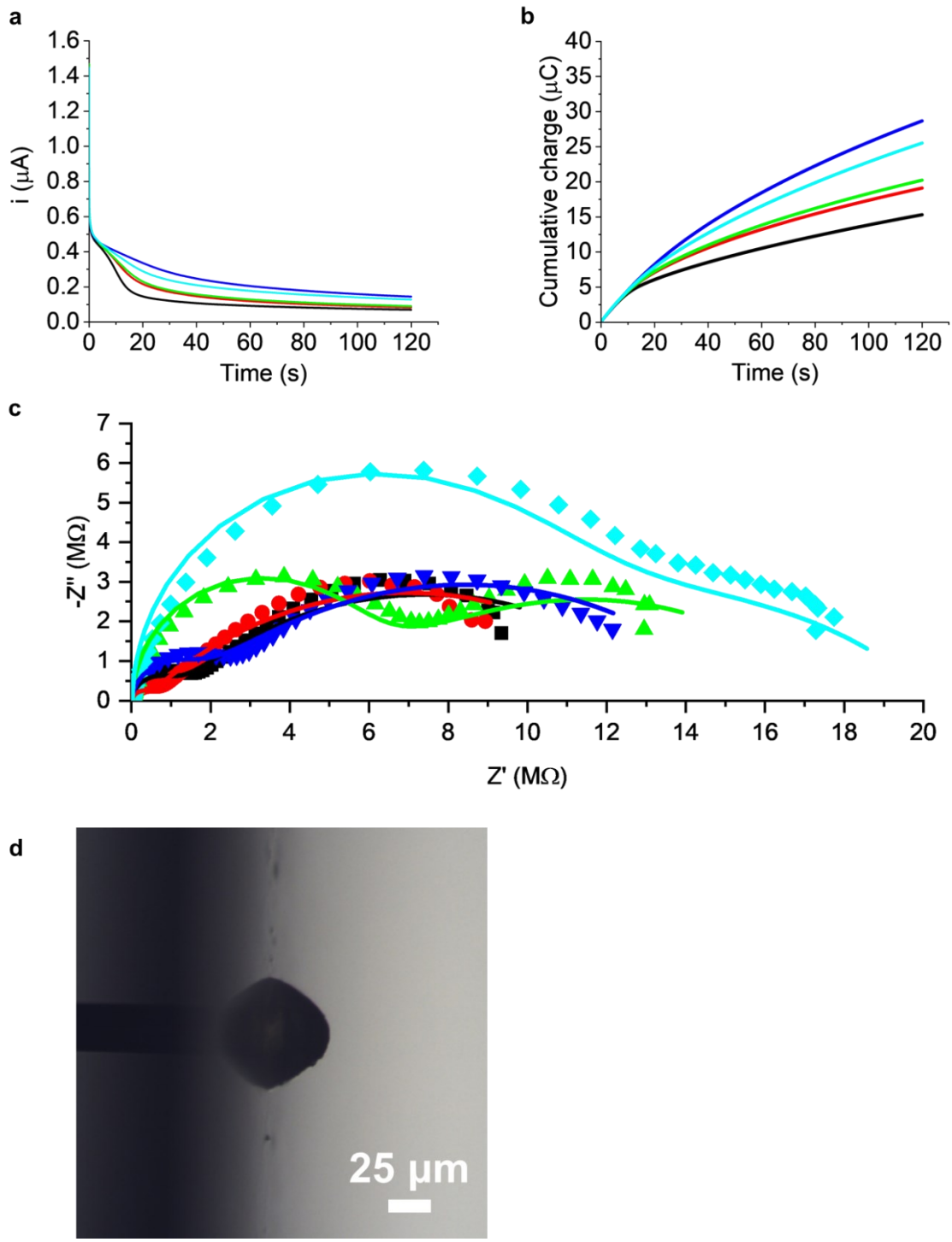

Figure 3.35 Potentiostatic growth of Carb-Ala gels on a Pt microelectrode (25 μm diameter) at 1.0 V for 120 seconds, 25 °C. (a) Current-time transients of hydroquinone oxidation in gelator solution. (b) Cumulative charge passed during gel-growth step, calculated by integrating area under current-time transients in (a). (c) Recorded (scatter points) and fitted (solid lines) Nyquist plots of gel-functionalised electrodes in ferrocyanide solution, obtained with weight factor off and R_S fixed to R_S obtained from weighted fit. Black squares = experiment 1, red circles = experiment 2, green triangles (up) = experiment 3, blue triangles (down) = experiment 4, teal diamonds = experiment 5. (d) Example capture of Carb-Ala gel at commercial microelectrode surface, side-on view, 100x magnification.

Table 3.16 Data and estimated errors for 120 second, 1.0 V Carb-Ala gels grown at 25 µm diameter Pt disc electrodes. Features total charge passed during gel-growth step (as shown in Figure 3.35b), fitted EIS data of gel functionalised microelectrodes (as shown in Figure 3.35c) to the modified Randles circuit with weight factor off and R_S fixed to weighted value (Figure 2.11, Chapter 2 Section 2.2.6). Diffusion coefficients D_L and D_{NL} were calculated using Equation 2.29 and Equation 2.31 respectively, and dimensions of gels (an example of which is featured in Figure 3.35d) are also tabulated.

1.0 V 120s gels, 25 µm dia. Pt disc micro., weight factor off, fixed R_S					
Component	**1**	**2**	**3**	**4**	**5**
Cumulative Charge (µC)	15.3	19.1	20.2	28.7	25.5
R_S (kΩ)	*21.6*	*20.6*	*32.2*	*21.8*	*28.7*
C_{DL} (pF)	149 ± 24	108 ± 41	205 ± 8	141 ± 14	242 ± 10
R_{CT} (kΩ)	1000 ± 80	365 ± 66	5680 ± 140	1550 ± 100	10100 ± 500
Y_0 (nS)	50.8 ± 1.8	54.2 ± 1.6	54.4 ± 3.2	33.5 ± 1.1	30.9 ± 4.9
R_{NL} (MΩ)	12.9 ± 0.3	13.1 ± 0.3	12.0 ± 0.4	13.9 ± 0.2	10.1 ± 0.4
χ^2	0.286	0.289	0.182	0.151	0.219
D_L (× 10^{-10} m^2 s^{-1})	1.21 ± 0.08	1.38 ± 0.08	1.39 ± 0.16	0.527 ± 0.034	0.449 ± 0.141
D_{NL} (× 10^{-10} m^2 s^{-1})	1.65 ± 0.04	1.62 ± 0.03	1.77 ± 0.05	1.53 ± 0.02	2.10 ± 0.09
Gel Width (µm)	83.2	78.4	88.0	94.4	90.4
Gel Height (µm)	38.4	40.8	40.8	51.0	49.4
Gel Cross-Sectional Area ($µm^2$)	2400	2120	2130	3510	3060

Surprisingly, cumulative charge increased with each successive use of the 10 mg/mL Carb-Ala gelator solution in this experiment (Figure 3.35b, Table 3.16). However, this observation is likely coincidental: variations like this have been observed throughout this work and are for the most part random and not tied to gel dimensions or cumulative charge. Whilst Y_0 and corresponding *D* values for microelectrodes 4 and 5 were significantly lower than estimated for the first three microelectrodes, R_{NL} and corresponding *D* values did not feature any trends congruous with charge and hydrogel dimensions.

Likewise, C_{DL} and R_{CT} values, which would increase with the concentration of adsorbed Carb-Ala polymer, also did not show any correlation with the increasing magnitude of cumulative

charges passed. For example, microelectrodes 3, 4 and 5 were estimated with R_{CT} values of 5.7 MΩ, 1.6 MΩ and 10 MΩ respectively. Additionally, the entire group of electrodes demonstrated great variability/inconsistency in amount of polymer adsorbed at the Pt surfaces, according to the variations in C_{DL} and R_{CT} values (Table 3.16).

The most notable feature of these gels were their sizes: compared to previous experiments at lower potentials, these 1.0 V gels were smaller on average. The cause of this – as with the 0.8 V gels in Section 3.4.8 – is likely from competition between Carb-Ala gelator and hydroquinone oxidation, and the production of a polymer layer that reduces available Pt surface area. A reduction in surface area for hydroquinone oxidation to occur would reduce currents passed (Figure 3.35a), leading to a reduced expansion of the acidic zone compared to experiments at lower potentials (Figure 3.33a, Figure 3.34a). Finally, it was also surprising to see how well the Nyquist plots for these 1.0 V gels were fitted to the modified Randles circuit (Table 3.16). The χ^2 values were all comparably low when compared to those of obtained in the 0.8 V experiment (Table 3.15).

3.4.10 Summary of data for applied potentials 0.6-1.0 V, gel growth time 120 seconds

As in Section 3.4.5, the data for the potential-varied potentiostatic gel growth experiments were compiled together to inform on trends with the increasing promotion of Carb-Ala oxidation and electropolymerisation (Figure 3.36, Table 3.17).

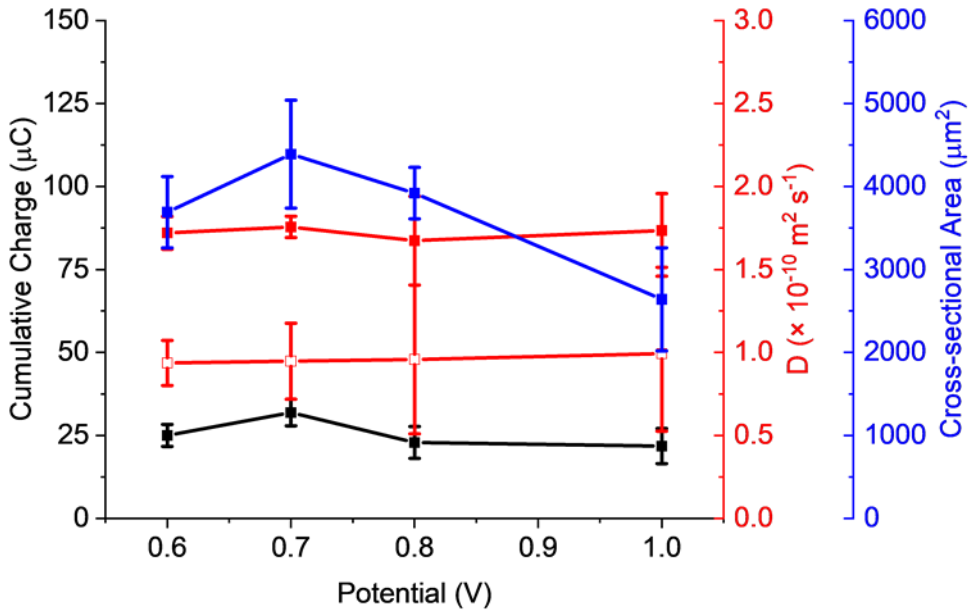

Figure 3.36 Plots summarising trends in gel cross-sectional area, cumulative charge, and diffusion coefficients in relation to varying potential applied for potentiostatic growth of Carb-Ala gels, 120 seconds, grown at 25 µm diameter Pt disc electrodes (data from Table 3.17). Square points represent averages; error bars represent standard deviations. Black squares = Cumulative charge, red squares (filled) = D_{NL}, red squares (hollow) = D_L, blue squares = gel cross-sectional area.

Table 3.17 Averages and standard deviations of data the 120 second Carb-Ala gel-coated 25 µm diameter Pt disc electrodes (compiled from Table 3.5, Table 3.7, Table 3.14, Table 3.15, Table 3.16). Average and standard deviation R_{CT} for 0.6 V, 0.8 V and 1.0 V (italicised) were obtained after excluding values for the gels grown on microelectrodes 1 in the 0.6 V and 0.8 V groups (Table 3.14, Table 3.15) and on microelectrode 3 and 5 in the 1.0 V group (Table 3.16) from the calculations.

120 second Carb-Ala Gel Growth Experiments, 25 µm dia. Pt disc micro., weight factor off, fixed R_S				
Applied Potential (V)	0.6	0.7	0.8	1.0
Cumulative Charge (µC)	25.0 ± 3.3	31.9 ± 4.0	22.9 ± 4.8	21.8 ± 5.3
R_S (kΩ)	*16.7 ± 0.3*	*18.2 ± 0.7*	*19.9 ± 1.1*	*24.9 ± 5.3*
C_{DL} (pF)	94.6 ± 13.9	107 ± 6	118 ± 12	169 ± 54
R_{CT} (kΩ)	*298 ± 150*	583 ± 239	*619 ± 271*	*974 ± 595*
Y_0 (nS)	44.5 ± 3.3	44.6 ± 5.5	44.3 ± 9.6	44.8 ± 11.6
R_{NL} (MΩ)	12.4 ± 0.8	12.1 ± 0.4	12.9 ± 1.8	12.4 ± 1.4
D_L (× 10^{-10} m^2 s^{-1})	0.936 ± 0.136	0.947 ± 0.229	0.958 ± 0.448	0.993 ± 0.467
D_{NL} (× 10^{-10} m^2 s^{-1})	1.72 ± 0.10	1.76 ± 0.06	1.67 ± 0.27	1.74 ± 0.22
Gel Width (µm)	88.8 ± 6.5	104 ± 6	96.0 ± 2.6	86.9 ± 6.2
Gel Height (µm)	55.6 ± 4.1	55.1 ± 4.3	54.8 ± 1.9	44.1 ± 5.7
Gel Cross-Sectional Area ($µm^2$)	3690 ± 430	4390 ± 650	3920 ± 310	2640 ± 620

All told, there were not as many significant differences between potentiostatic Carb-Ala hydrogels when fixing growth time for two minutes. From 0.6 V to 1.0 V, cumulative charges during gel growth were the same within experimental error (Table 3.17, Figure 3.36). The average Y_0 and R_{NL} components and associated diffusion coefficients were also statistically identical across these four experiments. This meant that, within this short growth timeframe, varying potentials within this range made no difference to how these gels affected the transport of the FFC redox probe.

The application of higher potentials was expected to increase the amount of polymer close to or adsorbed at the electrode surface, which could be identified by C_{DL} and R_{CT}. However, C_{DL} values sat within two standard deviations of each other experiment, and average R_{CT} only

showed such a trend when outlying high values were removed from those calculations (italics, Table 3.17) – even then, the averages of those values were still within one to two standard deviations of the values for the other experiments at different potentials.

The cross-sectional areas for these gels were comparable, with each average sitting within the other's margins for error, within 1-2 standard deviations (Table 3.17, Figure 3.36). The 1.0 V gels were on average significantly smaller than the rest, which suggests that there is a downward trend in gel size with greater potentials applied (as gelator polymerisation is encouraged). As seen with the 0.7 V hydrogels (Table 3.12), gel height was consistently greater than gel half width (Table 3.17).

3.4.11 *In situ* study of electrochemical hydrogel growth with time, applied potential 1.0 V

To conclude this section of experiments, how gel growth would proceed at longer timescales when applying potentials that facilitated the electrochemical oxidation of both hydroquinone and the polymerisation of the Carb-Ala gel was investigated. Taking the experimental described in Section 3.4.6, this time ensuring both species would be involved in the electrochemistry, current and hydrogel dimensions were recorded for 3 hours whilst applying 1.0 V to a 10 mg/mL Carb-Ala gelator solution (Figure 3.37, Figure 3.38).

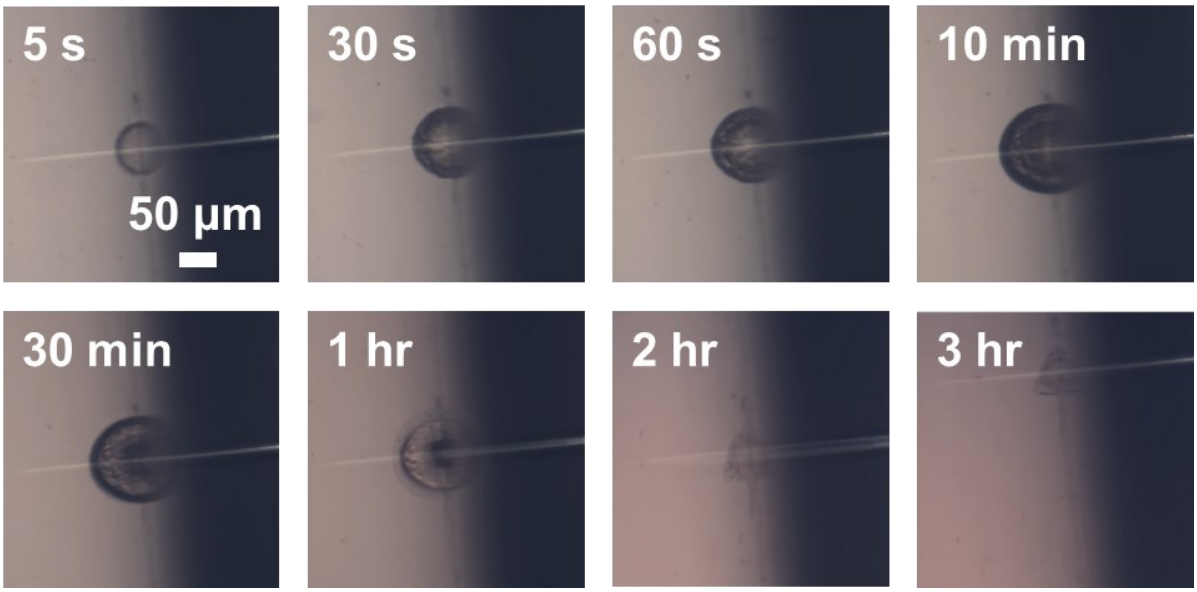

Figure 3.37 Images of Carb-Ala hydrogel at Pt microelectrode surface, side-on view, 100x magnification, at various stages of 3 hour 1.0 V potentiostatic gel growth experiment. From top left to bottom right: 5 seconds, 30 seconds, 60 seconds, 10 minutes, 30 minutes, 1 hour, 2 hours, 3 hours. Images showcase a gradual change in transparency, followed by a decrease in gel dimensions from 1 hour into the experiment to the end of the 3 hour period.

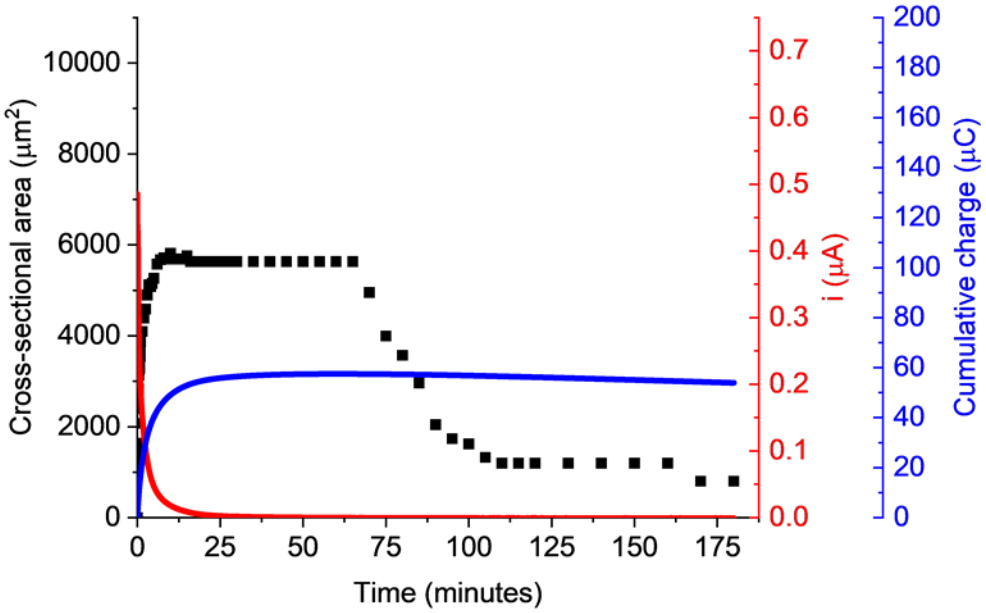

Figure 3.38 3 hours (10800 seconds) potentiostatic Carb-Ala gel growth at a Pt microelectrode (25 µm diameter), in 5 mL 10 mg/mL Carb-Ala gelator solution (pH 8), 1.0 V, T = 25 °C. Gel cross-sectional area (black squares), current-time transients of hydroquinone oxidation (red line) and cumulative charge (blue line, calculated by integrating area under current-time transient) plotted together.

This hydrogel experienced similar processes as in the previous 3 hour potentiostatic Carb-Ala gel growth experiment at 0.7 V in Section 3.4.6 of this chapter. Similarly, the cross-sectional area of the 1.0 V Carb-Ala gel jumped to 1000 μm^2 in the first second, and from 1-10 seconds grew at a rate of 112 $\mu m^2\ s^{-1}$ with a standard error of 12 $\mu m^2\ s^{-1}$ (Figure 3.38). It reached a maximum cross-sectional area of 5810 μm^2 after a period of 10 minutes, then settled to 5630 μm^2 until 65 minutes had elapsed (Figure 3.38). During this period of stabilised dimensions, the hydrogel underwent a process which led to increasing transparency (Figure 3.37).

It is no question at this point that Carb-Ala polymerisation has a significant effect on the rate of potentiostatic Carb-Ala gel growth. Whilst the dimensions of the 0.7 V and 1.0 V gels were arguably indistinguishable at the 120 second mark (Table 3.17, Figure 3.36), it was already clear that even after 10 minutes there were drastic differences in size between the two experiments, correlated with a markedly lower current in the 1 V experiment. For comparison, the 0.7 V gel had expanded to a size of 8000 μm^2 at the 10 minute mark (Figure 3.30).

A noteworthy similarity was also found in a shrinking "inner" layer of the gel: a similar effect was observed in the experiment at 0.7 V, with a non-uniform change in opacity progressing from the outermost region of the gel towards the electrode surface (Figure 3.27). Following the disappearance of this inner layer, the cross-sectional area of the 1.0 V gel diminished significantly after 67 minutes, reaching 1200 μm^2 at approximately 110 minutes, and then shrunk further to 800 μm^2 at 3 hours. It is also worth noting that this collapsing event followed after the hydroquinone oxidation current had effectively dropped to 0 A (there was in fact a

slightly negative background current observed after 3600 seconds, Figure 3.38), which caused a slight drop in cumulative charge for the remaining duration of the experiment. Assuming a re-organisation or change in fibre alignment was occurring, this could lead to the gel undergoing syneresis. However, the Carb-Ala gelator and other carbazole-functionalised oligopeptide gelators are not known to form hydrogels that undergo syneresis over time, let alone in solution. A more likely explanation for this gel shrinkage could be a loss of gel mass, as these gelators are known to disassemble when introduced pH is raised above the pK_a^{app}.

Due to the polymerisation of Carb-Ala, the transport and subsequent reaction of hydroquinone at the electrode surface was slowly be reduced over time, to a point where the entire Pt surface was inaccessible (when current became effectively 0 A). Once this had happened, the acidic volumes required to sustain the hydrogel will have ceased to be maintained, and the supramolecular gel would then be left to slowly deprotonate, disassemble and dissolve with the uncontested incoming flux of the naturally buffering pH 8 bulk solution. This explanation can be supported by earlier works studying the oxidation of hydroquinone to promote gelation.[2] All of these observations accumulate to further support the notion that electrochemically-driven gel growth and shrinkage is a dynamic process of gelator protonation and deprotonation, and that the remaining undissolved material at the electrode surface, presumably polymerised Carb-Ala, is stable once pH is raised above the gelator pK_a^{app} (Figure 3.37).

With regards to the shape of the gel, the measured cross-sectional area was compared with the calculated theoretical cross-sectional area of the gel. This was done by once again assuming the gel was a perfect hemisphere, using the height and half-width as radii and inserting values into Equation 3.4 to estimate what the cross-sectional area of the gel would be if this were the case (Figure 3.39).

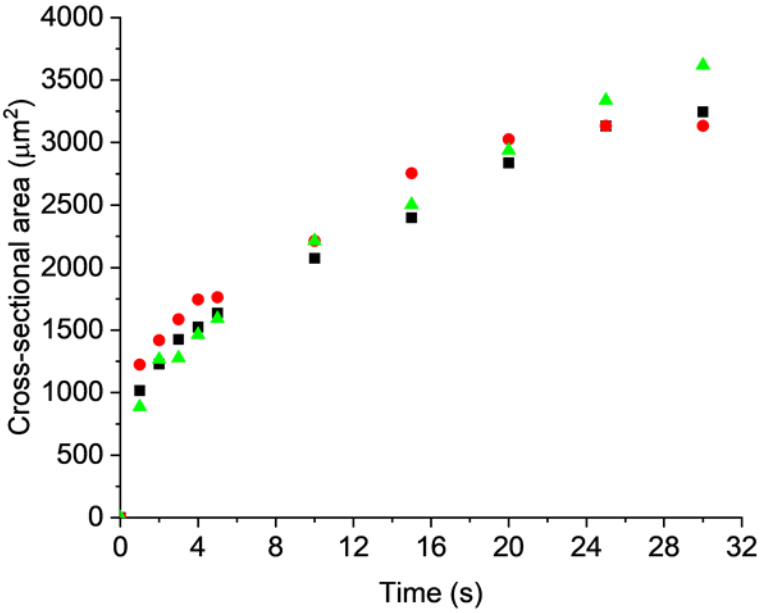

Figure 3.39 Initial 30 seconds of potentiostatic Carb-Ala gel growth at a Pt microelectrode (25 µm diameter) in 5 mL 10 mg/mL Carb-Ala gelator solution (pH 8), 1.0 V, T = 25 °C. Gel cross-sectional area (black squares), and calculated cross-sectional areas (Equation 3.4) using gel width (red circles) and height (green triangles) are plotted together.

Similar to what was seen in Section 3.4.6 with the 0.7 V gel, the parallel radius of the 1.0 V gel was greater than its perpendicular radius for the first 20 seconds of the current-time transient. This yielded calculated areas from the parallel radius of the gel that were greater in magnitude than those calculated from the perpendicular radius, though beyond this point there was a cross-over in magnitude of these two lengths (Figure 3.39). Surprisingly, there was also a second cross-over point at 100 minutes, after the self-assembled material had dissolved back into solution (Figure 3.40). The remaining polymer assumed a flatter shape than the supramolecular gel before it, with the theoretical cross-sectional area calculated from the gel height that was significantly lower (and more like the actual recorded cross-sectional area) than that of its recorded width (Figure 3.40). The shape of the polymeric material was reminiscent of that of the first 20 seconds of observed gel growth (Figure 3.39), which suggests that the diffusion of incoming Carb-Ala (and subsequent build-up of polymer at the Pt surface) was more linear than hemispherical.

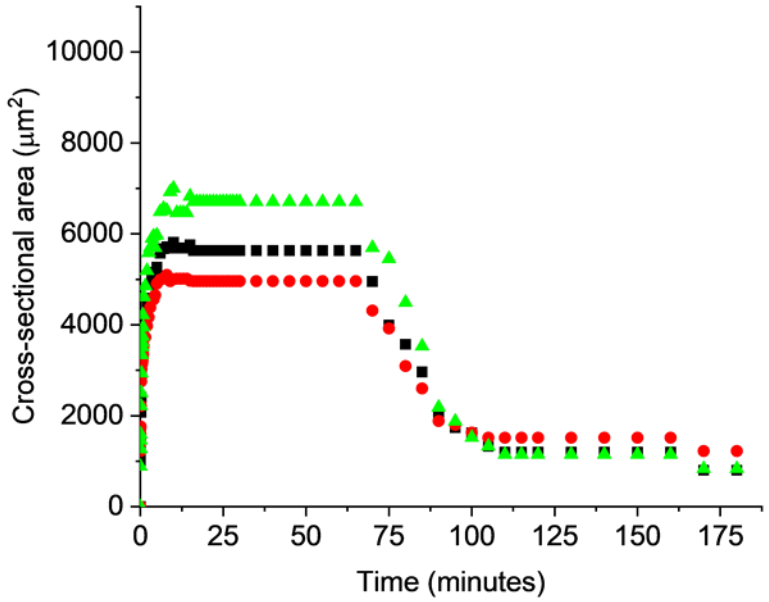

Figure 3.40 3 hours (10800 seconds) potentiostatic Carb-Ala gel growth at a Pt microelectrode (25 µm diameter) in 5 mL 10 mg/mL Carb-Ala gelator solution (pH 8), 1.0 V, T = 25 °C. Gel cross-sectional area (black squares), and calculated cross-sectional areas (Equation 3.4) using gel width (red circles) and height (green triangles) are plotted together.

3.5 Summary

Electrochemical growth of Carb-Ala hydrogels through the potentiostatic oxidation of hydroquinone as an electrochemical acid trigger has been explored at Pt surfaces, primarily at single 25 µm diameter disc Pt microelectrodes. The principles of potentiostatic control of hydrogel growth have been established here, with a demonstration of the control over which redox active species undergo electrochemistry. The oxidation and polymerisation of the Carb-Ala gelator can be selectively included under this methodology, and water splitting and the evolution of O_2 gas (which would otherwise introduce inhomogeneity into final gel structures) has been avoided. This has been achieved by controlling the time a fixed potential is applied for and the potential applied during potentiostatic gel growth. The dimensions of these hydrogels and their ability to slow the flow of electroactive species are particular properties which were both shown to be tuneable.

Optical microscopy under visible light has been employed to measure the widths, heights and cross-sectional areas of the Carb-Ala hydrogels, whilst EIS has been used to understand the internal structure of these hydrogels. The modified Randles circuit used in this study models the electrochemical processes occurring at single microelectrodes from raw Nyquist plot data. From estimated Y_0 and R_{NL} values, diffusion coefficients were extracted, which provided information on the extent to which the transport of a FFC electrochemical probe was affected with the presence of hydrogel at the microelectrode surfaces. This in turn informed on the controllable densities of electrochemical hydrogels achievable under potentiostatic control.

When applying 0.7 V at single Pt disc microelectrodes, a potential that would achieve mass-transport limited currents due to hydroquinone oxidation, longer periods of continued electrochemical hydroquinone oxidation allowed for the formation of larger, denser Carb-Ala hydrogels. Hydrogels grown by applying potentials of 0.6 V or 0.7 V for time periods of 120 seconds were indistinguishable, though when fixing potentials above the oxidation potential of the Carb-Ala gelator, this enabled the polymerisation of the gelator to compete with the oxidation of hydroquinone. At these short 120 second time periods, this had no effect on the density of the hydrogels. However, Carb-Ala hydrogels grown at 1.0 V showed a noticeable reduction in size in comparison to those grown at 0.6 V and 0.7 V, as a result of the formation of polymer passivating the electrode surface.

A new hemispherical feature found within the recorded Nyquist plots for 1.0 V gel-coated microelectrodes suggests that some additional electrochemical process has been unaccounted for in the equivalent circuit model used in this work. The inclusion of such a process as new components into a new equivalent circuit model would require strong theoretical justification in order to be presented here, a task that is beyond the scope of this work. Despite this, the modified Randles circuit used here has still proven to be a useful tool to understand relative changes in hydrogel density that develop during potentiostatic growth at microelectrode surfaces.

In addition to observing these hydrogels *ex situ* and recording their properties post-experiment, a system was constructed to enable the continuous visual and electrochemical monitoring of supramolecular hydrogel growth at single Pt microelectrodes *in situ*. By pairing

visual recordings under microscopy with the corresponding current-time transient, valuable information on how hydrogel growth proceeds over time was obtained. When applying 0.7 V, a Carb-Ala gel was found to reach a maximum cross-sectional area after approximately 16 minutes, then retained this size for a further 5 minutes before shrinking slightly, and remained in these new dimensions for the remaining duration of a 3 hour gel growth experiment. Unexpectedly, this Carb-Ala hydrogel was discovered to undergo a change in opacity over the period of this 3 hour experiment under constant applied potential. This change occurred non-uniformly, starting from the outermost edge of the gels towards the electrode surface. This indicated changes in gel structure due to a dynamic process, between gelator self-assembly driven by proton flux, and gelator deprotonation and dissolution driven by bulk solution flux.

This observed visual change was understood to be a loss of gel mass over time, rather than a realignment of the supramolecular network. This theory was compounded by further observations in a similar experiment, conducted by applying 1.0 V to the Carb-Ala gelator solution. A hydrogel was grown to a maximum cross-sectional area after a period of 10 minutes, however passivation through polymer build-up (evident from a drop in oxidation current to zero after 1 hour of continued potentiostatic gel growth at 1.0 V) prevented any continued hydroquinone oxidation beyond this timeframe. This led to the neutralisation of the proton diffusion zone (restoring conditions where the pH was greater than pK_a^{app} of the gelator), which sped up the visual change in gel opacity, and furthermore allowed the supramolecular gel to dissolve. Interestingly however, there was not complete dissolution, but rather a stable gel remained at the electrode surface, which presents the potential for gel formation and polymerisation to give a stable gel layer resistant to dissolution above the pK_a^{app}.

Multiple visual observations in this work provide insight towards a degree of inhomogeneity within these potentiostatically-grown hydrogels: the dynamic process of gelator self-assembly and gel disassembly, the near-hemispherical shapes of these hydrogels, and the discrepancy between theoretical expansion of the acidic volume and real hydrogel dimensions all contribute to a new understanding of these materials. When combined with an increased separation between D_L and D_{NL} with increasing gel growth time, these observations suggest that the potentiostatically-grown hydrogels possess networks of self-assembled structures that are most dense at the electrode surface, and that diminish in density (on the microscale) further from the electrode surface.

With these initial studies completed, it was now possible to control Carb-Ala hydrogel growth and predict the final properties of the microelectrodes they were grown upon. Further work could now commence in applying these hydrogels to biosensing applications as anti-biofouling membranes.

3.6 References

1 E. R. Cross, K. McAulay and D. J. Adams, in *Polypeptide Materials*, ed. M. G. Ryadnov, Humana, New York, 2021, pp. 179–188.

2 E. K. Johnson, D. J. Adams and P. J. Cameron, Directed Self-Assembly of Dipeptides to Form Ultrathin Hydrogel Membranes, *J. Am. Chem. Soc*, 2010, **132**, 5130–5136.

3 M. Quan, D. Sanchez, M. F. Wasylkiw and D. K. Smith, Voltammetry of quinones in unbuffered aqueous solution: Reassessing the roles of proton transfer and hydrogen bonding in the aqueous electrochemistry of quinones, *J. Am. Chem. Soc.*, 2007, **129**, 12847–12856.

4 E. R. Draper and D. J. Adams, Low-Molecular-Weight Gels: The State of the Art, *Chem*, 2017, **3**, 390–410.

5 D. J. Adams, M. F. Butler, W. J. Frith, M. Kirkland and P. Sanderson, A new method for maintaining homogeneity during liquid – hydrogel transitions using low molecular weight hydrogelators †, 2009, 1856–1862.

6 E. R. Cross, The electrochemical fabrication of hydrogels: a short review, *SN Appl. Sci.*, 2020, **2**, 1–11.

7 Y. Liu, Y. Cheng, H. Wu, E. Kim, R. V Ulijn, G. W. Rubloff, W. E. Bentley and G. F. Payne, Electroaddressing Agarose Using Fmoc-Phenylalanine as a Temporary Scaffold, *Langmuir*, 2011, **27**, 7380–7384.

8 Y. Liu, E. Kim, R. V Ulijn, W. E. Bentley and G. F. Payne, Reversible Electroaddressing of Self-assembling Amino-Acid Conjugates, *Adv. Funct. Mater.*, 2011, **21**, 1575–1580.

9 E. K. Johnson, L. Chen, P. S. Kubiak, S. F. Mcdonald, D. J. Adams and P. J. Cameron, Surface nucleated growth of dipeptide fibres, *Chem. Commun.*, 2013, **49**, 8698–8700.

10 J. Raeburn, B. Alston, J. Kroeger, T. O. McDonald, J. R. Howse, P. J. Cameron and D. J. Adams, Electrochemically-triggered spatially and temporally resolved multi-component gels, *Mater. Horizons*, 2014, **1**, 241–246.

11 P. S. Kubiak, S. Awhida, C. Hotchen, W. Deng, B. Alston, T. O. McDonald, J. Adams and P. J. Cameron, Polymerization of low molecular weight hydrogelators to form electrochromic polymers, *Chem. Commun.*, 2015, **51**, 10427–10430.

12 K. Ino, A. Tamura, K. Hiramoto, M. T. Fukuda, Y. Nashimoto and H. Shiku, Electrodeposition of thiolated polymer-based hydrogels via disulfide formation using electrogenerated benzoquinone, *Chem. Lett.*, 2020, 1–5.

13 S. Selmani, E. Schwartz, J. T. Mulvey, H. Wei, A. Grosvirt-Dramen, W. Gibson, A. I. Hochbaum, J. P. Patterson, R. Ragan and Z. Guan, Electrically Fueled Active Supramolecular Materials, *J. Am. Chem. Soc.*, 2022, **144**, 7844–7851.

14 C. Patterson, B. Dietrich, C. Wilson, A. R. Mount and D. Adams, Electrofabrication of large volume di- and tripeptide hydrogels via hydroquinone oxidation, *Soft Matter*, 2022, **18**, 1064–1070.

15 A. Piper, B. M. Alston, D. J. Adams and A. R. Mount, Functionalised microscale

nanoband edge electrode (MNEE) arrays: the systematic quantitative study of hydrogels grown on nanoelectrode biosensor arrays for enhanced sensing in biological media, *Faraday Discuss.*, 2018, **210**, 1–17.

16 C. M. A. Brett and A. M. O. Brett, *Electroanalysis*, Oxford University Press Inc., New York, 1st edn., 1998.

17 A. C. Fisher, *Electrode Dynamics*, Oxford University Press Inc., New York, 1st edn., 1996.

18 R. J. Forster, Microelectrodes : New Dimensions in Electrochemistry, *Chem. Soc. Rev.*, 1994, **23**, 289–297.

19 C. Amatore, C. Pebay, L. Thouin, A. Wang and J. Warkocz, Difference between Ultramicroelectrodes and Microelectrodes : Influence of Natural Convection, *Anal. Chem.*, 2010, **82**, 6933–6939.

20 P. N. Bartlett and D. J. Caruana, Electrochemical immobilization of enzymes part V.* Microelectrodes for the detection of glucose based on glucose oxidase immobilized in a poly(phenol) film, *Analyst*, 1992, **117**, 1287–1292.

21 W. Jia, K. Wang and X. Xia, Elimination of electrochemical interferences in glucose biosensors, *Trends Anal. Chem.*, 2010, **29**, 306–318.

22 V. Lakshminarayanan, L. Poltorak, E. J. R. Sudhölter, E. Mendes and J. van Esch, Electrochemically assisted hydrogel deposition, shaping and detachment, *Electrochim. Acta*, 2020, **350**, 136352–136362.

23 E. R. Draper and D. J. Adams, Controlling the Assembly and Properties of Low-Molecular-Weight Hydrogelators, *Langmuir*, 2019, **35**, 6506–6521.

24 J. D. Roberts and M. C. Caserio, in *Basic Principles of Organic Chemistry*, Addison-Wesley, Menlo Park, California, 2nd edn., 1977, pp. 1287–1341.

25 Y. Saito, A Theoretical Study on the Diffusion Current at the Stationary Electrodes of Circular and Narrow Band Types, *Rev. Polarogr.*, 1968, **15**, 177–187.

26 L. A. Estroff and A. D. Hamilton, Water Gelation by Small Organic Molecules, *Chem. Rev.*, 2004, **104**, 1201–1217.

27 J. Schindelin, I. Arganda-Carreras, E. Frise, V. Kaynig, M. Longair, T. Pietzsch, S. Preibisch, C. Rueden, S. Saalfeld, B. Schmid, J. Y. Tinevez, D. J. White, V. Hartenstein, K. Eliceiri, P. Tomancak and A. Cardona, Fiji: An open-source platform for biological-image analysis, *Nat. Methods*, 2012, **9**, 676–682.

28 A. J. Bard and L. R. Faulkner, *Electrochemical Methods: Fundamentals and Applications*, John Wiley & Sons, New York, 2nd ed., 2001, vol. 677.

29 N. Agmon, The Grotthuss mechanism, *Chem. Phys. Lett.*, 1995, **50**, 456–462.

30 P. Los, G. Zabinska, A. Kisza, L. Christie, A. Mount and P. G. Bruce, Electrochemical studies of heterogeneous reduction of tetracyanoquinodimethane in poly (ethylene oxide) electrolytes using ac impedance and cyclic voltammetry at an ultramicroelectrode, *Phys. Chem. Chem. Phys.*, 2000, **2**, 5449–5454.

31 H. L. Woodvine, J. G. Terry, A. J. Walton and A. R. Mount, The development and characterisation of square microfabricated electrode systems, *Analyst*, 2010, **135**, 1058–1065.

32 S. J. Konopka and B. Mcduffie, Diffusion Coefficients of Ferri- and Ferrocyanide Ions in Aqueous Media , Using Twin-Electrode Thin-Layer Electrochemistry IqT, *Anal. Chem.*, 1970, **42**, 1741–1746.

33 B. Roffel and J. J. van de Graaf, The Diffusion Coefficient of Ferricyanide Ions in Aqueous Potassium Chloride Solutions with and without Polyethylene Oxide Addition, *J. Chem. Eng. Data*, 1977, **22**, 300–302.

34 J. Heinze, Ultramicroelectrodes in Electrochemistry, *Angew. Chem. - Int. Ed.*, 1993, **32**, 1268–1288.

35 C. Amatore, S. Szunerits, L. Thouin and J.-S. Warkocz, The real meaning of Nernst's steady diffusion layer concept under non-forced hydrodynamic conditions . A simple model based on Levich ' s seminal view of convection, *J. Electroanal. Chem.*, 2001, **500**, 62–70.

Chapter 4 – Investigating the stability of electrochemical supramolecular hydrogels

4.1 Introduction

As outlined in the introduction chapter to this thesis, an intended application for potentiostatically-grown Carb-Ala hydrogels is in electrochemical biosensing, as anti-fouling layers and membranes that could be used to trap or encapsulate enzymes. Galvanostatically-grown Carb-Ala hydrogels have previously been applied as anti-fouling layers on a DNA biosensor,[1] which gives strong support for further study of this system and for application in other biosensing applications. Study with regards to maintaining enzyme stability should be considered when using this material, but consideration must also be given to maintaining hydrogel structural integrity. Membrane degradation is a prominent issue with polymerised gels,[2,3] so it stands to reason that matrices constructed with self-assembled structures could be even more susceptible to the effect, may readily fail to prevent fouling, and leak encapsulated enzymes with time.

In Chapter 3 Section 3.4.6, Carb-Ala hydrogels grown at Pt disc microelectrodes were found to be structurally unstable within the pH 8 gelator solutions without the maintenance of a local acidic pH gradient due to electrochemical hydroquinone oxidation. This is not surprising, as the pK_a^{app} of Carb-Ala is approximately 6 (Chapter 2 Section 2.3.1), meaning that gelator deprotonation and subsequent network disassembly is likely to occur when the current falls below a critical value such that the electrochemically-generated volume in which the pH is lower than 6 at the electrode is not maintained. Johnson *et al.* have also observed this effect by using surface plasmon resonance, noting that when turning the hydroquinone oxidation current off in their experiments, the thickness of their electrochemically-grown supramolecular hydrogels reduced over time.[4] Wu *et al.* found that, when writing with an electrode pen into a polysaccharide gel to generate local formation of protons and thus induce self-assembly of chitosan, the stability of the gels dropped after the generated pH gradients had dissipated into the surrounding medium.[5] Therefore, maintaining the pH within these electrochemical pH-triggered hydrogels below gelator pK_a^{app} is necessary in order to keep their supramolecular networks assembled.

Maintaining a single gel internal pH below the gelator pK_a^{app} after electrodeposition will likely severely limit the application of these materials only to mildly acidic environments. Therefore, if electrochemical supramolecular hydrogels are to be seriously considered for practical biomedical applications, the stability of these materials in specific environments of varying pH should be tested thoroughly. A typical buffered medium used to test enzymatic biosensors in is phosphate-buffered saline (PBS) solution (pH range 7.35-7.45), as it simulates the typical pH range of biological media such as human whole blood (7.35-7.45) and interstitial fluid (7.2-7.4).[6] Exposing the Carb-Ala hydrogels presented in Chapter 3 to PBS should shift the equilibrium of gelator protonation towards deprotonation, which in turn would cause the aggregated structures holding the gel together to destabilise due to increasing repulsive electrostatic forces between negatively charged aggregates, and then through disassembly of

the gelator units.[7,8] Therefore, the pH range of PBS is likely not one that would be suitable for testing an electrode or electrochemical biosensor functionalised with these hydrogels.

It is for this reason that Piper *et al.* chose to record EIS measurements of their gel-coated electrodes in a pH 4.3 trisaminomethane hydrochloride buffer solution (containing a 1 M FFC redox couple).[1] This buffer was chosen to avoid this hydrogel disassembly and to give the sensor the best chance of stability for this biosensing test. Piper *et al.* then demonstrated the ability of the electrochemically-grown Carb-Ala hydrogel to prevent short term biofouling at Pt nanoelectrodes.[1] However, a study of the long-term stability of these supramolecular hydrogels at micro/nanoelectrode surfaces in such mildly acidic aqueous media has yet to be conducted. This chapter therefore presents an exploration into the stability of electrochemically grown hydrogels in various aqueous media, to determine when these hydrogels can be considered to be suitable membranes for biosensing.

4.2 Supramolecular hydrogel stability in pH 4.3 citric acid/trisodium citrate buffer solutions

4.2.1 Carb-Ala gels grown at Pt disc microelectrodes

Repeating the experimental method first established in Chapter 3, a Carb-Ala hydrogel was formed within a 10 mg/mL Carb-Ala solution at a 25 µm diameter Pt disc microelectrode by applying 0.7 V for 120 seconds (Figure 4.1). The current-time transient and cumulative charge corresponding to electrochemical hydroquinone oxidation were consistent with previous observations for these experimental conditions (see Table 3.12, Chapter 3 Section 3.4.5). Due to the controlled conditions set for gel growth and the correspondence within experimental error to previous data, it was assumed with high confidence that this hydrogel possessed physical dimensions that matched previous measurements for the 0.7 V, 120 second hydrogels produced and discussed in Section 3.4.5.

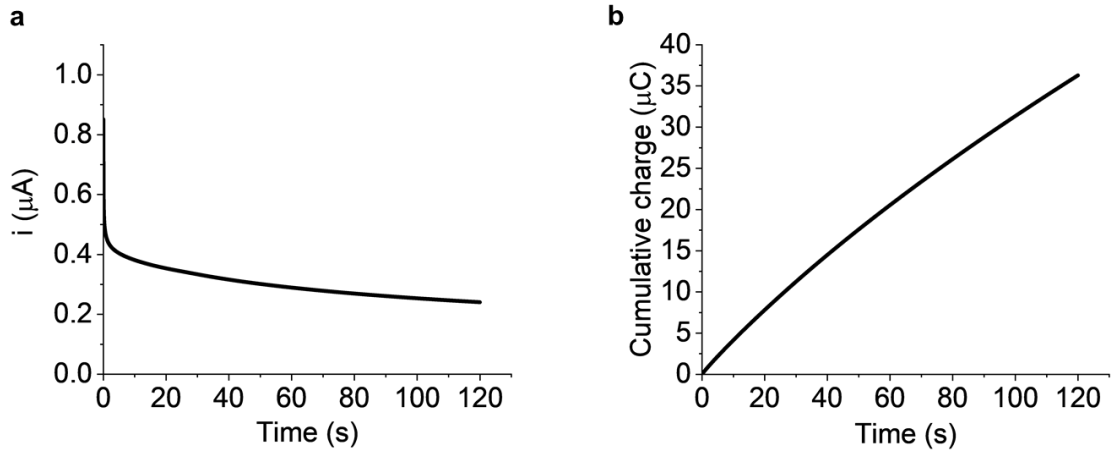

Figure 4.1 Current-time transient (a) and charge-time transient (b) (calculated by integrating area under current-time transients in (a)), recorded in 10 mL 10 mg/mL Carb-Ala gelator solution (pH 8) containing hydroquinone (67.5 mM) and NaCl (1 mM), at Pt microelectrode (25 µm diameter), 120 seconds at 0.7 V (stepped from open circuit potential), T = 25 °C.

The now gel-coated WE was then transferred to a pH 4.3 buffered ferrocyanide solution (Chapter 2 Section 2.4.4). Immediately after the electrode was introduced to the solution (denoted as t = 0 minutes), multiple EIS experiments were conducted sequentially, using the three-electrode system (fixed DC potential set at the formal potential for the FFC redox pair, found using DPV, Chapter 2 Section 2.2.5), with 10 minute spacing between initial EIS start times. The resulting Nyquist plots were fitted to the modified Randles circuit (Figure 2.11, Chapter 2 Section 2.2.6) using the procedure established in Chapter 3 Section 3.3, by determining and subsequently fixing the R_S component, and fitting without the weight factor in the Nova software. Figure 4.2 shows these Nyquist plots and fits as a function of time. Diffusion coefficients D_L and D_{NL} (calculated using Equations 2.29 and 2.31, Chapter 2 Section 2.2.7) for each Nyquist plot are tabulated below (Table 4.1).

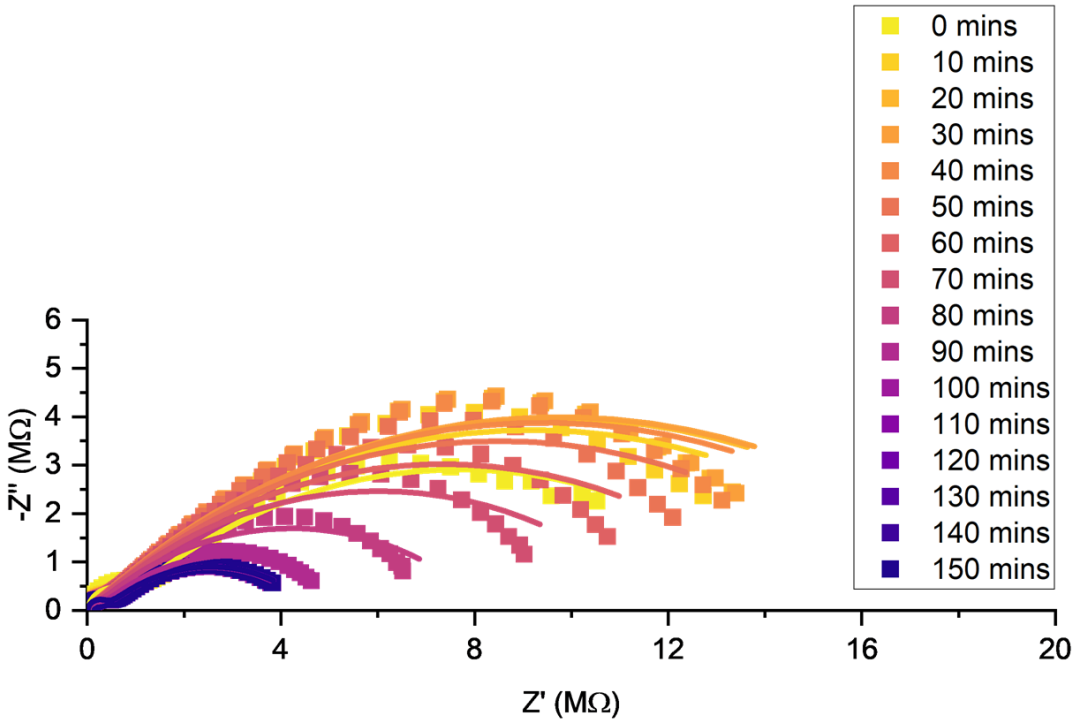

Figure 4.2 Nyquist plots of potentiostatic Carb-Ala gel coated (0.7 V, 120 seconds) Pt microelectrode (25 µm diameter) in pH 4.3 buffered ferrocyanide solution during EIS, T = 25 °C. Scatter points represent recorded impedance, lines represent unweighted fitted data with R_S values fixed to the weighted R_S values using the modified Randles circuit (Figure 2.11, Chapter 2 Section 2.2.6). Colour gradient of lighter to darker plots corresponds to increasing times of continued submersion of the gel-coated microelectrode in ferrocyanide solution.

Table 4.1 Y_0 and R_{NL} values, along with respective diffusion coefficients D_L and D_{NL}, obtained from fitted EIS data (and estimated errors) of Carb-Ala gel-functionalised Pt disc microelectrode (25 µm diameter) without weight factor applied (as shown in Figure 4.2), recorded at different time periods of continued submersion in pH 4.3 buffered ferrocyanide solution. D_L and D_{NL} values calculated using Equation 2.29 and Equation 2.31 respectively (Chapter 2 Section 2.2.7).

Time (minutes)	Y_0 (nS)	R_{NL} (MΩ)	D_L ($\times 10^{-10}$ m^2 s^{-1})	D_{NL} ($\times 10^{-10}$ m^2 s^{-1})
0	42.6 ± 1.1	14.0 ± 0.2	0.855 ± 0.042	1.52 ± 0.02
10	34.2 ± 1.5	17.9 ± 0.4	0.550 ± 0.047	1.19 ± 0.03
20	31.3 ± 1.4	19.0 ± 0.5	0.460 ± 0.041	1.12 ± 0.03
30	30.8 ± 1.4	19.2 ± 0.5	0.445 ± 0.041	1.11 ± 0.03
40	31.9 ± 1.8	18.6 ± 0.5	0.480 ± 0.053	1.15 ± 0.03
50	32.5 ± 1.8	16.7 ± 0.4	0.495 ± 0.056	1.27 ± 0.03
60	34.4 ± 1.9	14.5 ± 0.4	0.556 ± 0.061	1.47 ± 0.04
70	36.3 ± 2.0	11.8 ± 0.3	0.619 ± 0.069	1.81 ± 0.04
80	41.5 ± 1.6	8.12 ± 0.13	0.808 ± 0.064	2.62 ± 0.04
90	63.0 ± 1.2	5.44 ± 0.05	1.87 ± 0.07	3.91 ± 0.03
100	90.6 ± 0.9	4.30 ± 0.02	3.86 ± 0.07	4.95 ± 0.02
110	90.0 ± 1.0	4.35 ± 0.02	3.81 ± 0.08	4.90 ± 0.02
120	89.8 ± 1.0	4.35 ± 0.02	3.79 ± 0.08	4.89 ± 0.03
130	89.7 ± 1.0	4.35 ± 0.02	3.78 ± 0.08	4.89 ± 0.03
140	89.7 ± 1.0	4.35 ± 0.02	3.78 ± 0.08	4.90 ± 0.03
150	89.8 ± 1.0	4.34 ± 0.02	3.79 ± 0.09	4.91 ± 0.03

Surprisingly, a statistically significant decrease in Y_0 and increase in R_{NL} can be seen over the first 30 minutes of the experiment, from 42.6 nS to 30.8 nS and 14.0 MΩ to 19.2 MΩ respectively (Table 4.1). Translating these values to diffusion coefficients, this equates to decreases in D_L and D_{NL}, from 0.86×10^{-10} m^2 s^{-1} to 0.45×10^{-10} m^2 s^{-1} and from 1.52×10^{-10} m^2 s^{-1} to 1.11×10^{-10} m^2 s^{-1} respectively. Practically, this decrease in redox couple transport suggests an increase in hydrogel density shortly after the electrodes are introduced to the new buffered environment. This may indicate a change in structure and densification of the supramolecular network as the gel accommodates to the new environment.

Beyond this initial 30 minutes, R_{NL} begins to decrease and Y_0 to increase with time and reach constant values at t = 100 minutes. The experiment was ceased at the 150 minute mark, once the Y_0 and R_{NL} values had been established as being invariant with time, reaching maximum and minimum values of 89.8 nS and 4.34 MΩ respectively (Table 4.1). At t > 100 minutes, D_L and D_{NL} values for this gel-coated microelectrode were calculated to be 3.86×10^{-10} m^2 s^{-1} and 4.95×10^{-10} m^2 s^{-1} respectively. D_L and D_{NL} values characteristic for the bare Pt disc microelectrodes were previously calculated as 4.71 ± 0.78 and $6.10 \pm 0.27 \times 10^{-10}$ m^2 s^{-1} respectively (Chapter 3 Section 3.4.5). The changes in D_L and D_{NL} values observed here at the gel-coated microelectrode were gradual, and though the final values were much closer to these bare electrode values, they were not equal to nor appear to approach those values at

the end of the experiment (Table 4.1). This indicates that the increase in these diffusion coefficients from the 30 minute to 100 minute timeframe was not due to a sudden detachment of the gel from the electrode surface, but a gradual change in the structure of the gel. It is also interesting to see that the lower frequency range of the earlier scans (from 10 minutes to 80 minutes of submersion) are poorly fit to the real impedance data (Figure 4.2), whilst at later times this model fits better to the real data. The modified Randles circuit (Figure 2.11, Chapter 2 Section 2.2.6) appears not to be an ideal model for the gel-coated electrodes, though suitable changes/additions to the model have not been identified in this work.

To accompany this EIS data, the experiment was repeated by examining a second Carb-Ala gel (grown under the same conditions as the previous one) within a pH 4.3 buffer solution (0.1 M citric acid/trisodium citrate, without potassium ferrocyanide) for the same duration. Images were recorded under the microscope in 10 minute intervals, starting from t = 0 minutes (immediately after insertion of the electrode into solution, Figure 4.3).

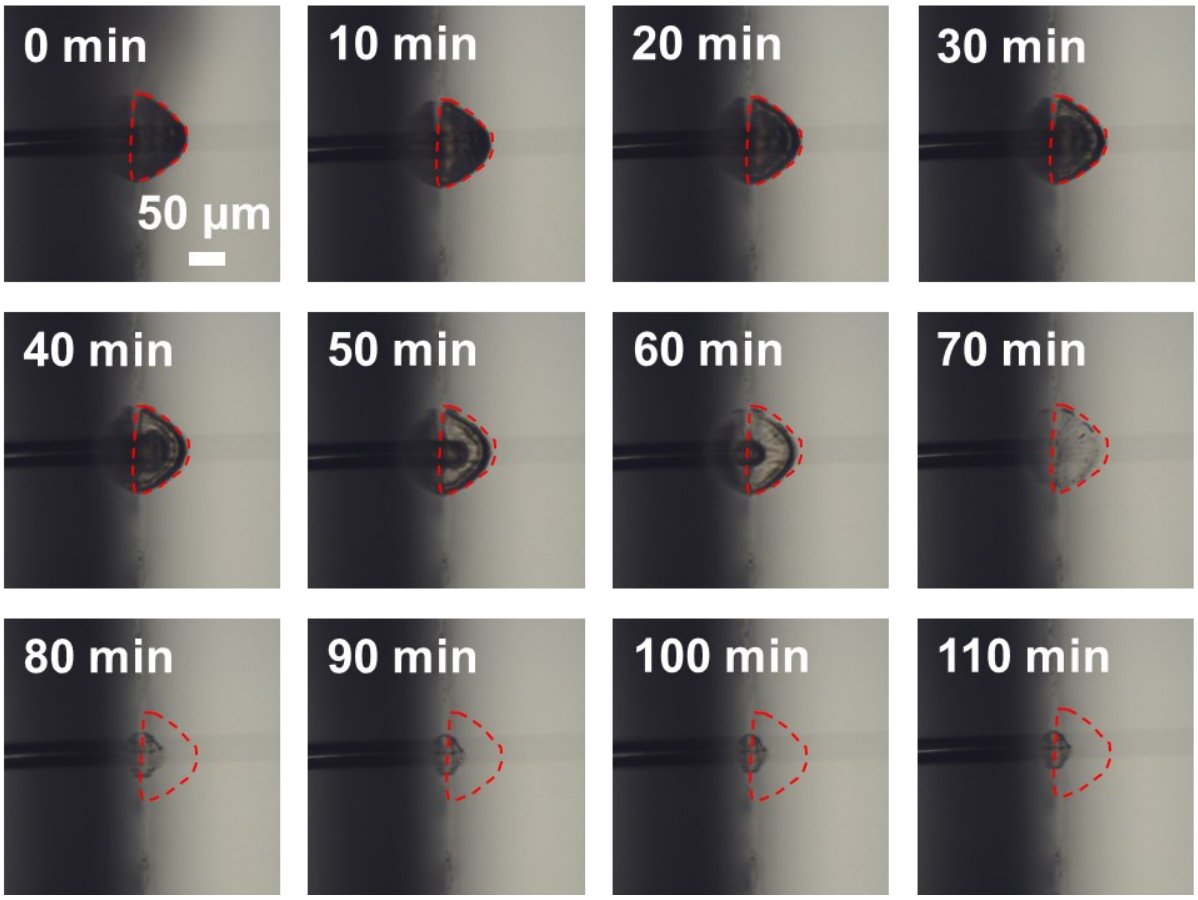

Figure 4.3 Images of Carb-Ala hydrogel at Pt microelectrode surface (25 µm) submerged in 0.1 M citric acid/trisodium citrate buffer (pH 4.3), side-on view, 100x magnification, post 0.7 V 120 second potentiostatic gel growth experiment. From top left to bottom right, in intervals of 10 minutes (from 0 minutes to 110 minutes). A red dashed line corresponding to the cross-section of the original gel at 0 minutes is displayed in each image. Note a gradual increase in transparency up to the 70 minute mark, followed by a significant decrease in gel size at 80 minutes.

Over the first 30 minutes, slight changes in opacity were observed. What appeared to be a darker "inner" layer slowly shrank towards to the electrode surface, becoming most pronounced in the image recorded at t = 20 minutes (Figure 4.3). From 30 minutes onwards, the shrinkage of this darker (presumably denser) layer continued until disappearing in the image recorded at 70 minutes, leaving a far more transparent structure. This structure then appeared to collapse in the image recorded at 80 minutes, and then retained an approximately constant size for the remaining duration of the experiment. These visual changes are consistent with those previously observed during long periods of potentiostatic gel growth within the pH 8 gelator solution, where a dynamic process between gel growth and gel dissolution was seen to tip in the favour of the latter mechanism (Chapter 3 Sections 3.5.6 and 3.5.11). This had occurred as the rate of electrochemical hydroquinone oxidation had reached a minimum or had ceased, which allowed the pH gradient to diminish as the high pH environment disassembled the gel structure. The similarities in visual observations between gels in this experiment and those in Section 3.4.6 and 3.4.11, coupled with EIS data, suggest that the process occurring in the pH 4.3 buffer is a similar one to that observed in the gelator solution. Again, this is an unexpected observation when the pH of the new buffered environment is below the Carb-Ala gelator pK_a^{app}.

The EIS and the microscopy experiments presented above were each repeated four more times (for a total of five), in order to determine the reproducibility of the observed phenomena. The cross-sectional area of the resulting gels' outer dimensions and darker (understood to be denser) inner component, as well as diffusion coefficients D_L and D_{NL}, are plotted together against time spent submerged in the pH 4.3 buffered solution (Figure 4.4). Both diffusion coefficients increased in magnitude over time from 30 minutes, with the highest rate occurring from 40 minutes to 100 minutes. At 110 minutes, D_L and D_{NL} reached maximum values for the remainder of the experiment, 3.92 ± 0.27 and $5.09 \pm 0.27 \times 10^{-10}$ m^2 s^{-1} respectively. Whilst these gels had significantly diminished in size in the buffer solution, they still inhibited the flow of the FFC redox pair to an extent after shrinking to this minimum size, as these D_L and D_{NL} values were relatively close but not identical to those calculated for the bare electrodes of 4.71 ± 0.78 and $6.10 \pm 0.27 \times 10^{-10}$ m^2 s^{-1} respectively. This suggests that the transport of the FFC redox couple was only slightly inhibited by the presence of residual gel by the end of these experiments.

The depletion of the darker, inner component of the hydrogel consistently preceded significant shrinkage of the entire gel structure. The completion of this first process occurred on average 60 minutes after submersion into the buffer solution (Figure 4.4). The loss of the inner layer began upon submersion, with a near linear rate of shrinkage in area estimated as approximately 1.35 μm^2 s^{-1} over the first 30 minutes. The outer hydrogel dimensions appeared to remain mostly unchanged in the initial 40 minutes. The rate of gel shrinkage then increased significantly at a loss of 1.44 μm^2 s^{-1} between 40 and 80 minutes after submersion into the buffer. Each of the Carb-Ala gels approached a minimum size rather than dissipating entirely. Rate of shrinkage decreased to approximately 0.03 μm^2 s^{-1} from 110 to 150 minutes, and at the end of the experiment the cross-sectional area of remaining material averaged 376 ± 87 μm^2.

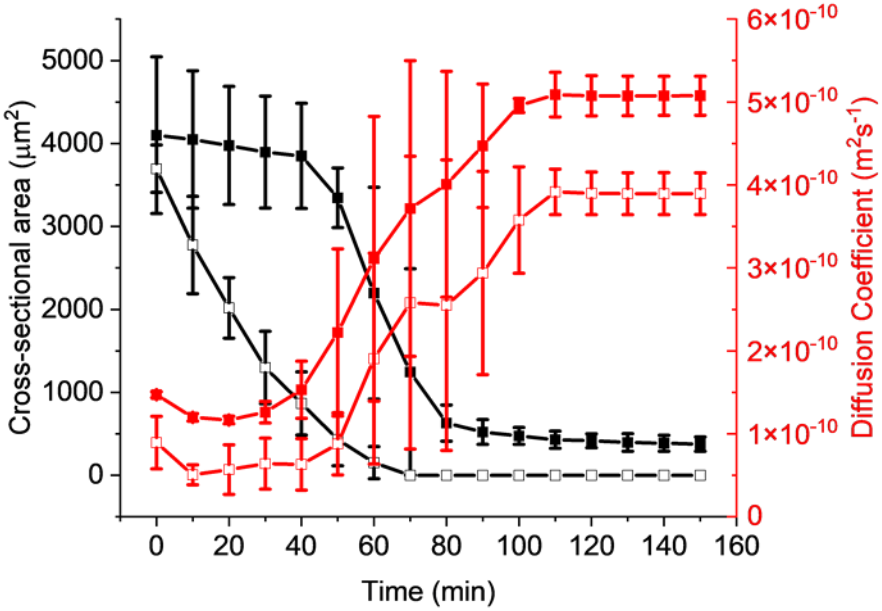

Figure 4.4 Compiled data of changing Carb-Ala gel cross-sectional area and microelectrode diffusion coefficients at gel-functionalised Pt disc microelectrodes (25 µm diameter) with time when submerged in 0.1 M citric acid/trisodium citrate buffer (pH 4.3), T = 25 °C. Sample size of electrodes observed under microscopy and under EIS to obtain these data sets numbered five each. Squares denote average values, respective error bars denote standard deviations. Black squares (filled) = gel-cross sectional area (outer dimensions), black squares (hollow) = gel-cross sectional area (inner dimensions), red squares (filled) = D_{NL}, red squares (hollow) = D_L.

It is also noteworthy that over the first 20 minutes average D_L decreased from 0.89 ± 0.32 to 0.57 ± 0.30 × 10^{-10} m^2 s^{-1}, and D_{NL} decreased from 1.47 ± 0.04 to 1.20 ± 0.05 × 10^{-10} m^2 s^{-1} (Figure 4.4). Though the high standard deviation of the D_L values across the five electrodes suggests that these values could be the same in this timeframe, the decrease in average D_{NL} is a significant change, which again suggests that each of the five gels increased in density during this timeframe: particularly, at long distances from the Pt surface.

To summarise, the shrinkage and loss of the hydrogel, along with an overall increase in redox couple transport over time during submersion into the pH 4.3 buffer, were both consistently occurring phenomena. Neither of these effects have been noted in previous work on this system, which warrants further study into how they occur, and to determine if this this case is isolated to this specific system. The next Sections in this Chapter aim to cover this ground.

4.2.2 Carb-Ala gels grown at Pt disc macroelectrodes

As Carb-Ala hydrogels grown at macroelectrode surfaces may experience the same but previously unidentified effects in the pH 4.3 citric acid/trisodium citrate buffer solution, an equivalent set of measurements was carried out at a macroelectrode. Baseline EIS measurements were first collected for a set of five bare 2 mm diameter Pt disc macroelectrodes (Figure 4.5). The standard Randles circuit (Figure 2.9, Chapter 2 Section 2.2.6)[9] was used to model the electrochemical processes occurring at the Pt macroelectrodes,

and the EIS data for each electrode were fitted to this equivalent circuit to obtain R_S, C_{DL}, R_{CT}, and Y_0 values and respective fit errors (Table 4.2). Linear diffusion coefficients for the redox pair, D_L, were obtained from respective Y_0 values. As with the microelectrode EIS data, the estimated values were obtained using the established fitting process, without an applied weight factor in the Nova software, and by fixing R_S values to weighted estimations that give more weight to data at high frequency.

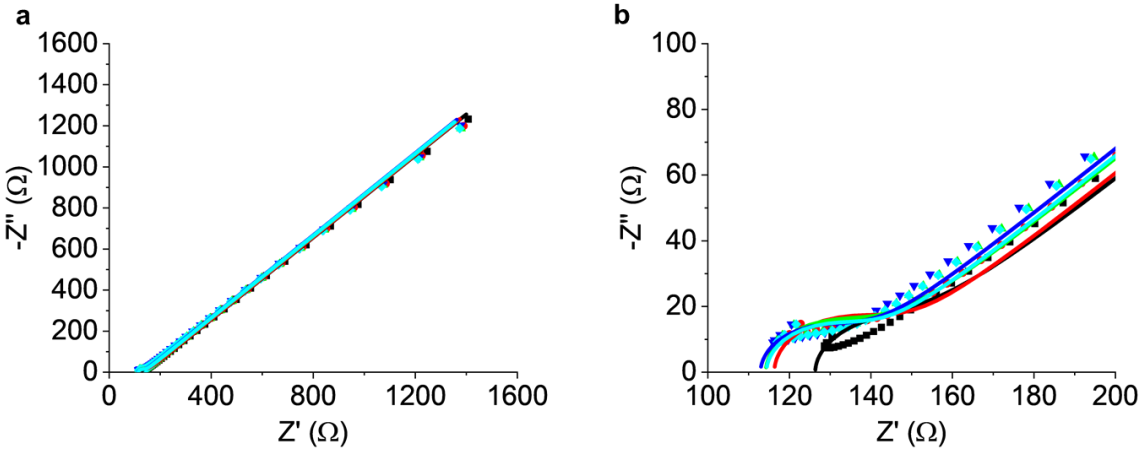

Figure 4.5 Nyquist plots of bare Pt macroelectrodes (2 mm diameter) in pH 4.3 buffered ferrocyanide solution during EIS, T = 25 °C. (a) Full range and (b) windowed range showing closeness of plot and fit overlap in high frequency range. Scatter points represent recorded impedance, solid lines represent unweighted fitted data using the Randles circuit (Figure 2.11, Chapter 2 Section 2.2.6) with R_S values fixed to the weighted R_S values: black squares = electrode 1, red circles = electrode 2, green triangles (up) = electrode 3, blue triangles (down) = electrode 4, teal diamonds = electrode 5.

Table 4.2 Nyquist plot data and estimated errors for bare 2 mm diameter Pt disc electrodes. Features fitted EIS data of bare macroelectrodes with R_S values fixed (italicised) without weight factor applied (as shown in Figure 4.5) to the Randles circuit (Figure 2.11, Chapter 2 Section 2.2.6). D_L values calculated using Equation 2.29 (Chapter 2 Section 2.2.7).

2 mm diameter Pt disc macroelectrodes, weight factor off, fixed R_S					
Component	**1**	**2**	**3**	**4**	**5**
R_S (Ω)	*126*	*116*	*114*	*113*	*114*
C_{DL} (nF)	2100 ± 450	939 ± 204	1050 ± 270	926 ± 239	929 ± 244
R_{CT} (Ω)	21.8 ± 2.0	26.6 ± 1.8	24.2 ± 2.0	21.9 ± 1.8	22.8 ± 1.9
Y_0 (μS)	711 ± 2	724 ± 2	728 ± 2	726 ± 2	732 ± 2
χ^2	0.0155	0.0215	0.0267	0.0214	0.0240
D_L ($\times 10^{-10}$ m^2 s^{-1})	5.80 ± 0.01	6.01 ± 0.02	6.09 ± 0.02	6.05 ± 0.02	6.16 ± 0.02

As seen with microelectrodes in Chapter 3, the estimated equivalent circuit components with the greatest estimated error after using this fitting method belong to the high-frequency components, particularly C_{DL} (Table 4.2). In addition, goodness of fit is high, as indicated by a low χ^2 for each electrode, and the most relevant factor relating to diffusion Y_0 also has low estimated error. The Y_0 values for these five macroelectrodes were converted to D_L values as shown above (Table 4.2), which were then calculated to be an average (and standard deviation) of $6.02 \pm 0.14 \times 10^{-10}$ m^2 s^{-1}. This rate is lower than literature values for the FFC redox pair, which range from around $6.5\text{-}7.5 \times 10^{-10}$ m^2 s^{-1} at 25 °C and at concentrations one and two orders of magnitude greater than used here.[10] In the presence of polymer suspended in solution, the diffusion coefficient of the FFC redox pair can be lower than this due to increased viscosity.[11] It is therefore unsurprising that the presence of gelator and supramolecular aggregates in solution would have a similar effect on D. It is also reassuring that these D_L values sit within the experimental error of the average D_L and D_{NL} values calculated for the bare Pt microelectrodes 4.71 ± 0.78 and $6.10 \pm 0.27 \times 10^{-10}$ m^2 s^{-1} (Table 3.12, Chapter 3 Section 3.4.5).

Having characterised the bare 2 mm diameter Pt disc macroelectrodes via EIS, the experiments detailed in Section 4.2.1 were repeated to characterise a similarly gel-coated macroelectrode. A Carb-Ala hydrogel was grown under the similar experimental conditions (Figure 4.6) and structural changes within the Carb-Ala hydrogel were then tracked via EIS (Figure 4.7). Nyquist plots were recorded for the same time intervals whilst the hydrogel was submerged in a pH 4.3 buffered ferrocyanide solution. Changes to the diffusion coefficient of the FFC redox pair D_L were calculated from estimated Y_0 values at each of these time intervals (Table 4.3).

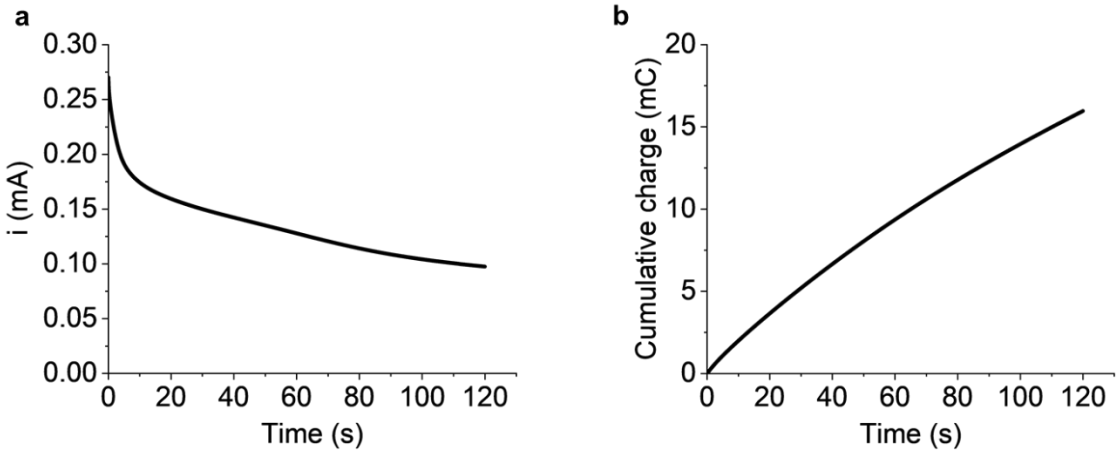

Figure 4.6 Current-time transient (a) and charge-time transient (b) (calculated by integrating area under current-time transients in (a)), recorded in 10 mL 10 mg/mL Carb-Ala gelator solution (pH 8) containing hydroquinone (67.5 mM) and NaCl (10 mM), at Pt macroelectrode (2 mm diameter), 120 seconds at 0.7 V (stepped from open circuit potential), T = 25 °C.

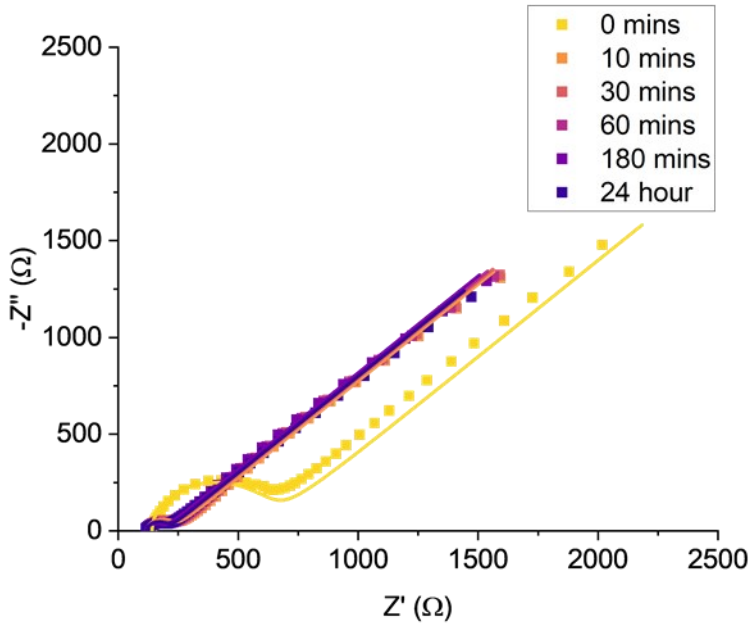

Figure 4.7 Nyquist plots of Pt macroelectrode (2 mm diameter) in pH 4.3 buffered ferrocyanide solution, T = 25 °C. Scatter points represent recorded impedance, lines represent unweighted fitted data with R_S values fixed to the weighted R_S values using the modified Randles circuit (Figure 2.11, Chapter 2 Section 2.2.6). Colour gradient of lighter to darker plots corresponds to increasing times of continued submersion of macroelectrode in the ferrocyanide solution (pH 4.3).

Table 4.3 Y_0 values, along with respective diffusion coefficients D_L, obtained from fitted EIS data (and estimated errors) of Carb-Ala gel-functionalised Pt disc macroelectrode (2 mm diameter), without weight factor applied (as shown in Figure 4.7), recorded at different time periods of continued submersion in pH 4.3 buffered ferrocyanide solution. D_L values calculated using Equation 2.29 (Chapter 2 Section 2.2.7).

Time	Y_0 (nS)	D_L ($\times 10^{-10}$ m^2 s^{-1})
0 minutes	565 ± 10	3.66 ± 0.06
10 minutes	666 ± 2	5.10 ± 0.02
30 minutes	660 ± 2	5.00 ± 0.02
60 minutes	665 ± 2	5.07 ± 0.02
180 minutes	674 ± 2	5.22 ± 0.02
24 hours	719 ± 2	5.93 ± 0.02

As with the microelectrodes in Section 4.2.1, the gel-coated macroelectrode also showed an increase in the mean FFC diffusion coefficient with time. The most significant change occurred in the first 10 minutes, as D_L increased from 3.66 × 10^{-10} m^2 s^{-1} to 5.10 × 10^{-10} m^2 s^{-1} (Table 4.3). As a reminder, the Carb-Ala gels grown at the 25 µm Pt disc microelectrodes under the same conditions (0.7 V, 120 seconds, T = 25°C) experienced a slight decrease in diffusion coefficients for the first 30 minutes of time submerged in the buffered solution (Table 4.1, Figure 4.4).

This suggests that the changes to the gel structure in these initial times may differ between the macroscale and microscale gels. 24 hours after submersion, D_L for the macroelectrode had increased to 5.93×10^{-10} m^2 s^{-1}, comparable to D_L for the bare macroelectrode which averaged $6.02 \pm 0.14 \times 10^{-10}$ m^2 s^{-1} (Table 4.2, Table 4.3). Whilst this gel may have undergone a similar process of shrinkage and gel loss, the final D_L for the FFC redox pair being identical to that of the bare electrode suggests that whatever gel had grown at the surface had completely disappeared after 24 hours. Accompanying this experiment, a second gel grown under the same conditions at a Pt macroelectrode was submerged in the pH 4.3 buffer, and images were recorded at 10 minutes, 30 minutes 60 minutes, 180 minutes, and 24 hours after submersion (Figure 4.8).

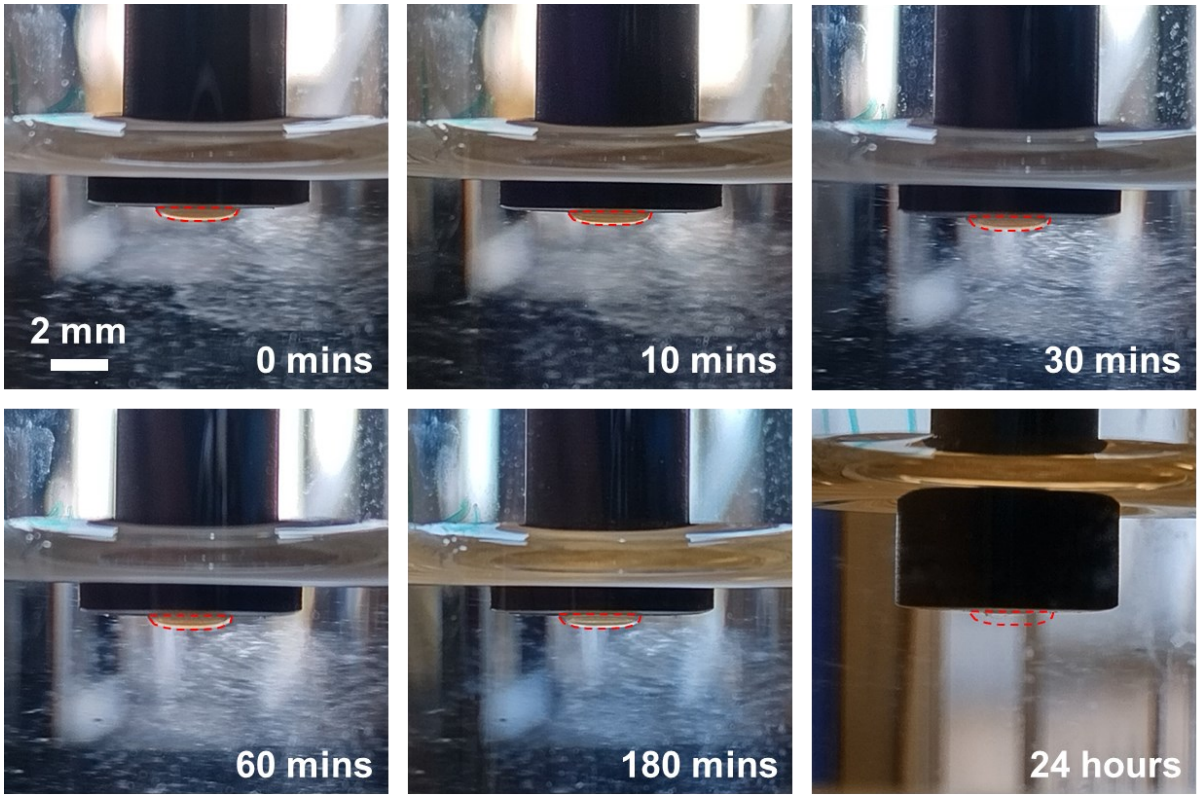

Figure 4.8 Images of Carb-Ala hydrogel at Pt macroelectrode surface (2 mm) submerged in 0.1 M citric acid/trisodium citrate buffer (pH 4.3), post 0.7 V 120 second potentiostatic gel growth experiment. From top left to bottom right: 0 minutes, 10 minutes, 30 minutes, 60 minutes, 180 minutes, and 24 hours. A red dashed line corresponding to the cross-section of the original gel at 0 minutes is displayed in each image. Note that after 180 minutes the electrode was submerged further into solution, so as not to allow the gel to be exposed to air due to potential solution evaporation overnight.

On initial submersion (0 minutes), the cross-sectional area (from this side-on view) of the macroscale gel measured 1.0 mm^2. The gel apparently retained this cross-sectional area for the first 3 hours submerged in the pH 4.3 buffer solution, and during this time the opaque orange tint of the gel gradually shrunk inwards to leave behind a transparent shell around the orange layer, most obvious in the image recorded after 180 minutes within the buffer (Figure 4.8). This latter process was proposed to be a loss in gel density with time, as seen with prior visual observations at the microelectrode (Figure 4.3), and in agreement with EIS

measurements and data at the macroelectrode (Figure 4.7, Table 4.3). The gel was left in solution for 24 hours, after which it had become completely transparent, thin, and flattened at the Pt surface. A cross-sectional area of 0.2 mm^2 was measured for the remaining mass (Figure 4.8). It is no surprise when seeing what remains after this time that this gel would have almost no barrier effect on the transport of the FFC redox pair during EIS. All told, these experiments in Sections 4.2.1 and 4.2.2 show that the phenomena of shrinkage and loss of density for these potentiostatically-grown Carb-Ala hydrogels is not determined by the scale of the discotic Pt surface on which they are grown, be it micro or macro.

4.2.3 Carb-Ala gels grown at carbon fibre disc microelectrodes

Angelerou *et al.* remark on how surfaces modified with hydrophilic and hydrophobic molecular species can influence the nucleation and aggregation of self-assembled structures of cytidine-based monomers, with favourable aggregate-aggregate interactions increasing at more hydrophobic surfaces.[12,13] However, this influence is also noted to be limited to very short distances at the surface, and does not extend into the bulk aqueous gelator solutions.[12,13] The way in which peptide-based gelators and their aggregates bind to electrode surfaces is not well understood, however it can be surmised that hydrophobic surfaces may interact more strongly with these structures. Peptide-gelator aggregates may not bind as strongly to Pt surfaces without such surface modifications. In order to rule out the possibility that the electrode surface/material has an effect on the stability of Carb-Ala hydrogels, a new question is considered: whether the structural changes to hydrogels observed in Sections 4.2.1 and 4.2.2 at catalytic Pt surfaces would also be observed at a more hydrophobic electrode surface. Glassy carbon macroelectrodes have been used in other works as the WE of choice for the electrochemical pH-triggered growth of peptide-based hydrogels,[14,15] and would be a good comparator for investigating the effects of different electrode materials on hydrogel growth. For comparison with the Pt microelectrodes, a carbon fibre disc microelectrode was used here (33 µm diameter). First, typical CVs for the carbon fibre microelectrode in pH 8 aqueous solutions containing hydroquinone with and without the Carb-Ala gelator were recorded (Figure 4.9).

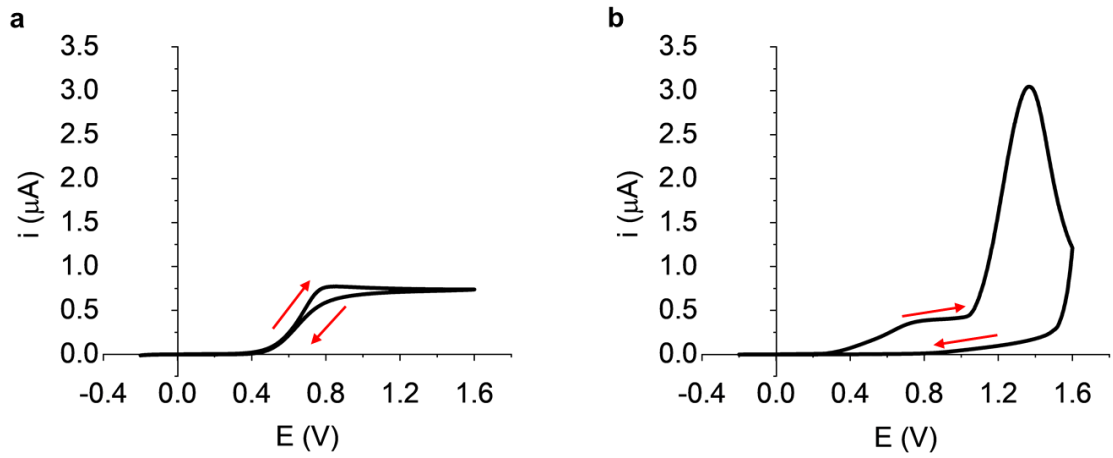

Figure 4.9 CVs in 10 mL aqueous solutions (pH 8) containing hydroquinone (67.5 mM) and NaCl (1 mM), at a carbon fibre microelectrode (33 µm diameter), with starting potential E = 0 V,

initial scan direction positive, scan rate v = 0.1 V s^{-1}, T = 25 °C. (a) E scanned between -0.2 V and 1.6 V. (b) With added 10 mg/mL Carb-Ala, E scanned between -0.2 V and 1.6 V.

In each CV, an oxidation wave corresponding to hydroquinone was identified, starting at +0.3 V. In the solution without gelator (Figure 4.9a), the hydroquinone oxidation wave became fully mass-transport limited at +1.2 V, with only a minor difference in half-wave potentials between the forward of reverse scans of approximately 20 mV. The maximum anodic currents for the forward and reverse scans in the solution without the Carb-Ala gelator were 0.77 µA and 0.71 µA respectively, the slight peak in the forward scan being attributed to the setting up of steady state conditions. In the case of the solution containing the Carb-Ala gelator (Figure 4.9b), the maximum anodic current for hydroquinone oxidation in the forward scan was 0.40 µA. As discussed in the previous chapter, according to the Stokes-Einstein equation this indicates an increase in viscosity due to the growing hydrogel reducing the diffusion coefficient of hydroquinone (Equation 3.1, Chapter 3 Section 3.2.1). In addition, an irreversible peak corresponding to the polymerisation of Carb-Ala was observed in the gelator solution, beginning at +1.0 V, reaching a peak current at +1.4 V of 3.05 µA, and decreasing towards the end of the forward scan and beyond in the reverse scan (Figure 4.9b). These CVs are unsurprisingly consistent those recorded in the same conditions with the commercial Pt microelectrode in Chapter 3 Section 3.2.1.

Next, baseline EIS measurements were recorded for the bare carbon fibre microelectrode. Three repeats of the same EIS experiment were conducted in the ferrocyanide solution, cleaning the microelectrode after each experiment. The Nyquist plots were individually fitted to the modified Randles circuit with the weight factor removed and R_S values fixed, and plotted together (Figure 4.10).

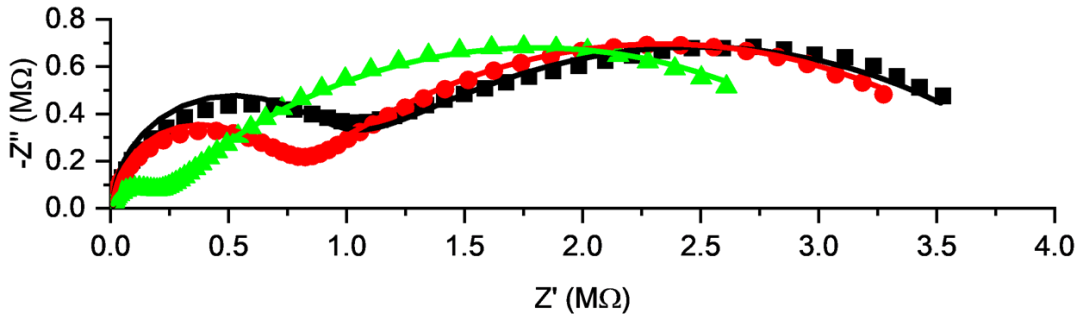

Figure 4.10 Nyquist plots of bare carbon fibre disc microelectrodes (33 µm diameter) in pH 4.3 buffered ferrocyanide solution during EIS, 25 °C. Scatter points represent recorded impedance, dotted lines represent unweighted fitted data using model the modified Randles circuit with R_S values fixed to the weighted R_S values: black squares = electrode 1, red circles = electrode 2, green triangles (up) = electrode 3.

The Nyquist plots showed significant variation in the high frequency range between repeated EIS experiments (Figure 4.10), expressed as a large variation in R_{CT} between electrodes (Table 4.4), comparable to those for the bare and gel coated Pt microelectrodes. The fixed R_S components (obtained from fitting with the weight factor applied in the Nova 1.11 software) have values that are indistinguishable from those recorded at the bare 25 µm Pt

microelectrodes in Chapter 3 Section 3.3. However, the C_{DL} values recorded for these carbon fibre microelectrodes show great variation, indicating that the surface of this electrode was not reproducibly cleaned. It is also reassuring to see the values for the fitted R_{NL} components produces D_{NL} values for the FFC redox pair that are very similar to those recorded at the bare Pt microelectrodes. D_{NL} averages $6.45 \pm 0.09 \times 10^{-10}$ m^2 s^{-1} for the bare carbon fibre microelectrode (Table 4.4), compared to $6.10 \pm 0.27 \times 10^{-10}$ m^2 s^{-1} for the bare Pt microelectrode (Table 3.12, Chapter 3 Section 3.4.5). Interestingly, the estimated Y_0 components for the bare carbon fibre microelectrode show more variation between electrodes, greater than those of the bare Pt microelectrodes. When translating to diffusion coefficients, average D_L for the bare carbon fibre microelectrodes is calculated to be $8.26 \pm 2.64 \times 10^{-10}$ m^2 s^{-1} (Table 4.4) compared to $4.71 \pm 0.78 \times 10^{-10}$ m^2 s^{-1} for the Pt microelectrodes (Table 3.12, Chapter 3 Section 3.4.5). As with the Pt microelectrodes, it appears as though the R_{NL} component (and thus D_{NL}) is a more accurate and consistent representation of FFC diffusion at the microelectrodes.

Table 4.4 Fitted EIS data and estimated errors for bare 33 µm diameter carbon fibre disc microelectrodes. Raw data fitted to the modified Randles circuit (Figure 2.11, Chapter 2 Section 2.2.6) with weight factor not applied (Figure 4.10), R_S values fixed (italicised). D_L and D_{NL} are calculated using Equation 2.29 and Equation 2.31 (Chapter 2 Section 2.2.7) respectively.

Bare 33 µm dia. Carbon fibre disc micro., weight factor off, fixed R_S			
Component	**1**	**2**	**3**
R_S (kΩ)	*10.6*	*10.8*	*9.36*
C_{DL} (pF)	165 ± 5	104 ± 2	91.0 ± 4.9
R_{CT} (kΩ)	864 ± 14	659 ± 6	155 ± 3
Y_0 (nS)	111 ± 2	131 ± 1	153 ± 1
R_{NL} (MΩ)	3.27 ± 0.03	3.35 ± 0.02	3.28 ± 0.01
χ^2	0.0414	0.0134	0.0103
D_L (x10^{-10} m^2 s^{-1})	5.75 ± 0.24	8.02 ± 0.15	11.0 ± 0.12
D_{NL} (x10^{-10} m^2 s^{-1})	6.52 ± 0.06	6.35 ± 0.03	6.49 ± 0.02

Next, a Carb-Ala hydrogel was grown at the carbon fibre disc microelectrode. A current-time transient was obtained by applying 0.7 V for 120 seconds within a 10 mg/mL Carb-Ala gelator solution. The resulting gel-coated microelectrode was then characterised using EIS, fitting the Nyquist plot to the modified Randles circuit using the established method with the weight

factor not applied and the R_S value fixed to the weighted estimation. The hydrogel was also imaged under microscopy. This experiment was repeated an additional four times, cleaning the microelectrode between each run (Figure 4.11, Table 4.5).

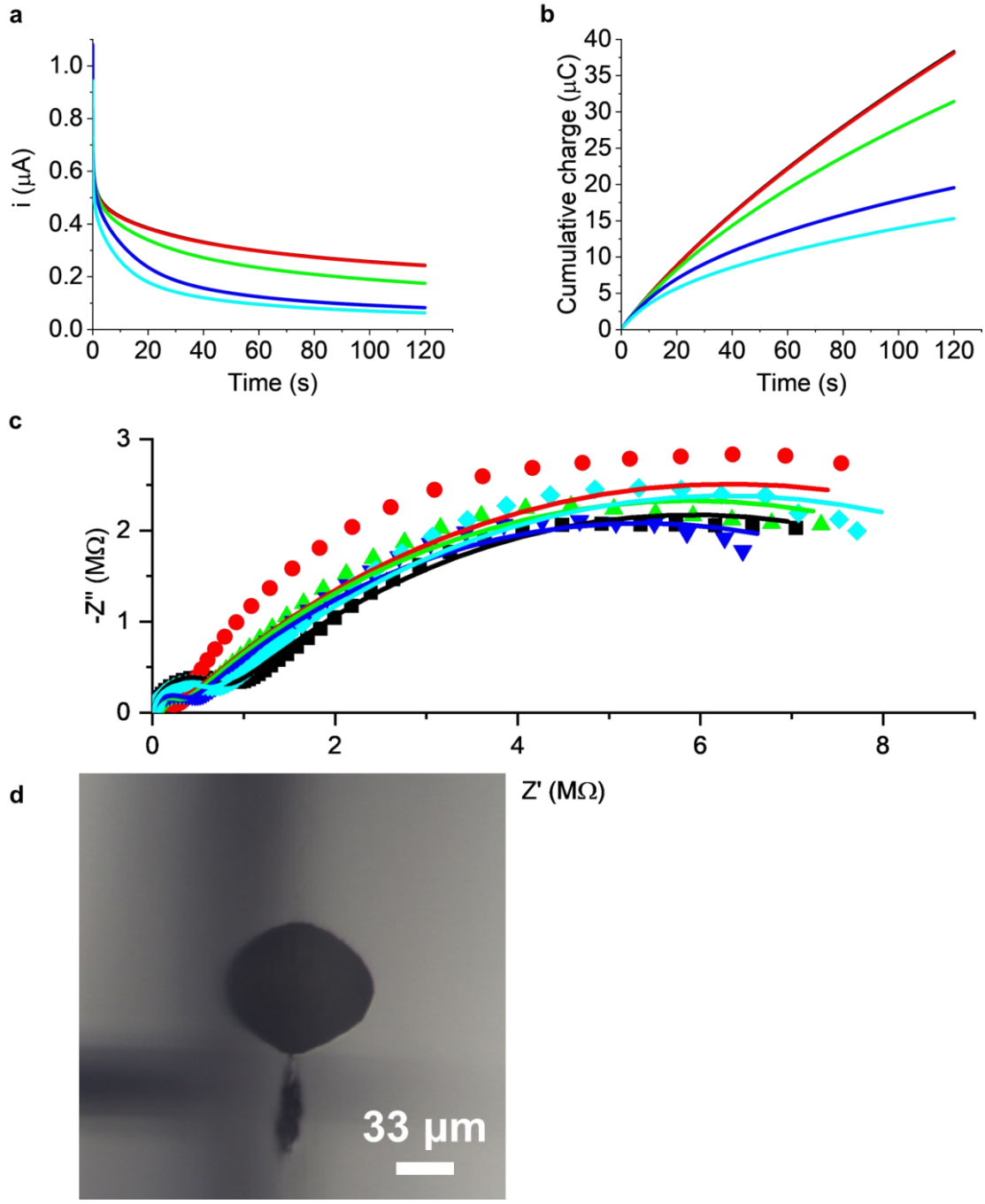

Figure 4.11 Potentiostatic growth of Carb-Ala gels on a carbon fibre disc microelectrode (33 μm diameter) at 0.7 V for 120 seconds, 25 °C. (a) Current-time transients of hydroquinone oxidation in gelator solution. (b) Cumulative charge passed during gel-growth step, calculated by integrating area under current-time transients in (a). (c) Recorded (scatter points) and fitted (solid lines) Nyquist plots of gel-functionalised electrodes in pH 4.3 buffered ferrocyanide solution, obtained with weight factor off and RS fixed to RS obtained from weighted fit. Black squares = electrodet 1, red circles = electrode 2, green triangles (up) = electrode 3, blue

triangles (down) = electrode 4, teal diamonds = electrode 5. (d) Example capture of Carb-Ala gel at commercial microelectrode surface, side-on view, 100x magnification.

Table 4.5 Data and estimated errors for 120 second, 0.7 V Carb-Ala gels grown at 33 µm diameter carbon fibre disc electrodes. Features total charge passed during gel-growth step (as shown in Figure 4.11b), fitted EIS data of gel functionalised microelectrodes (as shown in Figure 4.11c) to the modified Randles circuit with weight factor off and R_S fixed to weighted value. Diffusion coefficients D_L and D_{NL} were calculated using Equation 2.29 and Equation 2.31 (Chapter 2 Section 2.2.7) respectively, and dimensions of gels (an example of which is featured in Figure 4.11d) are also tabulated.

0.7 V 120s gels, 33 µm dia. carbon fibre disc micro., weight factor off, fixed R_S					
Component	**1**	**2**	**3**	**4**	**5**
Cumulative Charge (µC)	38.3	38.1	31.4	20	15.3
R_S (kΩ)	*14.8*	*14.1*	*13.6*	*14.3*	*15.3*
C_{DL} (pF)	114 ± 9	121 ± 133	57.6 ± 20.4	63.1 ± 11.9	72.6 ± 11.9
R_{CT} (kΩ)	683 ± 21	270 ± 127	270 ± 35	325 ± 22	540 ± 35
Y_0 (nS)	85.8 ± 1.1	77.0 ± 5.3	74.1 ± 1.6	80.9 ± 1.2	65.4 ± 1.3
R_{NL} (MΩ)	10.5 ± 0.1	12.1 ± 0.7	11.2 ± 0.2	10.0 ± 0.1	11.5 ± 0.2
χ^2	0.0639	2.26	0.216	0.101	0.139
D_L (x10^{-10} m^2 s^{-1})	3.46 ± 0.09	2.78 ± 0.38	2.58 ± 0.11	3.07 ± 0.09	2.01 ± 0.08
D_{NL} (x10^{-10} m^2 s^{-1})	2.03 ± 0.02	1.76 ± 0.11	1.90 ± 0.04	2.12 ± 0.03	1.86 ± 0.03
Gel Width (µm)	107	92.0	97.7	87.0	76.0
Gel Height (µm)	59.0	52.2	56.8	46.7	40.0
Gel Cross-Sectional Area (µm^2)	4880	3580	3910	2970	2130

As with the bare carbon fibre microelectrodes (Table 4.4), the lower frequency range components C_{DL} and R_{CT} gave values that varied greatly between electrodes (Table 4.5). The Y_0 and R_{NL} components produced D_L and D_{NL} values that averaged 2.78 ± 0.54 and 1.93 ± 0.14 × 10^{-10} m^2 s^{-1} respectively (Table 4.5), both as expected lower than those of the bare electrodes (Table 4.4) due to the presence of hydrogel. Compared to respective average D_{NL} for each type of bare microelectrode, D_{NL} at the Pt microelectrode dropped by 61 % and at the carbon fibre microelectrode dropped by approximately 60% after gel growth (Table 3.12,

Chapter 3 Section 3.4.5; Table 4.4, Table 4.5). This is reassuring to see, as it means that the final densities of these Carb-Ala hydrogels can be reproduced at different electrode surfaces of similar dimensions if the experimental conditions are consistent.

The current time transients and cumulative charges both displayed successive decreases (Figure 4.11, Table 4.5). As discussed in Chapter 3 Section 3.4.2, this appears to be due to an impurity building up in the gelator solution with time. As with the Pt microelectrodes this leads to a knock-on effect on the dimensions of the hydrogels, as a trend can be seen to emerge with the widths, heights and cross-sectional areas of the gels decreasing in magnitude from electrode 1 to 5. There was one exception to this apparent trend, electrode 2, however it is speculated that the hydrogel grown at this electrode may have collapsed on transfer to the microscope or had shrunken and lost material with solution evaporation. Surprisingly, none of the hydrogels grown at the 33 µm diameter carbon microeletrode grew to dimensions greater than those equivalent 120 second, 0.7 V Carb-Ala hydrogels grown at the 25 µm diameter Pt microelectrodes. Additionally, only the hydrogels grown at carbon microelectrodes 1 and 3 possessed dimensions that lay within the error ranges of those equivalent Pt microelectrode hydrogels (Table 3.12, Chapter 3 Section 3.4.5).

Next, the experiment in Section 4.2.1 was repeated within a freshly prepared 10 mg/mL gelator solution at the carbon fibre microelectrode. The current-time transient and cumulative charge passed (Figure 4.12) were both confirmed to be consistent with those recorded previously at the carbon fibre microelectrode (black and red transients, Figure 4.11a and Figure 4.11b). The three-electrode system was then transferred to a pH 4.3 buffered ferrocyanide solution, and EIS frequency scans were recorded in 10 minute intervals, starting from t = 0 minutes upon electrode submersion (Figure 4.13). Estimated Y_0 and R_{NL} values from fitted data, and their respective diffusion coefficients, are tabulated below (Table 4.6).

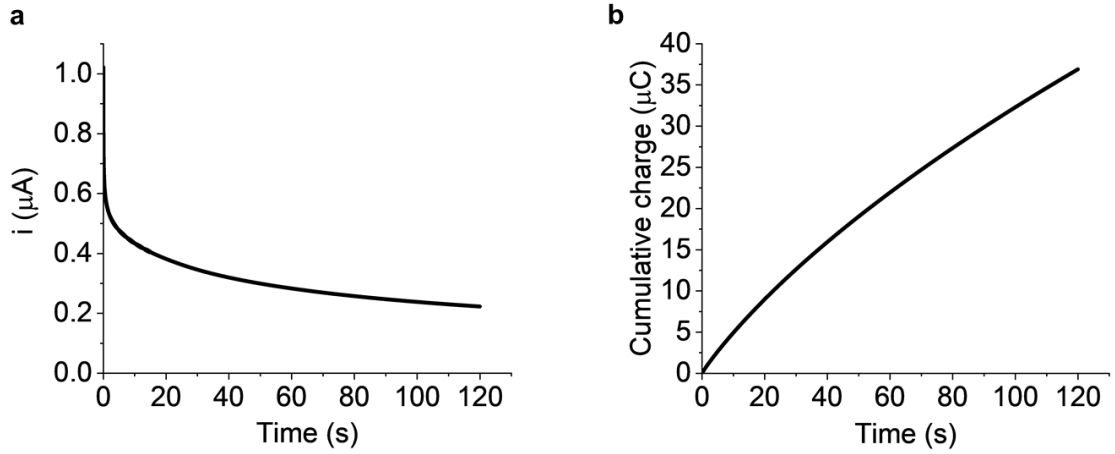

Figure 4.12 Current-time transient (a) and charge-time transient (b) (calculated by integrating area under current-time transients in (a)), recorded in 10 mL 10 mg/mL Carb-Ala gelator solution (pH 8) containing hydroquinone (67.5 mM) and NaCl (1 mM), at carbon fibre disc microelectrode (33 µm diameter), 120 seconds at 0.7 V (stepped from open circuit potential), T = 25 °C.

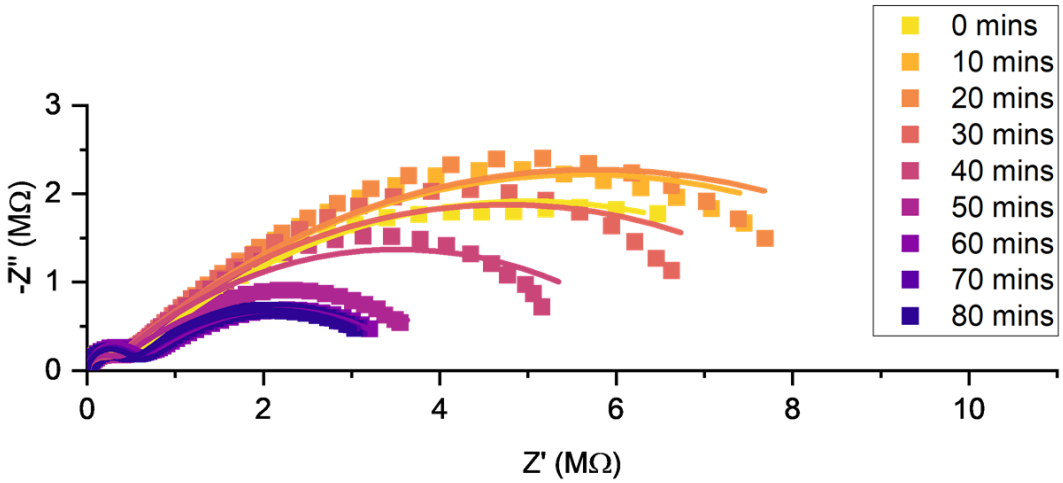

Figure 4.13 Nyquist plots of potentiostatic Carb-Ala gel coated (0.7 V, 120 seconds) carbon fibre disc microelectrode (33 µm diameter) in pH 4.3 buffered ferrocyanide solution during EIS, T = 25 °C. Scatter points represent recorded impedance, lines represent unweighted fitted data with R_S values fixed to the weighted R_S values using the modified Randles circuit (Figure 2.11, Chapter 2 Section 2.2.6). Colour gradient of lighter to darker plots corresponds to increasing times of continued submersion of microelectrode in ferrocyanide solution.

Table 4.6 Y_0 and R_{NL} values, along with respective diffusion coefficients D_L and D_{NL}, obtained from fitted EIS data (and estimated errors) of Carb-Ala gel-functionalised carbon fibre disc microelectrode (33 µm diameter) without weight factor applied (as shown in Figure 4.13), recorded at different time periods of continued submersion in pH 4.3 buffered ferrocyanide solution. D_L and D_{NL} values calculated using Equation 2.29 and Equation 2.31 respectively (Chapter 2 Section 2.2.7).

Time (minutes)	Y_0 (nS)	R_{NL} (MΩ)	D_L ($\times 10^{-10}$ m^2 s^{-1})	D_{NL} ($\times 10^{-10}$ m^2 s^{-1})
0	83.7 ± 0.9	9.24 ± 0.08	3.29 ± 0.07	2.30 ± 0.02
10	65.5 ± 1.4	10.7 ± 0.2	2.02 ± 0.09	1.99 ± 0.03
20	61.5 ± 1.8	11.0 ± 0.2	1.78 ± 0.10	1.94 ± 0.04
30	62.4 ± 1.9	9.04 ± 0.17	1.83 ± 0.11	2.35 ± 0.04
40	66.0 ± 2.0	6.60 ± 0.10	2.05 ± 0.12	3.22 ± 0.05
50	89.1 ± 1.2	4.13 ± 0.03	3.73 ± 0.10	5.15 ± 0.03
60	116 ± 1	3.30 ± 0.02	6.32 ± 0.15	6.45 ± 0.04
70	123 ± 1	3.29 ± 0.01	7.08 ± 0.13	6.48 ± 0.03
80	125 ± 1	3.28 ± 0.01	7.34 ± 0.12	6.49 ± 0.03

As with the experiment at the Pt microelectrode in Section 4.2.1, there was an initial decrease in Y_0 and increase in R_{NL} in initial times after submersion of the gel-coated carbon fibre microelectrode into the buffer solution (Table 4.6). Y_0 decreased from 83.7 nS at 0 minutes to 61.5 nS at 20 minutes, and R_{NL} increased from 9.24 MΩ to 11.0 MΩ in the same timeframe (Figure 4.13, Table 4.6). These equate to decreases in D_L of 3.29×10^{-10} m^2 s^{-1} to

1.78×10^{-10} m^2 s^{-1} and D_{NL} of 2.30×10^{-10} m^2 s^{-1} to 1.94×10^{-10} m^2 s^{-1}, which again suggest an increase in hydrogel density during this initial timeframe. As with gels grown at Pt microelecrodes, Y_0 and R_{NL} values (and their respective diffusion coefficients) also changed with time reaching values comparable to those of the bare carbon fibre disc microelectrodes. This experiment was ceased after 80 minutes, much earlier than those with the Pt microelectrodes, as Y_0 and R_{NL} appeared to have settled to final values of 116 nS and 3.30 MΩ after 60 minutes (Table 4.6). As a reminder, average (and standard deviation) Y_0 and R_{NL} values for the bare carbon fibre disc microelectrodes are 131 ± 21 nS and 3.30 ± 0.05 MΩ (Table 4.4). These final values at the once gel-coated microelectrode imply that either the gel had significantly shrunken or had completely dissolved, and had no significant impact on the diffusion of the FFC redox pair by the end of the experiment. In either case, this experiment confirms that the shrinkage and loss of Carb-Ala hydrogel occurs at electrode surfaces on the microscale at both carbon and Pt surfaces.

4.2.4 BrAV gels grown at Pt disc microelectrodes

To investigate whether the loss of Carb-Ala hydrogel in the pH 4.3 buffer was a phenomenon exclusive to the Carb-Ala gelator, a second peptide-based gelator BrAV was employed to form equivalent electrochemically-grown hydrogels (see Chapter 2 Section 2.3.2). A pH 8 10 mg/mL BrAV gelator solution was first characterised in a typical CV at a Pt disc microelectrode (Figure 4.14).

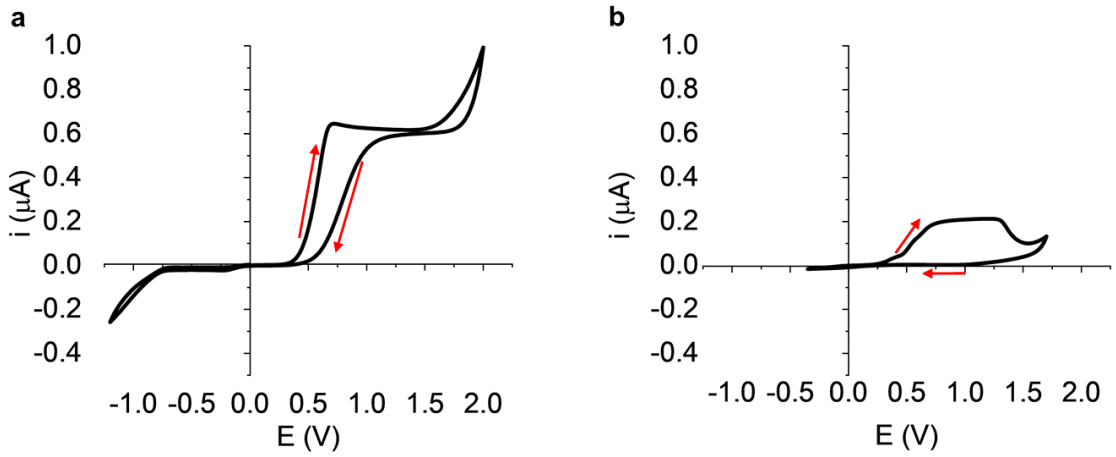

Figure 4.14 CVs in 10 mL aqueous solutions (pH 8) containing hydroquinone (44.4 mM) and NaCl (1 mM), at a Pt disc microelectrode (25 μm diameter), with starting potential E = 0 V, initial scan direction positive, scan rate v = 0.1 V s^{-1}, T = 25 °C. (a) E scanned between -1.2 V and 2.0 V. (b) With added 10 mg/mL BrAV, E scanned between -0.4 V and 1.6 V.

The CV without the gelator (Figure 4.14a) used here as a comparator to the CV with the BrAV gelator (Figure 4.14b) is analysed in detail in Chapter 3 Section 3.2.1. The hydroquinone oxidation wave was identified at the same starting potential of +0.3 V in both solutions. The limiting current in the BrAV gelator solution was reduced, from 0.65 μA without the gelator (Figure 4.14a) to 0.21 μA in the 10 mg/mL BrAV solution (Figure 4.14b). A similar observation as noted with Carb-Ala gelator solutions; this drop in current with the presence of BrAV signifies a drop in mass transport of hydroquinone, attributed to changes in solution viscosity with addition of BrAV gelator and the growth of a BrAV hydrogel slowing the flow of

hydroquinone at the microelectrode. Using the Saito equation[16] (Equation 2.6, Chapter 2 Section 2.1.3), *D* of hydroquinone at this gel-coated microelectrode in the BrAV gelator solutions equates to 3×10^{-10} m^2 s^{-1}, compared to 1×10^{-9} m^2 s^{-1} without the gelator present in solution.

Interestingly, the hydroquinone oxidation wave is not clearly defined in the reverse scan of the gelator solution CV (Figure 4.14b). From +1.3 V in the forward scan, current drops until the end of the forward scan when water oxidation begins, and continues to drop toward 0 A in the reverse scan before a sign of hydroquinone oxidation can be seen. This suggests that the diffusion of hydroquinone was not sustained after +1.3 V in the forward scan, which could be a result of the grown hydrogel and electropolymerised Carb-Ala at the electrode surface preventing further mass transport of hydroquinone to the electrode. Note also that there is no irreversible oxidation peak in the forward scan (Figure 4.14b) as was seen in the Carb-Ala CV (Figure 3.2, Chapter 3 Section 3.2.1). BrAV is not known to undergo polymerisation upon oxidation, so it makes sense that this would not be present here.

With electrochemical BrAV gel growth shown to be viable, five BrAV hydrogels were grown at the 25 µm Pt disc microelectrodes by applying 0.7 V for 120 seconds within a 10 mg/mL BrAV gelator solution. This potential and time were chosen for comparison to the Carb-Ala gels grown under the same conditions. The gel-coated microelectrodes were characterised via EIS using the same methodologies outlined in Chapter 3 and the gels were imaged under microscopy to record dimensions (Figure 4.15). Cumulative charge passed during gel growth, EIS data, and gel dimensions are tabulated below (Table 4.7).

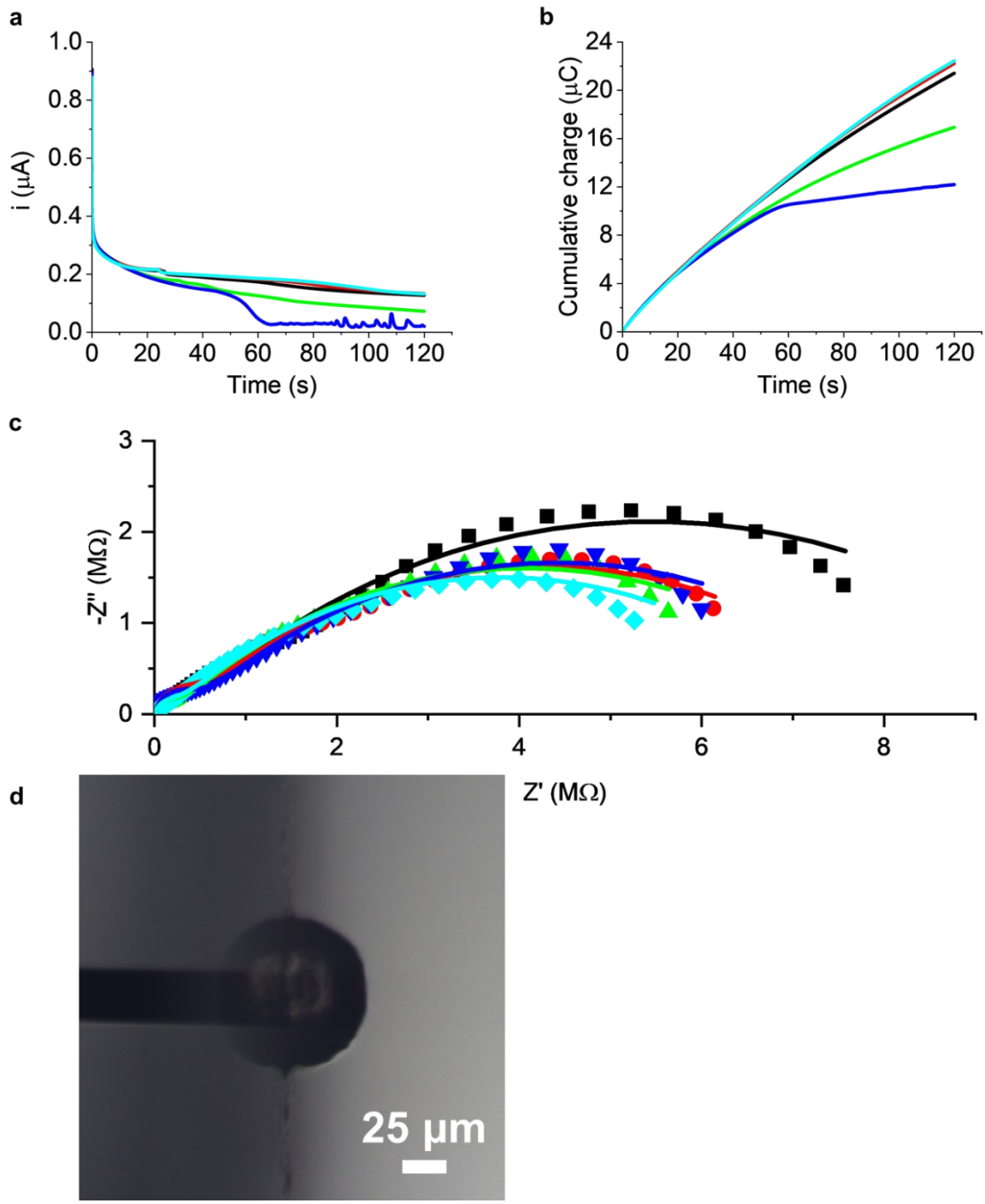

Figure 4.15 Potentiostatic growth of BrAV gels on a Pt microelectrode (25 μm diameter) at 0.7 V for 120 seconds, 25 °C. (a) Current-time transients of hydroquinone oxidation in gelator solution. (b) Cumulative charge passed during gel-growth step, calculated by integrating area under current-time transients in (a). (c) Recorded (scatter points) and fitted (solid lines) Nyquist plots of gel-functionalised electrodes in ferrocyanide solution, obtained with weight factor off and R_S fixed to R_S obtained from weighted fit. Black squares = electrode 1, red circles = electrode 2, green triangles (up) = electrode 3, blue triangles (down) = electrode 4, teal diamonds = electrode 5. (d) Example capture of Carb-Ala gel at commercial microelectrode surface, side-on view, 100x magnification.

Table 4.7 Data and estimated errors for 120 second, 0.7 V BrAV gels grown at 25 µm diameter Pt disc electrodes. Features total charge passed during gel-growth step (as shown in Figure 4.15b), fitted EIS data of gel functionalised microelectrodes (as shown in Figure 4.15c) to the modified Randles circuit with weight factor off and R_S fixed to weighted value. Diffusion coefficients D_L and D_{NL} were calculated using Equation 2.29 and Equation 2.31 respectively (Chapter 2 Section 2.2.7), and dimensions of gels (an example of which is featured in Figure 4.15d) are also tabulated.

0.7 V 120s gels, 25 µm dia. Pt disc micro., weight factor off, fixed R_S					
Component	**1**	**2**	**3**	**4**	**5**
Cumulative Charge (µC)	21.4	22.2	16.9	12.2	22.4
R_S (kΩ)	*16.0*	*15.7*	*14.9*	*16.2*	*13.2*
C_{DL} (pF)	192 ± 42	275 ± 37	197 ± 44	173 ± 24	238 ± 67
R_{CT} (kΩ)	389 ± 50	417 ± 36	224 ± 28	418 ± 29	211 ± 38
Y_0 (nS)	58.3 ± 1.4	66.8 ± 1.4	78.6 ± 1.5	77.1 ± 1.5	74.5 ± 1.8
R_{NL} (MΩ)	10.1 ± 0.14	7.75 ± 0.08	7.70 ± 0.09	7.99 ± 0.10	7.20 ± 0.09
χ^2	0.150	0.0916	0.0997	0.108	0.155
D_L ($\times 10^{-10}$ m^2 s^{-1})	1.60 ± 0.08	2.10 ± 0.09	2.91 ± 0.11	2.79 ± 0.11	2.61 ± 0.13
D_{NL} ($\times 10^{-10}$ m^2 s^{-1})	2.10 ± 0.03	2.75 ± 0.03	2.77 ± 0.03	2.67 ± 0.03	2.96 ± 0.04
Gel Width (µm)	117	114	98.9	95.1	121
Gel Height (µm)	58.7	58.8	59.5	41.3	61.6
Gel Cross-Sectional Area (µm^2)	5530	5640	4530	3100	5650

Though the current-time transients are expected to vary between the five electrodes, one of the current-time transients (blue line, electrode 4, Figure 4.15a) suddenly dipped to a minimum current of 30 nA at 60 seconds. From this time, the transient shows occasional spikes in current, but remains at a 30 nA base for the remainder of the experiment. This period of the experiment can also be observed in the charge-time transient. An "elbow bend" in the trace to a new rate in cumulative charge of 30 nC s^{-1} (from approximately 140 nC s^{-1} from the 35-55 second timeframe, blue line, electrode 4, Figure 4.15b) shows the transition to the 30 nA baseline for the remaining duration of the experiment. This unusual transient of the fourth electrode implies a significant reduction in diffusion of hydroquinone, which could occur due to a greater coverage of the electrode surface with gelator aggregates or the

increased concentration of an impurity formed in the gelator solution (with time) as speculated in Chapter 3 Section 3.4.2. Inconsistent with the latter explanation, this was not observed for the subsequent electrode (teal line, electrode 5, Figure 4.15a and Figure 4.15b), which passed currents that were more akin to the first two electrodes throughout the run (black and red lines, electrodes 1 and 2, Figure 4.15a and Figure 4.15b).

When grown under the same conditions using solutions of identical gelator concentration, estimated R_S, C_{DL}, Y_0, and R_{NL} values of BrAV gel-coated Pt microelectrodes do not closely match those of the Carb-Ala gel-coated Pt microelectrodes (Table 4.8). Average (and standard deviation) solution resistance R_S of 15.2 ± 1.2 kΩ is slightly lower in magnitude though within experimental error of R_S for the Carb-Ala gel-coated microelectrodes grown under the same conditions, 18.2 ± 0.7 kΩ. Average C_{DL} for the BrAV gel-coated electrode is almost double that of the Carb-Ala at 215 ± 41 pF. D_L and D_{NL} for the FFC pair through the BrAV gels are greater (and outside experimental error of) those for the Carb-Ala gels (Table 4.8), suggesting that the networks in these BrAV gels are less dense than that of the Carb-Ala gels. The dimensions of the BrAV gels are also the same within experimental error to the Carb-Ala gels, which suggests that whilst the gels grew to the same extent, dictated by the diffusion of protons from the electrode surface, the structures of the three-dimensional Carb-Ala and BrAV aggregates differ. This may be a result of the differing concentrations of the gelators in the 10 mg/mL Carb-Ala and BrAV solutions. For example, 1 mL of 10 mg/mL Carb-Ala solution contains 33.4 µmol of Carb-Ala, whilst the same volume of 10 mg/mL BrAV solution contains 22.2 µmol BrAV. It is plausible that the lower concentration of BrAV would lead to the production of gels with more open structures in the same volume.

Table 4.8 Averages and standard deviations of data 0.7 V Carb-Ala and BrAV gel-coated 25 µm diameter Pt disc electrodes (compiled from Table 3.12 in Chapter 3 Section 3.4.5 and Table 4.7).

0.7 V, 120 second Gel Growth Experiments, 25 µm dia. Pt disc micro., weight factor off, fixed R_S		
Component	**Carb-Ala**	**BrAV**
Cumulative Charge (µC)	31.9 ± 4.0	19.0 ± 4.4
R_S (kΩ)	18.2 ± 0.7	15.2 ± 1.2
C_{DL} (pF)	107 ± 6	215 ± 41
R_{CT} (kΩ)	583 ± 239	332 ± 104
Y_0 (nS)	44.6 ± 5.5	71.0 ± 8.5
R_{NL} (MΩ)	12.1 ± 0.4	8.15 ± 1.15
D_L ($\times 10^{-10}$ m^2 s^{-1})	0.947 ± 0.229	2.40 ± 0.55
D_{NL} ($\times 10^{-10}$ m^2 s^{-1})	1.76 ± 0.06	2.64 ± 0.32
Gel Width (µm)	104 ± 6	109 ± 11
Gel Height (µm)	55.1 ± 4.3	56.0 ± 8.3
Gel Cross-Sectional Area (µm^2)	4390 ± 650	4890 ± 1100

With a freshly prepared gelator solution, a final BrAV hydrogel was grown at a Pt disc microelectrode under the same conditions at 0.7 V for 120 seconds, in order to be used in a subsequent stability test in the pH 4.3 buffered ferrocyanide solution (Figure 4.16).

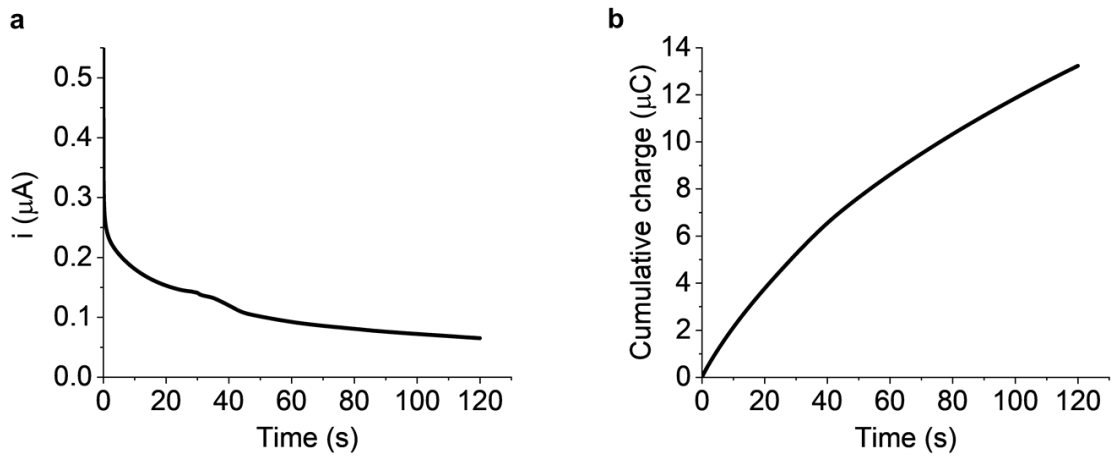

Figure 4.16 Current-time transient (a) and charge-time transient (b) (calculated by integrating area under current-time transients in (a)), recorded in 10 mL 10 mg/mL BrAV gelator solution (pH 8) containing hydroquinone (44.4 mM) and NaCl (1 mM), at Pt microelectrode (25 µm diameter), 120 seconds at 0.7 V (stepped from open circuit potential), T = 25 °C.

The currents passed when growing this hydrogel were similar to those in the past five experiments, with total cumulative charge reaching 13.2 µC (Figure 4.16b). This gel was then submerged in the ferrocyanide solution, and EIS was conducted in 10 minute intervals to observe hydrogel stability (Figure 4.17). Estimated Y_0 and R_{NL} values, with their corresponding diffusion coefficients, are tabulated below (Table 4.9).

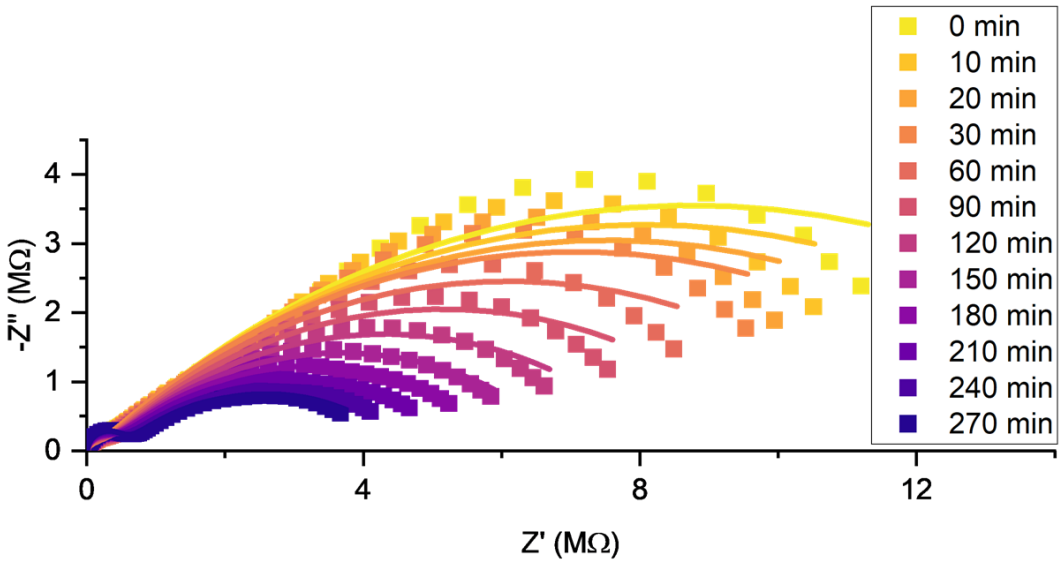

Figure 4.17 Nyquist plots of potentiostatic BrAV gel coated (0.7 V, 120 seconds) Pt microelectrode (25 µm diameter) in pH 4.3 buffered ferrocyanide solution during EIS, T = 25 °C. Scatter points represent recorded impedance, lines represent unweighted fitted data with R_S values fixed to the weighted R_S values using the modified Randles circuit (Figure 2.11, Chapter 2 Section 2.2.6). Colour gradient of lighter to darker plots corresponds to increasing times of continued submersion of microelectrode in ferrocyanide solution.

Table 4.9 Y_0 and R_{NL} values, along with respective diffusion coefficients D_L and D_{NL}, obtained from fitted EIS data (and estimated errors) of BrAV gel-functionalised Pt disc microelectrode (25 µm diameter) without weight factor applied (as shown in Figure 4.17), recorded at different time periods of continued submersion in pH 4.3 buffered ferrocyanide solution. D_L and D_{NL} values calculated using Equation 2.29 and Equation 2.31 respectively (Chapter 2 Section 2.2.7).

Time (minutes)	Y_0 (nS)	R_{NL} (MΩ)	D_L ($\times 10^{-10}$ m^2 s^{-1})	D_{NL} ($\times 10^{-10}$ m^2 s^{-1})
0	43.7 ± 1.5	17.1 ± 0.4	0.896 ± 0.062	1.24 ± 0.03
10	46.1 ± 1.7	15.8 ± 0.4	1.00 ± 0.08	1.35 ± 0.03
20	47.1 ± 1.7	14.7 ± 0.4	1.04 ± 0.08	1.45 ± 0.04
30	48.0 ± 1.7	13.9 ± 0.3	1.08 ± 0.08	1.54 ± 0.04
60	50.4 ± 1.5	11.8 ± 0.2	1.19 ± 0.07	1.80 ± 0.03
90	50.5 ± 1.3	9.87 ± 0.14	1.19 ± 0.06	2.16 ± 0.03
120	49.4 ± 1.0	8.12 ± 0.08	1.15 ± 0.05	2.62 ± 0.02
150	49.4 ± 0.7	6.81 ± 0.04	1.15 ± 0.03	3.13 ± 0.02
180	50.4 ± 0.7	5.87 ± 0.03	1.20 ± 0.03	3.63 ± 0.02
210	55.5 ± 0.9	5.05 ± 0.03	1.45 ± 0.04	4.21 ± 0.02
240	69.2 ± 1.0	4.34 ± 0.02	2.25 ± 0.06	4.91 ± 0.03
270	96.1 ± 0.5	3.89 ± 0.01	4.34 ± 0.04	5.45 ± 0.01

As is evident from the shrinking Nyquist plots of the time-dependant EIS data (Figure 4.17), the BrAV gel (pK_a^{app} = 5.8[8,14]) disappeared over time when transferred to the pH 4.3 buffer. R_{NL} and Y_0 values (and corresponding diffusion coefficients) transitioned to values that more closely resembled the bare Pt microelectrode over time, though this process took a greater period of time than seen with the Carb-Ala gels in Section 4.2.1, finalising at 96.1 nS and 3.89 MΩ at t = 270 minutes after submersion (Table 4.9). This experiment indicates that the instability of peptide-based supramolecular hydrogels grown at microelectrodes via the potentiostatic control of hydroquinone oxidation is not isolated to the Carb-Ala gelator. These gelators appear to consistently undergo fundamental structural changes when exposed to new aqueous environments, despite those environments being tailored to pH levels lower than the pK_a^{app} of the gelators in question to preclude deprotonation induced dissociation.

One minor point of note, the initial Nyquist plot for the gel-coated electrode at t = 0 minutes differs greatly from the prior five, most evident when examining Y_0 and R_{NL} components (Figure 4.17, Table 4.9). D_L and D_{NL} at this BrAV gel-functionalised electrode more closely resemble the average values of those 120 second, 0.7 V Carb-Ala hydrogels than the previous BrAV gels (Table 4.8). These initial values suggest that this BrAV hydrogel possessed a denser network than the previous five BrAV gels, though an explanation for this outlier cannot be given at this time.

4.3 Peptide-based hydrogel stability in other aqueous media

The experiments described in Section 4.2 are surprising in that they show peptide-based supramolecular hydrogels grown with potentiostatic control of hydroquinone oxidation are unstable when transferred to buffered solutions. These environments were previously thought to be suitable for ensuring the stability these gels due to the pH being fixed below the pK_a^{app} of the peptide-gelators. However, when moving these hydrogels to this low pH buffered environment, an unexpected process occurs wherein the gels dramatically change structure, first losing density before shrinking. Furthermore, this process occurs seemingly irrespective of the material and scale of the WE used, as this phenomenon is observed at commercial Pt microelectrodes, Pt macroelectrodes, and carbon fibre microelectrodes. Increases in diffusion coefficients D_L and D_{NL} calculated from EIS data have been consistently found to precede a reduction in hydrogel dimensions, suggesting an internal rearrangement of aggregate-aggregate interactions such that density is reduced before external structural collapse.

Gel syneresis was first considered as the cause for this observed phenomenon. Syneresis is a process exhibited by some peptide-based supramolecular hydrogels formed with less hydrophobic aggregates. Hydrogels that undergo shrinkage via syneresis do so due to negatively charged and more neutral fibres within the networks entangling further with time, in order to remove overall charge from the structures (Figure 4.18).[17,18] This process increases overall aggregate hydrophobicity, expelling aqueous solution from the entangled network, though this comes with the shrinking gel increasing in density. Contrary to this, the increasing D_L and D_{NL} recorded for the Carb-Ala gels in Section 4.2 indicate a reduction in gel density with time that precedes shrinkage. Electrochemically-grown Carb-Ala gels are suggested but not confirmed to undergo syneresis with further electrochemistry post-gelation.[19] In addition, bulk BrAV gels are reported to undergo syneresis,[18] and it is also noteworthy that the BrAV gels shown in Section 4.2.4 also shrank in size and showed similar signs of decreasing in density (Figure 4.17, Table 4.9). Therefore, it is unclear whether these microscale gels undergo syneresis, because whilst Carb-Ala and BrAv gels have been observed to shrink over long periods of time, the density of these gels appears to decrease with time according to EIS data.

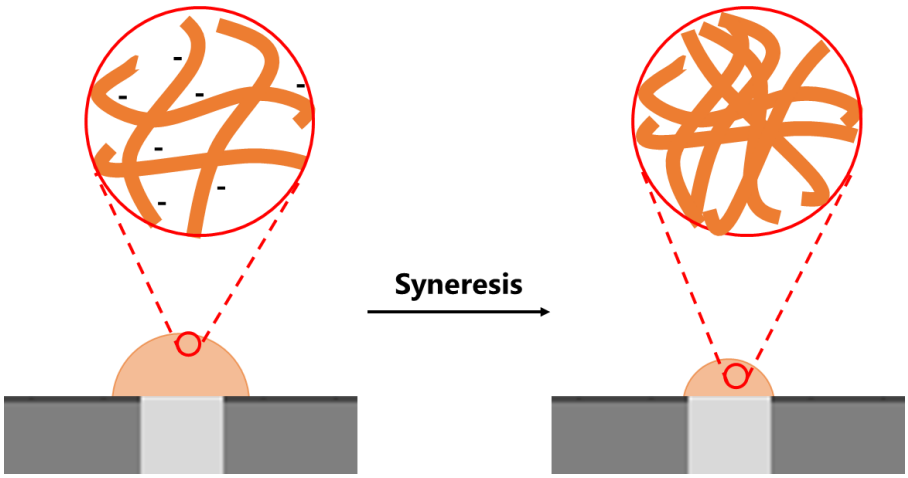

Figure 4.18 Graphical depiction of gel syneresis. Charges along aggregate structures are minimised by a collapse of the network to a denser entanglement.

The oxidation of hydroquinone through potentiostatic control to produce a proton gradient has seen limited use as a method for triggering supramolecular gelation,[19,20] and it is not widely known to be a method that produces inherently unstable gels. However, having now repeatedly observed this phenomenon, a question is raised as to whether evidence of such instability of supramolecular hydrogels has been observed previously. Kubiak *et al.*[19] note an unusual observation during the electropolymerisation of Carb-Ala via cyclic voltammetry within 1 M perchloric acid. The authors first describe growing a supramolecular Carb-Ala gel with potentiostatic control of hydroquinone oxidation at a commercial gold disc macroelectrode, before elecropolymerising the pre-formed hydrogel over a period of 240 seconds using cyclic voltammery, cycling from below to above the oxidation potential of the Carb-Ala gelator.

Kubiak *et al.* make two important observations for the macroscale electropoylmerised Carb-Ala hydrogel. First, they note a gradual loss of current at the gold WE due to gelator oxidation/polymerisation and the evolution of a reversible redox wave corresponding to the newly formed polymer is seen in the CV. Second, they report a visible collapse of the hydrogel towards the surface of the WE during electrochemical polymerisation, and state the collapsed structure formed part of the dense polymer at the WE.[19] The timescale over which this physical change was observed by the authors is notably much shorter than similar processes documented in this thesis, taking place on the order of minutes in 1M perchloric acid at gold macroelectrodes,[19] in comparison to hours in a pH 4.3 buffer at a platinum electrode of comparable dimensions (Figure 4.8). This is surprising when considering that 1 M perchloric acid has a pH << 0,[21] well below the pK_a^{app} of Carb-Ala aggregates. Despite this, the supramolecular network of the gel produced by Kubiak *et al.* appears to be more unstable in such conditions, suggesting that the process may have been accelerated during cyclic voltammetry as the polymer forms.[19]

Additionally, though there is no statement from the authors on the following matter, their figure (labelled Fig. 2a in Kubiak *et al.*[19]) depicting the electropolymerisation of this gel also shows the gel undergoing a gradual increase in transparency, with the outline of the gel being faint yet still present at 240 seconds into their experiment.[19] The authors suggest here that the supramolecular Carb-Ala structures may have collapsed towards and become a part of the growing polymer at the gold WE surface.[19] However, this appears to be a similar change as observed for Carb-Ala gels in Section 4.2, which according to EIS data undergo a reduction in density (according to EIS data) concurrent with the increase in transparency, before a structural collapse occurs. Kubiak *et al.* therefore appear to be the first to record the same phenomenon presented in Section 4.2, though further investigation is still required to explain it.

The visual and electrochemical observations made in Section 4.2 have run contrary to the expectation that these electrochemical pH-triggered peptide-based hydrogels would be stable in acidic environments. A common factor featured in both this thesis and the work of Kubiak *et al*.[19] is an exchange of aqueous environment post-gelation, preceding supramolecular network breakdown. Here, two Carb-Ala gels have been grown via the

potentiostatic method established in Chapter 3, one of which is electropolymerised in the acid, and the stability of these two gels are compared in 1M $HCl_{(aq)}$.

4.3.1 Supramolecular Carb-Ala gels submerged in 1.0 M $HCl_{(aq)}$

The aim for this experiment is to determine whether the Carb-Ala gels retain density and size post-gelation, or whether the time taken for these gels to undergo the loss in density and size seen in different aqueous media in prior sections changes in an environment of lower pH. As modelled in Figure 3.10 (Chapter 3 Section 3.2.3), the pH within these gels should approximate to pH 1 during 120 seconds of potentiostatic (+0.7 V applied potential) gel growth. 1M $HCl_{(aq)}$ (pH < 1) has been chosen to simulate the pH drop produced at the Pt working microelectrode during the electrochemical oxidation of hydroquinone. However, introducing the FFC redox pair to a solution of pH < 1 produces cyanide gas,[22] therefore EIS with the FFC redox pair has not been conducted here. Visual observations of hydrogels submerged in solution via optical microscopy remain a viable option for investigating whether the Carb-Ala hydrogels are stable or unstable in highly acidic environments. A Carb-Ala hydrogel was grown by applying 0.7 V for 120 seconds within a 10 mg/mL Carb-Ala solution at a 25 µm diameter Pt disc microelectrode. The current-time transient and cumulative charge for the hydrogel growth step can be found below (Figure 4.19).

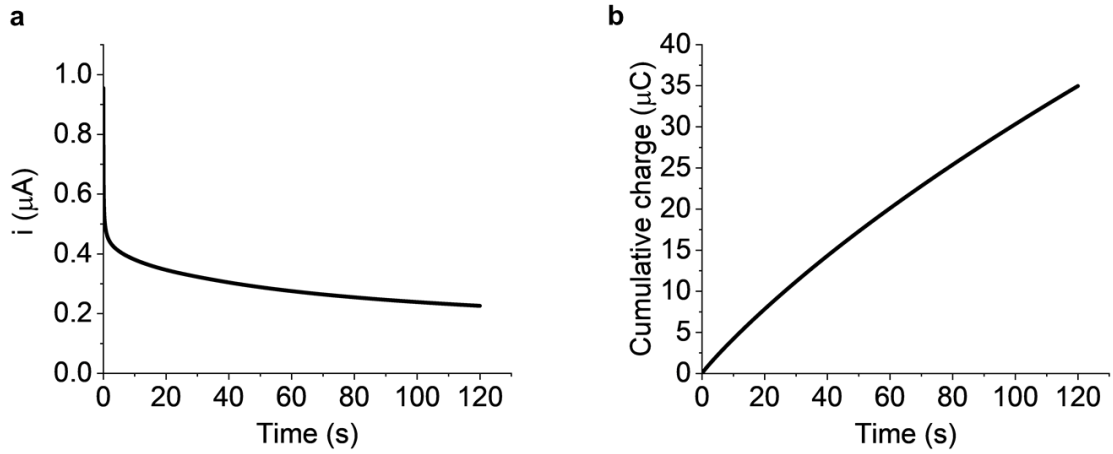

Figure 4.19 Current-time transient (a) and charge-time transient (b) (calculated by integrating area under current-time transients in (a)), recorded in 10 mL 10 mg/mL Carb-Ala gelator solution (pH 8) containing hydroquinone (67.5 mM) and NaCl (1 mM), at Pt microelectrode (25 µm diameter), 120 seconds at 0.7 V (stepped from open circuit potential), T = 25 °C.

The total charge passed for this gel growth experiment measured 35.0 µC (Figure 4.19b), in line with the average of 31.9 ± 4.0 µC (Table 3.12, Chapter 3 Section 3.5.5). This Carb-Ala gel was then submerged within 5 mL 1.0 M $HCl_{(aq)}$ solution (pH 0.2), and images of the gel were recorded, first in 10 minute intervals starting from t = 0 minutes, then in intervals of hours until 6 hours had elapsed (Figure 4.20). The visual observations made here are similar to those of the Carb-Ala hydrogel submerged in the pH 4.3 buffer in Section 4.2.1. An apparent loss in density through a shrinkage of a denser inner layer, separate from the "outer shell", can be seen from 30 minutes, and the shrinkage of the remaining structure post density-loss from 5 hours (Figure 4.20). This supports the supposition that these hydrogels are unstable in new aqueous environments ("new" in this case meaning any aqueous solution which does not

contain the gelator in the bulk solution). It is also interesting to see that these visual changes appear to occur over a much longer time period, with the gel retaining the same outer dimensions for 5 hours in the pH 0.2 solution (Figure 4.20), as oppose to beginning to shrink before the first 60 minutes in the pH 4.3 buffer (Figure 4.4). This suggests that pH of the environment plays a role in the stability of these materials, but that another mechanism is driving the loss of gel density even when the pH is far lower than the pK_a^{app} of the gelator.

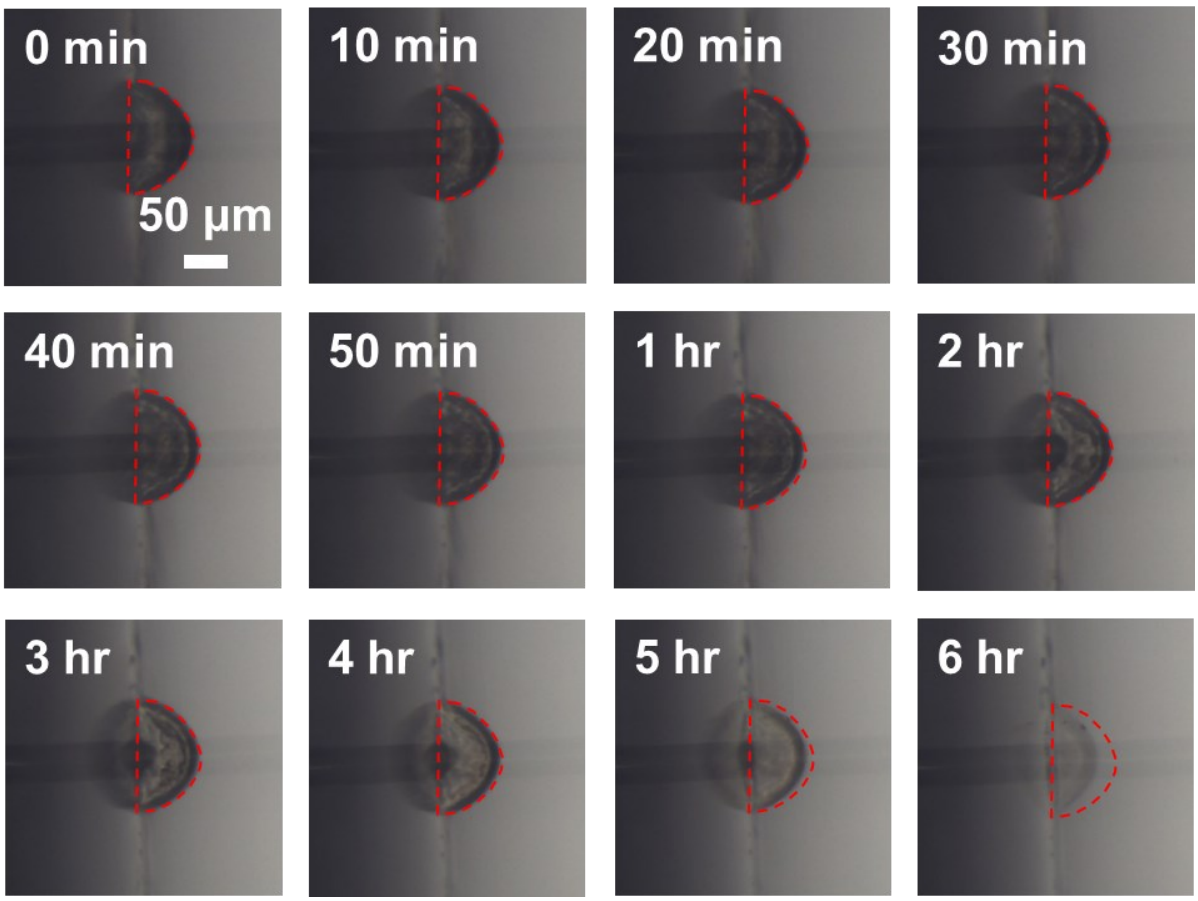

Figure 4.20 Images of Carb-Ala hydrogel at Pt microelectrode surface (25 µm) submerged in 1.0 M $HCl_{(aq)}$ (pH 0.2), side-on view, 100x magnification, post 0.7 V 120 second potentiostatic gel growth experiment. From top left to bottom right, in intervals of 10 minutes (from 0 minutes to 1 hour), then in intervals of hours (from 1 hours to 6 hours). A red dashed line corresponding to the cross-section of the original gel at 0 minutes is displayed in each image. Images showcase a gradual increase in transparency up to the 5 hour mark, followed by a significant decrease in gel size towards 6 hours.

4.3.2 Polymerised Carb-Ala gels submerged in 1.0 M $HCl_{(aq)}$

The electropolymerisation of Carb-Ala gels was then considered as a method of reducing the rate of gel loss or outright preventing the changes these gels would undergo after transfer to new aqueous solutions. Once more, a Carb-Ala hydrogel was grown by applying 0.7 V for 120 seconds within a 10 mg/mL Carb-Ala solution at a 25 µm diameter Pt disc microelectrode (Figure 4.21). As with the previous experiment, the charge passed due to hydroquinone oxidation here, 31.8 µC, also conformed with the average of 31.9 ± 4.0 µC from previous experiments (Table 3.12, Chapter 3 Section 3.5.5).

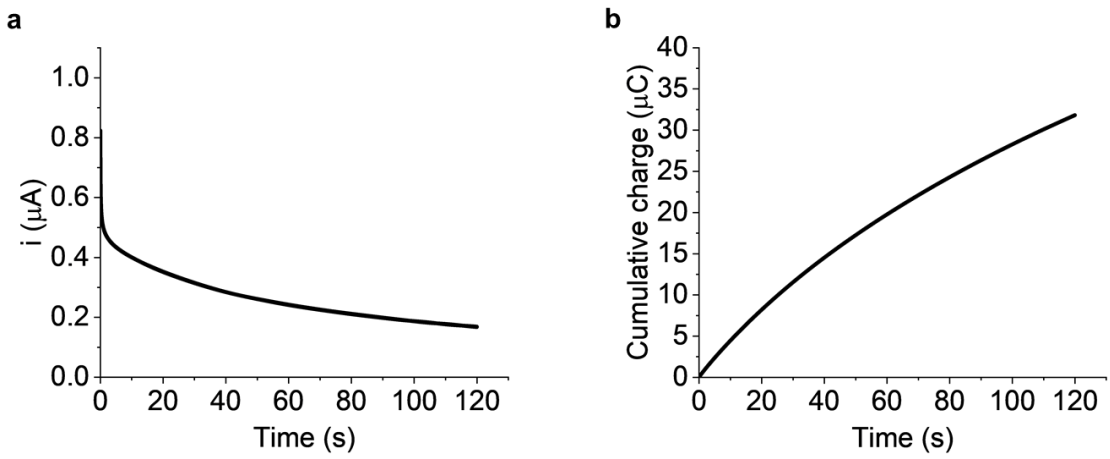

Figure 4.21 Current-time transient (a) and charge-time transient (b) (calculated by integrating area under current-time transients in (a)), recorded in 10 mL 10 mg/mL Carb-Ala gelator solution (pH 8) containing hydroquinone (67.5 mM) and NaCl (1 mM), at Pt microelectrode (25 μm diameter), 120 seconds at 0.7 V (stepped from open circuit potential), T = 25 °C.

The gel-coated Pt disc WE was then submerged in 5 mL 1.0 M $HCl_{(aq)}$ along with a CE and RE to complete a 3-electrode system, and imaged under microscopy (Figure 4.22). The dimensions of the hydrogel were measured, and were unsurprisingly found to be within expected dimensions for Carb-Ala gels grown under the same conditions (according to averages presented in Table 3.12, Chapter 3 Section 3.4.5): a width of 93.8 μm, height 55.0 μm, and cross-sectional area 3950 μm^2.

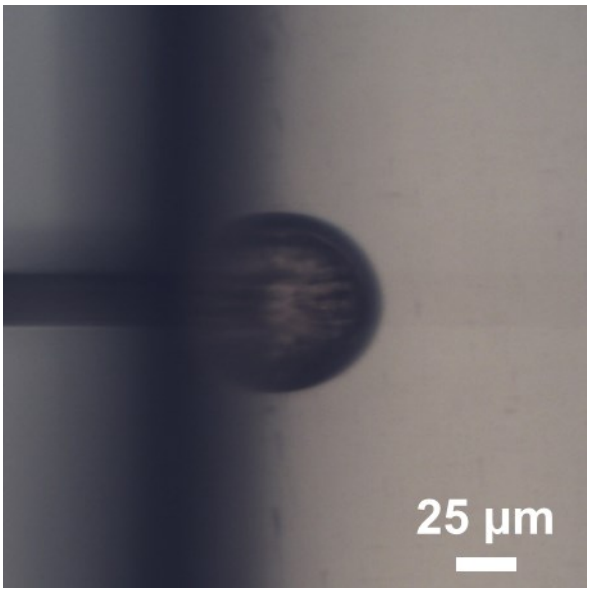

Figure 4.22 Image of Carb-Ala gel at commercial Pt microelectrode surface (25 μm diameter), grown at 0.7 V for 120 seconds, 25 °C. Side-on view, 100x magnification, submerged within 5 mL 1 M $HCl_{(aq)}$.

The irreversible oxidation of Carb-Ala begins at approximately +0.8 V (Figure 3.2, Chapter 3 Section 3.2). To compare with the observations made by Kubiak *et al.*[19], cyclic voltammetry was employed post-gelation to polymerise the pre-formed supramolecular hydrogel. *E* was

scanned between +0.6 V and +1.2 V to facilitate the polymerisation of Carb-Ala in a total of 10 cycles (Figure 4.23).

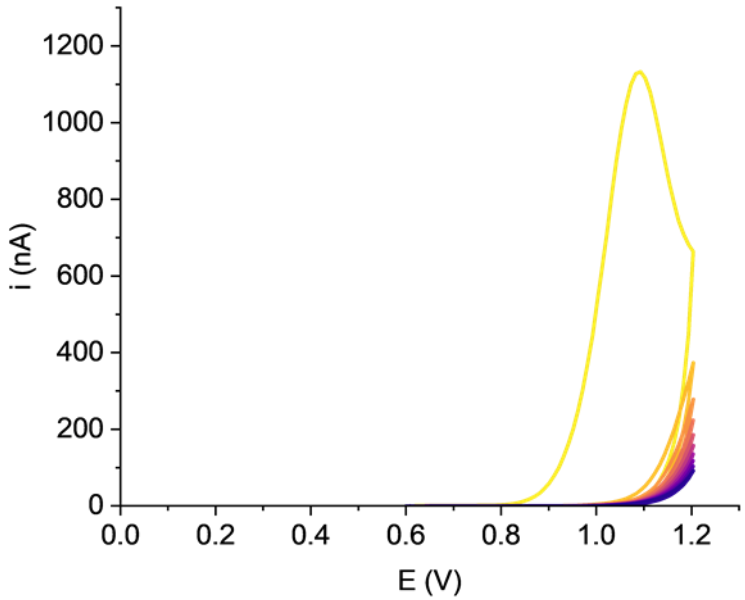

Figure 4.23 CV in 10 mL PBS (pH 7.4) at a Pt disc microelectrode (25 µm diameter) functionalised with an electrodeposited layer of supramolecular Carb-Ala hydrogel (see Figure 4.21), starting potential E = 0.6 V, E scanned between 0.6 V and 1.2 V, initial scan direction positive, scan rate v = 0.1 V s^{-1}, T = 25 °C. 10 cycles total, colour gradient of lighter (yellow) to darker (purple) plots corresponds to initial to final scans.

The initial scan (yellow, Figure 4.23) displays no current in the positive direction until an irreversible peak begins at +0.8 V, reaching a maximum current of 1.1 µA at +1.1 V. This peak is characteristic of the electrochemical oxidation of the Carb-Ala gelator (Figure 3.2, Chapter 3 Section 3.2.1). After this peak, and on the reverse of this initial scan, current continues to drop towards 0 A. From the second scan onward, the irreversible peak cannot be seen, and currents reach a maximum at +1.2 V, dropping from 370 nA on the second scan to 90 nA on the final tenth scan. This change from the first to second scan indicates a sudden depletion of available Carb-Ala to react near the electrode surface, and that all available Carb-Ala had been oxidised on the first scan. Images of the hydrogel submersed in the 1 M $HCl_{(aq)}$ were then recorded every hour under microscopy, initially over 6 hours (Figure 4.24).

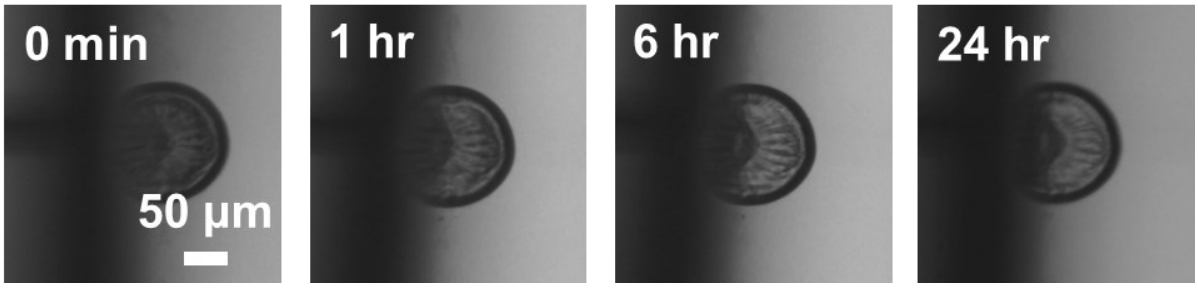

Figure 4.24 Images of polymerised Carb-Ala hydrogel at Pt microelectrode surface (25 µm) submerged in 1.0 M $HCl_{(aq)}$ (pH 0.2), side-on view, 100x magnification, post 0.7 V 120 second potentiostatic gel growth experiment. Images showcase a slight increase in transparency in the first hour and no change in gel dimensions over 24 hours of submersion in the acid.

An increase in gel transparency was observed in the first hour of submersion, however beyond this time no additional changes to transparency were apparent (Figure 4.24). Furthermore, the gel retained the same shape and size recorded pre-electropolymerisation for the first 6 hours it was submerged in the pH 0 environment. The submersion time was extended to 24 hours to see if any further changes would occur over a longer period of time, though after a day in the 1 M $HCl_{(aq)}$ the gel had not become more transparent nor changed in shape or size. As noted in Section 4.3, the macroscale Carb-Ala gel described by Kubiak *et al.*[19], which was electropolymerised using the same methodology within a far more acidic 1 M percholoric acid solution, underwent a collapse of structure towards the electrode surface. It is surprising that such a collapse or any shrinkage was not observed here for the microscale Carb-Ala gel (Figure 4.24). This implies that the process of electropolymerisation had occurred throughout the gel rather than only directly at the electrode surface (as is suggested to occur at the macroelectrode in the work of Kubiak *et al.*[19]). The mechanism for this process is unclear.

4.4 Summary

The experiments detailed in this chapter show that peptide-based supramolecular hydrogels grown via the potentiostatically controlled oxidation of hydroquinone are unstable when introduced to new aqueous environments. Carb-Ala and BrAV hydrogels grown at Pt disc microelectrodes and macroelectrodes appear to undergo a change from a translucent to transparent material in a pH 4.3 buffer. This process has also been shown to occur for microscale gels transferred to a pH 0 unbuffered solution, well below gelator pK_a^{app}, over a greater time period than in the pH 4.3 buffer. The transition towards increased transparency starts from the outer boundary of the gel and the surrounding aqueous medium, moving towards the surface of the electrode. This process precedes a shrinkage of the overall structure to a final smaller size. In line with the changes to gel opacity, diffusion coefficients calculated from EIS data of these submerged gels suggest a reduction in network density, as D_L and D_{NL} for the FFC redox pair increase over time towards values that more closely resemble those recorded at the bare electrodes.

The rate at which this visible change occurs seems to be affected by the pH of the new environment, with a lower pH solution slowing the rate of increase in transparency and subsequently delaying the shrinkage of the gel. The equilibrium between protonated and deprotonated gelator aggregates being shifted to either side by a modulation in environment pH is not surprising, given how the hierarchical self-assembly of gelator molecules is dependent on the degree gelator/aggregate protonation.[23–25] If lowering the environment pH well below gelator pK_a^{app} does not fully prevent the loss in gel density with time, this suggests that the change in environment from the gelator solution is a driving mechanism for the loss in density and eventual shrinkage. The gels featured in this chapter have all been transferred from a 10 mg/mL aqueous solution to a different aqueous solution with no gelator in the bulk.

The reduction in gel density with time, paired with a visual change in opacity before a shrinking of the structure, could be interpreted as syneresis (as described in Section 4.3, Figure 4.18) if it is assumed that aggregate rearrangement leads to an opening-up of space between aggregates within the gel. Alternatively, an internal loss of gel mass over time followed by a collapse of the remaining structure could also explain these observed changes to the gel (Figure 4.25). It may be possible for the aggregates in these gel networks to disentangle and diffuse into the new aqueous environment, driven by a concentration gradient between the gel-coated electrode surface and the bulk solution where the initial bulk concentration of gelator is nil. Further study would be required to confirm or deny either of these mechanisms for this unexpected phenomenon.

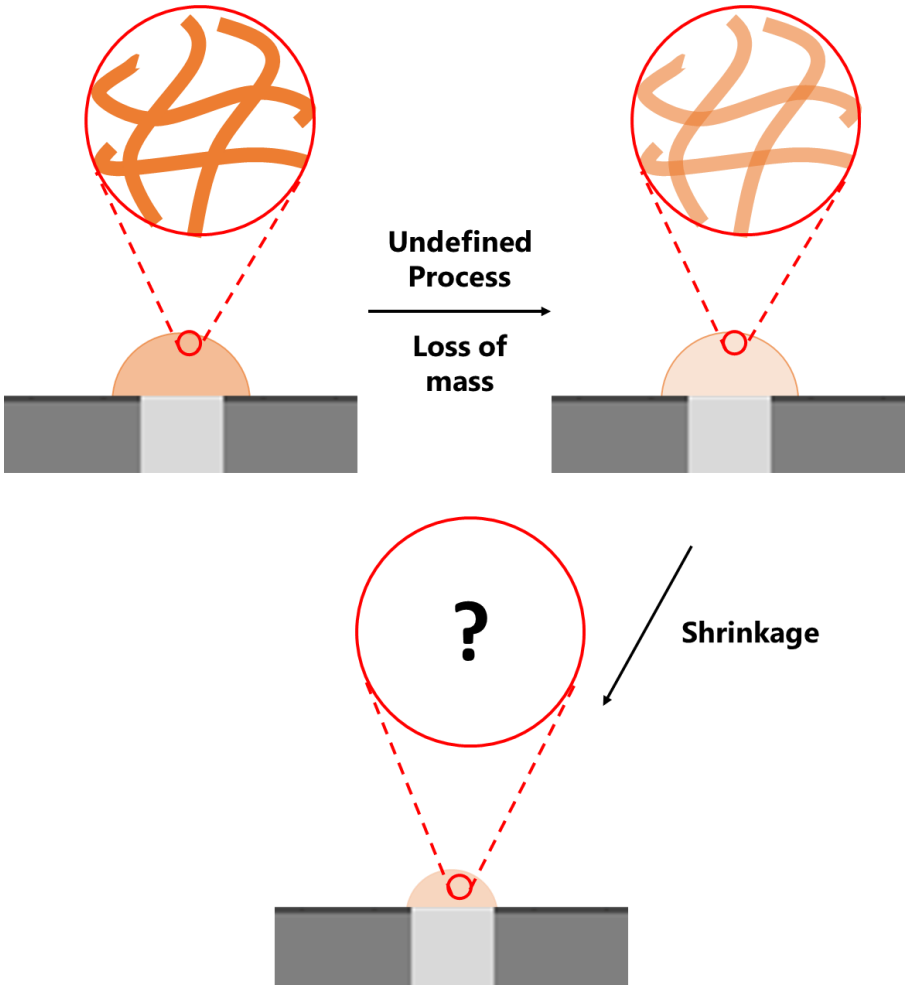

Figure 4.25 Graphical depiction of electrochemical pH-triggered gel density loss and shrinkage with loss of gelator mass. An unconfirmed postulation to the observations of experimental work in Section 4.2, where EIS data indicates a loss in hydrogel density with time, whilst visual information recorded in tandem shows these gels shrink after a period of density loss.

The instability of these supramolecular hydrogels in aqueous media does not lend well to the prospect of their long-term use as anti-fouling layers. Even if the gel density/porosity and size can be controlled and allow them to function well as semi-permeable membranes, their temporal nature is likely to extend to biological media, at least without further treatment. Fortunately, the electropolymerisation of microscale Carb-Ala gels post-supramolecular assembly could allow them to be used more reliably as semi-permeable membranes to trap or prevent the transport of large molecules without breaking down over time. Electropolymerisation has also been shown to retain the overall shape of the microscale supramolecular gels, which suggests that the internal gel matrix layout may also be retained to a certain degree. It is for this reason that the next chapter of this thesis focusses on the functionality of electropolymerised Carb-Ala gels in a simple, 1st generation biosensing application.

4.5 References

1 A. Piper, B. M. Alston, D. J. Adams and A. R. Mount, *Faraday Discuss.*, 2018, **210**, 1–17.

2 H. T. Imam, P. C. Marr and A. C. Marr, *Green Chem.*, 2021, **23**, 4980–5005.

3 D. Grieshaber, R. MacKenzie, J. Vörös and E. Reimhult, *Sensors*, 2008, **8**, 1400–1458.

4 E. K. Johnson, D. J. Adams and P. J. Cameron, *J. Am. Chem. Soc*, 2010, **132**, 5130–5136.

5 S. Wu, K. Yan, Y. Zhao, C. C. Tsai, J. Shen, W. E. Bentley, Y. Chen, H. Deng, Y. Du, G. F. Payne and X. Shi, *Adv. Funct. Mater.*, 2018, **28**, 1–12.

6 S. R. Corrie, J. W. Co, J. Islam, K. A. Markey and M. A. F. Kendall, *Analyst*, 2015, **140**, 4350–4364.

7 A. Z. Cardoso, A. E. Alvarez Alvarez, B. N. Cattoz, P. C. Griffiths, S. M. King, W. J. Frith and D. J. Adams, *Faraday Discuss.*, 2013, **166**, 101–116.

8 M. Wallace, J. A. Iggo and D. J. Adams, *Soft Matter*, 2015, **11**, 7739–7747.

9 J. R. Macdonald, W. B. Johnson, I. D. Raistrick, D. R. Franceschetti, M. C. H. McKubre, D. D. Macdonald, B. Sayers, N. Bonanos, B. C. H. Steele, E. P. Butler, W. L. Worrell, A. Goossens, E. Barsoukov, B. E. Conway and N. Wagner, *Impedance Spectroscopy Theory, Experiment, and Application*, John Wiley & Sons, Hoboken, New Jersey, 2nd edn., 2005.

10 S. J. Konopka and B. Mcduffie, *Anal. Chem.*, 1970, **42**, 1741–1746.

11 B. Roffel and J. J. van de Graaf, *J. Chem. Eng. Data*, 1977, **22**, 300–302.

12 M. G. F. Angelerou, A. Sabri, R. Creasey, P. Angelerou, M. Marlow and M. Zelzer, *Chem. Commun.*, 2016, **52**, 4298–4300.

13 M. G. F. Angelerou, B. Yang, T. Arnold, J. Rawle, M. Marlow and M. Zelzer, *Soft Matter*, 2018, **14**, 9851–9855.

14 J. Raeburn, B. Alston, J. Kroeger, T. O. McDonald, J. R. Howse, P. J. Cameron and D. J. Adams, *Mater. Horizons*, 2014, **1**, 241–246.

15 C. Patterson, B. Dietrich, C. Wilson, A. R. Mount and D. Adams, *Soft Matter*, 2022, **18**, 1064–1070.

16 Y. Saito, *Rev. Polarogr.*, 1968, **15**, 177–187.

17 D. J. Adams, L. M. Mullen, M. Berta, L. Chen and W. J. Frith, *Soft Matter*, 2010, **6**, 1971–1980.

18 K. McAulay, L. Thomson, L. Porcar, R. Schweins, N. Mahmoudi, D. J. Adams and E. R. Draper, *Org. Mater.*, 2020, **2**, 108–115.

19 P. S. Kubiak, S. Awhida, C. Hotchen, W. Deng, B. Alston, T. O. McDonald, J. Adams and P. J. Cameron, *Chem. Commun.*, 2015, **51**, 10427–10430.

20 V. Lakshminarayanan, L. Poltorak, E. J. R. Sudhölter, E. Mendes and J. van Esch, *Electrochim. Acta*, 2020, **350**, 136352–136362.

21 A. Trummal, L. Lipping, I. Kaljurand, I. A. Koppel and I. Leito, *J. Phys. Chem. A*, 2016,

120, 3663–3669.

22 P. L. Domingo, B. Garcia and J. M. Leal, *Can. J. Chem.*, 1990, **68**, 228–235.

23 L. A. Estroff and A. D. Hamilton, *Chem. Rev.*, 2004, **104**, 1201–1217.

24 K. Kajiwara, in *Gels Handbook Vol. 1*, eds. Y. Osada, K. Kajiwara, T. Fushimi, O. Irasa, Y. Hirokawa, T. Matsunaga, T. Shimomura, L. Wang and H. Ishida, Elsevier, 1st edn., 2001, pp. 122–171.

25 P. Terech and R. G. Weiss, *Chem. Rev.*, 1997, **97**, 3133–3159.

26 M. Criado-Gonzalez, J. Y. Runser, A. Carvalho, F. Boulmedais, P. Weiss, P. Schaaf and L. Jierry, *Polymer (Guildf).*, 2022, **261**, 125398–125404.

27 J. J. Panda, A. Mishra, A. Basu and V. S. Chauhan, *Biomacromolecules*, 2008, **9**, 2244–2250.

28 E. R. Draper, B. Dietrich, K. McAulay, C. Brasnett, H. Abdizadeh, I. Patmanidis, S. J. Marrink, H. Su, H. Cui, R. Schweins, A. Seddon and D. J. Adams, *Matter*, 2020, **2**, 764–778.

29 E. R. Cross, S. M. Coulter, A. M. Fuentes-Caparrós, K. McAulay, R. Schweins, G. Laverty and D. J. Adams, *Chem. Commun.*, 2020, **56**, 8135–8138.

30 K. McAulay, H. Wang, A. M. Fuentes-Caparrós, L. Thomson, N. Khunti, N. Cowieson, H. Cui, A. Seddon and D. J. Adams, *Langmuir*, 2020, **36**, 8626–8631.

31 A. M. Fuentes-Caparrós, F. De Paula Gómez-Franco, B. Dietrich, C. Wilson, C. Brasnett, A. Seddon and D. J. Adams, *Nanoscale*, 2019, **11**, 3281–3291.

Chapter 5 – Carb-Ala hydrogels as enzyme encapsulation agents and semi-permeable membranes in 1st generation glucose biosensing

5.1 Introduction

As covered in Chapter 4, electrochemically-grown peptide-based supramolecular hydrogels were found to be unstable when transferred to new aqueous media, losing mass over a period of hours even in environments where the pH was far below the pK_a^{app} of the gelator. This is an undesirable trait from the perspective of applying these materials as stable enzyme-encapsulating and anti-fouling membranes at electrochemical biosensors, as gel decomposition is also expected to lead to a loss of biosensor function via enzyme leaching. However, another path towards stabilising supramolecular gels (Carb-Ala in particular) for use as tuneable anti-fouling membranes lies in electropolymerisation. By intentionally polymerising self-assembled Carb-Ala gelator units, a new material which is far more resistant to degradation could be produced, potentially with the added benefit of retaining the diffusional properties of the electrochemically-tuned supramolecular gel.

Chronopotentiometry has been used in several works to control the electrochemical pH-triggered self-assembly of peptide-based gelators.[1–4] A fixed current ensures that a constant rate of proton generation is provided for the continued growth of hydrogels over extended periods of time at macroelectrodes.[2] The degree of supramolecular assembly can be controlled under this galvanostatic method by fixing the current applied and the time for which that current is applied for. However, the potential at the WE must increase over time to enable the fixed current, and species with greater oxidative potentials (such as the gelator and H_2O) will progressively react. Hydroquinone oxidation still occurs up to and beyond the redox potential of the gelator under the galvanostatic method, but that means that the electrochemistry of both species will occur simultaneously. In the case of Carb-Ala, electropolymerisation then also occurs when using chronopotentiometry, and as demonstrated by Piper *et al.* when growing Carb-Ala gels at nanoelectrode surfaces.[1] This means that gel growth via protonation can become convoluted with electropolymerisation under this method.

Alternatively, Carb-Ala electropolymerisation can be induced post-gelation to enable greater control of this electrochemical reaction. As discussed in Chapter 4 Section 3, Kubiak *et al.* describe transferring a gel-coated electrode to a separate solution (without gelator) post-gelation, and inducing polymerisation at the gel-coated WE using cyclic voltammetry within a narrow oxidative potential window.[5] This method separates the two electrochemical processes, by preventing further electrodeposition of Carb-Ala aggregates (due to switching to a solution without gelator). Electropolymerisation can then be seen through gradually decreasing peak redox currents in each consecutive voltammogram cycle. For these reasons, this method has been employed in the work presented in this chapter as the method of choice for the trapping of glucose oxidase (GOx) at electrode surfaces.

First generation glucose biosensing with GOx is a well-established, relatively inexpensive method to test the performance of novel biocompatible enzyme-entrapment layers such as Carb-Ala, and so forms the basis of all biosensing responses shown in this chapter. Many new glucose biosensors have been developed in recent years, and their properties have been documented and collated in comprehensive literature reviews.[6–9] Unsurprisingly, the methods of production, the materials used, and the methods of characterisation vary tremendously between studies, as do sensor properties such as sensitivity and operational stability. Though it would be ideal to only draw comparisons with recently developed 1st generation enzymatic glucose biosensors that have been characterised in PBS, studies featuring these sensors make up a very small fraction of all publications in this field. Given such variety, other amperometric glucose biosensors with GOx enzyme as the recognition agent have been considered when discussing the sensing properties of the microelectrodes presented in this chapter.

This chapter develops a method for producing functional microelectrode glucose biosensors prepared with drop-coated GOx enzyme layers covered with electropolymerised Carb-Ala hydrogel. The sensitivity, lifetime/operational stability, and limit of detection of these sensors are documented, and the properties of these sensors have been compared to other recently developed enzymatic, amperometric glucose biosensors. Lastly, a second batch of glucose biosensors has been prepared with non-polymerised supramolecular Carb-Ala films, to confirm a hypothesis (based on the findings in Chapter 4) that such sensors will not function as effectively as the sensors with polymerised Carb-Ala gel layers due to gel instability.

5.2 Preparing 1st generation glucose microelectrode biosensors with GOx trapped under electropolymerised Carb-Ala hydrogels

5.2.1 Electropolymerising Carb-Ala gels at GOx drop-coated microelectrodes

A 25 µm diameter Pt disc microelectrode was functionalised by first drop-coating the Pt surface (and surrounding glass casing flush with the metal) with 10 µL of a thawed (from -20 °C storage) 10 mg/mL GOx solution (Chapter 2 Section 2.4.5). The droplet of enzyme solution was allowed to dry open to air (ambient temperature 16-20 °C) over 24 hours. Over this time it evaporated to leave a thin yellow coat of hydrated GOx at the electrode surface. The enzyme-coated microelectrode was subsequently incorporated as the WE of the three-electrode system (Figure 2.17, Chapter 2 Section 2.5.2), which was then lowered into 1 mL of a 10 mg/mL Carb-Ala gelator solution with hydroquinone (for composition, see Chapter 2 Section 2.4.2). A pre-potential of +0.3 V was applied at the GOx-coated microelectrodes as the three-electrode system was lowered into solution. This was done as a precaution to mitigate enzyme leaching by introducing electrostatic attraction (and thus better adherence) between the overall negatively charged GOx enzyme and the Pt surface.[10,11] The potential was then switched to +0.7 V, approximately 5 seconds after initiating submersion, to initiate gel growth. This +0.7 V potential was fixed for a total of 120 seconds, and the current-time transient for this experiment can be found below (Figure 5.1), compared to similar transients at non-functionalised Pt surfaces with and without the gelator in solution.

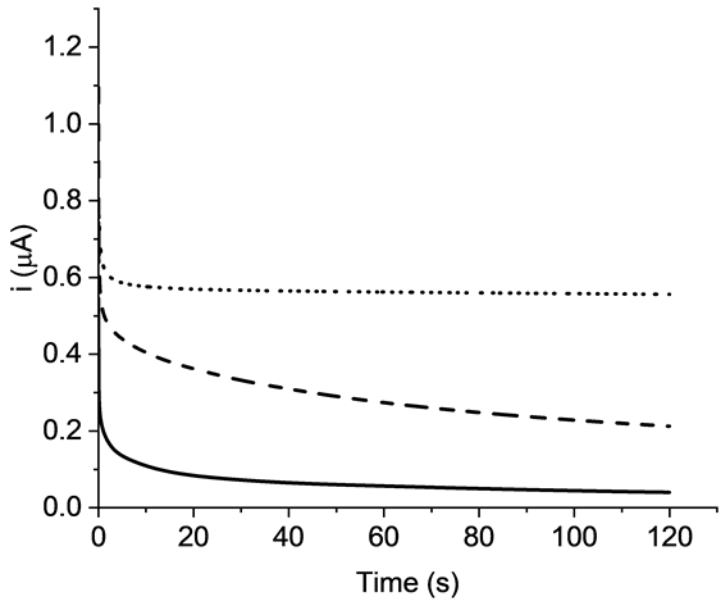

Figure 5.1 Comparison of current-time transients in 1 mL aqueous solutions (pH 8) at Pt microelectrodes (25 µm diameter), 120 seconds at 0.7 V (time measured after stepping from open circuit potential), T = 25 °C. Solid line = 10 mg/mL Carb-Ala gelator (34 mM), hydroquinone (67.5 mM) and NaCl (1 mM) at GOx drop-coated Pt surface; dashed line = 10 mg/mL Carb-Ala gelator (34 mM), hydroquinone (67.5 mM) and NaCl (1 mM) at clean Pt surface; dotted line = hydroquinone (67.5 mM) and NaCl (1 mM) at clean Pt surface.

The bare Pt microelectrode in the solution without gelator produced a steady-state current typical of a microelectrode, whilst the initially bare microelectrode in the gelator solution showed signs of gradual surface passivation with gel growth (Figure 5.1). In contrast, the gel-growth currents arising from hydroquinone oxidation at the microelectrode with the drop-coated GOx layer rapidly decreased compared to these initially bare electrodes. For example, currents at the GOx drop-coated microelectrode can be seen to have dropped below 0.1 µA 10 seconds into the transient (solid line, Figure 5.1), whereas currents at bare Pt microelectrode surfaces with and without the Carb-Ala gelator in solution measured 0.4 µA and 0.6 µA at this time (dashed and dotted lines respectively, Figure 5.1). Neither of these two transients for the initially bare electrodes gave currents as low as 0.1 µA in the 120 seconds timeframe. This indicates that the Pt surface of the GOx drop-coated electrode was still coated with the electrostatically-adhered GOx enzyme prior to initiating the electrochemically-controlled gelation of Carb-Ala. An image was then recorded of the resulting gel to inspect the effect this reduced hydroquinone oxidation had on the resulting gel (Figure 5.2).

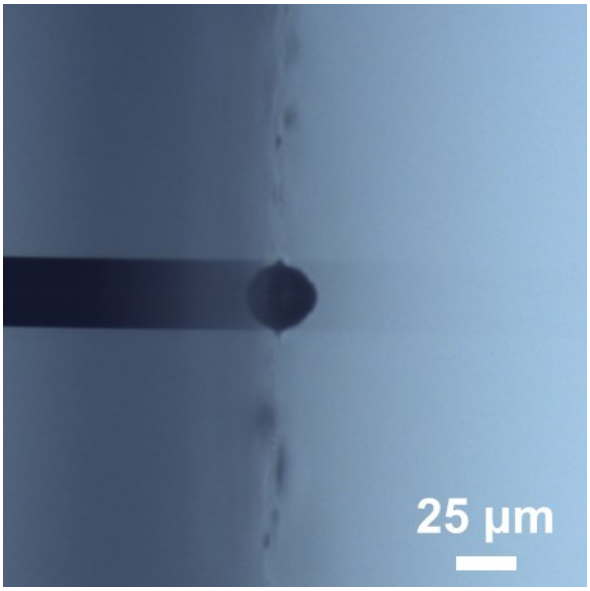

Figure 5.2 Example image of a Carb-Ala gel grown at a GOx drop-coated commercial Pt microelectrode surface (25 µm diameter), at 0.7 V for 120 seconds, 25 °C. Side-on view, 100x magnification. The gel can be seen protruding from the electrode surface (right of image). Note the Pt wire within the electrode glass casing, and the reflection of the hemispherical gel within the glass (left side of image).

The resulting size of the gel layer grown at the GOx-coated microelectrode was far smaller than Carb-Ala gels grown under the same electrochemical technique at the bare electrode. The measured dimensions of this gel were a width of 35.8 µm, a height of 18.8 µm, and a cross-sectional area of 466 μm^2 (Figure 5.2). In comparison, the gels grown at the bare surface measured linear dimensions that were on average three times the scale of this gel (Table 3.12, Chapter 3 Section 3.4.5). As with the current-time transient (Figure 5.1), these differences serve to highlight how the adsorbed GOx greatly affects the hydroquinone oxidation rate, and thus the rate of proton generation and resulting gel size. This again suggests that the GOx enzyme was successfully adhered to the Pt surface pre-gelation.

The three-electrode system with the GOx/Carb-Ala functionalised Pt working microelectrode was then transferred to a 10 mL solution of pH 7.4 PBS (Chapter 2 Section 2.4.3). PBS is selected here due to it being a common buffer medium used to represent the pH of human whole blood and interstitial fluid,[7,12] though it is important to also recognise that GOx from Aspergillus niger has an optimal operating pH range of 3.5-6.5.[13] Given the established instability of the hydrogel after exchanging the aqueous environment from the gelator solution to the buffer (as discussed in Chapter 4), cyclic voltammetry was promptly initiated upon submersion in order to electropolymerise the pre-deposited supramolecular gel directly at the electrode surface and form a more stable layer around the enzyme. As first described in Chapter 4 Section 4.3.2, *E* was scanned between +0.6 V and +1.2 V for a total of ten cycles to electropolymerise the Carb-Ala gel (Figure 5.3).

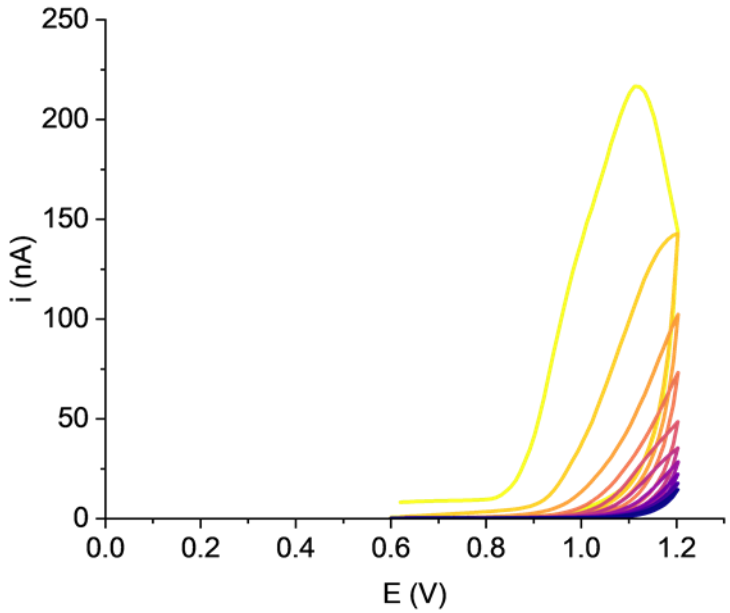

Figure 5.3 CV in 10 mL PBS (pH 7.4) at a Pt disc microelectrode (25 µm diameter) functionalised with a drop-coated layer of GOx enzyme and electrodeposited layer of supramolecular Carb-Ala hydrogel (see Figure 5.1), starting potential E = 0.6 V, E scanned between 0.6 V and 1.2 V, initial scan direction positive, scan rate v = 0.1 V s^{-1}, T = 25 °C. 10 cycles total, colour gradient of lighter (yellow) to darker (purple) plots corresponds to initial to final scans.

In the initial cycle of the CV, the chemically irreversible oxidation peak characteristic of electropolymerisation was visible near +1.1 V (yellow line, Figure 5.3), and this peak progressively disappeared in subsequent scans. The maximum current at this peak measured 225 nA, much lower than the peak current of 1.1 µA measured for the electropolymerisation of the Carb-Ala gel at the initially bare Pt microelectrode in Chapter 4 Section 4.3.2. This is consistent with the observations from the current-time transient during gel growth and microscope image (Figure 5.1 and Figure 5.2), that the amount of Carb-Ala deposited at the GOx-coated electrode surface was much less than at the bare Pt electrodes, so the maximum current due to Carb-Ala oxidation would likewise be less (with less deposited gelator available to oxidise).

The GOx/Carb-Ala polymer functionalised microelectrode was allowed to rest in the 10 mL PBS solution for 2 hours after these ten cycles were completed. This was done to provide ample time for any remaining unstable supramolecular network and loosely adhered GOx to diffuse into solution, with the intention of leaving only polymerised Carb-Ala and polymer-encapsulated GOx at the electrode surface. The three-electrode system was then transferred to a pH 4.3 buffered ferrocyanide solution and EIS was conducted (see Chapter 2 Section 2.4.4 for protocol). The Nyquist plot of the functionalised microelectrode was fitted to the established modified Randles circuit (see Figure 2.11, Chapter 2 Section 2.2.6) using the established Nova software method of fixing the R_S component to that of the weighted fit and then excluding the weight factor when fitting (Figure 5.4, Table 5.1).

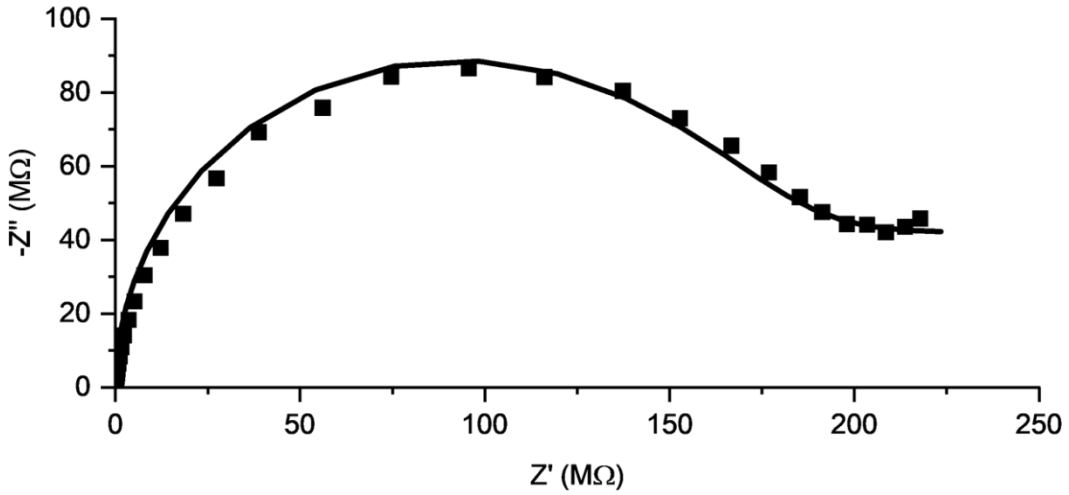

Figure 5.4 Nyquist plot of Pt microelectrode (25 µm diameter) functionalised with a GOx drop-coat and covered with an electropolymerised layer of Carb-Ala gel, in pH 4.3 buffered ferrocyanide solution, T = 25 °C. Scatter points represent recorded impedance, lines represent unweighted fitted data with R_S values fixed to the weighted R_S values using the modified Randles circuit (Figure 2.11, Chapter 2 Section 2.2.6).

The magnitudes of real and imaginary impedance for both axes of the above Nyquist plot (Figure 5.4) are far greater than previously seen for microelectrodes coated solely with potentiostatically grown Carb-Ala gels. The fitted value of R_{CT} for this GOx/Carb-Ala polymer microelectrode is strikingly large at 162 MΩ (Table 5.1). This is three orders of magnitude greater than for comparative gel-coated, non-polymerised, no GOx Pt microelectrodes; average R_{CT} for gels grown at 0.7 V for 120 seconds measured 583 ± 239 kΩ, and those grown at 1.0 V for 120 seconds (which allowed for Carb-Ala polymerisation during gel growth) measured 974 ± 595 kΩ (Table 3.17, Chapter 3 Section 3.4.10). As charge transfer is an electrode surface process, this difference suggests that electrode surface passivation is far more pronounced after enzyme drop-coating, gelation and electropolymerisation than after just gelation and electropolymerisation. In contrast, R_S here is only slightly higher at 34.0 kΩ (Table 5.1), slightly larger than the average for the 120 second 0.7 V gels at 18.2 ± 0.7 kΩ, though within two standard deviations of the 120 second 1.0 V gels at 24.9 ± 5.3 kΩ (Table

3.17, Chapter 3 Section 3.4.10). It is interesting to see R_S for the post-gelation polymerised gel and the 1.0 V gels to be so similar, as this would suggest that the ionic conductivity and permeation in the polymerised Carb-Ala gel layer in these two cases is similar.

Table 5.1 Data and estimated errors for GOx/Carb-Ala polymer functionalised 25 µm diameter Pt disc electrodes. Feature, EIS data of gel functionalised microelectrodes fitted to the modified Randles circuit (Figure 2.11, Chapter 2 Section 2.2.6) with weight factor not applied (as shown in Figure 5.4), R_S value fixed (italicised). D_L and D_{NL} are calculated using Equation 2.29 and Equation 2.31 respectively.

25 µm dia. Pt disc micro., functionalised with drop-coated GOx sensing layer and electropolymerised Carb-Ala protective layer	
Component	
R_S **(kΩ)**	*34.0*
C_{DL} **(pF)**	253 ± 3
R_{CT} **(MΩ)**	164 ± 2
Y_0 **(nS)**	12.0 ± 1.0
R_{NL} **(MΩ)**	181 ± 17
χ^2	0.0534
D_L **(× 10^{-10} m^2 s^{-1})**	0.068 ± 0.011
D_{NL} **(× 10^{-10} m^2 s^{-1})**	0.117 ± 0.011

The components pertaining to diffusion also reflect a significant decrease in transport for the FFC pair through the GOx/Carb-Ala polymer to the functionalised WE. Y_0 and R_{NL} values for this GOx/Carb-Ala polymer functionalised microelectrode translate to D_L and D_{NL} of 0.068 and 0.117 × 10^{-10} m^2 s^{-1} respectively (Table 5.1). These are an order of magnitude lower than D_L and D_{NL} values calculated at Pt microelectrode surfaces with non-polymerised supramolecular Carb-Ala gels (Table 3.17, Chapter 3 Section 3.4.10). Overall, mass transport of the FFC redox pair at this test 1st generation glucose biosensor microelectrode is heavily reduced by a combination of the polymer and enzyme, suggesting a far less open structure than the supramolecular gels and/or a reduced electrode surface area due to passivation.

To establish the presence of active GOx and to determine a relation between concentration of glucose and magnitude of current due to generated H_2O_2 oxidation, CVs were recorded in 10 mL PBS solutions at varied concentrations of dissolved glucose substrate at 37 °C (Figure 5.5). This temperature, though slightly outside the optimum operating temperature of GOx

derived from A. niger of 40-60 °C,[14] was chosen to gauge the efficacy of the 1st generation biosensor by matching the internal temperature of the human body. Three of these solutions were prepared, without excluding oxygen from the PBS: one containing 0 mM glucose, another 5 mM glucose (9.95 mL PBS, 50 uL 1M glucose, simulating normal concentrations in human blood[9]), and another 100 mM glucose (9 mL PBS, 1 mL 1 M glucose). The three-electrode system was allowed to sit in each solution at 37 °C for 40 seconds before a CV was recorded. This interval was introduced as a standard procedure to allow a sufficient concentration of H_2O_2 to build up at the electrode surface (Chapter 2 Section 2.3.5) for a reproducible current response. The optimum H_2O_2 electro-oxidation potential was expected to be +0.6 V at a Pt WE against Ag/AgCl/Cl^- (3M),[15–18] so scans were conducted in the range of 0 V to +1.0 V, at 10 mV s^{-1} to capture the peroxide redox wave arising from glucose oxidation catalysed by GOx.

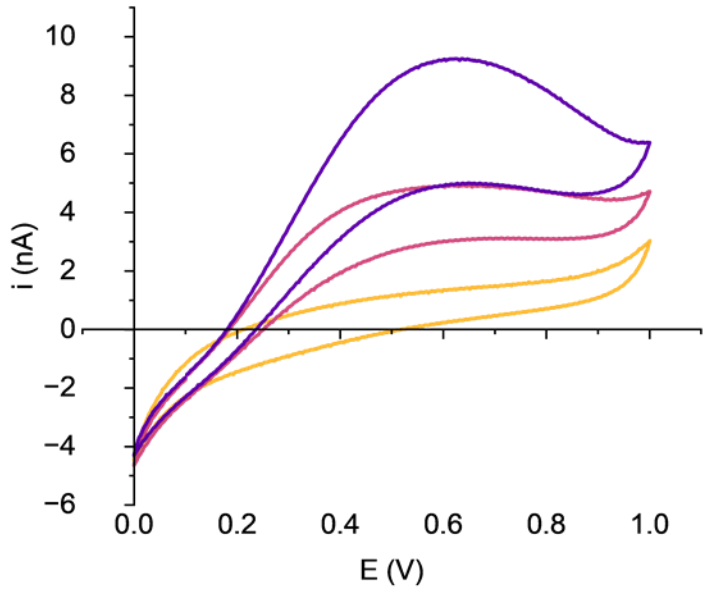

Figure 5.5 CVs in 10 mL buffered aqueous solutions (pH 7.4), at a Pt disc microelectrode (25 µm diameter), with starting potential E = 0 V, starting potential E = 0 V, E scanned between 0 V and 1.0 V, initial scan direction positive, scan rate v = 10 mV s^{-1}, T = 37 °C. Yellow line = 0 mM glucose; magenta line = 5 mM glucose; purple line = 100 mM glucose.

The presence of glucose was confirmed in the 5 mM and 100 mM glucose solutions through a significant and successive increase in currents compared to the 0 mM solution. A plateau in the forward scan can be seen at approximately +0.6 V in the voltammogram for the 5 mM glucose solution (magenta line, Figure 5.5), and in the 100 mM solution a peak at this potential is even more pronounced (purple line, Figure 5.5). This potential corresponds to the potential at which maximum steady state oxidation of H_2O_2 was achieved at Pt against a Ag/AgCl/Cl^- (3M) reference,[19] confirming this is due to peroxide, and thus was chosen as the potential to apply at the WE in later experiments to detect the presence of and measure the amount of glucose dissolved in solution. At +0.6 V in the forward scans, currents measured 1.36 nA in the solution containing 0 mM glucose, 4.90 nA in the 5 mM solution, and 9.21 nA in the 100

mM solution (Figure 5.5). That the CV recorded in the 0 mM solution shows a significant current at all voltages including +0.6 V, dependent on scan direction (though one order of magnitude lower than those recorded in the solutions containing glucose), indicates that non-Faradaic double layer charging is also contributing to the baseline response.

5.2.2 Calibration curves for GOx/Carb-Ala polymer functionalised microelectrodes

As described in Section 5.2.1, two more (for a total of three) 25 µm diameter Pt disc microelectrodes were functionalised via the sequential processes of GOx enzyme solution drop-coating, potentiostatic Carb-Ala gel growth, gel-layer polymerisation, and allowing the gel to rest in PBS for 2 hours. A three-electrode system with one of the three GOx/Carb-Ala polymer functionalised microelectrode as the WE was then submerged in a cell of 90 mL PBS heated to a maintained temperature of 37 °C. The solution was stirred for 10 seconds, and an additional 30 seconds was allowed to pass. After this 40 second interval, chronoamperometry was conducted at +0.6 V for 10 seconds (red line, Figure 5.6).

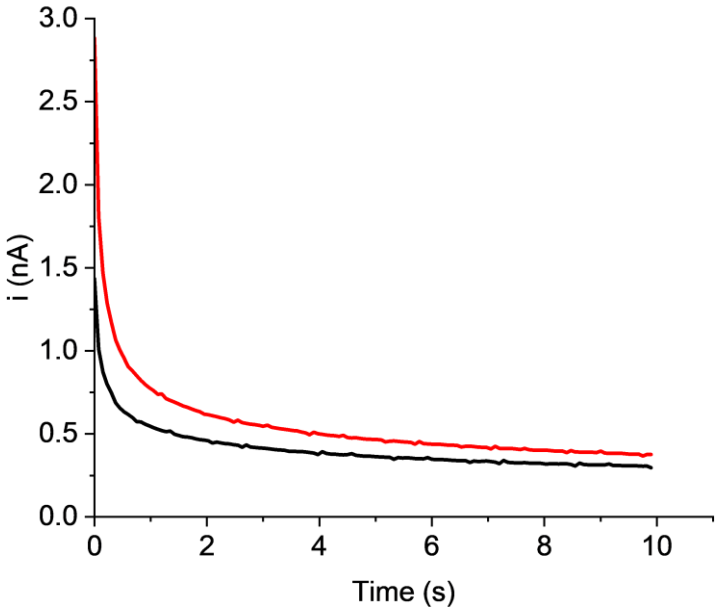

Figure 5.6 First and last of thirteen current-time transients recorded in PBS (pH 7.4, 0 mM glucose) at GOx/Carb-Ala polymer functionalised Pt microelectrodes (25 µm diameter), 10 seconds at 0.6 V (time measured after stepping from open circuit potential), T = 37 °C. Red line = first transient; black line = last transient. Separation in currents between first and last transient displays significant effect that recording successive transients has on removing non-Faradaic charge at WE.

The current-time transient recorded here represented the glucose-biosensor blank signal (response to a 0 mM glucose), giving the additional background current which is most likely due to non-Faradaic charging (red line, Figure 5.6). To reduce this background current, the 40 second wait duration was repeated to condition the film before recording an additional current-time transient under the same conditions. This process of re-recording transients was

repeated a total of 13 times, when the current at the microelectrode approached a minimum after each successive transient. After three successive transients were coincident at this minimum, this non-Faradaic current was considered to be sufficiently minimised. The last recorded transient (black line, Figure 5.6) was hence treated as the actual background current response to the 0 mM solution.

After reducing these background currents to a minimum, 0.1 mL 1 M glucose was added to the cell (giving 1.11 mM glucose in 90.1 mL of solution). 10 seconds of stirring was applied, followed by a further 30 second wait time, before recording a current-time transient at +0.6 V for 10 seconds. This process of adding glucose, stirring and pausing, and recording current responses was repeated for additions of 0.1 mL 1 M glucose until a total of 1 mL 1M glucose (11.0 mM in 91 mL) had been added to the cell. These recordings were continued with 1 mL additions of 1 M glucose (from 11.0 mM in 91 mL) until a final current-time transient was recorded once a total of 10 mL glucose solution had been added to the cell (giving 100 mM in 100 mL). These transients have been compiled in Figure 5.7. This procedure of recording current-time transients in PBS solutions containing incrementally increasing concentration of glucose became the standard procedure in latter experiments detailed within this chapter for the purpose of recording glucose concentration series.

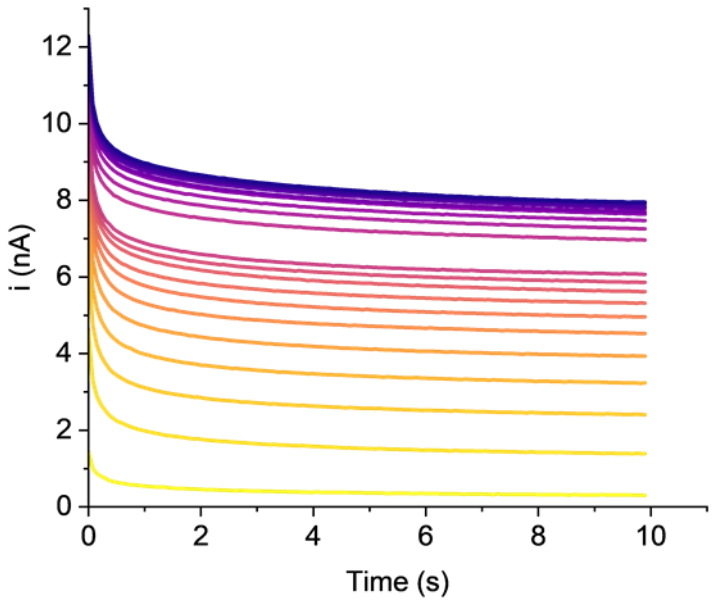

Figure 5.7 Current-time transients in PBS (pH 7.4) at GOx/Carb-Ala polymer functionalised Pt microelectrodes (25 µm diameter), 10 seconds at 0.6 V (time measured after stepping from open circuit potential), T = 37 °C. Colour gradient of lighter (yellow) to darker (purple) plots corresponds to increasing concentrations of glucose in the PBS solution, starting at 0 mM glucose in 90 mL PBS and ending in 100 mM glucose in 100 mL.

As in the preliminary CV study (Figure 5.5), current responses due to H_2O_2 oxidation increased after each addition of glucose (Figure 5.7). The successive transients (as concentration of glucose was increased) displayed a gradual approach to a maximum current, this being

approximately 8 nA towards 100 mM glucose (Figure 5.7). This approach could signify Michaelis-Menten kinetics, with the GOx enzyme becoming saturated at the highest concentrations of glucose. This is more clearly defined in a calibration curve, as shown below in Figure 5.9, where currents measured at 5 seconds along the transients have been plotted against the concentration of glucose in solution.

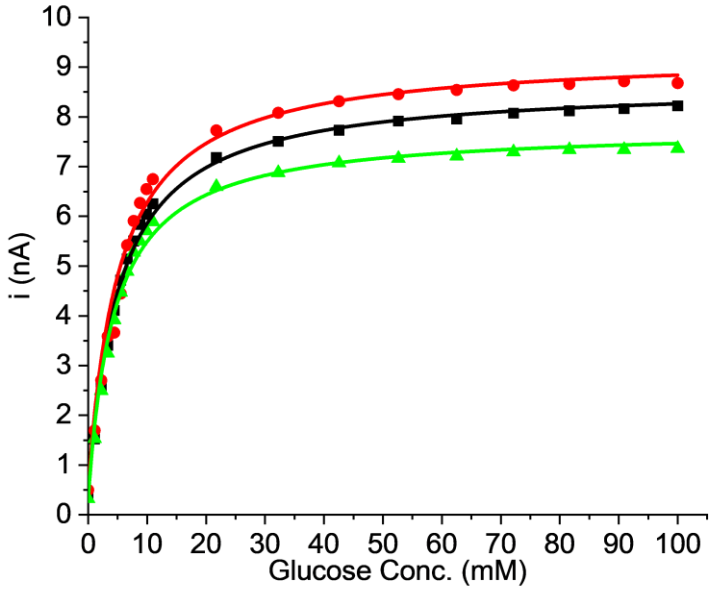

Figure 5.8 Calibration curves (points) and Michaelis-Menten fits (lines, see Table 5.2 for relevant fitting parameters) of GOx/Carb-Ala polymer functionalised Pt microelectrodes (25 µm diameter). Current responses recorded (5 seconds into 10 second 0.6 V current-time transient) as a function of glucose concentration from 0-100 mM, T = 37 °C. Black squares/lines = electrode 1, red circles/lines = electrode 2, green triangles/lines = electrode 3.

It is reassuring to see that the variation in current responses for each glucose concentration between each of the three electrodes is low (Figure 5.8). Aside from the 0 mM glucose response, the standard deviations of each data point are limited to <9% of the magnitude of the respective averages (Figure 5.9). These currents being of the same order of magnitude across each of the three identically prepared biosensors is likely coincidental, as natural variations out of experimental control (e.g. how many enzymes have lost functionality after dehydration, how much enzyme covers the Pt surface after drying/initial submersion into gelator solution, how the enzymes are oriented) are a common cause of differences in current responses between electrodes.

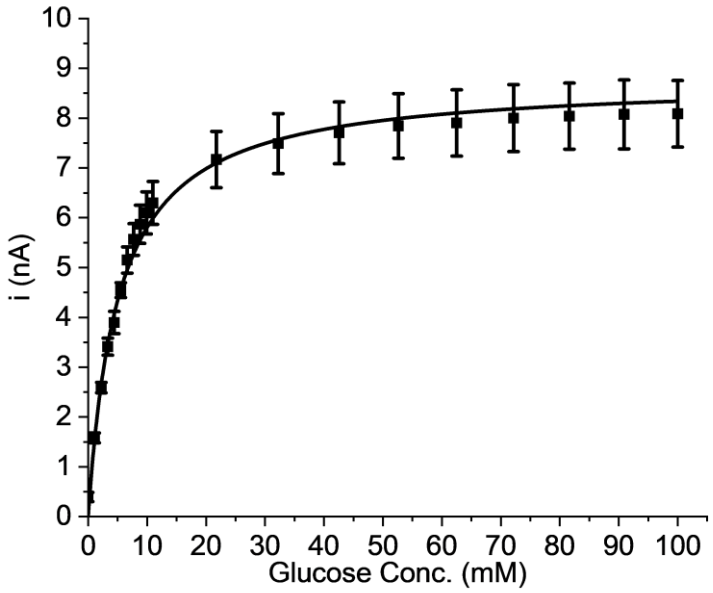

Figure 5.9 Averaged calibration curve (points with standard deviation error bars, calculated from data points of three electrodes featured in Figure 5.8) with Michaelis-Menten fit (line, see Table 5.2 for relevant fitting parameters) of GOx/Carb-Ala polymer functionalised Pt microelectrodes (25 µm diameter).

When enzyme reaction is rate limiting, the maximum current i_{max} observed due to enzyme-substrate saturation, and the Michaelis-Menten constant K_M (the concentration of substrate at half the saturation current) can be extracted from the curve presented in Figure 5.9 using the Michaelis-Menten equation:[20]

$$\frac{v_R}{v_{max}} = \frac{i - i_b}{i_{max}} = \frac{c_S}{K_M + c_S} \qquad \textit{Equation 5.1}$$

where v_R is the volumetric reaction rate (proportional to i), v_{max} is maximum rate of reaction achieved by the system (proportional to i_{max}), i_b is the blank signal (background) current, and c_S is the concentration of the substrate. These calibration curves shown in Figure 5.8 and Figure 5.9 have a sigmoidal shape characteristic of Michaelis-Menten kinetics, and each were fitted to Equation 5.1 to obtain a Michaelis-Menten curve (represented by the fitted lines in those respective figures) by fixing i_b to the recorded blank signals, and those values and the calculated K_M^{app} and i_{max} can be found in Table 5.2.

Table 5.2 i_{max}, K_M^{app}, and i_b for three GOx/Carb-Ala polymer functionalised Pt disc microelectrodes (25 µm diameter). Values calculated for calibration curves (Figure 5.9 and Figure 5.9) using the Michaelis-Menten equation (Equation 5.1), and are stated with associated standard errors. Blank signals i_b taken from recorded (Figure 5.9) or average (Figure 5.9) current responses to 0 mM glucose.

Value	1	2	3	Averaged curve
i_{max} (nA)	8.30 ± 0.07	8.77 ± 0.10	7.46 ± 0.08	8.59 ± 0.20
K_M^{app} (mM)	5.10 ± 0.19	5.18 ± 0.28	4.43 ± 0.20	6.10 ± 0.29
i_b (nA)	0.36	0.50	0.32	0.39

K_M of the free enzyme can vary due to limitations on the mass transfer of substrate but also if the movement of the enzyme (as it changes conformations) is restricted. This usually occurs when incorporating an enzyme into a membrane, as the microenvironment of the membrane affects the kinetics of the enzyme reaction. This affects the thermodynamics of binding between the enzyme and substrate. In this case, K_M should be treated as an apparent Michaelis-Menten constant K_M^{app}.[21] As a result of this change in enzyme environment, K_M^{app} of the three microelectrodes were reduced to values 12-14% that of the K_M for GOx from Aspergillus niger, 33 mM.[20] This low spread in K_M^{app} indicates that the activity of enzyme at each electrode (and thus the drop-coating and amount of GOx immediately before encapsulation) was similar. Note here that the K_M^{app} of the average calibration curve, 6.10 ± 0.29 mM (Table 5.2), is reported in the same way as the K_M^{app} of the individual calibration curves with a standard error from fitting to the Michaelis-Menten equation (Equation 5.1). This value should not be confused with an average of K_M^{app} values calculated for the three individual electrodes, which comes to 4.90 mM. The same goes for i_{max}, which if calculated as an average of i_{max} values for microelectrodes 1-3 is 8.16 nA rather than the tabulated 8.59 ± 0.20 nA obtained from fitting to Equation 5.1.

Linearity between glucose concentration and current response was found within 0-4 mM for all three glucose biosensor electrodes (Figure 5.10, Figure 5.11), with the linear fits in this calibration range possessing correlation coefficients (Pearson's r) > 0.99. The sensitivities (slopes of the linear relationship between concentration of glucose and current response, reported in nA mM^{-1} and µA mM^{-1} cm^{-2}) of all three electrodes were the same within experimental error (Table 5.3). The intercepts of these linear fits are also within error of their respective recorded blank signals i_b (Table 5.3), the current responses recorded without the presence of glucose in solution (Table 5.2). Given the linear relationship between i and c_S at low c_S, a limit of detection, (LOD), was also calculated for each using the following equation:

$$\mathrm{LOD} = 3.3\frac{\sigma}{m} \qquad \textit{Equation 5.2}$$

where *m* is the sensitivity (Table 5.3), *σ* is the standard error of the intercept (Table 5.3), and 3.3 represents a confidence factor of 95% assuming a Gaussian distribution.[22]

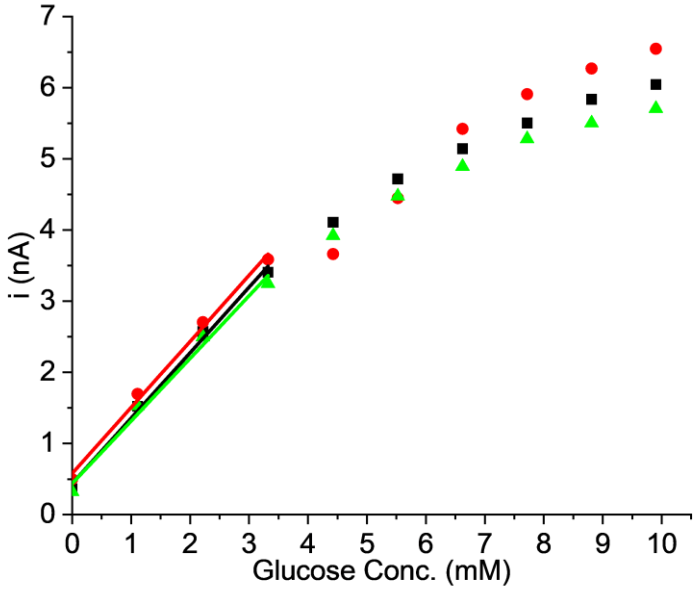

Figure 5.10 Narrowed concentration range for calibration curves of individual electrodes featured in Figure 5.9. Current responses recorded (5 seconds into 10 second 0.6 V current-time transient) as a function of glucose concentration from 0-10 mM, T = 37 °C. Linear calibration range of 0-4 mM fitted for each curve. Black squares/lines = electrode 1, red circles/lines = electrode 2, green triangles/lines = electrode 3.

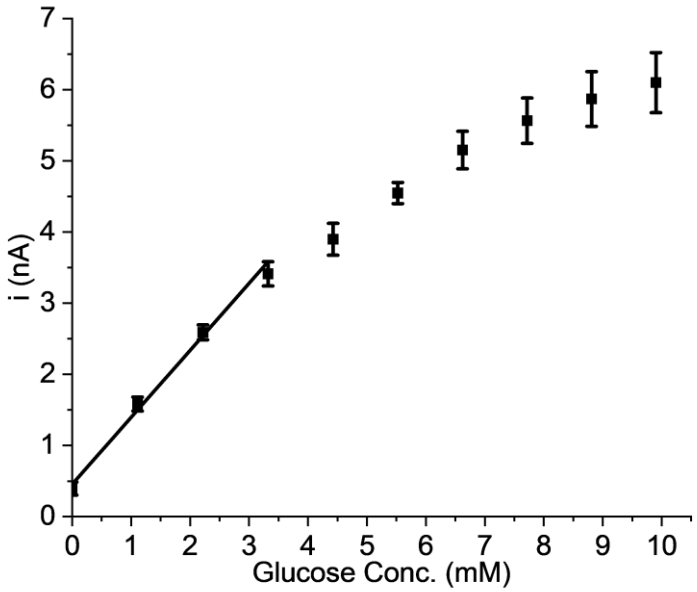

Figure 5.11 Narrowed concentration range for averaged calibration curve featured in Figure 5.9. Linear calibration range of 0-4 mM fitted.

Table 5.3 Sensitivity, intercept, and LOD for 0-4 mM linear calibration range (Figure 5.10 and Figure 5.11) of three GOx/Carb-Ala polymer functionalised Pt disc microelectrodes (25 µm diameter). Sensitivity and intercept stated with associated standard errors. Sensitivity presented in nA mM^{-1}, as well as standardised units of µA mM^{-1} cm^{-2} for comparison with similar glucose biosensors in other studies. LOD calculated using Equation 5.2.

Value	1	2	3	Averaged curve
Sensitivity (nA mM^{-1})	0.92 ± 0.05	0.93 ± 0.04	0.88 ± 0.06	0.94 ± 0.05
Sensitivity per unit area (µA mM^{-1} cm^{-2})	187 ± 9	189 ± 9	179 ± 13	191 ± 9
Intercept (nA)	0.44 ± 0.10	0.58 ± 0.10	0.44 ± 0.13	0.46 ± 0.09
LOD (mM)	0.34	0.33	0.50	0.39

The LOD for these three sensors sits below 1 mM (Table 5.3), well below the 2 mM required to measure blood glucose or interstitial fluid concentrations as low as in severe hypoglycaemic cases.[23] The concentration ranges of glucose in urine, saliva, tears and sweat are far more narrow, and unfortunately the LOD for these sensors all rest above the minimum of those ranges.[6] The sensitivities of other 1st generation amperometric glucose biosensors can be significantly lower than those recorded in this chapter (189 ± 9 µA mM^{-1} cm^{-2}, Table 5.3). Differences in enzyme loading were initially considered to be a possible reason to explain this (GOx/Carb-Ala polymer electrodes have been loaded with 2.48 U/µL GOx, 248 U/mg in 10 mg/mL drops, Chapter 2 Section 2.4.5). However, reduced sensitivity appears to be more related to the use of permselective layers at electrode surfaces (below enzyme immobilisation layers) such as phenylenediamine (4.47 µA mM^{-1} cm^{-2}, 12 U/µL)[24] and Nafion (1.20 µA mM^{-1} cm^{-2}, 0.6 U/µL).[25]

5.2.3 Operational stability of GOx/Carb-Ala polymer functionalised microelectrodes

Operational stability is a definition of biosensor functional lifetime that describes the reproducibility of a given sensor's responses to a fixed set of analyte and environment conditions, and can be considered on a continuous or intermittent basis of sensor use.[12,26] It was decided that the operational stability of the three biosensor microelectrodes prepared in Section 5.2.1 and 5.2.2 would be examined by testing sensor current responses at a fixed concentration of glucose, to garner information on how long the Carb-Ala polymer could keep the GOx enzyme trapped and active at the Pt microelectrode. This would be done by recording sensor responses at periodic intervals, starting on "day 0" (the day on which experimental work with these biosensors began, Section 5.2.2), and continuing over the course of several weeks. Though continuous sensing was initially considered, periodic exposure of the sensors to glucose was seen as the more suitable method, as only one of the three electrodes could

be tested at any given time due to limitations with the experimental equipment and time available.

The chosen conditions for observing changes in enzyme activity were to obtain current responses to 5 mM glucose at 37 °C. This was initially accomplished by extracting current values from calibration curves of 0-10 mM glucose, though from days 1-14 this was instead done by measuring the current responses in a solution of PBS containing 5 mM glucose. It was initially assumed that both methods would yield similar results, but that the former could probe changes in both K_M^{app} and sensitivity. Between recordings of current responses (recorded using the same method described in Section 5.2.2), the three GOx biosensor electrodes were stored in PBS at room temperature overnight (20-23 °C). After calibration curves were recorded on day 0 (Figure 5.8), current values were recorded in the 5 mM glucose solution on day 1, 3, 7 and 14. From day 21 onwards, new calibration curves were again produced for the three sensors from 0-10 mM glucose every 7 days, until 42 days had elapsed. A record of these current responses, representative of the relative activity of each biosensor at that given time, can be found in Table 5.4.

Table 5.4 Currents recorded at three GOx/Carb-Ala polymer functionalised 25 µm diameter Pt disc microelectrodes, in response to exposure to 5 mM glucose in PBS at 37 °C. Italicised values recorded from day 1 to 14 were obtained by recording individual current-time transients in a 10 mL PBS solution containing 5 mM glucose. All other values were extracted from sensitivities in the 3-8 mM range.

Day	**Current response to 5 mM glucose (nA)**		
	1	**2**	**3**
0	4.33	4.50	4.12
1	*4.45*	*4.93*	*4.38*
3	*3.11*	*4.72*	*3.60*
7	*3.48*	*4.49*	*3.27*
14	*0.37*	*4.24*	*3.45*
21	-	4.50	3.48
28	-	4.11	3.04
35	-	3.19	1.99
42	-	2.61	1.61

Overall, following an initial jump in current recorded from day 0 to day 1 for each electrode, the current at each electrode gradually decreased over time/successive use, corresponding to a decrease in bound enzyme activity (Table 5.4). Microelectrode 1 failed between day 7 and 14, with a current response on day 14 that was an order of magnitude lower than prior measurements and similar in magnitude to the 0 mM response (Table 5.4), which suggested a significant or complete loss of enzyme at the electrode surface. To investigate this case further, microelectrode sensor 1 was imaged using optical microscopy to look for physical changes to the polymer at the electrode surface which could have caused the sudden change in activity. The resulting image shows no gel present at the Pt surface (Figure 5.12a). This is clear confirmation that the significant drop in current on day 14 was a result of the Carb-Ala

polymer (and thus the GOx enzyme) having delaminated/detached from the electrode surface. For comparison, microelectrode 3 was also examined under microscopy. Though a mass of GOx/Carb-Ala at the Pt surface was still visible at this time (Figure 5.12b), the size of the polymer had significantly decreased from what was initially observed on day 0 (Figure 5.2). This suggests that the gel membrane had undergone some degradation over the 2 weeks it had remained submerged in the PBS.

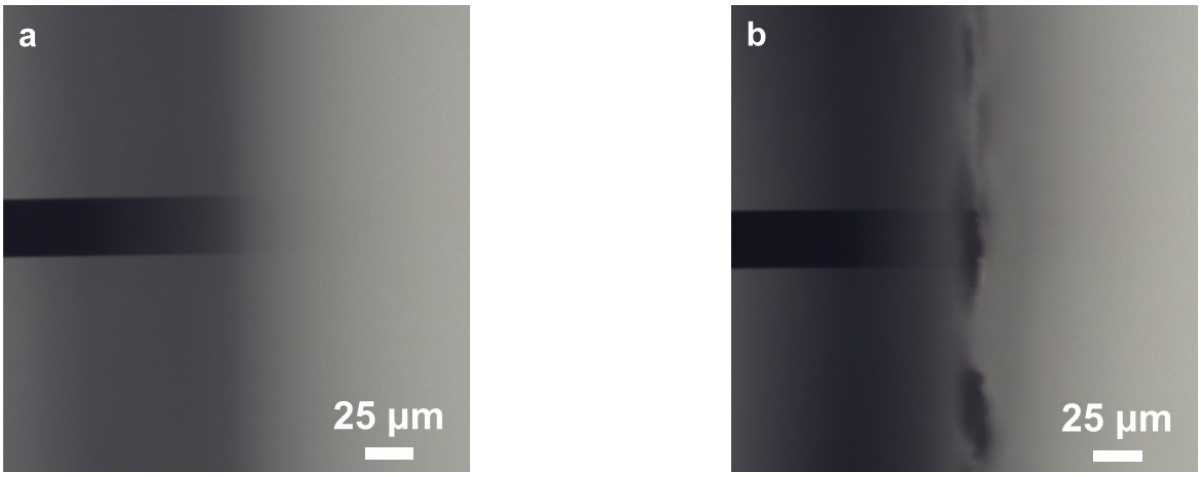

Figure 5.12 Images of GOx/Carb-Ala polymer functionalised Pt microelectrodes (25 µm diameter) recorded 14 days after sensor production, side-on view, 100x magnification. (a) Microelectrode biosensor 1 has a bare surface, no visible sign of polymer or enzyme present, indicating membrane delamination; (b) Microelectrode biosensor 3 shows sign of GOx/Carb-Ala polymer presence at electrode surface, with dark mound covering end of glass-encased Pt wire, indicating (in comparison with Figure 5.2) gel has undergone degradation over time.

The single measurements of the biosensor current responses (Table 5.4) provided information on the upper limit of time that GOx enzyme could remain encapsulated. Although this study revealed that these sensors could produce a readable current after several weeks of use, an operational lifetime is more appropriately described through the change in sensitivity of a given sensor.[26] As stated prior (Table 5.4), the sensitivities of microelectrodes 2 and 3 were determined on day 0, and on the 21st day and onwards by recording calibration curves in the 0-10 mM glucose range on these dates. These sensitivities, as well as i_{max} and K_M^{app} are presented in Table 5.5 and Table 5.6. Note that i_{max} and K_M^{app} in these data sets were calculated by fitting a Michaelis-Menten curve to the 0-10 mM glucose range, as the calibration curves from day 21 and onward were recorded to a maximum of 10 mM glucose. As a result, the i_{max} and K_M^{app} values for day 0 presented below differ greatly from those presented in Table 5.2 (where the Michaelis-Menten curve was fitted to a 0-100 mM range).

Table 5.5 i_{max}, K_M^{app}, and sensitivities of GOx/Carb-Ala polymer functionalised 25 µm diameter Pt disc microelectrode 2, calculated from Michaelis-Menten (0-10 mM glucose range) and linear fits (0-4 mM glucose range) in PBS at 37 °C.

Day	i_{max} (nA)	K_M^{app} (mM)	Sensitivity (nA mM^{-1})
0	11.7 ± 0.4	9.27 ± 0.52	0.93 ± 0.04
21	11.1 ± 1.8	8.98 ± 2.63	1.07 ± 0.23
28	8.04 ± 0.13	5.69 ± 0.21	0.91 ± 0.08
35	6.94 ± 0.16	7.47 ± 0.34	0.66 ± 0.03
42	5.43 ± 0.08	7.23 ± 0.21	0.52 ± 0.03

Table 5.6 i_{max}, K_M^{app}, and sensitivities of GOx/Carb-Ala polymer functionalised 25 µm diameter Pt disc microelectrode 3, calculated from Michaelis-Menten (0-10 mM glucose range) and linear fits (0-4 mM glucose range) in PBS at 37 °C.

Day	i_{max} (nA)	K_M^{app} (mM)	Sensitivity (nA mM^{-1})
0	9.28 ± 0.23	7.02 ± 0.35	0.88 ± 0.06
21	7.87 ± 1.04	8.27 ± 2.06	0.75 ± 0.11
28	5.79 ± 0.23	6.06 ± 0.51	0.64 ± 0.03
35	16.0 ± 2.3	34.2 ± 6.2	0.41 ± 0.01
42	4.91 ± 0.35	15.8 ± 1.67	0.25 ± 0.01

For microelectrode biosensor 2, i_{max} underwent significant changes from day 28 onwards, whilst no trend could be discerned for K_M^{app} values over the 42 days (Table 5.5). This suggests that the sensor experienced no significant loss in activity until a time between days 28 and 35, where i_{max} decreased from 8.04 ± 0.13 nA to 6.94 ± 0.16 nA to. Microelectrode 2 also only began to show a significant change in sensitivity from the initial value on day 0 (0.93 ± 0.04 nA mM^{-1}) somewhere between day 28 and day 35, going from 0.91 ± 0.08 nA mM^{-1} to 0.66 ± 0.03 nA mM^{-1}. Microelectrode biosensor 3 experienced approximately the same rate of degradation, only showing a significant drop in i_{max} and sensitivity between days 21 and 28, and a significant deviation from the sensitivity on day 0 after day 28 (Table 5.6). Taking a linear fit of sensitivity for both sensors from day 21 onwards (Table 5.5, Table 5.6), the rate of sensitivity degradation calculates to 24.5 ± 0.4 pA mM^{-1} per day for microelectrode 2 and 24.0 ± 0.1 pA mM^{-1} per day for microelectrode 3.

Microelectrode 3 also displayed a surprising increase in i_{max} and K_M^{app} on day 35, followed by a decrease in those values (though not to what was seen on days 0-28) on day 42 (Table 5.6). In the case of day 35, this may have stemmed from the Michaelis-Menten curve being significantly, inexplicably different from those on the previous dates of experimentation (Figure 5.13). The sensitivity on day 35 remained within the expected linear trend in degradation, and the sensitivity over the extended 0-8 mM calibration range on this date was also identical to the sensitivity in the 0-4 mM range (Table 5.6), at 0.40 ± 0.01 nA mM^{-1}. K_M^{app}

being estimated as 15.8 ± 1.67 mM on day 42 is also probably a result of the Michaelis-Menten equation being fit to the narrow 0-10 mM calibration curve, rather than a sudden increase in enzyme activity on this date.

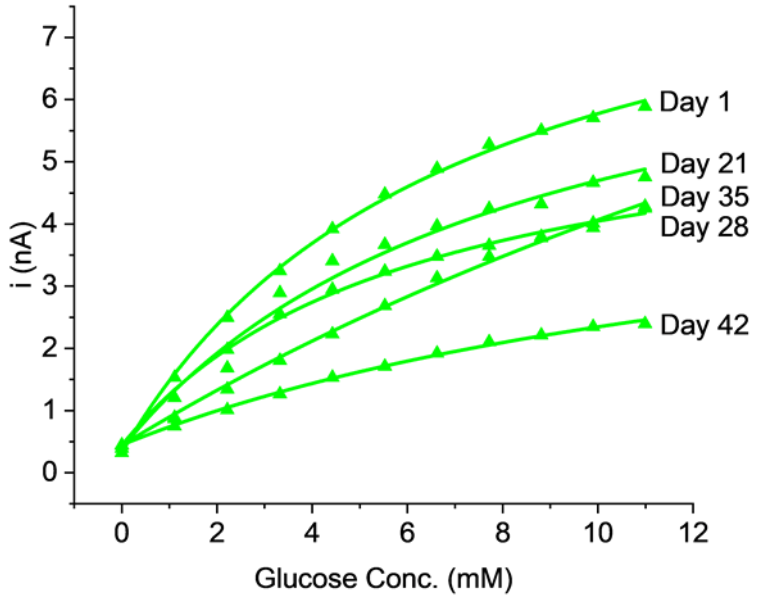

Figure 5.13 Calibration curves of GOx/Carb-Ala polymer functionalised Pt microelectrode 3 (25 µm diameter), current responses (5 seconds into 10 second 0.6 V current-time transient) as a function of glucose concentration, T = 37 °C. Fitted Michaelis-Menten curves are drawn as lines through each of the calibration curves (correlation coefficient > 99). Day 35 has an unusual shape compared to the others, with an increased linear range of 0-8 mM. i_{max}, K_M^{app} and sensitivities can be found in Table 5.6.

These changes in sensitivity can also be presented as a half-life $t_{1/2}$ for the sensor, i.e. the time after initial tests at which residual activity (the ratio between sensitivity at a given time and the initially measured sensitivity) of the biosensor becomes 0.5.[21] The residual activity of GOx/Carb-Ala polymer functionalised glucose biosensors 2 and 3 with time can be found in Figure 5.14.

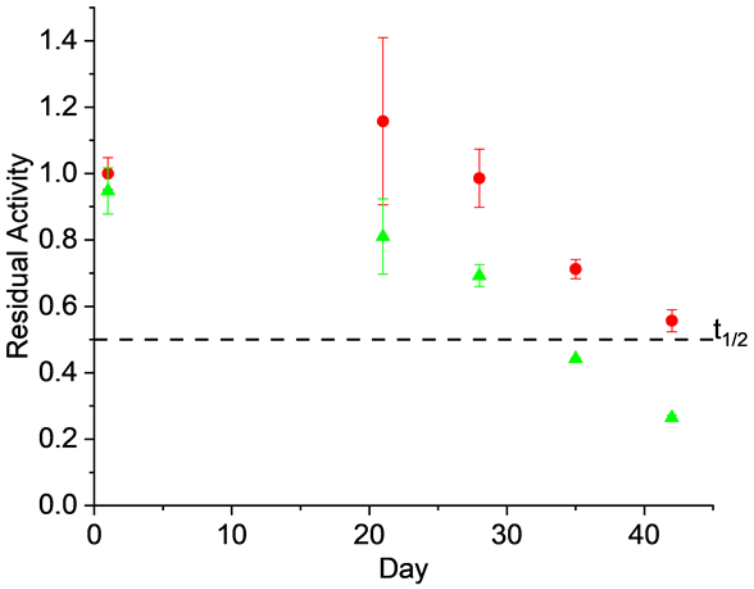

Figure 5.14 Residual activities of GOx/Carb-Ala polymer functionalised 25 µm diameter Pt disc microelectrodes 2 and 3 within 0-4 mM linear calibration range, T = 37 °C. Points represent ratio of sensitivities on a given date against the sensitivities recorded on day 0, and error bars represent standard errors obtained from linear fits (Table 5.5, Table 5.6). Horizontal dotted line at 0.5 residual activity represents $t_{1/2}$. Red circles = electrode 2, green triangles = electrode 3.

The activity of both sensors can again be seen to undergo a significant decrease between 20 and 30 days, and following what appears to be a linear trend, $t_{1/2}$ for microelectrode 2 (red circles, Figure 5.14) and microelectrode 3 (green triangles, Figure 5.14) are approximately 44 and 34 days respectively. This operational stability is comparable to the lifetime of other 1st generation glucose biosensors tested *in vitro* in other works ($t_{1/2}$ approx. 14 days[24]) whilst 2nd generation amperometric GOx sensors appear to be able retain as high as 80% initial sensitivity after several months.[27,28] This is usually due to the long-term stability of 1st generation glucose biosensors being greatly affected by H_2O_2 degrading the activity of the GOx enzyme over time.[29] The gradual reductions in i_{max} (Table 5.5, Table 5.6) also suggest that the biosensors in this chapter are undergoing a natural loss in activity with time. It is reassuring to see then that the polymerised Carb-Ala gel is capable of trapping GOx, and that the sensor can function for more than a month *in vitro*, demonstrating promise for this enzyme immobilisation method.

5.3 Preparing 1st generation glucose microelectrode biosensors with GOx trapped under supramolecular Carb-Ala hydrogels

It was expected that the omission of the Carb-Ala electropolymerisation step post-electrochemical gel growth would have a negative effect on the stability of an enzyme biosensor produced with such a layer. This is because the degradation of semi-permeable membranes is an established cause of biosensor failure via enzyme leakage,[30] and as concluded in Chapter 4 of this thesis, the supramolecular potentiostatically grown Carb-Ala gels are unstable in aqueous media (even where pH is less than pK_a^{app} of the gelator). It was expected that these sensors would therefore possess operational lifetimes far lower than those produced by polymerising the Carb-Ala gel (Section 5.2.3).

To confirm this, three 25 µm diameter Pt disc microelectrodes were first functionalised by drop-coating 10 mg/mL GOx enzyme solution, allowing the drop to dry over 24 hours as in prior experiments, before potentiostatic Carb-Ala gel growth at 0.7 V for 120 seconds was conducted. The three functionalised microelectrodes were again allowed to rest in 10 mL PBS for 2 hours before being incorporated into a three-electrode system and conducting the same potentiostatic experiments as described in Section 5.2.2, recording current responses to incrementally increasing concentrations of glucose. The transients for the first of these GOx/Carb-Ala polymer functionalised Pt disc microelectrodes, measuring from 0-100 mM glucose, are shown in Figure 5.15.

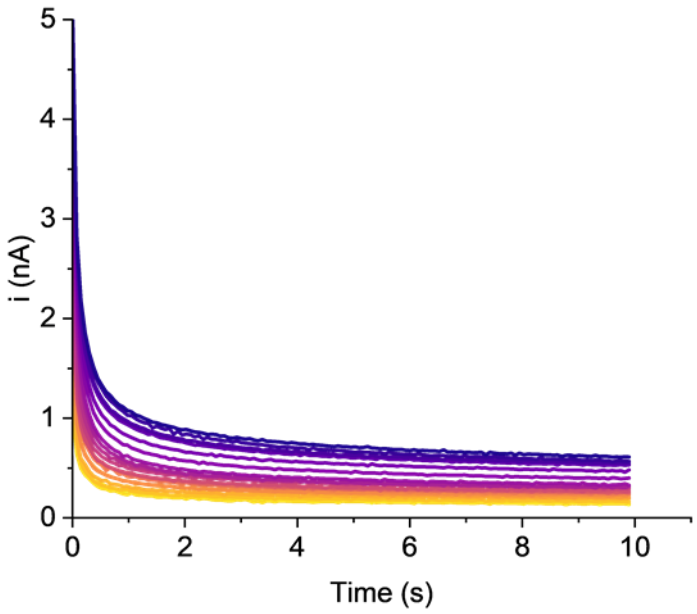

Figure 5.15 Current-time transients in PBS (pH 7.4) at GOx/Carb-Ala supramolecular gel functionalised Pt microelectrodes (25 µm diameter), 10 seconds at 0.6 V (time measured after stepping from open circuit potential), T = 37 °C. Colour gradient of lighter (yellow) to darker (purple) plots corresponds to increasing concentration glucose added to the PBS solution, starting at 0 mM glucose in 90 mL PBS and ending in 100 mM glucose in 100 mL.

Primarily, an order of magnitude lower currents were recorded at this microelectrode (e.g. 0.36 nA at 5.5 mM glucose, Figure 5.15) compared to those at the same concentrations of glucose at the sensors with the polymerised Carb-Ala layers (5 nA at 5.5 mM glucose, Figure 5.7). This resulted in currents comparable in magnitude to the background. This lower enzyme activity is unlikely to be a result of poorer initial adhesion of the enzyme to the surface, because the same methods of drop-coating and the pre-application of +0.3 V to electrostatically attract the enzyme to the Pt surface were used here (as first described in Section 5.2.1). Instead, this lower enzyme activity indicates that significant membrane degradation (thus leaching of GOx) had occurred over the 2 hours that the microelectrode glucose biosensor had spent in PBS prior to any additions of glucose. This experiment was repeated for two more electrodes prepared with the same method, and the current responses for each addition of glucose at 5 seconds of each transient were used to plot calibration curves for the three microelectrodes (Figure 5.16).

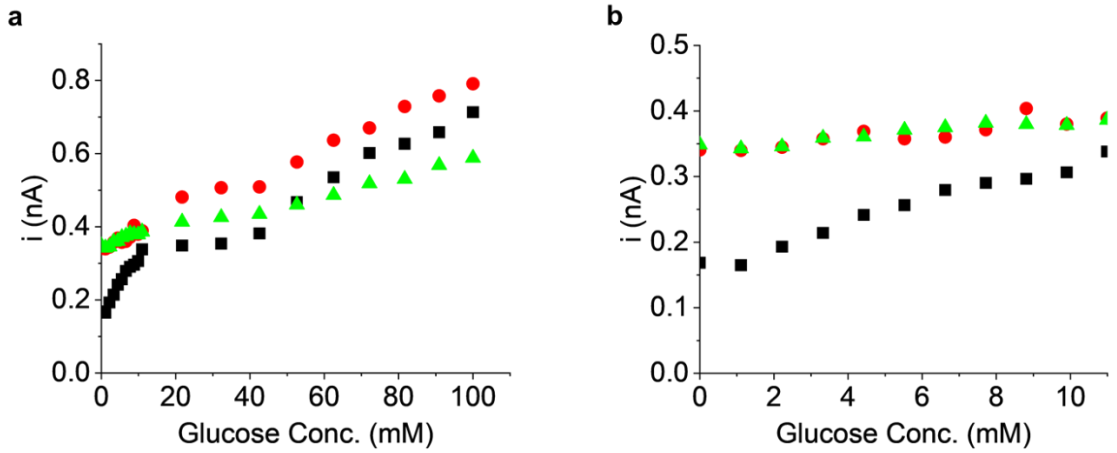

Figure 5.16 Calibration curves of GOx/Carb-Ala supramolecular gel functionalised Pt microelectrodes (25 µm diameter), current responses (5 seconds into 10 second 0.6 V current-time transient) as a function of glucose concentration, T = 37 °C. Black squares = electrode 1, red circles = electrode 2, green triangles = electrode 3. (a) 0-100 mM glucose range; (b) 0-10 mM glucose range, blown-up from (a).

All three of these GOx/Carb-Ala surpramolecular gel functionalised microelectrodes experienced lower current responses to glucose concentrations (Figure 5.16) compared to the GOx/Carb-Ala polymer electrodes tested in Section 5.2.2 (Figure 5.9). Current responses for these electrodes did not exceed 1 nA, compared to the GOx/Carb-Ala polymer electrodes which had pushed currents an order of magnitude greater. These GOx/Carb-Ala gel microelectrodes all apparently followed a linear trend from 0-10 mM glucose range (Figure 5.16b). However, these had reduced and varying sensitivities far lower than seen for the electrodes produced in Section 5.2. For example, in the 0-4 mM range, the sensitivities calculate to 15, 5, and 3 pA mM^{-1} for the three electrodes in respective order, all up to two orders of magnitude lower than those of the sensors with the polymerised Carb-Ala membranes (Table 5.5).

Most importantly, none of the three curves presented a shape characteristic of Michaelis-Menten kinetics diagnostic of adsorbed enzyme activity (Figure 5.16a). Neither approached a

maximum current, even towards 100 mM glucose, and dips in current can be seen across each of the full calibration curves. For example, microelectrodes 1 and 2 (black squares and red circles respectively, Figure 5.16a) appeared to follow a Michaelis-Menten curve up to approximately 40 mM glucose, but then produced an almost linear current increase in the 50-100 mM regime of similar magnitude. Microelectrode 2 also features dips in current between glucose additions as early as in the 0-10 mM range (red circles, Figure 5.16b). Compounded in the averaged calibration curve (Figure 5.17), the overlapping errors of each corresponding current exemplify the inability of these sensors to differentiate between differing glucose concentrations.

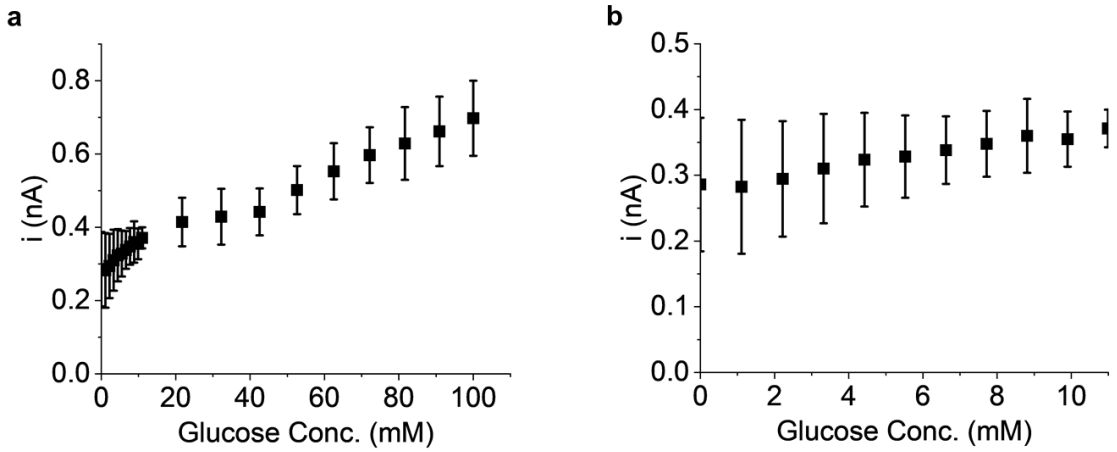

Figure 5.17 Averaged calibration curve (points with standard deviation error bars, calculated from data points of three electrodes featured in Figure 5.16) of GOx/Carb-Ala polymer functionalised Pt microelectrodes (25 µm diameter). (a) 0-100 mM glucose range; (b) 0-10 mM glucose range, blown-up from (a).

It is clear that the current responses of these biosensors were already far too low and varied between the electrodes to make them useful as biosensors. Even if some surface enzyme current is contributing, these unusual curves are likely a consequence of almost complete GOx enzyme leaching, and it is likely that all three of these sensors would fail completely after a day of storage in PBS. Without electropolymerisation, the instability of these supramolecular Carb-Ala hydrogels results in sensors that are unsuitable for reliably quantifying glucose concentrations.

5.4 Summary

By drop-coating the commercial Pt microelectrodes used throughout this thesis with 10 mg/mL GOx enzyme solutions, subsequently electrochemically growing Carb-Ala hydrogels over these drop-coated electrodes, and then electropolymerising these supramolecular hydrogels, 1st generation enzymatic glucose biosensors have been produced and tested *in vitro*. The polymerised gels act as a membrane to trap the GOx enzyme at the electrode whilst allowing glucose to reach the enzyme through the layer and be electrochemically detected. A progressive increase in current responses was recorded when recording cyclic voltammograms in PBS containing 0 mM, 5 mM, and 100 mM glucose, corresponding to increases in H_2O_2 concentration produced by the oxidation of glucose catalysed by the GOx enzyme. Three sensors were prepared in total, and after recording concentration series from 0-100 mM, calibration curves were produced which showed the sensors exhibited Michaelis-Menten kinetics.

The three GOx/Carb-Ala polymer sensors were shown to each possess a biologically relevant, low concentration linear calibration range of 0-4 mM. The maximum sensitivity of these three electrodes was 189 ± 9 µM mM^{-1} cm^{-2}, and the LOD was as low as 0.33 mM. When conducting operational stability studies, one of the three sensors failed after 14 days due to delamination of the GOx/Carb-Ala polymer from the electrode surface. Gel adhesion to surfaces like Pt and glass is unfortunately not well understood at this time. The $t_{1/2}$ of the remaining two sensors was found to be up to 44 days, when tested at 37 °C and stored at room temperature conditions (20-23 °C) between tests. Though the sample size of functioning sensors in this work is small, it is still reassuring to see two of the three microelectrodes prepared with this method have retained their sensitivity for a duration comparable to those of 1st generation enzymatic glucose sensors featured in other works even in these initial proof of principle studies.

As expected from work carried out in Chapter 4, a problem was identified in using supramolecular Carb-Ala gels as the semi-permeable membrane for these biosensors without electropolymerisation. Enzyme leaching occurs rapidly due to gel breakdown/loss in PBS, characterised by enzyme current responses two orders of magnitude lower than those of the sensors prepared with the electropolymerised Carb-Ala just 2 hours after sensor production. It can be concluded here that Carb-Ala gels grown using the potentiostatic method need to undergo further electropolymerisation treatment before use as enzyme-trapping, semi-permeable membranes.

5.5 References

1 A. Piper, B. M. Alston, D. J. Adams and A. R. Mount, *Faraday Discuss.*, 2018, **210**, 1–17.

2 C. Patterson, B. Dietrich, C. Wilson, A. R. Mount and D. Adams, *Soft Matter*, 2022, **18**, 1064–1070.

3 E. K. Johnson, D. J. Adams and P. J. Cameron, *J. Am. Chem. Soc*, 2010, **132**, 5130–5136.

4 J. Raeburn, B. Alston, J. Kroeger, T. O. McDonald, J. R. Howse, P. J. Cameron and D. J. Adams, *Mater. Horizons*, 2014, **1**, 241–246.

5 P. S. Kubiak, S. Awhida, C. Hotchen, W. Deng, B. Alston, T. O. McDonald, J. Adams and P. J. Cameron, *Chem. Commun.*, 2015, **51**, 10427–10430.

6 L. Johnston, G. Wang, K. Hu, C. Qian and G. Liu, *Front. Bioeng. Biotechnol.*, 2021, **9**, 1–17.

7 S. R. Corrie, J. W. Co, J. Islam, K. A. Markey and M. A. F. Kendall, *Analyst*, 2015, **140**, 4350–4364.

8 A. Rebel, M. A. Rice and B. G. Fahy, *J. Diabetes Sceience Technol.*, 2012, **6**, 396–411.

9 B. Purohit, A. Kumar, K. Mahato and P. Chandra, in *Miniaturized Biosensing Devices*, eds. P. Chandra and K. Mahato, Springer Singapore, Singapore, 1st edn., 2022, pp. 149–175.

10 H. J. Hecht, D. Schomburg, H. Kalisz and R. D. Schmid, *Biosens. Bioelectron.*, 1993, **8**, 197–203.

11 P. N. Bartlett, Z. Ali and V. Eastwick-Field, *J. Chem. Soc. Faraday Trans.*, 1992, **88**, 2677–2683.

12 G. Rocchitta, A. Spanu, S. Babudieri, G. Latte, G. Madeddu, G. Galleri, S. Nuvoli, P. Bagella, M. I. Demartis, V. Fiore, R. Manetti and P. A. Serra, *Sensors*, 2016, **16**, 1–21.

13 S. Nakamura and S. Fujiki, *J. Biochem.*, 1968, **63**, 51–58.

14 S. B. Bankar, M. V. Bule, R. S. Singhal and L. Ananthanarayan, *Biotechnol. Adv.*, 2009, **27**, 489–501.

15 P. N. Bartlett and D. J. Caruana, *Analyst*, 1992, **117**, 1287–1292.

16 P. Kavanagh and D. Leech, *Phys. Chem. Chem. Phys.*, 2013, **15**, 4859–4869.

17 P. D'Orazio, *Clin. Chim. Acta*, 2003, **334**, 41–69.

18 S. B. Hall, E. A. Khudaish and A. L. Hart, *Electrochim. Acta*, 1998, **43**, 579–588.

19 S. B. Hall, E. A. Khudaish and A. L. Hart, *Electrochim. Acta*, 1999, **44**, 2455–2462.

20 P. M. Doran, in *Bioprocess Engineering Principles*, Elsevier, Oxford, Second Edi., 2013, pp. 599–703.

21 A. Illanes and L. Wilson, in *Immobilization of Enzymes and Cells*, eds. J. M. Guisan, F. López-Gallego, J. Rocha-Martín and G. Fernandez-Lorente, Springer Science+Business Media, New York, 1st edn., 2020, pp. 65–81.

22 D. E. Brunetti B, *Pharm. Anal. Acta*, 2015, **6**, 1–4.

23 P. Loumpardia and M. S. B. Huda, in *Blood Glucose Levels*, ed. L. Szablewski, IntechOpen, 1st edn., 2020, pp. 1–9.

24 R. J. Soto, J. B. Schofield, S. E. Walter, M. J. Malone-Povolny and M. H. Schoenfisch, *ACS Sensors*, 2017, **2**, 140–150.

25 C. A. Cordeiro, A. Sias, T. Koster, B. H. C. Westerink and T. I. F. H. Cremers, *Sensors Actuators B. Chem.*, 2018, **263**, 605–613.

26 D. R. Thévenot, K. Toth, R. A. Durst and G. S. Wilson, *Biosens. Bioelectron.*, 2001, **16**, 121–131.

27 A. Jędrzak, M. Kuznowicz, T. Rębiś and T. Jesionowski, *Bioelectrochemistry*, 2022, **145**, 108071–108080.

28 J. Chen, X. Zheng, Y. Li, H. Zheng, Y. Liu and S. Suye, *J. Electrochem. Soc.*, 2020, **167**, 067502.

29 J. M. Harris, C. Reyes and G. P. Lopez, *J. Diabetes Sci. Technol.*, 2013, **7**, 1030–1038.

30 D. Grieshaber, R. MacKenzie, J. Vörös and E. Reimhult, *Sensors*, 2008, **8**, 1400–1458.

Chapter 6 – Conclusion

6.1 Lessons learned

The potentiostatic method of electrochemical acid-triggered gelation was shown to be a viable method of tuning gel growth whilst selectively excluding gelator electrochemistry. Increasing the time for which a potential is applied increases the cumulative number of protons generated from hydroquinone oxidation, which determines the final amount of gel at an electrode surface. By pairing optical microscopy (*in* and *ex situ*) with EIS, the dimensions and diffusional properties of peptide-based supramolecular gel-coated microelectrodes have been analysed in tandem. When applying potentials above the redox potential of the gelator, hydroquinone and gelator electrochemistries both occur. Since the rate of gel growth is tied directly to the production of protons, this rate is limited by the diffusion of hydroquinone, which itself decreases over time as the gel increases in size and density. This is unlike in galvanostatically-controlled gel-growth where water oxidation provides a continuous source of protons to facilitate this.[1] Additionally, by applying a suitable potential to allow both Carb-Ala and hydroquinone electrochemistries to occur, gel growth rate is reduced further due the electropolymerisation of the gel network, though this effect is most noticeable over long periods of continued applied gelator/hydroquinone oxidative potentials.

Over periods of minutes to hours of time, the potentiostatically-grown gels did not retain their shape and density when transferred to buffered and unbuffered solutions where pH < pK_a^{app} (i.e. where protons would be supplied by the solution). This change has been observed with EIS as a gradual increase in redox probe coefficients, but also under optical microscopy where the transition has been found to be directional. It is unclear whether what is being observed here is gel syneresis or if another process is occurring whereby gel mass is lost, for example by disentanglement/diffusion of weekly-bound aggregates. It is speculated here that the latter of these processes could be driven by the concentration gradient between the gel and bulk solution (to which the gel is transferred), where a low energy barrier for gelator aggregate disentanglement allows them to diffuse into the bulk. This may also differ from instability within the gelator solution, which is driven by a competition between flux of the basic bulk gelator solution and generation of protons at electrode surface. Overall, this phenomenon presents an obvious stability problem with regards to using peptide-based, electrochemically grown supramolecular hydrogels as porous films for point-of-care biosensing applications. It is thus fortunate that Carb-Ala can be electropolymerised to form a far more stable material.

It is with confidence that the objectives for this thesis, stated in Chapter 1, have been met. Gel dimensions and densities can be tuned under the potentiostatic method, the gels can be characterised using low-cost electrochemical and optical analytical techniques *in situ*, and the ability to electropolymerise Carb-Ala allows these particular hydrogels to be used as stable porous membranes and enzyme-immobilising agents for 1st generation biosensing applications. Though more questions have been opened up with regards to the stability of the supramolecular systems, especially those composed of other peptide gelators, the use of polymerised Carb-Ala to trap GOx in a favourable aqueous environment can be considered a

success. From this platform, more work should be conducted to explore the anti-fouling and possible inhibitor-excluding capabilities of this system *in vitro*, and if this yields more success, studies *in situ* with real biological media should also be considered.

6.2 Future directions

A fundamental gap of missing information regarding electrochemically-driven/assisted peptide gelator self-assembly is in the aggregation of gelator molecules on all length scales, from the electrode surface to the bulk solution. In Chapter 4, the gels were found to undergo a gradual loss in density, characterised by directional transitions in gel opacity that precede the apparent collapse of the remaining gel structure. This directionality suggests that the gels may be inhomogeneous in density from the electrode surface towards the bulk. This could be a result of different aggregates coexisting in the gels, with distance from the electrode surface being a determining factor for a gradient of structures. Some scaffolding structures may be lost over time during these transitions from opaque to transparent gels, whilst others may be retained and collapse when the scaffolding aggregates are lost. These hypotheses could be confirmed using small-angle x-ray (SAXS) and neutron (SANS) scattering techniques. These have been established in other works to deduce the structure of bulk peptide-based supramolecular aggregates to entangled network length scales, providing inference on aggregate properties such as morphology, fibre diameters, and hydration shell dimensions.[2–7] SAXS and SANS data of these gels could also be complemented with data obtained from cryo-SEM (scanning electron microscopy) and cryo-TEM (transmission electron microscopy), which can be used to image and measure the dimensions of the entangled gelator aggregates within frozen gel samples.[2,4,8–11] Combined, these scattering and electron microscopy techniques could help to elucidate why the potentiostatically-grown peptide-based supramolecular hydrogels are not structurally stable, and whether they undergo syneresis or another process of density loss.

The modified Randles circuit, as described in Chapter 2 Section 2.2.6, is a suitable model for single microelectrodes, but should be adapted further to better describe the diffusional and surface-related effects at gel-coated microelectrodes. In Chapter 3 Section 3.4.4, an additional hemispherical feature can be seen emerging in the Nyquist plots of the single Pt microelectrodes coated with Carb-Ala gels that were grown for 300 seconds. This indicates that there may be yet unaccounted-for processes that are not modelled with this equivalent circuit. As asserted by Piper *et al.*,[12] additional circuit components may be required to model an overall negative charge along the fibrous network of the hydrogels, which could repel other negatively charge molecules (such as the FFC redox pair). A new model should be constructed, but only after these theories are confirmed by a firm understanding of the nature of aggregate entanglement and charge along fibres is first acquired. This is once again an avenue that could be explored with the aid of neutron and x-ray scattering techniques.

As a final point of note, this work has demonstrated that suppositions regarding peptide-based hydrogel stability in different aqueous media can be incorrect, and that maybe more than an acid-trigger is required to produce stable electrochemical hydrogels. For many peptide-based supramolecular hydrogels induced into electrochemical acid-trigged assembly, potentiometric electrochemistry is a common method of choice,[1,12–18] though the effects of

its use on the gelator molecules in question seem to not be explored. Without consideration for the electrochemistry of those gelators, it comes into question whether those localised gels are simply composed of assemblages of the bulk gelator, or if these materials are assemblages of a redox product. Even if other peptide-based gelators do not undergo the same or similar electropolymerisation as Carb-Ala does, without control over which species are undergoing redox electrochemistry, fundamental changes to those gelators (which could be crucial in affecting the final properties) of these materials may be occurring without notice. It is then the author's opinion that future works consider carefully what electrochemistry is employed within gelator solutions, and that the electrochemistry of those gelators is studied to a fuller extent. In addition, the instability of these gels could even open up new avenues of research with regards to exploiting the transient nature of these systems in applications that demand the release of a trapped chemical, such as in drug delivery.

6.3 References

1 C. Patterson, B. Dietrich, C. Wilson, A. R. Mount and D. Adams, *Soft Matter*, 2022, **18**, 1064–1070.

2 E. R. Draper, B. Dietrich, K. McAulay, C. Brasnett, H. Abdizadeh, I. Patmanidis, S. J. Marrink, H. Su, H. Cui, R. Schweins, A. Seddon and D. J. Adams, *Matter*, 2020, **2**, 764–778.

3 E. R. Cross, S. M. Coulter, A. M. Fuentes-Caparrós, K. McAulay, R. Schweins, G. Laverty and D. J. Adams, *Chem. Commun.*, 2020, **56**, 8135–8138.

4 K. McAulay, H. Wang, A. M. Fuentes-Caparrós, L. Thomson, N. Khunti, N. Cowieson, H. Cui, A. Seddon and D. J. Adams, *Langmuir*, 2020, **36**, 8626–8631.

5 A. M. Fuentes-Caparrós, F. De Paula Gómez-Franco, B. Dietrich, C. Wilson, C. Brasnett, A. Seddon and D. J. Adams, *Nanoscale*, 2019, **11**, 3281–3291.

6 A. Z. Cardoso, A. E. Alvarez Alvarez, B. N. Cattoz, P. C. Griffiths, S. M. King, W. J. Frith and D. J. Adams, *Faraday Discuss.*, 2013, **166**, 101–116.

7 K. McAulay, L. Thomson, L. Porcar, R. Schweins, N. Mahmoudi, D. J. Adams and E. R. Draper, *Org. Mater.*, 2020, **2**, 108–115.

8 J. J. Panda, A. Mishra, A. Basu and V. S. Chauhan, *Biomacromolecules*, 2008, **9**, 2244–2250.

9 M. Criado-Gonzalez, J. Y. Runser, A. Carvalho, F. Boulmedais, P. Weiss, P. Schaaf and L. Jierry, *Polymer (Guildf).*, 2022, **261**, 125398–125404.

10 S. Selmani, E. Schwartz, J. T. Mulvey, H. Wei, A. Grosvirt-Dramen, W. Gibson, A. I. Hochbaum, J. P. Patterson, R. Ragan and Z. Guan, *J. Am. Chem. Soc.*, 2022, **144**, 7844–7851.

11 Y. Wang, F. Versluis, S. Oldenhof, V. Lakshminarayanan, K. Zhang, Y. Wang, J. Wang, R. Eelkema, X. Guo and J. H. van Esch, *Adv. Mater.*, 2018, **30**, 1707408–1707414.

12 A. Piper, B. M. Alston, D. J. Adams and A. R. Mount, *Faraday Discuss.*, 2018, **210**, 1–17.

13 E. K. Johnson, D. J. Adams and P. J. Cameron, *J. Am. Chem. Soc*, 2010, **132**, 5130–5136.

14 Y. Liu, E. Kim, R. V Ulijn, W. E. Bentley and G. F. Payne, *Adv. Funct. Mater.*, 2011, **21**, 1575–1580.

15 E. K. Johnson, L. Chen, P. S. Kubiak, S. F. Mcdonald, D. J. Adams and P. J. Cameron, *Chem. Commun.*, 2013, **49**, 8698–8700.

16 J. Raeburn, B. Alston, J. Kroeger, T. O. McDonald, J. R. Howse, P. J. Cameron and D. J. Adams, *Mater. Horizons*, 2014, **1**, 241–246.

17 P. S. Kubiak, S. Awhida, C. Hotchen, W. Deng, B. Alston, T. O. McDonald, J. Adams and P. J. Cameron, *Chem. Commun.*, 2015, **51**, 10427–10430.

18 E. R. Cross and D. J. Adams, *Soft Matter*, 2019, **15**, 1522–1528.